
Light-waveform control of molecular processes

Irina Znakovskaya



München 2012

Light-waveform control of molecular processes

Irina Znakovskaya

Dissertation
an der Fakultät für Physik
der Ludwig-Maximilians-Universität
München

vorgelegt von
Irina Znakovskaya
aus Charkow

München, den 26. September 2012

Erstgutachter: Prof. Dr. Matthias F. Kling

Zweitgutachterin: Prof. Dr. Regina de Vivie-Riedle

Tag der mündlichen Prüfung: 18. Dezember 2012

Abstract

The control of chemical reactions is of great interest from both a fundamental and an industrial perspective. Among the many different ways to control the outcome of chemical reactions, control with the electric field waveform of laser pulses offers the possibility to control dynamics on the femtosecond, or even attosecond, timescale. This thesis presents work on a recently developed approach to control molecular processes by guiding electron motion inside molecules with the waveform of light.

The work presented in this thesis started right after the pioneering experiment on laser-induced electron localization in the dissociative ionization of molecular hydrogen with phase-stabilized few-cycle laser pulses. First, electron localization was studied for the different isotopomers H_2 , HD, and D_2 . The laser waveform driven strongly coupled electron and nuclear dynamics was investigated with single and two-color control schemes using near-infrared pulses as the fundamental. Furthermore, the subcycle control of charge-directed reactivity in D_2 at mid-infrared wavelengths ($2.1\ \mu\text{m}$) was both observed experimentally and investigated quantum-dynamically. Two reaction pathways could be detected and controlled simultaneously for the first time.

Extending the approach from the prototype hydrogen molecules, which contain only a single remaining electron after initial ionization, towards complex multielectron systems was a major goal of this thesis and first achieved for carbon monoxide. Experimental and theoretical results (by our collaborators from the de Vivie-Riedle group) on the waveform control of the directional emission of C^+ and O^+ fragments from the dissociative ionization of CO shed light on the complex mechanisms responsible for the waveform control in multi-electron systems. In particular, it was found that not only the dissociation dynamics but also the ionization can lead to an observable asymmetry in the directional ion emission. In CO the contributions from these two processes could not be experimentally distinguished. Studies on another heteronuclear target, DCl, showed that for this molecule mainly the ionization step is responsible for an asymmetry in the fragment emission that can be controlled with the laser waveform. Another result of the studies on complex molecules was that the angular distributions of emitted ions from the breakup of the molecules in few-cycle laser fields showed the contributions of various orbitals in the ionization step. These results were supported by a new theoretical treatment by our collaborators from the de Vivie-Riedle group based on electronic structure theory for diatomic and larger

systems, where multi-orbital contributions could be taken into account. Studies of the angle-dependent ionization of both homonuclear N_2 , O_2 and heteronuclear CO and DCl molecules in few-cycle laser fields clearly show the importance of multi-orbital contributions (two HOMOs or HOMO+HOMO-1).

Finally, waveform-controlled laser fields have been applied to orient molecules. Our findings on DCl suggested that samples of oriented molecular ions can be generated under field-free conditions, where the angle-dependent preferential ionization with a near single-cycle pulse is responsible for the orientation. The control of rotational wave packet dynamics by two-color laser fields was observed for CO and can be interpreted in the framework of two mechanisms: A) the hyperpolarizability orientation mechanism that dominates at low intensities, where the ionization probability is quite low and B) the ionization depletion mechanisms that prevails at high intensities, where substantial ionization occurs.

Zusammenfassung

Die Kontrolle chemischer Reaktionen ist sowohl von größtem fundamentalen wie auch technischen Interesse. Unter den verschiedenen Möglichkeiten, das Ergebnis einer chemischen Reaktion zu kontrollieren, bietet die Kontrolle mittels der Wellenform des elektrischen Feldes von Laserpulsen eine Möglichkeit die Dynamik auf Femto- bis Attosekunden-Zeitskalen zu steuern. Diese Dissertation befasst sich mit einem kürzlich entwickelten Ansatz, molekulare Prozesse durch die Steuerung der Elektronenbewegung in Molekülen mit der Wellenform des Lichts zu steuern.

Die Arbeiten, die in dieser Dissertation beschrieben werden, haben direkt auf dem Pionierexperiment zur laserinduzierten Elektronenlokalisierung in der dissoziativen Ionisation molekularen Wasserstoffs mit phasenstabilen Wenig-Zyklen-Laserpulsen aufgebaut. Zunächst wurde die Elektronenlokalisierung für die verschiedenen Isotope H_2 , HD und D_2 untersucht. Die durch die Laser Wellenform angetriebene, stark gekoppelte Kern- und Elektronendynamik wurde mittels Ein- und Zwei-Farben Kontrollschemas untersucht. Hierbei lag die Fundamentalwellenlänge im Nahinfraroten. Ferner wurde die Sub-Zyklus-Kontrolle der ladungstransfergesteuerten Reaktivität in D_2 im Mittelinfrarot (bei $2.1 \mu\text{m}$ Wellenlänge) experimentell beobachtet und die Ergebnisse mit quantendynamischen Simulationen verglichen. Zwei Reaktionspfade wurden identifiziert und konnten zum ersten Mal gleichzeitig kontrolliert werden.

Die Ausweitung des Ansatzes von den prototypischen Wasserstoff Molekülen, die nur ein verbleibendes Elektron nach der Ionisation enthalten, zu komplexen Multi-Elektronen-Systemen war eines der wesentlichen Ziele dieser Dissertation und wurde erstmals für Kohlenmonoxid realisiert. Experimentelle und theoretische Arbeiten (von unseren Kollaborationspartnern von der de Vivie-Riedle Gruppe) zur Wellenform-Kontrolle der gerichteten Emission von C^+ und O^+ Fragmenten aus der dissoziativen Ionisation von CO haben Licht auf die komplexen Mechanismen geworfen, die für die Wellenform Kontrolle in Multi-Elektronen-Systemen verantwortlich sind. Insbesondere wurde herausgefunden, dass nicht nur die Dissoziationsdynamik sondern auch die Ionisation zu einer beobachtbaren Asymmetrie in der gerichteten Ionenemission beitragen kann. Allerdings konnte bei der experimentellen Untersuchung des CO s der Beitrag der beiden Prozesse nicht unterschieden werden. Untersuchungen an einem anderen heteronuklearen Target, DCl , haben gezeigt, dass für dieses Molekül vorwiegend der Ionisationsschritt für die Asymmetrie in der Emis-

on der Fragmente verantwortlich ist und mit der Wellenform des Lasers kontrolliert werden kann. Ein weiteres Ergebnis dieser Untersuchungen zu komplexen Molekülen war, dass die Winkelverteilungen der emittierten Ionen aus dem Zerfall der Moleküle in Wenig-Zyklen-Laserfeldern Beiträge verschiedener Orbitale zur Ionisation aufweisen. Diese Ergebnisse wurden durch neuartige Rechnungen unserer Kollaborationspartner aus der de Vivie-Riedle Gruppe, die auf elektronischer Strukturtheorie für zweiatomare und größere Systeme basierten und Beiträge mehrerer Orbitale berücksichtigen konnten, gestützt. Untersuchungen zu der winkelabhängigen Ionisation der beiden homonuklearen Moleküle N_2 und O_2 sowie der heteronuklearen Moleküle CO und DCl in Wenig-Zyklen-Laserfeldern haben klar die Bedeutung von Beiträgen mehrerer Orbitale (zwei HOMOs oder HOMO+HOMO-1) zeigen können.

Schließlich wurden Laserfelder mit kontrollierter Wellenform auch eingesetzt, um Moleküle gezielt zu orientieren. Unsere Ergebnisse an DCl weisen darauf hin, dass orientierte molekulare Ionen unter feldfreien Bedingungen erzeugt werden können. Hierbei ist die winkelabhängige präferentielle Ionisation mit nahezu Einzel-Zyklen-Pulsen für die Orientierung verantwortlich. Die Kontrolle der Dynamik von Rotationswellenpaketen durch Zwei-Farben-Laserfelder wurde für CO beobachtet und kann im Rahmen von zwei Mechanismen interpretiert werden: A) dem Hyperpolarisierbarkeits-Orientierungsmechanismus, der bei niedrigen Intensitäten mit sehr niedriger Ionisationswahrscheinlichkeit eine Rolle spielt und B) dem Ionisations-Ausbleichmechanismus, der bei hohen Intensitäten mit substanzieller Ionisation dominiert.

Contents

Abstract	v
Zusammenfassung	vii
Contents	ix
List of Figures	xiii
List of Abbreviations	xv
1 Steering of chemical reactions with the waveform of light	1
1.1 Introduction into light-waveform control	1
1.2 A prerequisite of CEP-stabilization	2
1.3 Subcycle control of molecular reactions	3
1.4 Molecular hydrogen as a prototype system for studying molecular dynamics	4
1.5 Light-waveform control of the dissociative ionization of molecular deuterium	5
2 Experimental techniques	9
2.1 Near-IR few-cycle CEP-stabilized laser source	9
2.2 Velocity map imaging of ionic fragments in molecular dissociation	10
2.3 Mid-IR few-cycle self-CEP-stabilized laser source	11
2.4 Setup to induce and monitor field-free molecular orientation	13
3 Coherent control of electron localization in molecular hydrogen and its isotopes	15
3.1 Theoretical interpretation of laser-induced electron localization	15
3.2 Time-dependent electron localization in the dissociative ionization of D ₂ . .	18
3.3 Experimental observation of electron localization in molecular hydrogen and its isotopes in few-cycle near-IR laser fields	20
3.3.1 Imaging the asymmetric breakup	20
3.3.2 Photodissociation channels in D ₂	22
3.3.3 Asymmetry in the bond softening dissociation	23
3.3.4 Waveform control of the electron localization in hydrogen deuteride	24
3.3.5 Angle-dependent asymmetry by the example of D ₂ and HD	26

3.4	Optimal pulse duration for maximal control of electron localization	27
3.4.1	Asymmetry amplitude vs. pulse duration	27
3.4.2	Asymmetric dissociation of D ₂ in a two-color femtosecond laser field	29
3.5	Asymmetric dissociation of molecular hydrogen in a two-color, attosecond XUV–femtosecond near-IR field	29
3.6	Subcycle-controlled, charge-directed reactivity employing mid-IR few-cycle fields	32
3.6.1	Wavelength dependence of the subcycle control of charge-directed reactivity	32
3.6.2	Quantum dynamical analysis of the control	35
3.7	Conclusions and outlook	38
4	Subcycle control of electron dynamics in multielectron systems	39
4.1	Attosecond control of electron dynamics in carbon monoxide	39
4.1.1	Experimental observation of asymmetric fragment emission	39
4.1.2	The dissociative ionization of carbon monoxide	41
4.1.3	Angle-dependent ionization of molecules: a theoretical approach . .	43
4.1.4	Ionization of CO in few-cycle laser fields	46
4.1.5	Dissociation dynamics of CO in few-cycle laser fields	49
4.1.6	Conclusion and perspectives	52
4.2	Waveform control of orientation-dependent ionization of DCl in few-cycle laser fields	52
4.2.1	Experiment	53
4.2.2	The dissociation pathways	54
4.2.3	Angle-dependent ionization rate of DCl	55
4.2.4	Conclusions and outlook	58
5	Two-color laser-induced field-free molecular orientation	59
5.0.1	Orientation vs. alignment of molecules	59
5.0.2	Previous work on molecular orientation	60
5.1	Experimental results	61
5.2	The two-color field phase assignment	63
5.3	Theoretical interpretation of the experimental data	64
5.3.1	The hyperpolarizability orientation mechanism	64
5.3.2	The ionization depletion mechanism	67
5.4	Conclusions and outlook	70

Contents	xi
Acknowledgments	73
References	75
List of Publications	89
Selected Papers (I - VII)	95
Paper I	97
Paper II	111
Paper III	117
Paper IV	129
Paper V	135
Paper VI	145
Paper VII	153

List of Figures

1.1	Electric field and envelope of few-cycle CEP-stabilized laser pulse	2
1.2	Schematic diagram for the dissociation of D_2^+	6
1.3	Phase dependence of the H_2^+ dissociation probabilities	7
2.1	Schematic diagram of the VMI setup	11
2.2	Schematic setup for field-free molecular orientation	14
3.1	Electron wave functions of ground and excited states of H_2^+	17
3.2	Time-dependent asymmetry in the dissociative ionization of D_2 . Results of the TDSE simulations	19
3.3	Dissociative ionization of D_2 : momentum distribution and asymmetry map	21
3.4	Kinetic energy spectrum and angular distribution of D^+ fragments	23
3.5	Momentum distribution and asymmetry data obtained for H^+ fragments from the dissociative ionization of HD	25
3.6	Angle-dependent asymmetry amplitude in photodissociation of D_2 and HD	27
3.7	Experimental dependence of the D^+ asymmetry on the laser pulse duration	28
3.8	Asymmetry of D^+ ion emission from D_2 in a two-color laser field	28
3.9	Experimentally measured kinetic energy distributions and asymmetry in XUV–near-IR dissociative ionization of D_2	31
3.10	Mechanisms that lead to asymmetry in XUV–near-IR dissociative ionization of H_2	31
3.11	Potential energy surfaces of D_2 , D_2^+ and D_2^{2+}	33
3.12	Momentum distribution and a spectrum of D^+ ions from the dissociation of D_2 in mid-IR few-cycle laser fields	34
3.13	Asymmetry parameter obtained from experimental data and calculations .	36
3.14	Calculated asymmetry of D^+ fragments at subsequential multiple recollisions at $2.1 \mu\text{m}$	37
4.1	C^+ momentum distribution, calculated ionization rate of CO and asymmetry data for the dissociative ionization of CO	40
4.2	Potential energy surfaces of CO and CO^+	42
4.3	Kinetic energy spectra of C^+ fragments obtained in the experiment and theory	42
4.4	Angle-dependent ionization probability of N_2 and O_2	45

4.5	Calculated asymmetry from the ionization step	48
4.6	Time-dependent populations of CO^+ excited states after RCE	50
4.7	Momentum distribution of D^+ fragments from the dissociative ionization of DCl	53
4.8	Asymmetry maps $A(W, \varphi_{CEP})$ for D^+ and Cl^+ ions from the dissociative ionization of DCl	55
4.9	Calculated orientation-dependent ionization probability for the HOMOs of DCl	56
4.10	Angle-dependent asymmetry amplitude of D^+ fragments from the dissociative ionization of DCl	56
4.11	Orientation-dependent ionization of DCl	58
5.1	Schematic illustration of the difference between orientation and alignment for a diatomic polar molecule	60
5.2	Experimentally observed evolution of alignment and orientation parameters vs. pump-probe delay	62
5.3	Theoretically obtained time evolution of alignment and orientation parameters	66
5.4	Field-free orientation parameter for different pump intensities	68
5.5	Calculated field-free orientation parameter vs. the intensity of the two-color pump pulse: comparison of hyperpolarizability orientation and ionization depletion mechanisms	69

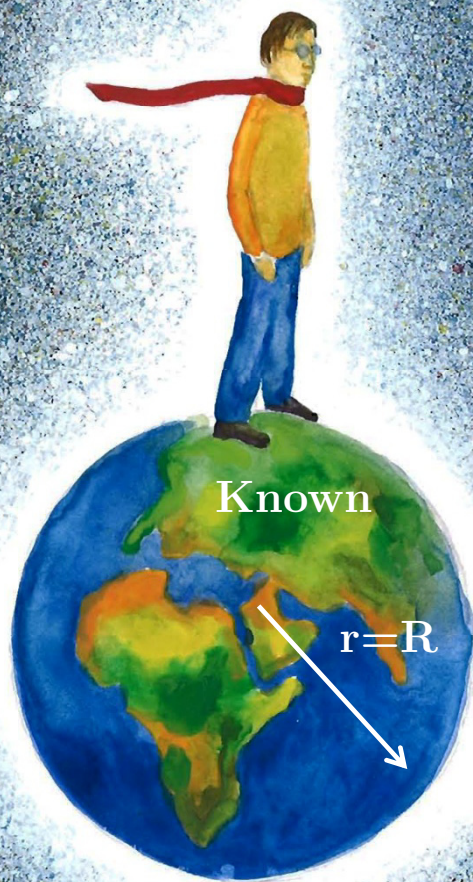
List of Abbreviations

ADK	tunneling ionization model of Ammosov-Delone-Krainov
ATD	above-threshold dissociation
ATI	above-threshold ionization
BS	bond softening
CCD	charge-coupled device
CEP	carrier-envelope phase
COLTRIMS	COLd Target Recoil Ion Momentum Spectrometer
CREI	charge-resonance-enhanced ionization
DF	difference frequency
DFG	difference frequency generation
EI	enhanced ionization
FROG	frequency-resolved optical gating
FWHM	full width at half maximum
HHG	high-order harmonic generation
HOMO	highest occupied molecular orbital
IR	infrared
KER	kinetic energy release
MCP	microchannel plate
Mid-IR	middle infrared
MO	molecular orbital
MO-ADK	molecular-ADK
MO-SFA	molecular strong-field approximation
Near-IR	near-infrared
OPCPA	optical parametric chirped-pulse amplification
QRS	quantitative rescattering theory
RCE	recollisional excitation
RES	rescattering
SFA	strong-field approximation
TDSE	time-dependent Schrödinger equation
THG	third-harmonic generation
TOF	time-of-flight
UV	ultraviolet

- VMI velocity map imaging
- XUV extreme ultraviolet

The only true wisdom is in knowing
you know nothing.

—SOCRATES



Unknown

$$A = 4\pi r^2$$

if $r \rightarrow \infty$ then $A \rightarrow \infty$

Steering of chemical reactions with the waveform of light

1

1.1 Introduction into light-waveform control

Control and tracing of molecular dynamics is one of the ultimate goals of chemical physics and is directly related to the elementary motion of nuclei and electrons inside molecules. The time scale of nuclear motion in molecules typically lies in the femtosecond regime ($1 \text{ fs} = 10^{-15} \text{ s}$). The much lighter electrons move faster than nuclei and can reach the attosecond ($1 \text{ as} = 10^{-18} \text{ s}$) time scale. Active attention to the field of the control of molecular processes has been stimulated largely by the progress in ultrashort laser source development.

Experimental femtochemistry, introduced by Nobel laureate Ahmed H. Zewail in the mid-1980s, utilizes laser pulses of femtosecond duration to control and track chemical dynamics via direct observation of the nuclear wave packet motion [1], and has become a well-established field of research (see e.g. [1, 2, 3, 4]). Recent development of intense few-cycle laser pulses and the birth of attosecond physics [5] has provided tools for exploring and controlling electron processes on sub-laser-cycle time scales. Steering electrons in molecules on their natural time scale can be seen as a new tool for controlling chemistry. The approach for controlling electron motion in molecules employing multi-color laser fields was first introduced by Brumer and Shapiro [6, 7]. Among many laser field configurations, the $\omega_2 = 3\omega_1$ phase control of the ionization and dissociation of a variety of diatomic molecules has been investigated (see e.g. Refs. [8] and [9]). Ultrashort laser pulses consisting of only few field oscillations, that became available recently, provide an additional parameter for controlling electron dynamics: the offset of the maximum of the carrier wave with respect to the pulse envelope (carrier-envelope phase, CEP).

This thesis summarizes the successful application of CEP-stabilized few-cycle laser pulses to the waveform control of molecular processes, including their ionization, recollision induced excitation and dissociation.

1.2 A prerequisite of CEP-stabilization

Multicycle femtosecond laser pulses have been intensively used in many different fields in both physics and chemistry. For the case of even shorter few-cycle pulses the pulse duration of the laser approaches the optical cycle period. An optical cycle of light derived from a Ti:sapphire laser at 800 nm lasts only 2.7 fs. The electromagnetic field waveform of such a pulse starts to play an important role in strong-field processes and controlled field waveforms have opened up new avenues for coherent control through the control of electron motion [10, 11]. Controlled light waveforms have become available through the ground-breaking frequency comb metrology of Nobel laureate Theodor W. Hänsch and coworkers [12]. The extension of this metrology to amplified laser systems was achieved by Baltuška et al. [13]. In this approach, the CEP of a laser waveform, given as $E(t) = E_0(t) \cos(\omega t + \varphi_{CEP})$ for an envelope function $E_0(t)$, angular carrier frequency ω and a phase offset of the carrier φ_{CEP} , can be actively stabilized. Fig. 1.1 illustrates the time evolution

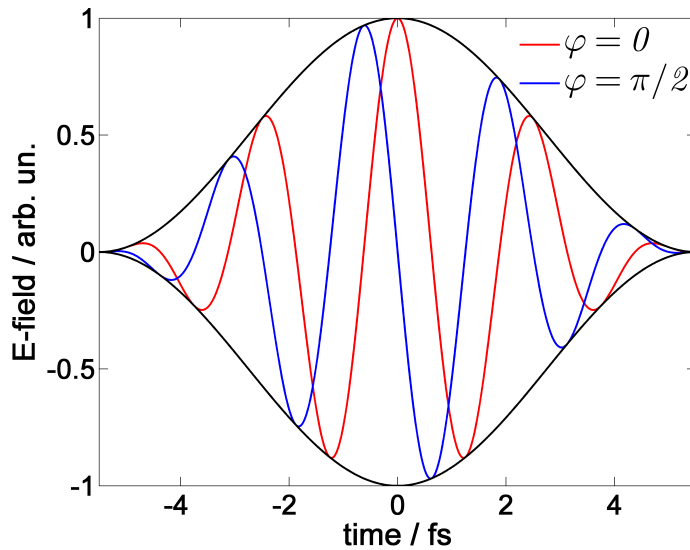


Figure 1.1: Illustration of two typical carrier electric field waves (red and blue) with pulse envelope (black line) of a 4 fs laser pulse (FWHM) with a central wavelength of 750 nm. CEP equals to 0 (red line) and $\pi/2$ (blue line). The amplitude of the electric field is normalized to 1 at its maximum.

of a few-cycle laser field where the envelope $E_0(t)$ has a cosine square functional form (see Eq. 1.1) similar to how it was introduced in [14] and used in our recent work [15]. The electric field is defined in a time interval $-T_p/2 \leq t \leq T_p/2$, where $T_p = n_p T = 2\pi n_p / \omega$

is the total pulse duration with the number of cycles n_p , so that the envelope function possesses its maximum value at $t = 0$

$$E(t) = E_0 \cos^2(\pi t/T_p) \times \cos(\omega t + \varphi_{CEP}). \quad (1.1)$$

A temporally symmetric (with respect to time zero) electric field that has $\varphi_{CEP}=0$ is a so-called cosine pulse. Analogically the temporally antisymmetric field with $\varphi_{CEP}=\pi/2$ is called a sine pulse [16].

The first CEP-effects in an atomic system were observed in above-threshold ionization (ATI) of xenon [17], where the direction of electron emission from photoionized xenon atoms was controlled by varying the phase of the field. The electron emission was detected in two opposite directions along the laser polarization vector by two time-of-flight (TOF) detectors with a stereographic ATI phase-meter. Stabilization and control of the CEP with comparably high precision has made many experiments possible that are directly related to attosecond physics [5]. CEP-controlled laser pulses can be used to control the electron localization during molecular dissociation, as has been demonstrated for the first time for the homonuclear D_2 and heteronuclear HD molecules [10, 11]. Recently, a novel approach in which single-shot measurements using a COLd Target Recoil Ion Momentum Spectrometer (COLTRIMS) or velocity map imaging (VMI) have been combined with the single-shot tagging of the CEP by a stereographic ATI phase meter, was introduced [18, 19]. This method enables experiments on CEP-control without active stabilization. This considerably simplifies measurements and allows days-long experimental data acquisition and much improved statistics in experiments on CEP effects. Therefore, single shot measurements can have a higher precision as compared to the case of employing CEP-locking, where the locking duration is typically limited to a few hours.

1.3 Subcycle control of molecular reactions

Photochemistry involves the making and breaking of bonds between atoms with light fields. Coherent control of photochemical reactions has been achieved in the last decades by manipulating the laser frequency, phase, and polarization [20]. An exciting prospect is to directly control a photoinduced molecular reaction by preparing and guiding an electronic wave packet inside a molecule to form or even break chemical bonds. Whereas early experiments focused mainly on the control of the nuclear motion of relatively heavy molecules, modern ultrashort laser pulses allow the control of the nuclear motion in lighter molecules

such as molecular hydrogen [20, 21]. A novel scheme employing waveform-controlled light fields to directly control a molecular reaction in the sense of charge-directed reactivity [22] offers the promise of significantly enhancing the possibilities for achieving control by steering the electrons by the light waveform rather than allowing the electrons to move freely. The steering of electron motion can be achieved by superimposing different electronic states with a controlled phase relationship.

The state-of-the art of the CEP-control of molecular processes and the advancement that was achieved within the framework of this thesis will be introduced. CEP-stabilized few-cycle pulses in the near-infrared (near-IR) have been used to control molecular ionization and dissociation [10, 11, 23, 24, 25, 26, 27]. The control metrology was extended recently to the mid-infrared (mid-IR) and the subcycle control of charge-directed reactivity of the dissociative ionization of molecular hydrogen [28].

1.4 Molecular hydrogen as a prototype system for studying molecular dynamics

Ionization and dissociation of molecular hydrogen with ultrashort laser pulses has raised interest in the femtochemistry and strong field communities (see [29] and references cited therein). The research on the hydrogen molecule and its isotopes remains very active and important. Molecular hydrogen has also lend itself as a prototype system for studying the control of nuclear and electronic motion for the following reasons:

- 1) The H_2^+ vibrational wave packet dynamics are extremely fast and can only be resolved with a temporal resolution in the few-fs regime [30, 31].
- 2) The H_2^+ molecular ion contains two protons and only one electron. The dynamics in the presence of a strong laser field can be numerically modeled with a high accuracy.

An additional important benefit of the hydrogen molecular ion is that its lower electronic states, the $X^2\Sigma_g^+$ and $A^2\Sigma_u^+$ states, are energetically well separated from higher excited states (see e.g. Fig. 3.11 for the case of D_2). The coherent superposition of these electronic states, that can be controlled by the CEP, is responsible for electron localization during the dissociation of the molecular ion [10, 32, 33, 34]. Experimental and theoretical studies on molecular hydrogen play an important role for the understanding of ultrafast processes in molecules. At the same time, studies of molecular hydrogen are a point of departure for studies on complex molecules, in particular with regard to the manipulation of electron dynamics in multielectron systems.

1.5 Light-waveform control of the dissociative ionization of molecular deuterium

For the molecular dissociation of a diatomic molecule, the effect of the CEP can be complex. In general, the waveform control of molecular dissociation can be determined by i) the ionization step (see e.g. [26] for the CEP control of the ionization of DCl), ii) the recollision dynamics leading to the coherent excitation of various excited states of the molecular ion, and iii) laser induced coupling between various electronic states of the molecular ion, which in turn can result in electron localization (see e.g. [10, 23, 35]). For heteronuclear molecules, all three mechanisms can contribute to the final outcome [24]. This thesis first introduces the CEP-control in the simple homonuclear molecule D_2 and compares the mechanism of its dissociation with its isotopomer HD. The waveform control of multielectron heteronuclear molecules is discussed in chapter 4. Note that for homonuclear molecules step i) does not contribute to the asymmetry as confirmed for the D_2 molecule by the study of Kremer *et al.* [23]. When we consider a prototype homonuclear molecule D_2 interacting with an intense few-cycle near-IR laser field, the D_2 molecule is typically ionized in the first step by the intense laser field (red arrow at the Fig. 1.2) and a nuclear wave packet is launched on the $X^2\Sigma_g^+$ potential of the resulting ion. This initial step can be followed by several processes leading to the dissociation of the molecular ion: i) the electron released into the laser field via tunnel or multiphoton ionization [36] might return back at a later time. According to Ref. [37] the recollision is most probable around 2/3 of an optical cycle. Recollision with the D_2^+ ion can lead to excitation to the repulsive $A^2\Sigma_u^+$ state (identified as recollisional excitation RCE), whereby the molecular ion starts to break apart (Fig. 1.2a). In the alternative mechanism (ii) laser-induced coupling of the $X^2\Sigma_g^+$ and $A^2\Sigma_u^+$ states leads to dissociation via bond softening (BS) [29, 38, 39, 40] (Fig. 1.2b). Some other possible dissociation paths such as the dissociative autoionization of highly excited neutral states are omitted here.

While the molecular ion dissociates either via BS or RCE the laser field continues to interact with it. The symmetry of the system is broken by a coherent superposition of two electronic states with different parity ($X^2\Sigma_g^+$ and $A^2\Sigma_u^+$). So that the final state wave function can be represented in terms of localized electronic states. That leads to time-dependent electron localization. Physically, the electron wave packet is oscillating between two D^+ ions till it becomes localized at one of the nuclei. When the D_2^+ molecule dissociates, the interatomic barrier that builds up between the two D^+ ions rises and blocks

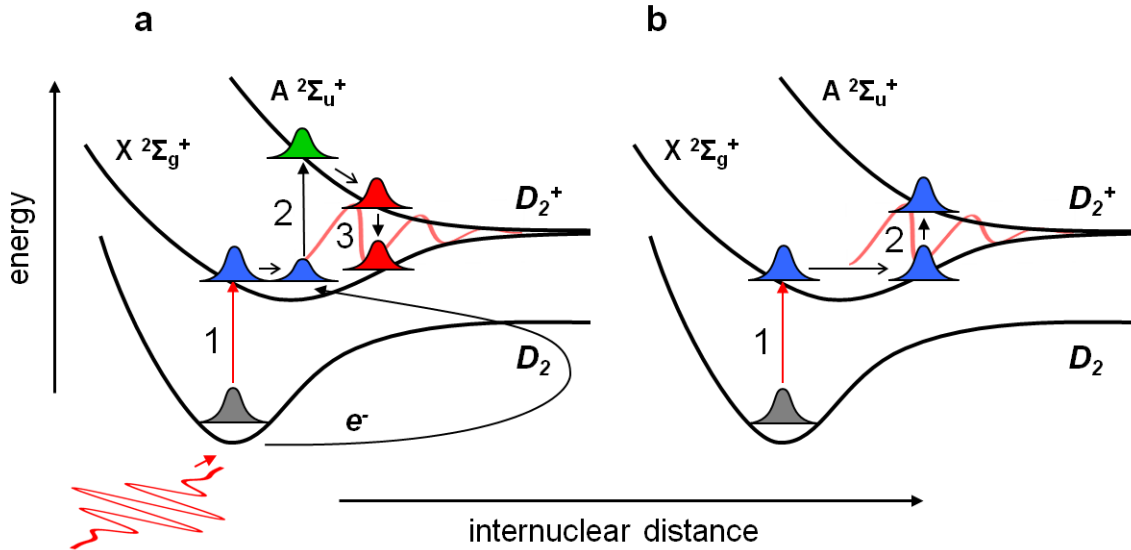


Figure 1.2: Schematic diagram for the dissociation of D_2^+ involving two different mechanisms i) via recollisional excitation (RCE) and ii) via bond softening (BS). Note that the states $X^2\Sigma_g^+$ and $A^2\Sigma_u^+$ are sometimes referred to as $1s\sigma_g$ and $2p\sigma_u$ respectively.

further oscillations of the electron density such that the electron localizes and an ion leaves to one side and a neutral D atom (containing the electron) to the other.

The first theoretical discussion of CEP-effects in the dissociation of HD^+ and H_2^+ molecular ions came out in 2004 [41]. The authors numerically solved the time-dependent Schrödinger equation taking into account the interaction of molecular ion with a 10 fs (full width at half maximum, FWHM) laser pulse at a central wavelength of 790 nm. For calculations reported there, the initial state was the ground state of the molecular ion, initial population of higher excited states were not taken into account. A strongly correlated ratio of the probabilities to measure the products of the dissociation at 0° and 180° (up and down directions) relative to the vertical polarization vector was predicted. The calculated dissociation probability refers to the detection of a neutral H atom as a product of the dissociation of the H_2^+ molecular ion (see Fig. 1.3). The degree of control can be characterized using directional asymmetry of electron or fragment emission (as described in detail in chapter 3). The maximum amplitude of the asymmetry corresponding to the calculated dissociation probability in Ref. [41] is equal to about 0.5. It should be noted that excluding the ionization step can significantly simplify the analysis of the light-waveform control process.

Due to the rapid advance in laser technology, CEP-dependent molecular experiments

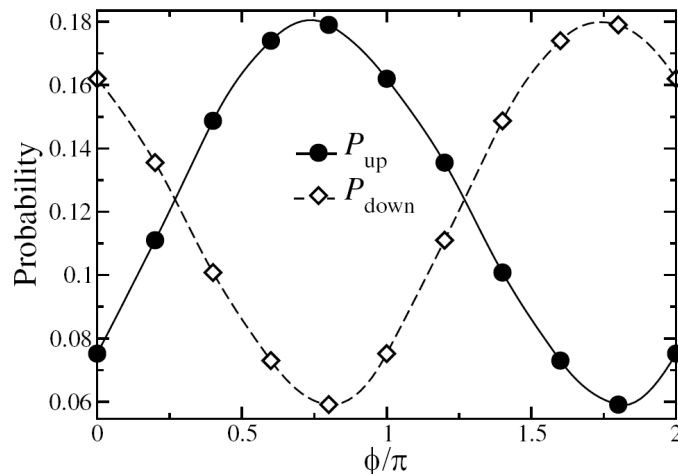


Figure 1.3: Phase dependence of the H_2^+ dissociation probabilities to detect H atom at 0° (solid lines) and at 180° (dashed lines) for the peak intensity of $9 \times 10^{14} \text{ W cm}^{-2}$ [41].

have also progressed rapidly. The first experimental implementation of the field-controlled electron localization in the dissociative ionization of the D_2 molecule appeared in 2006 [10]. This thesis contains work that follows the first experiment on the CEP control of molecular dynamics [10].

The thesis is organized in 5 chapters. The introduction in chapter 1 is followed by experimental techniques in chapter 2. Chapter 3 presents studies on the role of strongly-coupled electron and nuclear dynamics on the isotopomers H_2 , HD , and D_2 in few-cycle CEP-stabilized laser fields applying diverse single and two-color control schemes using near-IR pulses as the fundamental. Furthermore, studies on the control of charge-directed reactivity in D_2 at mid-IR wavelengths are presented. Chapter 4 describes the extension of the approach of coherent control with few-cycle fields to the multielectron heteronuclear molecules CO and DCl , elucidating the roles of the CEP control in ionization and dissociation processes. Chapter 4 also contains studies on the angle-dependent ionization of both homonuclear N_2 , O_2 and heteronuclear CO and DCl molecules in few-cycle laser fields, taking into account multi-orbital contributions. Finally, chapter 5 describes the waveform control of rotational wave packets and field-free orientation of CO by two-color laser fields.

Experimental techniques

2

2.1 Near-IR few-cycle CEP-stabilized laser source

The laser sources used in the experiments on the light-waveform control for the molecules HD, CO, and DCl as well as for the experiments on the imaging of molecular orbitals of N₂ and O₂ are briefly described here. Near-IR few-cycle CEP-stabilized laser systems are part of the attosecond infrastructures AS-1 and AS-5 in the Laboratory for Attosecond Physics (LAP) at the Max Planck Institute of Quantum Optics. The experimental schemes of both laser setups are similar. Detailed descriptions of the AS-1 setup can be found in Refs. [10, 42]. This section essentially describes further details of the AS-5 infrastructure, which has been built during the duration of this Ph.D. project and has been applied for the first time in some of the studies that are described here.

Transform-limited, phase-stable laser pulses at 790 nm central wavelength of ~ 25 fs duration with 1.3 mJ energy/pulse at 1 kHz repetition rate have been generated by an amplified Ti:sapphire laser system described elsewhere [43, 44]. The pulses were spectrally broadened using a 1 m long hollow-core fiber of 250 μm diameter filled with 2.5 bar neon gas. The laser pointing into the fiber was controlled with high precision using a commercial beam stabilization system (Beamlock, TEM Messtechnik). The output pulses from the fiber were compressed in a chirped-mirror compressor to a near-transform limited duration of 5 fs at a central wavelength of 720 nm and with up to 600 μJ pulse energy. Note that recently the pulse duration was improved to sub-4 fs.

The pulse duration was monitored online with a commercial dispersion balanced autocorrelator (Femtometer, Femtolasers). CEP-stabilization is realized by managing the dispersion inside the laser oscillator with an active feedback loop. The measurement method employed is an f-to-0 technique [45] and consists of measuring the interference beat signal arising from the difference frequency generation of the high-frequency wing and the low-frequency wing of a more than octave spanning spectrum generated from a mode-locked oscillator [46, 47]. In its implementation at the AS-5 beamline, CEP stabilization has been realized by two feedback loops as described in [48]. The CEP jitter was smaller than 150 mrad over a period average of several hours. The φ_{CEP} was varied in the experiment by insertion of dispersive material via a pair of wedged fused silica plates. As the laser pulse propagates through the dispersive material, the carrier wave and the pulse envelope

travel with different velocities, the phase velocity and the group velocity, respectively. The difference in the velocities induces a shift of the CEP, which is proportional to the glass thickness, therefore the material thickness can be employed as the CEP-controlling parameter. Note that the thickness of the fused silica wedges modifying the CEP needs to be varied only by tens of micrometers such that the induced group delay dispersion is small and does not significantly affect the pulse duration.

2.2 Velocity map imaging of ionic fragments in molecular dissociation

The phase-stabilized, linearly polarized pulses were focused with a spherical mirror into a VMI spectrometer [49, 50]. The VMI spectrometer consists of the ion optics (repeller, extractor, ground plate) and a microchannel plate (MCP)/phosphor screen detector (see Fig. 2.1). Focusing mirrors of focal lengths in the range of 12.5 cm to 80 cm were used for different measurements. The peak intensity in the focus (typically in the range of 10^{13} to 10^{14} W cm⁻²) was determined via the cutoff in electron spectra recorded for ATI of Xe [51, 52] under the same experimental conditions as for molecular experiments. An adjustable iris was used to vary the intensity in the focus. Ions or electrons that were generated at the crossing point between the laser focus and the molecular beam in the VMI were accelerated and projected onto the detector using a static electric field. The 2-dimensional velocity map images were recorded with a low-noise, Peltier-cooled CCD (charge-coupled device) camera (Sensicam, PCO). Different ionic species were distinguished by their TOF spectra towards the detector and appropriate gating of the MCP with a laser-triggered, fast high-voltage switch (Behlke).

3D momentum distributions of recorded ions and electrons are obtained from the 2D projections by an iterative inversion procedure [53]. The ion distribution at the detector in Fig. 2.1 shows the 2D projection of the 3D momentum distribution. Illustrated here is the fragment distribution of C⁺ ions from the dissociation of CO in the presence of a 4 fs cosine pulse ($\varphi_{CEP} = 0$) at a central wavelength of 740 nm [24]. The laser is linearly polarized along the p_y -axis and propagates along p_x . The experimental data exhibit cylindrical symmetry with the symmetry axis being the laser polarization axis. In our notation of the axes we have followed the original work by Vrakking [53]. In this thesis the measured ion distributions lie in the x-y plane with the symmetry axis being parallel to the y-direction. The polar angle θ is defined as the angle between a vector \vec{p} in the detector plane and the

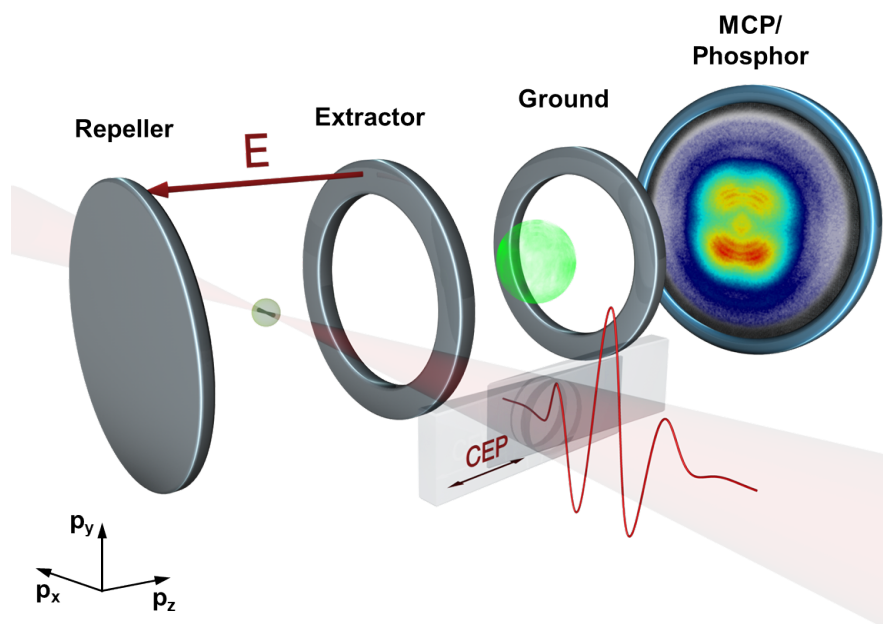


Figure 2.1: Setup for the measurement of molecular dissociation with ultrashort intense laser pulses: the waveform of the laser pulses is controlled with a pair of glass wedges. The laser pulses interact with the molecules in a velocity map imaging (VMI) spectrometer, in which the resulting distribution of ions (here C^+ fragments from dissociative ionization of CO) after the break-up of the molecules is imaged onto a detector (MCP/phosphor screen assembly). The image on the detector displays an up/down asymmetry along the vertical polarization axis of the laser that was measured for a certain CEP value. Figure courtesy: Christian Hackenberger, Max Planck Institute of Quantum Optics (MPQ).

y-axis. The z-axis is the projection coordinate along the spectrometer axis.

2.3 Mid-IR few-cycle self-CEP-stabilized laser source

Details of the mid-IR laser source used in the experiment on charge-directed reactivity in D_2 molecules can be found in Ref. [54]. Briefly, the home-built few-cycle mid-IR light source with a central wavelength of $2.1 \mu\text{m}$ is based on three optical parametric chirped-pulse amplification (OPCPA) stages pumped by an optically synchronized 50 ps, 11 mJ Nd:YLF laser. Difference frequency (DF) mixing was employed for generating the mid-IR seed, resulting in a signal that is self CEP-stabilized without the need for an active feedback loop [54]. The difference of the high- and low- frequency wings f_m and f_n from a spectrally broadened Ti:sapphire laser pulse was generated in a periodically poled lithium

niobate (PPLN) crystal. The frequency comb of the DF signal can be written as:

$$f_{m-n} = f_m - f_n = (mf_r + f_{offset}) - (nf_r + f_{offset}) = (m - n)f_r \quad (2.1)$$

where f_r is the pulse repetition rate of a mode-locked oscillator. The carrier-offset frequency f_{offset} cancels out, thus resulting in a stable self-CEP-stabilized signal. The quality of the self-stabilization of the CEP was demonstrated by imaging the directional control of the electron emission in the photoionization of xenon [55]. As shown in Ref. [55] the difference frequency generation (DFG) stabilization scheme significantly simplifies CEP-dependent measurements, allowing for longer continuous data acquisition.

The generated seed was stretched with a pair of gratings and an acousto-optic programmable dispersive filter (DAZZLER) to about 50 ps. The output of the OPCPA system (~ 50 ps, 740 μ J) can be compressed to 16–25 fs (FWHM) by propagating the pulses through a 10 cm-long silicon rod. The resulting output pulses were characterized using a home-built third-harmonic generation (THG) frequency-resolved optical gating (FROG) device [54]. After compression linearly polarized self-CEP-stabilized few-cycle laser pulses with an energy of 350 μ J, a repetition rate of 1 kHz and a central wavelength of 2.1 μ m are available. The D₂ measurements were done with about 25 fs (FWHM) laser pulses. The relative phase in the experiment was varied by changing the position of a pair of silica wedges in the beam path. The laser beam was sent through an adjustable iris and focused to a spot size of approximately 50 μ m diameter in the center of the VMI spectrometer with a $f = 30$ cm CaF₂ lens. The focal size was estimated using Gaussian beam propagation on the ground of the known aperture diameter and the beam quality factor M^2 that was determined separately by a knife-edge scan. The peak intensity of the laser field was determined from first principles, i.e. using the energy of the laser pulse, radius of the iris, laser spectrum and M^2 parameter of the laser. All systematic errors and particularly the error in the determination of the M^2 parameter result in the error bar of the peak intensity of approximately $\pm 24\%$. The fragments of dissociative ionization of D₂ were recorded employing a VMI spectrometer that was described above.

2.4 Setup to induce and monitor field-free molecular orientation

Field-free orientation of carbon monoxide [56] was controlled by an intense two-color laser field $E(t) = E_1(t)\cos(\omega t) + E_2(t)\cos(2\omega t + \varphi_{two-color})$ with ω and 2ω in the experiment corresponding to the wavelength of 800 nm and 400 nm, respectively. The laser pulses were generated by the Kansas Light Source (KLS) of the James R. Macdonald Laboratory at Kansas State University (KSU).

Pulses with 45 fs duration at 800 nm produced from a Ti:sapphire laser (1.5 kHz, 2mJ) were split into a pump and a probe arm of a Mach-Zehnder interferometer. The setup scheme is displayed in Fig. 2.2. In the pump arm, the second harmonic of 800 nm was created using a 250 μm thick β -Barium borate (BBO) crystal cut at $\theta = 29^\circ$. The difference in the group velocity dispersion of the fundamental and the second harmonic causes a delay between two pulses when both beams propagate through dispersive optics. Two calcite plates with a thickness of 600 μm were used to temporal overlap the two colors from the pump arm. The first is used for a course overlap of the two fields in time. The second calcite plate controlled by a motorized rotation stage shapes the excitation field by adjusting the relative phase $\varphi_{two-color}$ between the two fields. The excitation field for $\varphi_{two-color}=0$ is schematically shown in the inset of Fig. 2.2). To compensate the effect that the two pulses are orthogonally polarized after the BBO crystal, a thin-film zero-order quartz half wave plate with a thickness of 200 μm was used. The plate acts as a half-wave plate (rotates by 90°) for the fundamental and as a full-wave plate (rotates by 180°) for the second harmonic field. The resulting polarization of all laser pulses used in the experiment is vertical. The intensity of the excitation field was optimized by an iris in the pump arm. Laser pulses were focused onto a supersonic jet of CO molecules ($T_{rot} = 60$ K) inside a VMI spectrometer by a spherical mirror ($f = 75$ mm) placed in the vacuum chamber at the rear side of the chamber just outside the spectrometer.

The pump-probe scheme employs the Coulomb explosion imaging of CO molecules by a single-color (800 nm) laser pulse from the probe arm at a varying time delay to the two-color induced field-free orientation by the pump arm. The resulting C^{2+} fragment ions were projected by ion optics of the VMI onto the detector and recorded by a CCD camera. Note that in contrast to the VMI spectrometer described above, the high-energy VMI designed by N. G. Johnson and build by S. De is based on multiple electrodes. The ion optics in total comprise 11 electrodes: the repeller and a sequence of 9 plates with

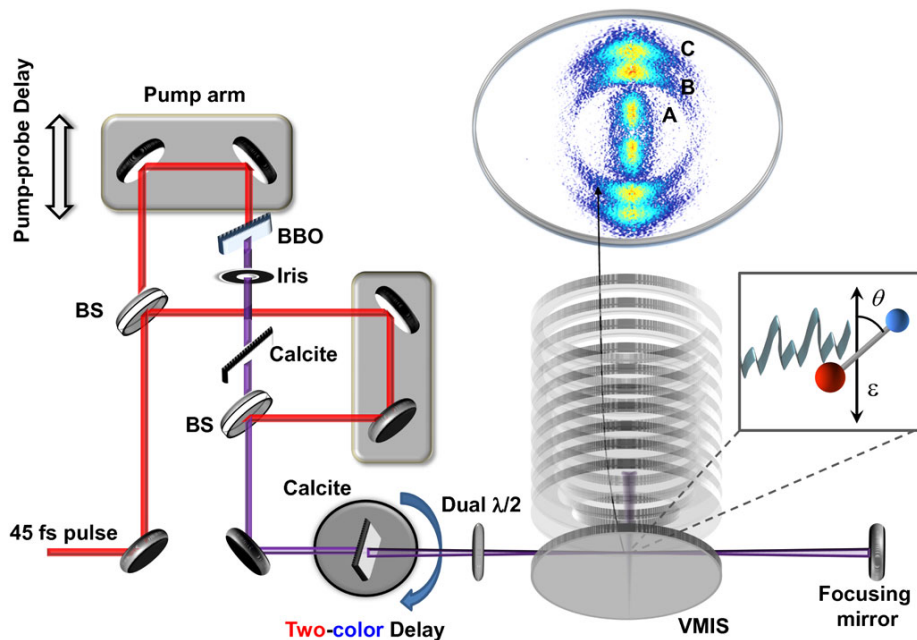


Figure 2.2: Schematic setup used to induce and monitor field-free molecular orientation. A, B and C indicate channels for the formation of C^{2+} ions from the Coulomb explosion of CO as described in the text. From [56].

decreasing voltage and a ground electrode [57]. The design of the ion optics and focusing voltages were optimized by SIMION simulations. The high energy VMI at KSU can image charged fragments with kinetic energies up to 300 eV at 10 kV repeller voltage.

An example of C^{2+} ionic fragments from the Coulomb explosion of CO recorded in our experiment is shown in Fig. 2.2. The cut through the momentum distribution is reconstructed from the 2D-projection that is recorded in the experiment with an iterative inversion procedure [53]. Different channels for the production of C^{2+} ions are visible, where together with a C^{2+} ion a neutral O atom (A), singly charged O^+ ions (B) and doubly charged O^{2+} ions (C) are formed. It is apparent that the momentum distributions of all three channels peak along the vertical laser polarization axis.

Coherent control of electron localization in molecular hydrogen and its isotopes

3

3.1 Theoretical interpretation of laser-induced electron localization

The asymmetric dissociative ionization of molecular hydrogen and its isotopes can be modeled by semi-classical approaches and by solving the time-dependent Schrödinger equation (TDSE). The TDSE approach used in Refs. [10] and [11] is described briefly here to introduce the general concept of how CEP-controlled few-cycle laser pulses can control the electron localization in the dissociative ionization of molecular hydrogen. The molecules are assumed to be aligned along the laser polarization axis. This simplification reduces the calculations to 1 dimension for the nuclear motion. The approximation is somewhat validated by experimental and calculated ionization rates of molecular hydrogen in the presence of a strong laser field: the ionization rate for the highest occupied molecular orbital (HOMO) has a maximum along the laser polarization axis [58]. A consequence is that the molecular ion is predominantly aligned along the laser polarization axis. Note that the calculations reported in Refs. [10] and [11] assume an ionization at the peak of the few-cycle laser pulse. The ionization of a molecule in a strong laser field is typically modeled as a Franck-Condon transition. Here, the vibrational ground state wave function of the neutral molecule is projected onto electronic states of the molecular ion [59, 60]. Successive RCE of the ion to the A-state is assumed to occur at the time of recollision between the released electron and the molecular ion. The successive dynamics are modeled as follows.

The interaction Hamiltonian between electronic states of the molecular ion in the presence of the laser field is given by:

$$\hat{H} = \hat{T}(R) + \hat{V}(R). \quad (3.1)$$

Inserting the full wave function of the molecular ion (Eq. 3.3) and the interaction Hamil-

tonian into the TDSE $i\hbar\frac{\partial\Psi}{\partial t} = \hat{H}\Psi(R, t)$, the coupled equations of nuclear wave functions can be written as:

$$i\frac{\partial}{\partial t} \begin{pmatrix} \psi_g(R, t) \\ \psi_u(R, t) \end{pmatrix} = \begin{pmatrix} \frac{-1}{M} \frac{\partial^2}{\partial R^2} + V_g(R) & V_{gu}(R) \\ V_{gu}^*(R) & \frac{-1}{M} \frac{\partial^2}{\partial R^2} + V_u(R) \end{pmatrix} \begin{pmatrix} \psi_g(R, t) \\ \psi_u(R, t) \end{pmatrix} \quad (3.2)$$

where $V_g(R)$, $V_u(R)$, and $V_{gu}(R)$ are the binding and dissociative potentials and the coupling between them. In the treatment reported in Refs. [10] and [11] tabulated values for the potentials from Ref. [61] were used. Integrating and solving Eq. 3.2 yields the time-dependent nuclear wave functions $\psi_{g/u}(R, t)$. For the calculation of the asymmetric electron localization a basis of localized states (as described below) is used.

Similar theoretical approaches for the coupled electron-nuclear dynamics are described in detail in [10, 11, 62, 63]. Considering only the two lowest-lying electronic states of the hydrogen molecular ion, the full wave function for the electronic coordinate r and internuclear distance R at an arbitrary time t is given by:

$$\Psi(R, t) = \psi_g(R, t)\phi_g(r; R) + \psi_u(R, t)\phi_u(r; R) \quad (3.3)$$

where $\phi_{g/u}(r; R)$ describe the single electron wave functions in H_2^+ (field-free electronic states), identified in Refs. [10] and [11] as $|g\rangle$ and $|u\rangle$, respectively, and $\psi_{g/u}(R, t)$ represent the nuclear wave functions for the $1s\sigma_g$ and $2p\sigma_u$ Born-Oppenheimer potential energy surfaces. In a quantum-mechanical representation electronic wave functions of a diatomic molecule can be described as a linear combination of wave functions of atomic electronic states, in our case electronic states of the hydrogen atom. The electron becomes localized on the left or right nucleus with corresponding electronic wave functions $\phi_{left}(R)$ and $\phi_{right}(R)$, the electronic coordinate r is dropped from here for simplicity:

$$\phi_{g/u}(R) = \frac{1}{\sqrt{2}}(\phi_{left}(R) \pm \phi_{right}(R)). \quad (3.4)$$

A simplified example of localized states is shown in Fig. 3.1 in terms of electronic wave functions. Electronic wave functions of the ground $1s\sigma_g$ and the first excited $2p\sigma_u$ states of the H_2^+ molecular ion along with their probability densities are shown in Figs. 3.1a-d. Figs. 3.1e and f illustrate the probability of detecting the electron on the left or right hydrogen atom [64].

Using the definition in Eq. 3.4 the corresponding nuclear wave functions are obtained:

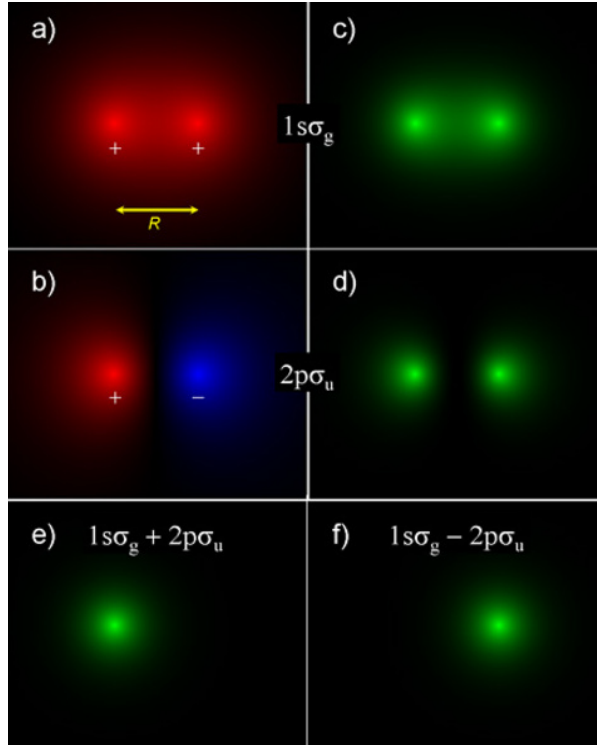


Figure 3.1: (a), (b) Electron wave functions of the ground $1s\sigma_g$ and the first excited $2p\sigma_u$ states of the H_2^+ molecular ion. (c),(d) represent the corresponding probability densities as a square of the absolute value of the wave functions. (e) and (f) illustrate the probability to detect the electron on the left or right atom, respectively. For more details see [64].

$$\psi_{g/u}(R, t) = \frac{1}{\sqrt{2}}(\psi_{left}(R, t) \pm \psi_{right}(R, t)) \quad (3.5)$$

and *vice versa*:

$$\psi_{left/right}(R, t) = \frac{1}{\sqrt{2}}(\psi_g(R, t) \pm \psi_u(R, t)). \quad (3.6)$$

In such a way $\psi_{left/right}(R, t)$ can be interpreted as nuclear wave functions associated with localized electronic states. Consequently, the description in terms of localized nuclear or electronic states appears naturally. Following Ref. [63] the spatial representation of the electron localization can be extracted directly as a probability to detect the nucleus on the left or right part of the molecule:

$$L_e(R, t) = \psi_{left}(R, t)^* \psi_{left}(R, t) - \psi_{right}(R, t)^* \psi_{right}(R, t). \quad (3.7)$$

Applying the Fourier transformation and thereby converting the wave functions into momentum space, the momentum-dependent asymmetry is obtained as follows:

$$L_e(p, t) = \psi_{left}(p, t)^* \psi_{left}(p, t) - \psi_{right}(p, t)^* \psi_{right}(p, t). \quad (3.8)$$

The momentum-dependent asymmetry calculated using equation Eq. 3.8 can be directly compared with experimental data. In the experiment, left and right are defined as the directions along the laser polarization, so that the experimental asymmetry follows the equation:

$$A(E, \alpha) = \frac{N_{left}(E, \alpha) - N_{right}(E, \alpha)}{N_{left}(E, \alpha) + N_{right}(E, \alpha)}, \quad (3.9)$$

where $N_{left/right}$ are the number of ions detected on the left or right side of the detector as a function of the kinetic energy of detected fragments E and the parameter α . The parameter α can be the CEP: $\alpha = \varphi_{CEP}$ [10, 11, 23, 28, 65] or alternatively α can be a delay between an attosecond extreme ultraviolet (XUV) pulse and a few-cycle near-IR pulse [62, 63, 66], $\alpha = \tau$.

3.2 Time-dependent electron localization in the dissociative ionization of D_2

The treatment summarized above may qualitatively explain the physics for the observed phase-control that occurs after the ionization of the molecule by the maximum of the laser field. Note that the calculations are based on some simplifications. For example, the ionization is assumed to occur as a single event at the peak of the laser field. In reality, however, tunneling theory (such as MO-ADK [67]) would predict that the initial ionization occurs for multiple half-cycles of the laser field with a different weight of the individual contributions. This has been considered by Lin and coworkers in their theoretical treatment [68], which gives qualitatively similar results. Furthermore, the recollision excitation occurs 1.7 fs after the ionization [37, 69] and is modeled by placing the vibrational ground state wave packet of H_2 on the dissociative potential curve of the molecular ion. The approach neglects recollision events beyond the first recollision assuming that later recollisions are sufficiently suppressed in experiments employing few-cycle pulses [68, 70]. Recent results by W. Siu [65] at low intensities (about $4 \times 10^{13} \text{ W cm}^{-2}$), however, show

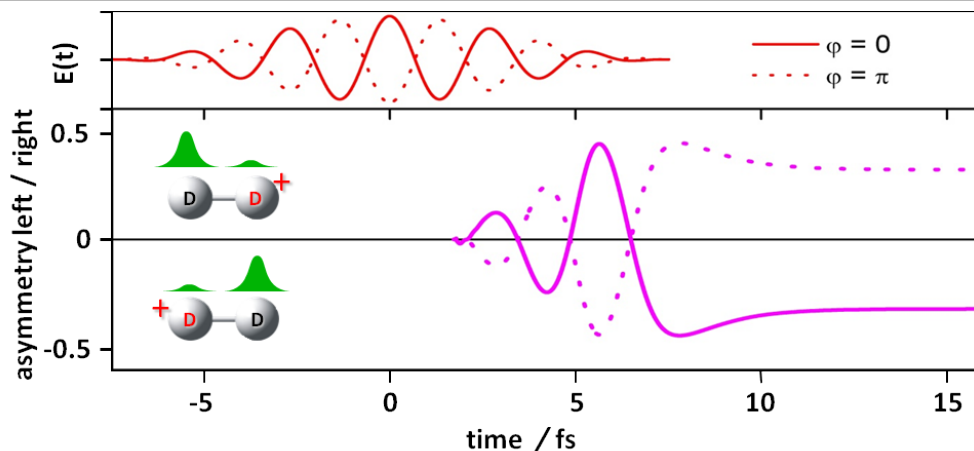


Figure 3.2: Time-dependent asymmetry in the dissociative ionization of D_2 . Results of the TDSE simulations described in the text. After the ionization at time $t=0$ the electron wave packet moves on the $1s\sigma_g$ ground state of molecular ion. At ~ 1.7 fs after an electron has been liberated from the neutral molecule this electron comes back, scatters with the parent ion and excites part of the population to the $2p\sigma_u$ state. Superposition of both $1s\sigma_g$ and $2p\sigma_u$ states is formed by the population transfer in the presence of the laser field. This breaks the parity of the electronic wave function and allows control of the final charge localization on the left and the right part of the molecular ion. Presented calculations are done for two reverse phases: the solid line corresponds to the phase 0 and the dashed line to the phase π . The probability to detect the electron on the left/right part is illustrated by green color and the final charge localization by the red D^+ ion. From [11].

the contributions of later recollisions in about 6.5 fs pulses. In the mid-IR waveform-controlled charge-directed reactivity in D_2 the 2^{nd} and 3^{rd} recollision appear to play a role (for more details see chapter 3.6.2). Results of the simulations from Refs. [10] and [11] help to clarify the final charge localization in the molecular dissociation. The temporal evolution of the laser field and the time-dependent asymmetry are shown in Fig. 3.2. The time-dependent asymmetry was calculated as a probability of detecting the nucleus on the left or right part of the molecule integrating Eq. 3.7 over the internuclear distance R . The oscillations of the asymmetry at earlier times are synchronized to the laser frequency. While the molecule dissociates via RCE (see Fig. 1.2a) the bond distance increases and the energy gap $\Delta W(t) = \hbar\omega(t)$ between the binding and repulsive states decreases until the laser starts populating the ground state [10]. The laser drives the electron back and forth (on attosecond timescales) between the two nuclei (see Fig. 3.2). At a certain point, the oscillatory motion of the electron between the two nuclei stops due to emergence of a potential barrier between the two nuclei and thus leaves the electron on one of the atoms.

Shifting φ_{CEP} by π changes the sign of the laser field and therefore changes the direction of the electron localization. This is in agreement with the experimental observation of the control of electron localization in D_2 and HD molecules.

A quantitative analysis of the dissociative ionization of D_2 , including ionization, recollision-induced excitation, dissociation, and laser-induced electron localization, was done in [68], where both the recollision electron and the nuclear motion are treated classically and the Born-Oppenheimer (BO) approximation is used. Seminal work by Gräfe and Ivanov describes the process fully quantum mechanically. Here, ionization as well as correlated two-electron dynamics during laser-induced recollision between an electron and its parent ion are included in the modeling of electron localization [32]. A recent semiclassical treatment [62] describes electron localization during molecular dissociation of D_2 in the presence of a 4.8 fs (FWHM) 800 nm laser field using quasi-static states. The resulting dynamics have revealed that the CEP controls the electron localization in an intermediate regime between an adiabatic and a diabatic regime for the coupling of the two involved states. The final result is an electron density that can be steered with the CEP and in this respect represents charge-directed reactivity [71].

3.3 Experimental observation of electron localization in molecular hydrogen and its isotopes in few-cycle near-IR laser fields

3.3.1 Imaging the asymmetric breakup

The first experimental implementation of steering a chemical reaction via guiding electrons with the light waveform was reported in 2006 [10]. The experiment was conducted on the simple diatomic D_2 molecule as a prototype system with only two electrons. In the experiment, the asymmetric D^+ ion ejection in the dissociative ionization of D_2 in the presence of phase-stabilized few-cycle laser pulses was studied [10]. The momentum distributions of ionic fragments were measured with a VMI spectrometer. Fig. 3.3a shows a typical experimental momentum map of D^+ ions recorded with 5 fs pulses at a central wavelength of 760 nm and an intensity of about 10^{14} W cm⁻² without CEP stabilization. The laser was polarized along the p_y axis.

In order to elucidate the effect of the CEP on the D^+ ion momentum distributions, the phase φ_{CEP} was stabilized and scanned. For each ionic species with mass m and

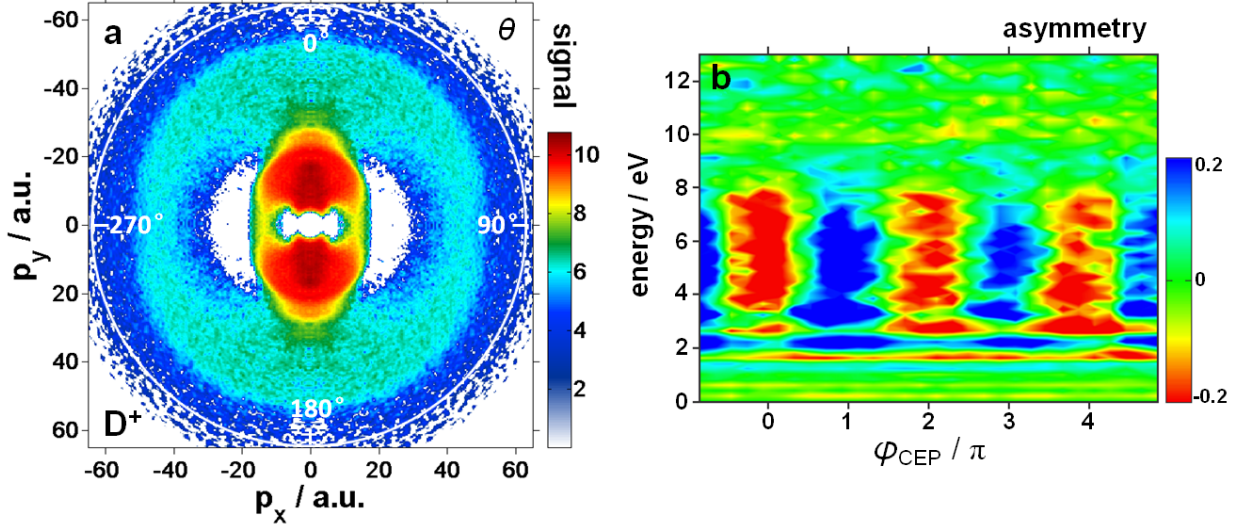


Figure 3.3: (a) A typical velocity map image from the detection of D⁺ ions in the dissociation of D₂ with 5 fs pulses at 10¹⁴ W cm⁻² without phase stabilization. The color scale is logarithmic. (b) Map of asymmetry parameter $A(W, \varphi_{CEP})$ as a function of the D⁺ kinetic energy W and the carrier envelope phase φ_{CEP} (measured over a range of 6π with a step size of 0.2π). Adapted from [10].

energy $W = p^2/(2m)$ the asymmetry $A(W, \theta, \varphi_{CEP})$ in the ion momentum distribution $P(W, \theta, \varphi_{CEP})$ was obtained for the right half of the image ($p_x > 0$) from:

$$A(W, \theta, \varphi_{CEP}) = \frac{P(W, \theta, \varphi_{CEP}) - P(W, 180^\circ - \theta, \varphi_{CEP})}{P(W, \theta, \varphi_{CEP}) + P(W, 180^\circ - \theta, \varphi_{CEP})}, \text{ for } \theta \in [0, 90^\circ]. \quad (3.10)$$

The angle-integrated asymmetry $A(W, \varphi_{CEP})$ within the angular range $[0, \alpha]$ can be derived as follows:

$$A(W, \varphi_{CEP}) = \frac{\int_0^\alpha P(W, \theta, \varphi_{CEP}) \sin \theta \, d\theta - \int_0^\alpha P(W, 180^\circ - \theta, \varphi_{CEP}) \sin \theta \, d\theta}{\int_0^\alpha P(W, \theta, \varphi_{CEP}) \sin \theta \, d\theta + \int_0^\alpha P(W, 180^\circ - \theta, \varphi_{CEP}) \sin \theta \, d\theta}. \quad (3.11)$$

The measured angle-integrated asymmetry $A(W, \varphi_{CEP})$ of D⁺ fragments is illustrated in Fig. 3.3b as a function of the carrier-envelope phase φ_{CEP} (x axis) and the kinetic energy W of the D⁺ ion fragment (y axis). The angular integration range $[0, \alpha]$ was chosen so that $\alpha=30^\circ$. The laser phase in Fig. 3.3b is only given as a relative number as the absolute phase has not been determined in the experiments in Ref. [10].

The CEP-control of the electron localization in the fragmentation of D₂ involves the recollision excitation of the molecular ion by the returning electron from the first ionization

(see Fig. 1.2a). However, recollision excitation by itself is not enough in this case to cause the electron localization and observed asymmetry in the D^+ ion momentum distribution. A second ingredient is the laser-induced coupling of the $1s\sigma_g$ and $2p\sigma_u$ states of the molecular ion, which breaks the parity of the electronic wave function.

3.3.2 Photodissociation channels in D_2

The fact that recollision excitation plays an important role in the dissociative ionization of D_2 can be demonstrated experimentally by comparison of the D^+ fragment distributions measured with linear and circular polarized laser pulses (Fig. 3.4a). In this case the peak intensity of the circular polarized pulse was 2 times larger than the peak intensity of the linearly polarized pulse, i.e. $(2.4 \pm 0.2) \times 10^{14} \text{ W cm}^{-2}$ vs. $(1.2 \pm 0.2) \times 10^{14} \text{ W cm}^{-2}$, to maintain the same E-field amplitude in the longitudinal direction (parallel to the p_y axis). Resulting spectra were derived by integrating the momentum distributions over the full solid angle.

The molecular dynamics in the presence of the laser can be distinguished by ionization and dissociation. Initially, the molecule is ionized by the laser field with the central wavelength of 760 nm (red arrow in Fig. 1.2). The Keldysh parameter for the experimental conditions is $\gamma = 1.1$ indicating ionization close to the tunneling regime (as discussed in details in 3.6). The measured D^+ fragment momentum images illustrate three dissociation channels for linear polarized pulses (Fig. 3.4b) as detailed below.

Bond softening (BS) [29, 38, 39, 40] leads to dissociation of the molecular ion D_2^+ and creates $D^+ + D$ fragments at low kinetic energies. In the field-dressed molecular potential formalism BS process occurs when the energy gaps open up at avoided crossings between the field-dressed (usually dressed with 1 or 3 photons) adiabatic potential energy surfaces. BS has been studied in great detail for different light intensities and pulse durations in Ref. [72].

Enhanced ionization (EI), sometimes mentioned as charge-resonance-enhanced ionization (CREI), is a Coulomb explosion channel. Enhanced ionization results in the formation of a D_2^{2+} ion that dissociates into $D^+ + D^+$ fragments. This channel is unwanted in the present investigations since there is no electron left that can be controlled. EI was suppressed by employing the 5 fs pulses and only a minor contribution is visible between 2 and 3 eV with a narrow angular distribution. Enhanced ionization starts to play an important role when the molecule interacts with longer pulses [10, 73].

Recollisional excitation (RCE) by the returning electron [69, 74] from the $1s\sigma_g$ state to

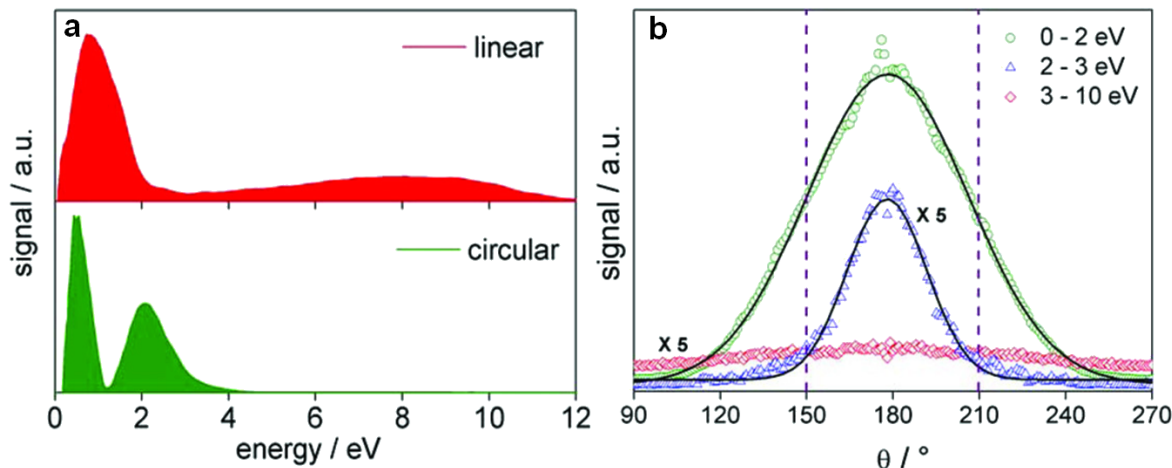


Figure 3.4: (a) Kinetic energy spectrum of D^+ fragments from the interaction of D_2 with linear (red) and circular (green) polarized 5 fs laser pulses. (b) Angular distribution of the D^+ fragments within three energy windows corresponding to the BS (0–2 eV), EI (2–3 eV) and RCE (3–8 eV) channels measured with linear polarization. Adapted from [11].

the $2p\sigma_u$ state of D_2^+ leads to the formation of D^+ and D fragments. This channel appears at energies above 3 eV and shows a broad angular distribution in agreement with earlier observations [70]. As mentioned above (Fig. 3.4a) almost no ions at these energies are observed with circular polarized light, strongly supporting that a recollision is responsible for their production.

3.3.3 Asymmetry in the bond softening dissociation

A recent study revealed the CEP-dependence of the BS dissociation of H_2 with 6 fs laser pulses at 760 nm at an intensity of $4.4 \times 10^{14} \text{ W cm}^{-2}$ for linearly polarized laser pulses [23]. The measurements were implemented with a COLTRIMS Target Recoil Ion Momentum Spectrometer (COLTRIMS) [75, 76, 77]. The COLTRIMS technique allows measurement of the momentum components of all charged particles from the molecular dissociation and can therefore give a complete kinematic description of the dissociation. Clear CEP-dependent asymmetries for H^+ fragments at low kinetic energy release (KER, being the sum of the energy deposited into all fragments) between 0 and 3 eV were observed. The observed fragments were attributed to BS dissociation (Fig. 1.2b). In contrast to Ref. [10] the CEP-dependent H^+ fragment asymmetry shows a distinct dependence on the KER. The COLTRIMS technique furthermore allowed implementation of coincidence measurements of the charged fragments [23]. The authors found that the CEP-dependent asymmetry

of the emitted electron measured in coincidence with the proton doesn't show a KER-dependence. Whereas the CEP-dependence of the first step (ionization of H₂) is observed, no correlation between the ionization and final electron localization was found. It was thus concluded that the asymmetry in the ionization step is not responsible for the observed dissociation asymmetry.

3.3.4 Waveform control of the electron localization in hydrogen deuteride

Following the experimental demonstration of CEP-dependent charge-directed reactivity in D₂ [10], further experiments were conducted on isotopes of molecular hydrogen. Here, experiments on electron localization in hydrogen deuteride (HD) [11] are described, which were part of the work performed within this thesis. Hydrogen deuteride is a prototype system that contains a single remaining electron after the ionization step and is a heteroatomic molecule, where the charged dissociation fragments H⁺ and D⁺ could be easily distinguished by their TOF spectra. The dissociation scheme for HD is shown in Eq. 3.12:



The experimental conditions for the presented study are very similar to the previously discussed experiments with D₂ [10]. CEP-stabilized laser pulses with a central wavelength of 760 nm and an intensity of about 10¹⁴ W cm⁻² were applied to a hydrogen deuteride target. Momentum distributions of D⁺ and H⁺ fragments, products of the dissociative ionization of HD, reveal reaction pathways analogues to the case of D₂. Fig. 3.5a shows the CEP-averaged momentum distribution of H⁺ ions. The distribution is left-right symmetrized with respect to the vertical polarization of the laser. Fig. 3.5b illustrates an angle-integrated energy spectrum. Note that H⁺ and D⁺ momenta are found to be approximately equal, thus the kinetic energies $W = p^2/(2m)$ of the species differ by about a factor of their mass ratios, i.e. $W_{H^+}/W_{D^+} \simeq m_{D^+}/m_{H^+} = 2$.

We chose to analyze the ion emission within a restricted angular range of $[0, \alpha]$ with $\alpha=20^\circ$ where the angle-dependent asymmetry $A(W, \theta, \varphi_{CEP})$ is maximal. This angle-integrated asymmetry $A(W, \varphi_{CEP})$ for H⁺ ions is displayed in Fig. 3.5c. The asymmetry map was energy integrated to obtain the data points shown in (d), red and blue curves are offset by approximately $\pi/2$. In general, the proton signal tends to show more noise,

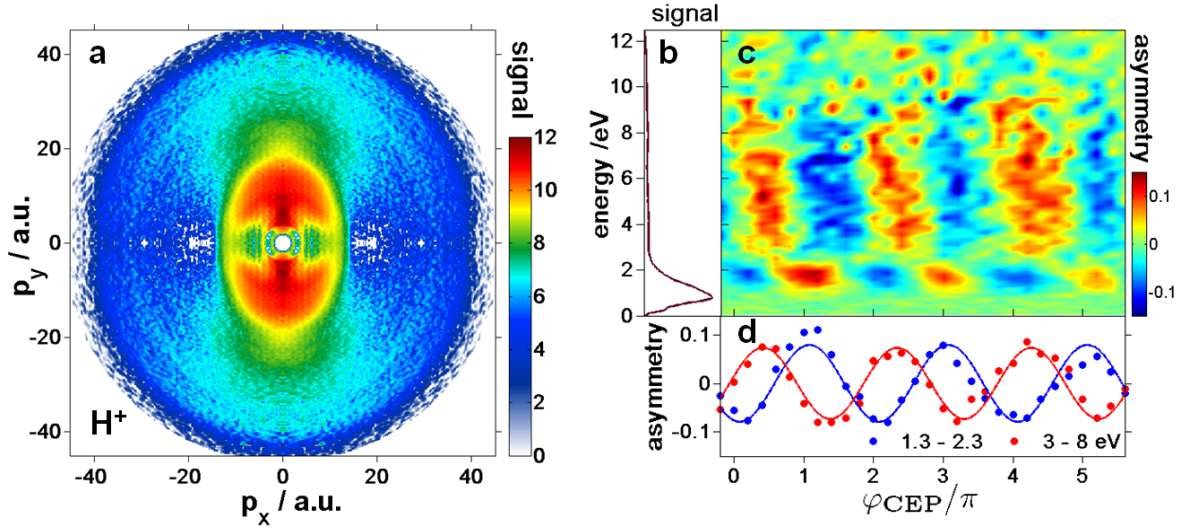


Figure 3.5: Asymmetry data obtained for H^+ fragments from the dissociative ionization of HD. (a) Momentum distribution of H^+ after inversion. (b) Spectra (linear scale) integrated over the full angle. (c) Asymmetry map obtained for an angular integration of 40° (2α). (d) Asymmetry within integrated energy ranges of 1.3–2.3 eV (blue dots) and 3–8 eV (red dots) fitted by cosine functions.

because of an additional H^+ contribution from ionization of H_2O that was present as background in the experimental chamber. Apart from this additional noise, the D^+ and H^+ ion spectra exhibit comparable asymmetry features. The asymmetry of H^+ fragments distinguishes the different dissociation pathways even more clearly than the spectra alone: the asymmetry from the RCE channel appears between 3 and 9 eV and the asymmetry from the BS channel appears between 1 and 3 eV.

The HD measurements were accompanied by reference measurements of ATI in xenon, allowing to assign absolute phases for the H^+ and D^+ scans. Taking into account the angle-integrated asymmetry $A(W, \varphi_{CEP})$ with $\alpha = 20^\circ$, the absolute phase φ_{CEP} was set to zero at a position where the cutoff electron emission from ATI of xenon reaches its maximum in the upward direction [52]. Note that measurements of the electron emission from ATI of xenon are often considered as a standard reference [18, 19, 24, 78, 79, 80]. The absolute phase calibration used here is based on classical arguments. For a better calibration of the absolute phase we have compared the ATI spectra in xenon to results from the recently developed quantitative rescattering (QRS) theory [51, 81, 82, 83].

Interestingly, accordingly to the findings by Tong and Lin [68] and by D. Geppert *et al.* [34], the preferential emission of ions to one of the two sides of the laser polarization does

not necessarily coincide with phase values of $\varphi_{CEP} = n\varphi$ where n is an integer number. The resulting asymmetry appears as a sum over contributions of all peaks of the laser field with sufficient amplitude to contribute to the ionization of the target. This might result in differences when the experimental results are compared to theoretical results considering just one peak of the laser contributing to the ionization.

3.3.5 Angle-dependent asymmetry by the example of D₂ and HD

The angular distributions of the D⁺ and H⁺ fragments from the dissociative ionization of D₂ and HD, respectively, are further explored in Fig. 3.6. The angle-dependent asymmetries obtained via Eq. 3.10 as functions of kinetic energy W , fragment emission angle θ and phase φ_{CEP} were fitted to a φ_{CEP} -dependent cosine function of the following form:

$$A(W, \theta, \varphi_{CEP}) = A_0(W, \theta) \cos(\varphi_{CEP} + \Delta\varphi(W, \theta)). \quad (3.13)$$

This was done in order to determine the amplitude of the asymmetry $A_0(W, \theta)$. Although CEP-dependent observables do not necessarily have to follow a cosine (or sine) function, the fits shown in Fig. 3.5 give an indication that the asymmetries follow to a good approximation a cosine (or sine)-like behavior. This finding is in agreement with molecular studies described in this thesis and other studies [17, 18, 52, 84], where CEP-dependent asymmetries were explored.

Taking a closer look at Fig. 3.6, it becomes clear that for fragment emission angles above 45–50° the asymmetry vanishes. In general, the angle- and energy-dependent asymmetry amplitudes obtained for D⁺ fragments from the dissociative ionization of D₂ and H⁺ fragments from HD look very similar. The BS channel of H⁺ fragments from HD (1.3–2.3 eV) is more visible than an analogous low energy contribution for D⁺ from D₂. Note that the H⁺ data were binned in momentum (Δp) and angular ($\Delta\theta$) intervals to improve the signal-to-noise ratio. Also, a lower number of iterations in the iterative inversion procedure was used to reduce the noise. As a result, the asymmetry amplitude for H⁺ ions from HD looks smoothed, but the contribution from the BS channel appears more visible. The angle- and energy-dependent asymmetry amplitude obtained for D⁺ fragments from HD (not shown) exhibits a similar structure. A butterfly shape of the asymmetry amplitudes further indicates different mechanisms for the generation of the asymmetry at low and high energies, identified above as BS and RCE channels.

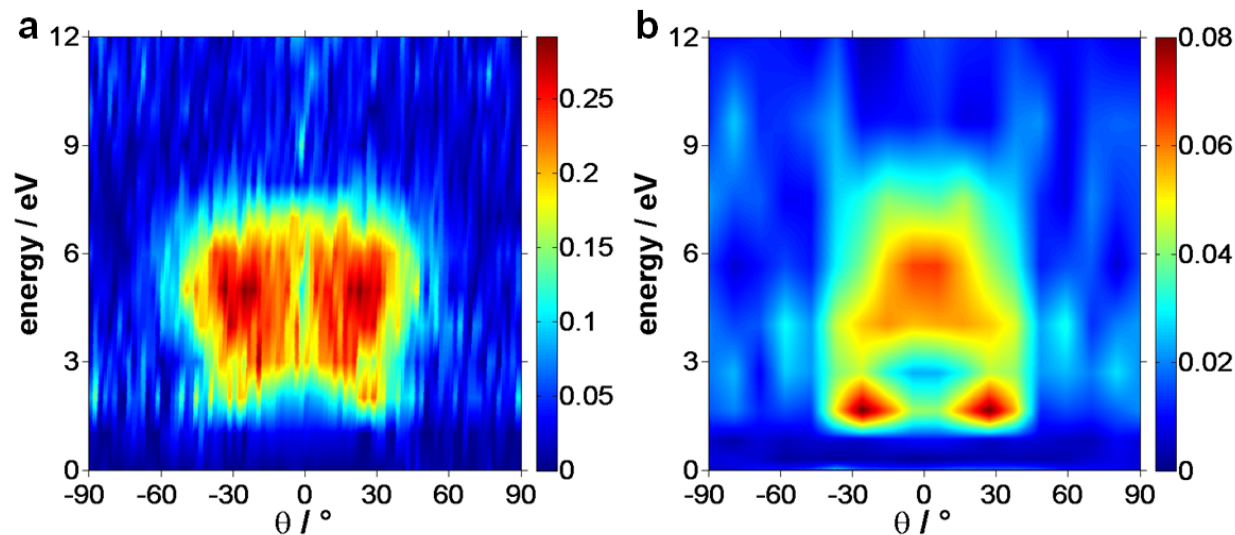


Figure 3.6: Amplitude of the asymmetry $A_0(W, \theta)$ in the emission of: (a) D^+ ions from the dissociative ionization of D_2 and (b) H^+ fragments from the dissociative ionization of HD as a function of the emission angle θ and kinetic energy W . Fig. 3.6a is adapted from [11].

3.4 Optimal pulse duration for maximal control of electron localization

3.4.1 Asymmetry amplitude vs. pulse duration

The degree of CEP-control of the electron localization in the dissociative ionization of molecular hydrogen has been explored as a function of the laser pulse duration [10, 11]. Fig. 3.7 shows the result of that study and demonstrates that the asymmetry amplitude depends on the pulse duration. It was found that the asymmetry modulation depth (twice the asymmetry amplitude) decays exponentially from approximately 45% for 5 fs laser pulses towards 1% for pulse durations more than 9 fs [10, 11]. This finding was theoretically supported in [34, 68, 85] and can be explained by the number of peaks of the electric field contributing to ionization. The electron localization is determined by complex coupled electron-nuclear dynamics initiated by ionization by the most pronounced peaks of the laser field. Ionization at different half-cycles can lead to different final electron localization [34, 68]. As longer pulses include multiple contributing ionizations the asymmetry amplitude is smaller for longer pulses. Few-cycle pulses appear therefore a significant prerequisite for the electron localization control that has been achieved.

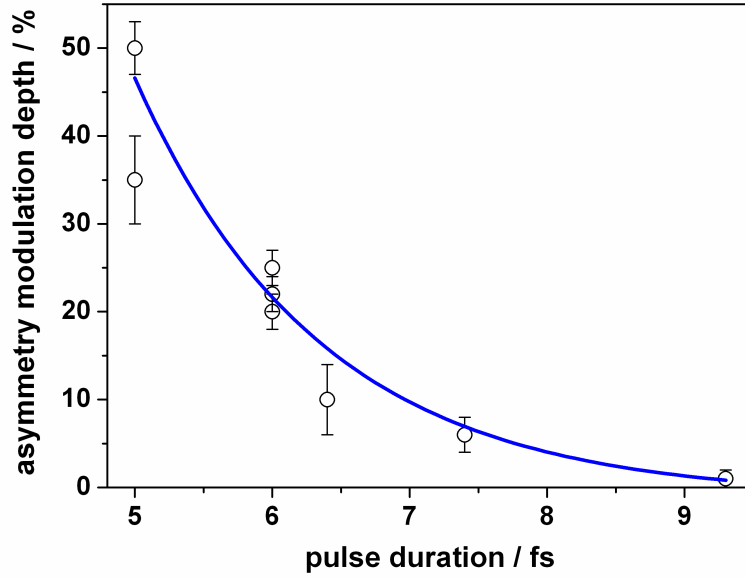


Figure 3.7: Experimental asymmetry modulation depth in the emission of D^+ ions between 3 and 8 eV from dissociation of D_2 vs. the laser pulse duration [11]. Individual data points correspond to single measurements within the intensity range of $(1.2 \pm 0.4) \times 10^{14} \text{ W cm}^{-2}$. The solid blue line is an exponential decay fit of the data points.

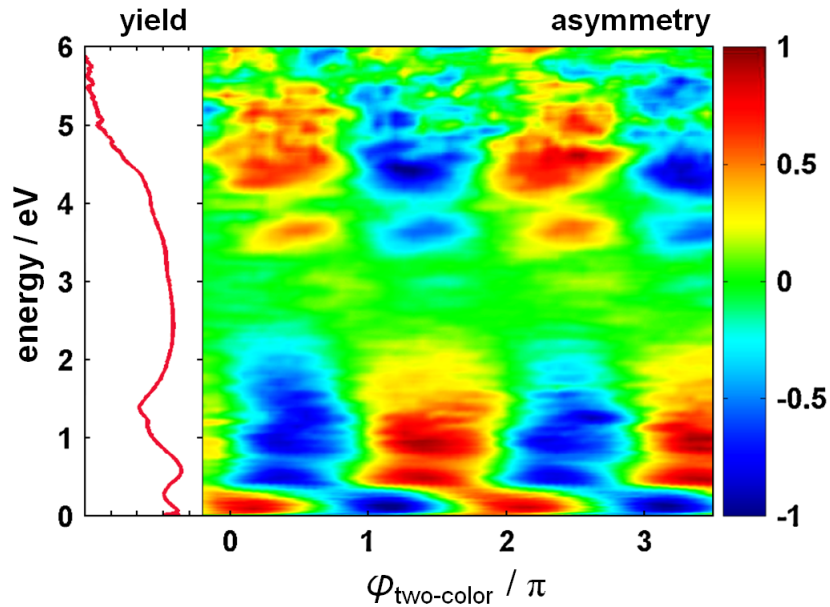


Figure 3.8: Asymmetry of D^+ ion emission from D_2 as a function of ion energy and $\varphi_{two-color}$ being a phase between 800 nm and 400 nm pulses from Ref. [73]. The asymmetry is obtained similar to Eq. 3.11 taking into account the number of ions integrated over an angle of 30° along the polarization axis. The ion spectrum (left panel) is shown in a logarithmic scale.

3.4.2 Asymmetric dissociation of D₂ in a two-color femtosecond laser field

Controlling electron motion employing subcycle field waveform control has been shown above to be feasible with CEP-controlled few-cycle waveforms. The duration of such a pulse, with a force controlled via φ_{CEP} , varying on sub-femtosecond scale is critical, as shown in Fig. 3.7. The subcycle control of electric field waveforms can also be achieved by waveform synthesis [5, 86]. A recent example of applying a simple waveform synthesis in the femtosecond domain to the control of the dissociative ionization of D₂ demonstrates that a similar, although not identical control can be achieved with much longer femtosecond laser pulses [73]. The asymmetric dissociation of D₂ can be tailored with the relative phase $\varphi_{two-color}$ of a two-color laser field $E(t) = E_1(t)\cos(\omega t) + E_2(t)\cos(2\omega t + \varphi_{two-color})$ with the wavelength 800 nm and 400 nm corresponding to ω and 2ω , respectively.

Ray *et al.* have observed a very strong asymmetry in the emission of D⁺ ions from D₂ (see Fig. 3.8), where relatively long ~ 45 fs linear polarized pulses were employed [73]. The experimental results were further interpreted in terms of a model based on the dynamic coupling of the gerade and ungerade states in the D₂⁺ molecular ion by the laser field [73].

The experiment shows a dependence of the phase-dependent asymmetry on the energy of the emitted ion (see Fig. 3.8). The asymmetries were associated with various dissociation channels including one-photon BS, visible between 0–0.3 eV, two-photon above-threshold dissociation (ATD) [39] with a strong signal in the range of 0.3–2 eV and rescattering (RES). The rescattering was introduced in this thesis as recollisional excitation (RCE). RES results in an asymmetry at high energies from 4 to 6 eV. The strong signal centered near an ion energy of 3 eV corresponds to CREI [87, 88] or enhanced ionization (EI), involving the double ionization of D₂ and the generation of two deuteron ions and therefore no asymmetry is observed in this energy range, as is seen in Fig. 3.8.

3.5 Asymmetric dissociation of molecular hydrogen in a two-color, attosecond XUV–femtosecond near-IR field

Control of electron dynamics in molecular hydrogen can also be achieved using a pump-probe scheme: an attosecond extreme ultraviolet (EUV or XUV) pulse as the "pump"

pulse and a weak, CEP-stabilized few-cycle near-IR pulse as the "probe" pulse. Such a scheme was first implemented by Sansone *et al.* [66] where electron charge localization was observed in the dissociative ionization of H₂ and D₂ molecules.

Isolated attosecond XUV pulses with a duration of 300–400 as extending from 20 to 40 eV [89] were generated through high-order harmonic generation (HHG) in krypton. The XUV pulses and time-delayed linear polarized IR pulses of 6 fs (FWHM) were crossed with an effusive H₂ or D₂ gas jet inside a VMI spectrometer [50] and the resulting H⁺ or D⁺ ions were detected. Fig. 3.9a shows measured kinetic energy distributions for D⁺ fragments integrated over 45° along the laser polarization direction as a function of the time delay τ . The dominating process at low kinetic energies ($W < 1$ eV) is the BS of the bound X² Σ_g^+ state of D₂⁺ caused by the near-IR pulse. The signal attributed to the vibrational wave packet peaks near $\tau \approx +11$ fs in good agreement with previous results on vibrational wave packet motion in the D₂⁺ ground state [31]. When the XUV and near-IR pulses overlap ($\tau \approx 0$ fs), the D⁺ signal strongly increases around 8 eV. The enhancement of the signal at high energies can be attributed to a growth in the excitation cross-section of the A² Σ_u^+ continuum state caused by infrared-laser-induced mixing of the A² Σ_u^+ and X² Σ_g^+ states. The increase may also contain contributions from photoionization of the Q₁¹ Σ_u^+ doubly excited autoionizing states by the near-IR laser. Fig. 3.9b shows the asymmetry of D⁺ ion emission in opposite directions along the laser polarization vector. The time-dependent asymmetry parameter $A(W, \tau)$, as defined in Eq. 3.11 and obtained by integration of the fragment emission over $\alpha = 45^\circ$, exhibits pronounced oscillations as a function of the delay between the pump and probe pulses τ .

Recent progress in computational methods allows the inclusion of excited neutral states of H₂ that can be reached in the ionization (e.g. by a XUV pulse) and then decay via autoionization [90]. To solve a complex case of XUV–near-IR pump-probe dynamics in H₂ [66] full dimensional integration of the TDSE was used. Comparison of the experiment to the calculations for ionization of H₂ reveals two main mechanisms responsible for the observed asymmetry oscillations. For the small delays when the pump and the probe pulses overlap ($\tau < 8$ fs) the few-cycle near-IR field influences the photoexcitation process as illustrated in Fig. 3.10a. Excitation of H₂ molecule involving absorption of XUV and near-IR photons can produce a wave packet in the A² Σ_u^+ state. At the same time the XUV pulse can excite the Q₁¹ Σ_u^+ state, which can subsequently autoionize into the X² Σ_g^+ state. At larger pump-probe delays the IR pulse can induce population transfer between the A² Σ_u^+ and X² Σ_g^+ states (see Fig. 3.10b). The interference between the A² Σ_u^+ and X² Σ_g^+ wave packets results in the observed asymmetry.

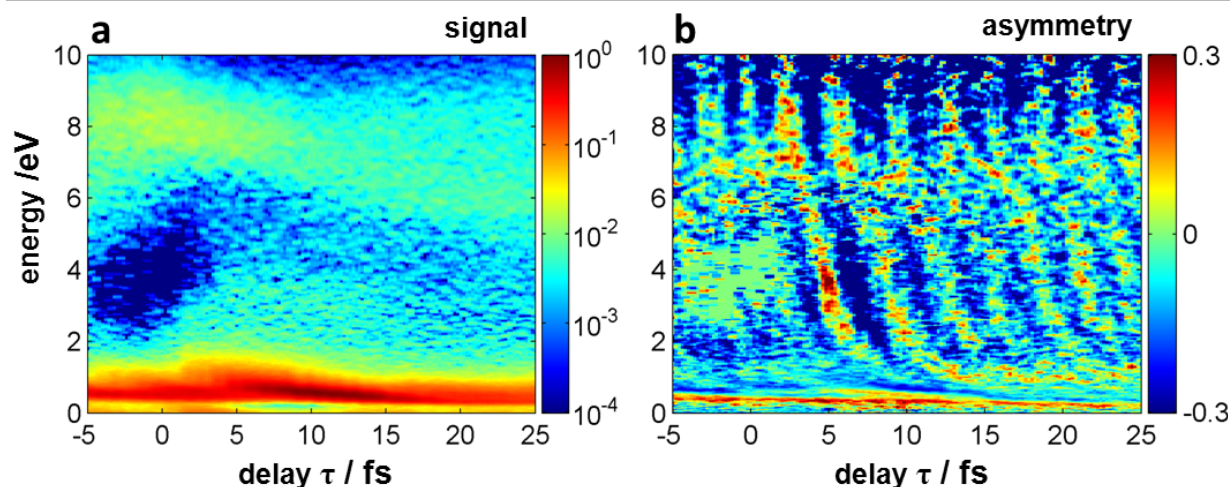


Figure 3.9: Experimentally measured (a) kinetic energy distributions and (b) asymmetry parameter for the formation of D^+ ions in two-color attosecond XUV–femtosecond near-IR dissociative ionization of D_2 , as a function of the fragment kinetic energy W and the delay between the pump and probe pulses τ . Adapted from [66].

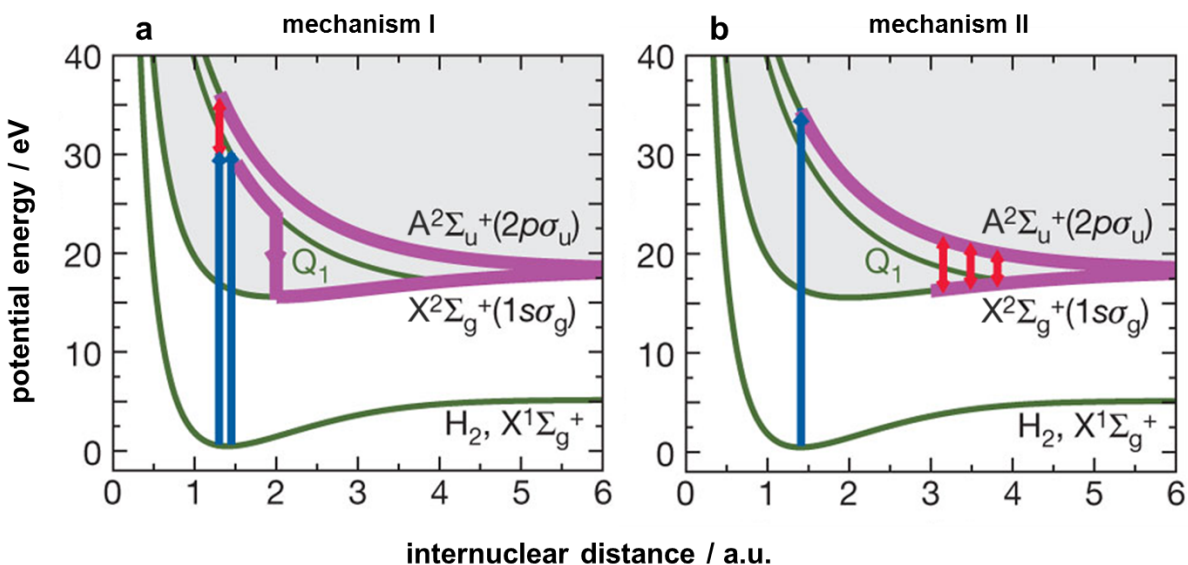


Figure 3.10: Mechanisms that lead to asymmetry in XUV–near-IR dissociative ionization (adapted from Ref. [66]). (a) Mechanism I: asymmetry caused by the interference of a wave packet launched in the $A^2\Sigma_u^+$ state by direct XUV ionization or rapid ionization of the $Q_1^1\Sigma_u^+$ doubly-excited autoionizing states by the IR pulse and a wave packet in the $X^2\Sigma_g^+$ state resulting from autoionization of the $Q_1^1\Sigma_u^+$ states. (b) Mechanism II: asymmetry caused by the interference of a wave packet in the $A^2\Sigma_u^+$ populated by direct XUV ionization and a wave packet in the $X^2\Sigma_g^+$ state that results from stimulated emission during the dissociation process. Blue and red arrows indicate the XUV and near-IR pulses correspondingly. Molecular dynamics are marked by purple lines.

3.6 Subcycle-controlled, charge-directed reactivity employing mid-IR few-cycle fields

3.6.1 Wavelength dependence of the subcycle control of charge-directed reactivity

In order to achieve efficient laser-driven, charge-directed reactivity [71], the timescale of the laser control over the electronic motion should match the timescale of the nuclear motion. For example, the dissociation time for the molecular hydrogen ion via BS may be estimated as approximately half of a vibrational period, thus requiring laser control over about 12 fs [31]. At the same time CEP-control of the electron motion requires the number of contributing laser cycles to be small. Longer wavelengths λ allow pulses with optical periods $T = \lambda/c$ (where c is the speed of light) which are significantly longer in time as compared to the pulses (with the same numbers of cycles) in the near-IR. Consequently, few-cycle laser pulses in the mid-IR fulfill both criteria and therefore can be better suited for CEP-control of charge-directed reactivity.

In addition, mid-IR laser fields allow studying atomic and molecular systems deep in the tunneling regime. For example $\gamma = 0.54$ for the D_2 experiments described below, while $\gamma = 1.1$ – 1.2 in experiments on D_2 and HD with near-IR laser pulses that were described above. Here γ is the Keldysh parameter [36]: $\gamma = \sqrt{\frac{I_p}{2U_p}}$, where I_p is ionization potential of an atom or a molecule and U_p is the ponderomotive potential. U_p represents the average energy of the electron's quiver motion in the electric field:

$$U_p(\text{eV}) = \frac{e^2 E_0^2}{4m_e \omega^2} = 9.33 \times 10^{-14} I [\text{Wcm}^{-2}] \lambda^2 [\mu\text{m}] \quad (3.14)$$

where m_e and e are the mass and charge of the electron, E_0 is the field amplitude, ω the angular frequency and λ the wavelength of the electric field. γ much less than one corresponds to the tunneling regime, γ much greater than one corresponds to the multiphoton regime. Considering a decreasing photon energy at longer wavelengths, nonlinear field-effects in the multiphoton regime would require a higher number of involved photons. The tunneling ionization determines the time window at which the nuclear dynamics starts. A smaller γ parameter might help to confine the ionization time [91] and contribute to the higher temporal control of the dynamics.

We have experimentally studied the subcycle control of the dissociative ionization of D_2

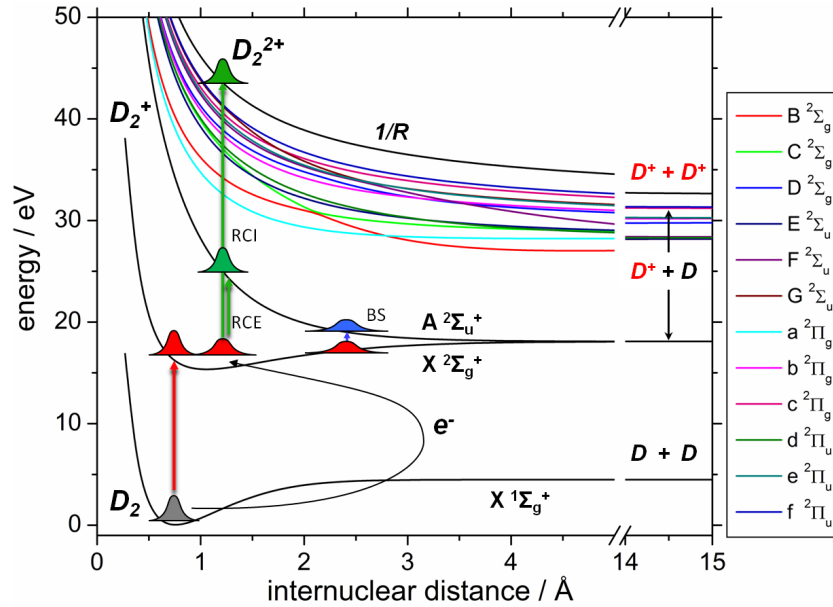


Figure 3.11: Relevant potential energy surfaces of D_2 , D_2^+ and D_2^{2+} obtained by *ab-initio* calculations described in the text. The higher-lying excited electronic states of D_2^+ above the A-state are labeled alphabetically accordingly to their symmetry. The red arrow indicates tunnel ionization of D_2 , the blue arrow BS and the green arrows recollision induced excitation (RCE) and ionization (RCI). From [28].

in intense few-cycle CEP-stable mid-IR (2.1 μm) laser fields and compared the results with TDSE calculations. A detailed description of the laser setup can be found in chapter 2 and Ref. [54]. The laser pulses of approximately 25 fs duration were focused to an intensity of $(6.2 \pm 1.5) \times 10^{13} \text{ W cm}^{-2}$ and D^+ fragments resulting from the dissociative ionization of D_2 were measured via VMI.

The multiple pathways for the investigated dissociative ionization of D_2 are summarized in Fig. 3.11. D_2^+ is produced from D_2 by tunnel ionization (red arrow) whereby a nuclear wave packet is launched on the potential of the $X^2\Sigma_g^+$ state. Several subsequent processes leading to the dissociation of the molecular ion can be identified: i) BS (blue arrow), ii) RCE, and iii) recollisional ionization (RCI) (green arrows). In our study fragments resulting from both BS and RCE channels can be distinguished and controlled simultaneously [28].

Fig. 3.12a shows a cut for $p_z=0$ through the 3D momentum distribution of the D^+ ions. The polarization of the laser is vertical. The corresponding D^+ kinetic energy spectrum, integrated over the full solid angle, is displayed in Fig. 3.12b (red line). The spectrum reveals 4 regions, which are also indicated in Fig. 3.12a by white dashed circles. The most intense contribution in the spectrum between 0 to 1 eV is assigned to BS. Three additional

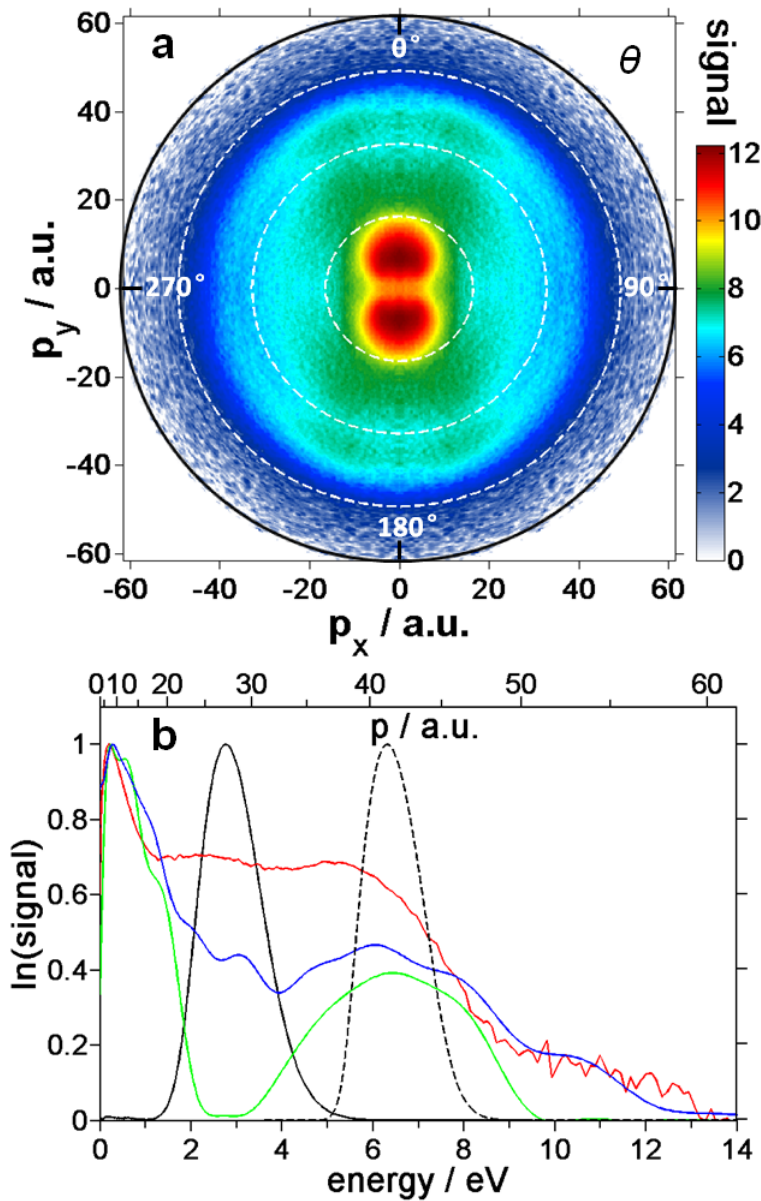


Figure 3.12: (a) Inverted CEP-averaged D^+ momentum distribution (p_y vs. p_x at $p_z=0$), the signal was left-right as well as up-down symmetrized, a logarithmic color scale was used. The laser is polarized along the p_y axis. The dashed circles separate the four contributions discussed in the text. (b) Angle-integrated kinetic energy spectrum of D^+ ions obtained from the experimental data (red curve) and calculated spectra for the BS dissociation involving only the X and A-states of D_2^+ (green curve) and also the 11 higher states of D_2^+ shown in Fig. 3.11 (blue curve). The theoretical results for the dissociation via recollision induced excitation (RCE) and ionization (RCI) are shown as solid and dashed black lines, respectively. All spectra are normalized by their maximum values. Adapted from [28].

contributions in the ranges 1–4 eV, 4–9 eV and 9–13 eV are discussed in detail below together with theoretical analysis of the control.

The directional D^+ ion emission as a function of phase φ and momentum p is analyzed by the angle-integrated asymmetry parameter $A(p, \varphi)$ with $\alpha=10^\circ$ similar to Eq. 3.11 and is shown in Fig. 3.13a. The experimental phase offset was calibrated achieving best agreement between experimental and calculated CEP-dependent asymmetry oscillations for the BS channel. A high degree of asymmetry (with an amplitude of approximately 0.2) is found for the BS channel (energies below 1 eV). The observation of such a strong asymmetry in the BS channel is very remarkable when compared to earlier results obtained in the near-IR [23]. A second asymmetry contribution in the energy range 1–4 eV has a weaker (max. 0.1) amplitude.

3.6.2 Quantum dynamical analysis of the control

The dissociative ionization of D_2 was modeled using the approach published in [34] to treat the coupled electron and nuclear wave packet dynamics. For details, see Ref. [28] and the Supplemental Material of that paper. The relevant potential energy surfaces were calculated using the quantum chemistry package Molpro [92] on the CASSCF (1; 15) level of theory using the (11s; 7p)→[6s; 5p] contracted Gaussian basis set introduced by Whitten and Huzinaga [93, 94]. The calculations were performed for molecules aligned along the laser polarization axis and for the experimental pulse duration and intensity. The theoretical analysis is focused on the dissociation via the BS and RCE channels.

Fig. 3.12b shows the theoretical results for different dissociation channels and conditions. The green curve shows the calculated D^+ kinetic energy spectrum for the laser-induced dissociation including only the $X^2\Sigma_g^+$ and $A^2\Sigma_u^+$ surfaces of D_2^+ . The blue curve shows the result, where also the 11 higher excited states shown in Fig. 3.11 have been included. The experimental spectrum below 2 eV is assigned to the BS channel. The contribution in the energy range 4–9 eV results from the direct population of the A-state during the ionizing half-cycle. The high-energy tail of the measured D^+ spectrum above 9 eV is only captured by the calculations that include the higher excited states (blue line). The spectrum resulting from a calculation for the RCE dissociation is illustrated as the solid black curve and shows a strong signal between 2 and 4 eV. The spectrum resulting from RCI is shown as the dashed black curve. RCI is induced by rescattering of the energetic mid-IR laser driven electrons with the parent molecule. The recollision energy can be estimated using the classical cutoff $E_{rec,max} = 3.17 U_p$ and is equal to 84.5 eV at

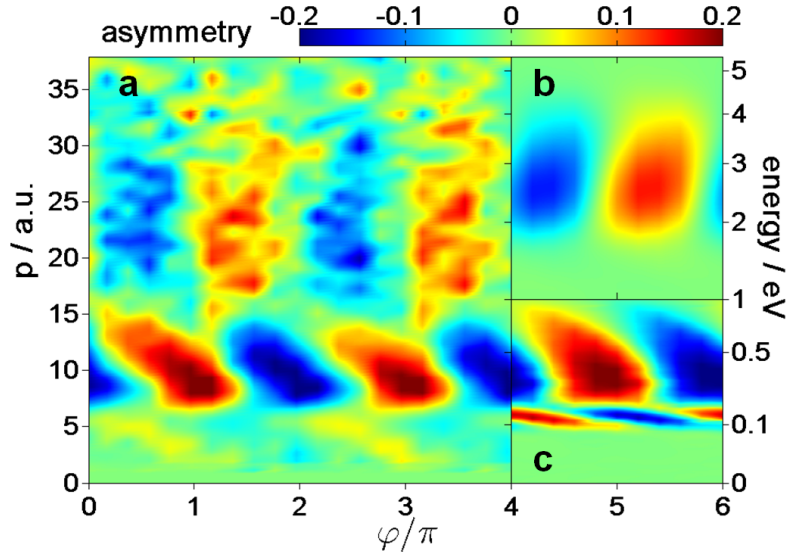


Figure 3.13: (a) D⁺ ion emission asymmetry as a function of the fragment momentum (corresponding kinetic energy scale on the right) and relative phase φ_{CEP} of the D⁺ ion emission obtained by integrating over a full opening angle $2\alpha=20^\circ$ along the laser polarization axis. (b) Asymmetry obtained by the calculations for the RCE channel. (c) same as (b) for the BS channel. From [28].

$6.2 \times 10^{13} \text{ W cm}^{-2}$ laser intensity.

The calculated asymmetries corresponding to the dissociation of D₂⁺ by RCE and BS are shown in Fig. 3.13b and c, respectively. In order to facilitate a quantitative comparison of the theoretical results with the experimental data, the asymmetries were calculated assuming ionization by the 5 most intense peaks of the laser electric field. Inclusion of further peaks did not lead to significant changes. The asymmetry amplitude and its energy-dependent oscillatory behavior with the CEP are well reproduced by the calculations. Both calculations were performed for the same CEP φ and were not shifted against each other afterwards. The origin of a π phase shift between the two channels at 1 eV might be explained by a difference in their nature. The electronic states are superimposed in the BS and RCE mechanisms with different phases (in the RCE mechanism the A-state is populated at later time), resulting in the phase-jump. The observed tilt of the asymmetry with kinetic energy and a phase jump at 0.17 eV in the BS-channel in Fig. 3.13c are reproduced well by the calculations. The phase-jump at 0.17 eV likely originates from the laser coupling with the slowest components of the dissociating wave packet. Future studies involving semiclassical approaches [62] and full two-electron calculations including correlation effects [32] might be helpful to elucidate this aspect in more detail.

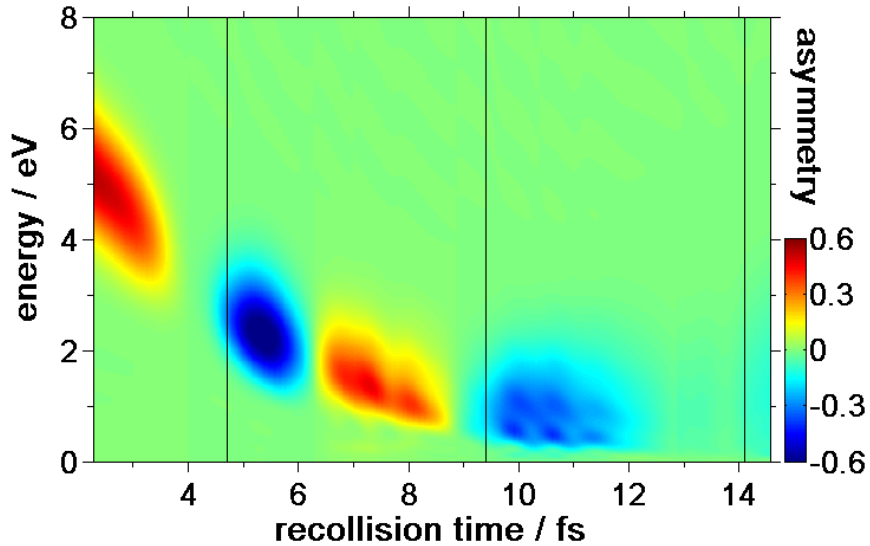


Figure 3.14: Calculated asymmetry of D^+ fragments as a function of the fragment kinetic energy and the recollision time. The vertical lines indicate the first (4.7 fs), second (9.2 fs) and third (14.1 fs) recollision time calculated according to Ref. [37] as most probable around $\frac{2}{3}$ of an optical cycle at $2.1 \mu\text{m}$. From Supplemental Material of Ref. [28].

In the calculations shown in Fig. 3.13b only the first recollision after the initial ionization was included. The results of calculations considering later recollisions at the experimental laser conditions and $\varphi_{CEP} = 0$ are shown in Fig. 3.14. The experimentally observed lower kinetic energies in the RCE channel (below 2 eV) may arise from subsequent recollisions. As shown in Fig. 3.14 at $2.1 \mu\text{m}$ used in the experiment, the first three recollision events result in the same sign the asymmetry, in agreement with the experimental observation of an energy independent phase of the asymmetry oscillation in the energy range of 1–4 eV. Therefore fragments generated by subsequent recollision events can potentially fill the gap between the BS and RCE channels in Figs. 3.13b and c. According to recent studies of H_2 and D_2 in the presence of ~ 6 fs near-IR laser pulses with a central wavelength of 750 nm at smaller intensities (about $4 \times 10^{13} \text{ W cm}^{-2}$) [65] later recollisions may play an important role and cause an asymmetry at low kinetic energies closer to the kinetic energies typical for BS. Autoionization and/or photo-ionization of highly excited neutral D_2 molecules, which is more likely in the tunneling regime [95], may also produce an asymmetry in the breakup of hydrogen [66].

The sign of the asymmetry in the two dissociation channels (BS and RCE) is strongly dependent on the wavelength. This suggests that the relative phase between the CEP-dependent asymmetry oscillation of the two channels depends on the wavelength as well.

Particular at a wavelength of 2.1 μm the asymmetries of the two channels (see Figs. 3.13b and c) exhibit an opposite sign, reproducing the experimental observation (see Fig. 3.13a). The wavelength dependence of the asymmetry amplitude and its sign are analyzed in detail in Ref. [28] and the Supplemental Material of that paper. Increasing the wavelength extends the recollision time, leading to an excitation to the A-state at larger internuclear distances. Consequently, the kinetic energy of D^+ fragments resulting from RCE (even taking into account only the first recollision) is reduced from ~ 6 eV at 760 nm to less than 3 eV at 2.1 μm .

3.7 Conclusions and outlook

Control of charge localization during dissociative ionization of hydrogen-like molecules (H_2 , D_2 , HD) was demonstrated recently for various field configurations [10, 11, 23, 73, 66].

Comparing the latest results [28] to earlier work using near-IR few-cycle laser pulses [10, 23], it is evident that the CEP-control of electron localization in the dissociation of D_2 is much more efficient for the BS channel when mid-IR pulses are applied. The longer wavelength implies a better match between the duration of the laser period and the dissociation time of the molecule. In addition, for the few-cycle pulses used in the studies described above, the wave packet in the X-state can be efficiently coupled to the A-state at large internuclear distances. Both aspects lead to the observed high degree of control of charge-directed reactivity in the dissociation reaction.

The demonstration of efficient control of charge-directed reactivity is relevant to the control of larger molecules and complex molecular processes. As an example, the branching ratio at conical intersections is expected to be strongly dependent on charge localization induced by a mid-IR few-cycle pulse [96].

Subcycle control of electron dynamics in multielectron systems

4

Waveform-controlled few-cycle pulses have been used to control electron localization in the dissociative ionization of the prototype molecules D_2 [10, 11], H_2 [23], HD [11]. The asymmetric D^+ (H^+) ion ejection in the dissociative ionization of hydrogen-like molecules was also theoretically studied (see e.g. [32, 33, 34, 41, 68]). The control of electron localization in hydrogen-like molecules is described in detail in the previous chapter. These prototype systems contain only a single remaining electron after initial ionization. First experimental studies on simple molecules stimulated the question, whether the steering of electrons in more complex systems is feasible. If yes—could a similar scheme of control be used and which step in this scheme is more important: the initial ionization or excitation process or the following strong-field coupling of the various potential energy surfaces? CEP-control of electron dynamics in diatomic molecules with multiple electrons can be seen as an essential stride towards molecules of chemical or biological interest. This chapter focuses on the steering of electron motion in multielectron systems, namely CO and DCl . The chapter starts with carbon monoxide (CO) being the first multielectron system where the attosecond control of electron dynamics by the light waveform was achieved [24].

4.1 Attosecond control of electron dynamics in carbon monoxide

4.1.1 Experimental observation of asymmetric fragment emission

Phase-stabilized, 4–5 fs, linearly polarized laser pulses at 740 nm and at an intensity of $8 \times 10^{13} \text{ W cm}^{-2}$ were applied to dissociatively ionize CO . The directional emission of ionic fragments was monitored via VMI. Fig. 4.1a shows the momentum distribution of C^+ ions for a $\varphi_{CEP} \simeq \pi$ pulse. Momenta are given in atomic units (a.u.), the colorscale of the momentum distribution is linear. Contribution of different dissociation channels may

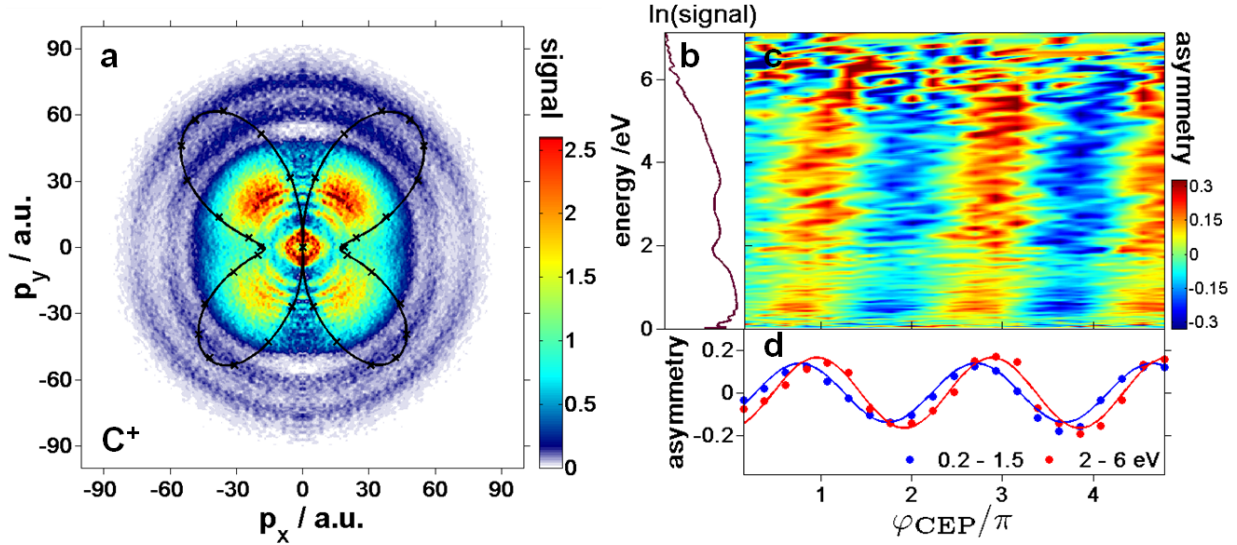


Figure 4.1: (a) Inverted two-dimensional C^+ momentum distribution (left-right symmetrized) measured for $\varphi_{CEP} \simeq \pi$. The laser polarization is vertical, the colorscale of the C^+ signal is linear. Black crosses and solid curve (a fit by Legendre polynomials) correspond to the calculated ionization rate from HOMO and HOMO-1 (3σ and $1\pi_{x/y}$) of CO for different orientations of the molecule with respect to the laser polarization as described in details in [97]. (b) Measured spectrum (logarithmic scale) and (c) asymmetry $A(W, \varphi_{CEP})$ are integrated over $\theta = [0^\circ, \alpha]$ with $\alpha = 60^\circ$. (d) Asymmetry integrated over indicated energy ranges vs. φ_{CEP} fitted by cosine functions. The φ_{CEP} was calibrated by reference measurements of ATI in xenon and comparison to calculations based on the QRS theory [51]. Adapted from [24].

be identified as three rings, where the first ring is the broadest (from $p = 0$ a.u. to 50 a.u.) and most intense, and also contains sharp lines. Other two rings appear between momenta of about 55 a.u. to 68 a.u. and 71 a.u. to 81 a.u. The dominant features show angular distributions with minima around 0° , 90° , 180° and 270° with varying modulation depths. The angular distribution of the C^+ fragments shown in Fig. 4.1a differs from the findings in Ref. [98] where the shape of the HOMO with a maximum along the laser polarization axis was observed. The shape of the angular distribution in Fig. 4.1a indicates contributions from both the HOMO (5σ) and the HOMO-1 ($1\pi_{x/y}$) orbitals as detailed below. The solid black line in Fig. 4.1a displays the calculated volume-averaged angle-dependent ionization rate as described below in the theory section. The angle-integrated kinetic energy spectrum for C^+ ions derived from Fig. 4.1a is shown in Fig. 4.1b, note that the scale here is logarithmic. The effect of the CEP on the C^+ fragment emission direction is perceptible to the eye (see Fig. 4.1a). A detailed analysis of the directional emission

is represented by the angle-integrated asymmetry $A(W, \varphi_{CEP})$ (Eq. 3.11) with $\alpha = 60^\circ$ in Fig. 4.1c. The data points of angle- and energy-integrated asymmetry $A(\varphi_{CEP})$ of C^+ ions are displayed in Fig. 4.1d. The phase φ_{CEP} was calibrated as an absolute phase. CO measurements were consistently combined with reference scans of ATI in xenon, so that the comparison of experimental high-energy photoelectron spectra to calculations based on the QRS theory [51] obtained the absolute CEP value with an error of $\pm 0.04\pi$. The observed asymmetry is almost equally strong throughout the whole kinetic energy spectrum. A similar asymmetry for O^+ ions exhibits the same features. However it is not shown here due to a lower signal-to-noise ratio of O^+ fragments. Note that the $C^+ + O$ channel of the fragmentation of CO^+ is energetically favored over the $C + O^+$ channel (see Fig. 4.2). Ref. [99] found the yield of C^+ ions from the multiphoton induced dissociative ionization of CO to be more than an order of magnitude higher than that of O^+ fragments. In our measurements [24] the yield of C^+ ions is approximately 20 times larger than the yield of O^+ .

Electron recollision is experimentally verified to be a crucial step for the production of the observed C^+ ions. With circular polarization (CP) at twice the intensity as for linear polarization (LP) to achieve the same field strength, the ion yield is significantly less than with LP, in addition ions are only observed at energies below 2 eV, see Fig. 4.3a. Therefore most of the observed C^+ ions originate from the population of repulsive excited states of CO^+ through recollision. Coupling of the bound X and A states of CO^+ to dissociative states (BS) plays only a minor role under the current laser conditions (see Fig. 4.3b).

4.1.2 The dissociative ionization of carbon monoxide

The formation of ionic fragments in the dissociative ionization of CO might occur via a three-step mechanism (schematically shown in Fig. 4.2) similar to the previously discussed electron localization in hydrogen-like molecules. At first the CO molecule in the ground state $X^2\Sigma^+$ is ionized by the laser field (orange arrow with label $h\nu$) and vibrational wave packets are created on the low-lying bound potential energy surfaces (PES) $X^2\Sigma^+$ (ionization from HOMO) and $A^2\Pi$ (ionization from HOMO-1). The dissociation is triggered by RCE to higher-lying electronic states CO^+ (brown arrow with the text RCE). Shown here are the bound $C^2\Sigma^+$ and repulsive $E^2\Pi$ and $H^2\Pi$ states, and laser-induced population transfer between these excited electronic states is indicated by the orange curve. The PES for the CO electronic ground state and for CO^+ electronic states are calculated with Molpro [92]. The upper energetic limit for the excited states participating in the

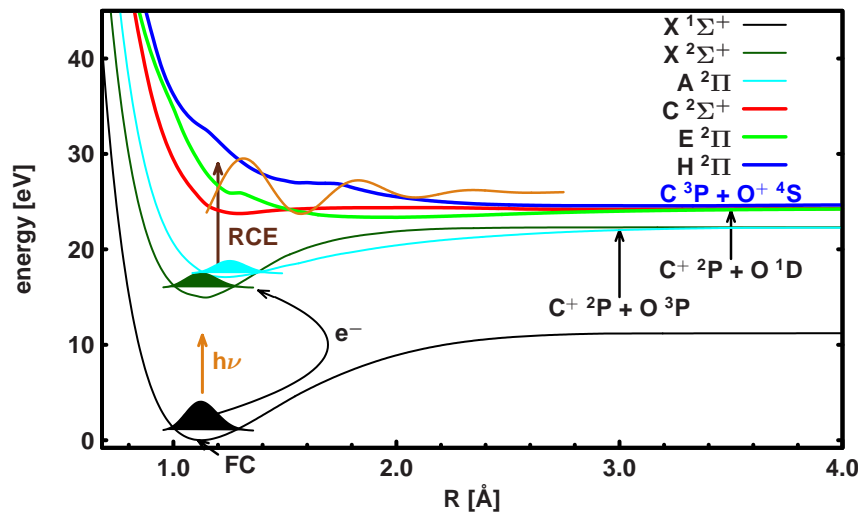


Figure 4.2: Potential energy surface (PES) of the CO ground state $X^1\Sigma^+$, selected PES of CO^+ states and Franck-Condon point (FC) for the ionization from neutral CO obtained by calculations described in detail in [35]. Ionization and RCE are identified by arrows with labels $h\nu$ and RCE, respectively. The orange line shows electronic states coupled by the remaining laser field.

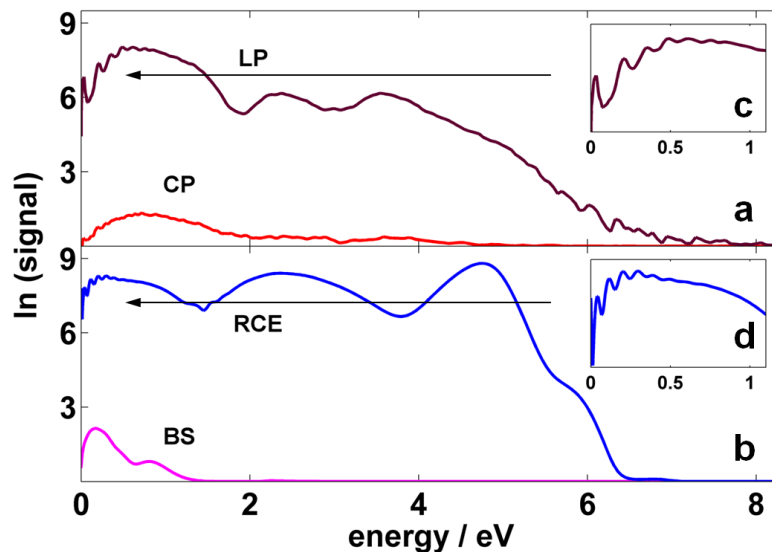


Figure 4.3: a) Experimentally observed C^+ kinetic energy spectra for CO dissociative ionization by linear (LP) and circular (CP) polarized light pulses without phase stabilization (using the same field strength), integrated over $\theta = [0^\circ, \alpha]$ with $\alpha = 60^\circ$. (b) Calculated C^+ kinetic energy spectrum including recollision excitation (RCE) and multiphoton excitation (BS) mechanisms. The insets in (c) and (d) are zooms in the low energy range for experimental and calculated spectra. Adapted from [35].

dissociative ionization is related to the cutoff energy of the recolliding electron ($3.17 U_p$), which is about 13 eV with the present laser parameters. The experimentally observed asymmetry (see Fig. 4.1c) can arise from contributions of all three mentioned steps. Note that the initial population of excited states by recollision is likely dependent on the CEP, but its calculation is currently out of scope for larger molecules [32]. The remaining two steps, namely the orientation-dependent ionization and the time-dependent electron localization during the dissociation in the few-cycle laser fields were theoretically treated in Refs. [24, 35] and are discussed in detail below.

4.1.3 Angle-dependent ionization of molecules: a theoretical approach

The ionization of atoms in strong laser fields has long been a subject of investigation for theorists [100, 101, 102, 103, 104, 105]. Classical approaches to calculate the ionization rate of atoms are the tunneling ionization model of Ammosov-Delone-Krainov (ADK) [102] and the strong-field approximation (SFA) [106]. Their extensions to the molecular case introducing molecular orbitals (MOs) lead to the MO-SFA [107] and MO-ADK [67, 108] models that could describe the ionization rate of small linear molecules. Both approaches provide orientation-dependent ionization rates for ionization from a given molecular orbital, e.g. the HOMO, within the one-center approximation. It is important to have a method capable to calculate the angle-dependent ionization rates of larger molecules. In general, such molecules are not necessarily symmetric, so that one-center approximation is no longer valid. In addition, smaller energetic spacing between outer molecular orbitals might introduce a multi-orbital contribution to the angle-dependent ionization probability. Recent strong-field experiments provide evidence of ionization from energetically close-lying valence orbitals, so that ionization occurs not only from the HOMO but also from lower-lying orbitals, e.g. the HOMO-1 [24, 109, 110, 111].

This section outlines an approach to calculate angle-dependent ionization probabilities that is applicable to complex molecular systems. It is based on electronic structure calculations and supports ionization from more than a single MO. A detailed description of the method can be found in Refs. [58, 97], where it was in particular shown that for diatomic heteronuclear molecules it is important to go beyond the one-center approximation in order to achieve good agreement with experimental data. In this context, the ability of the method was demonstrated comparing the theoretical results with MO-ADK calculations and with experimentally measured data for angle-dependent ionization probabilities of the

diatomic molecules D₂, N₂, O₂, and CO. In the experiments, the angular distribution of ionic fragments from the ionization of molecules in strong (about 10¹⁴ W cm⁻²) and sufficiently short laser pulses (here 4–5 fs) reflects the angle-dependent ionization probabilities [58]. In this case RCE and post ionization alignment of the molecules do not significantly change the angular distributions of detected fragments [112].

The theoretical calculations are performed as follows. The orientation-dependent ionization rate $w(\theta, t)$ of a molecule in an intense laser field can be calculated as the induced electron flux through the barrier of the combined molecular and external electric fields [101]:

$$\omega(\theta, t) = -\frac{d}{dt} \int_V \rho(\vec{r}, \theta, t) dV \quad (4.1)$$

where $\rho(\vec{r}, \theta, t) = \sum_{n \leq n_{HOMO}} |\psi_n(\vec{r}, \theta, t)|^2$ is the electron density and $\psi_n(\vec{r}, \theta, t)$ are the MOs of the molecule in the presence of the external field. The angle θ is the angle between the intramolecular axis and the external field. Within the axial recoil approximation this angle corresponds to the angle θ in the experimental images, under which the fragments formed by the dissociation of the molecule are observed. The MOs are calculated in the adiabatic approximation using a static electric field with the quantum chemistry package Molpro [92] and are represented on a three dimensional grid.

In order to evaluate the tunneling probability numerically the electronic wave function with and without the external field are necessary. In this sense Eq. 4.1 was integrated from the initial time t_i corresponding to a time where the electric field is zero to the final time t , where the field and therefore the ionization rate is maximal:

$$T(t, \theta; S) = \int_V \rho(\vec{r}, \theta, t_i) dV - \int_V \rho(\vec{r}, \theta, t) dV. \quad (4.2)$$

The integral in Eq. 4.2 is taken over the volume V which is confined by the surface S . For the surface S it is convenient to choose a plane perpendicular to the direction of the electric field. As the ionization takes place only at the edges of the electronic wave function, it was chosen to follow the basic idea of MO-ADK [67] to calculate the induced electron flux, so the surface S is spanned by all the outer turning points $\psi_n(\vec{r}, \theta, t)$. Beyond these points the exponentially decaying term in the electron wave function becomes dominant and the wave function enters the classical forbidden region relevant for the tunneling process. The surface S can be determined on the three dimensional grid by numerical evaluation of the

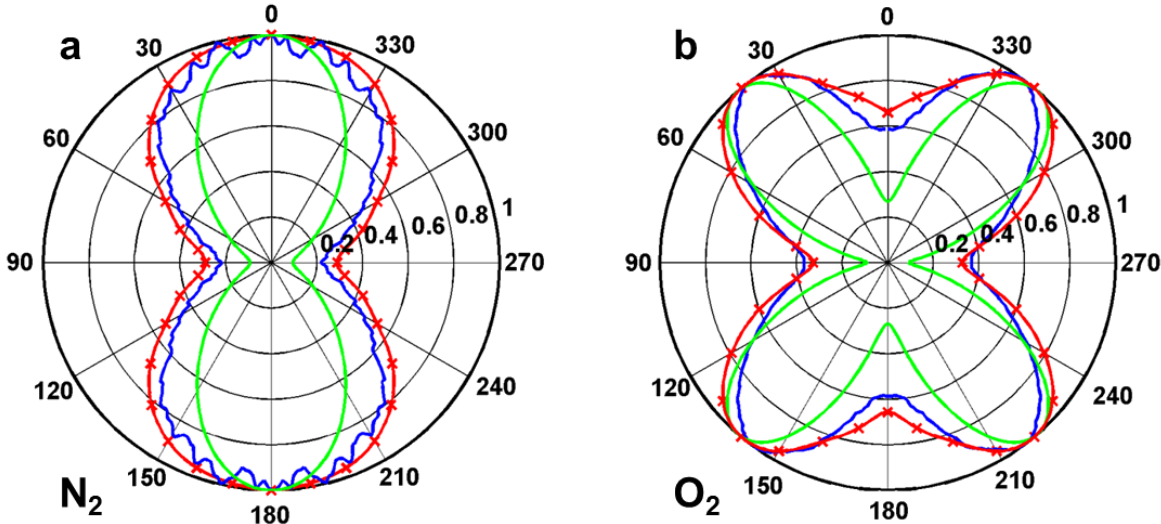


Figure 4.4: Angle-dependent ionization probability for (a) the HOMO ($3\sigma_g$) of N_2 and (b) linear combination of HOMOs ($1\pi_x^*$ and $1\pi_y^*$) of O_2 . Red crosses connected by the red lines indicate results of calculations by the method described in the text. Obtained values are compared directly to ionization probabilities measured in the experiment (blue lines) and calculated with the MO-ADK model (green lines). All lines were normalized by their maximum values. The laser polarization is vertical. Adapted from [58].

first and second derivative of $\psi_n(\vec{r}, \theta, t_i)$ starting from maximal \vec{r} values.

In order to make a direct comparison with an experiment where molecules were not aligned or oriented, the calculations were performed for series of orientations from 0° to 360° with steps of 10° . Figs. 4.4a and b illustrate a comparison of experimentally measured angle-dependent ionization rates (blue lines) for N_2 and O_2 molecules and angle-dependent ionization probabilities of these molecules calculated with the method introduced above (red lines) and with MO-ADK theory (green lines). The laser polarization is vertical. Experimental N^+ and O^+ momentum distributions were obtained by dissociative ionization of N_2 and O_2 molecules in the presence of 5 fs laser pulses at the central wavelength of 730 nm, 1kHz repetition rate and intensity of $1.6 \times 10^{14} \text{ W cm}^{-2}$ with a VMI spectrometer. Resulting ion distributions were integrated over the momentum ranges of $(1.2\text{--}2.2) \times 10^{-22} \text{ N}\cdot\text{s}$ for N_2 and $(1.1\text{--}2.2) \times 10^{-22} \text{ N}\cdot\text{s}$ for O_2 thereby excluding the background signal from doubly ionized parent ions. Detected N^+ and O^+ fragments and their doubly ionized parent ions N_2^{2+} and O_2^{2+} have the same mass-to-charge ratio and thus the same TOF. These species can not, therefore, be separated from each other with the VMI spectrometer.

In the case of N_2 , the electric field strength was set to 0.067 a.u., equivalent to the experimental peak intensity of $1.6 \times 10^{14} \text{ W cm}^{-2}$. Hartree Fock and MCSCF calcula-

tions for N_2 carried out with basis sets larger than STO-3G predict the wrong energetic ordering of the valence orbitals. The HOMO of the N_2 molecule is the $3\sigma_g$ orbital (not the $1\pi_u$), so that the ground state of N_2^+ has $X^2\Sigma_g^+$ symmetry. To overcome the wrong energetic ordering the HF/STO-3G level of theory was used to calculate correct ionization probabilities for N_2 . This calculated angular distribution looks very similar to the experimental one. The parallel vs. perpendicular ionization ratio is about 3.5 from the calculations (see red line in Fig. 4.4a) and about 4.5 for the experimental data (blue line in Fig. 4.4a) in excellent agreement with the published value of 4.5 [113]. The shape of the angle-dependent ionization probabilities obtained from MO-ADK theory (green line) also follows the experimental data. However, the predicted parallel vs. perpendicular ratio of 10.5 doesn't fit the experimental value well.

The electronic wave functions for the O_2 molecule are calculated on the CASSCF(12,10)/6-311+G* level of theory and an electric field strength of 0.067 a.u. Molecular oxygen is a stable diradical. It has two unpaired electrons occupying two degenerate $1\pi_x^*$ and $1\pi_y^*$ molecular orbitals in its electronic ground state. The degeneracy of the two orbitals is not broken in the presence of the electric field and ionization from both orbitals can occur. Taking into consideration the fact that tunneling from both orbitals is allowed with the same probability, the ionization probability from the linear combination of both HOMOs of O_2 was calculated. The resulting angle-dependent ionization rate is shown in Fig. 4.4b as red crosses fitted by the red line. This result is in good agreement with the experimental data (Fig. 4.4b blue line) and the literature [114].

For the MO-ADK calculations, consistent with the literature [67, 114], only the π_g orbital lying in the plane perpendicular to the rotation axis was used. In general, the result of MO-ADK is also in good agreement with the experimental data (Fig. 4.4b green and blue lines). However, the minima in the ionization rate along and perpendicular to the laser polarization direction are overestimated. This arises mainly from the assumption of an ionization only from one HOMO [58]. Taking into account both HOMOs provides good agreement with the experimental data, especially with respect to the minima at $\pm 0^\circ$ and $\pm 90^\circ$.

4.1.4 Ionization of CO in few-cycle laser fields

The angle-dependent ionization probability of CO was calculated for an instantaneous electric field of 0.047 a.u., corresponding to the experimental peak intensity. Ionization was treated as a coherent process, since a linear combination of the HOMO and HOMO-1 (3σ

and $1\pi_{x/y}$ molecular orbitals of CO) was used. A tunneling electron has equal probability to be in either of the included orbitals, so equal weights in the linear combination were applied. The resulting ionization rate qualitatively reproduces the experimentally observed angular distribution in Fig. 4.1a. For better visibility, the calculated curve (black crosses and black solid line) has been normalized. The HOMO-2 wasn't included in the calculations as its tunneling probability is too small. The energy difference between the HOMO-2 and HOMO orbitals is 3 times larger than the one between the HOMO-1 and the HOMO orbitals (0.083 a.u. vs. 0.257 a.u.). When ionization from the HOMO only is considered as in Ref. [98], the calculated angular distribution peaks along the field vector and matches the results reported at a slightly lower intensity of $6 \times 10^{13} \text{ W cm}^{-2}$). However, in the previous work by Alnaser *et al.* [98], the observed angular distribution was a result of the Coulomb explosion channel $\text{CO}^{2+} \rightarrow \text{C}^+ + \text{O}^+$, which cannot directly be compared with the present experimental results for the dissociative ionization of CO, where the recollision or dissociation doesn't significantly alter the angular distribution produced by the ionization step. The good agreement between theory and experiment in Fig. 4.1a indicates that the angular distribution arises from an ionization out of two orbitals. Also for the N_2 molecule (isoelectric to CO), a contribution from the HOMO-1 was recently observed in high-harmonic generation [110].

The calculated asymmetry in the ionization step caused by a CEP-stabilized laser field can be extracted by integration of the calculated ionization probabilities over suitable orientation angles. Assuming ionization only at the extrema of the field, the asymmetries for various contributions of half-cycles as shown in Fig. 4.5 (red line) were calculated for a $\varphi_{CEP} = \pi$ pulse. The volume-averaged angle-dependent ionization probability was obtained for a Gaussian spatial intensity profile. The corresponding volume-averaged asymmetries for the combination of the three most prominent half-cycles are presented in Fig. 4.5 as blue crosses connected by a blue line. Comparing the calculated and experimentally observed asymmetry it's clear that the calculated asymmetry amplitude is below the total asymmetry amplitude in the experiment (~ 0.2). It should be noted that the contribution of different half-cycles might change the direction for preferential ionization of the molecule by the laser field. For instance an ideal single-cycle minus cosine pulse (with one minimum A and $\varphi_{CEP} = \pi$) mainly ionizes randomly aligned CO molecules such that the C atom points upwards (asymmetry of approximately +0.98). This is in agreement with Ref.[115] where the orientation dependence of the ionization of CO was studied in great detail. Ionization caused by a slightly longer laser pulse with local extrema at B', A, and B results in a negative value of asymmetry, hence the C atom of resulting CO^+

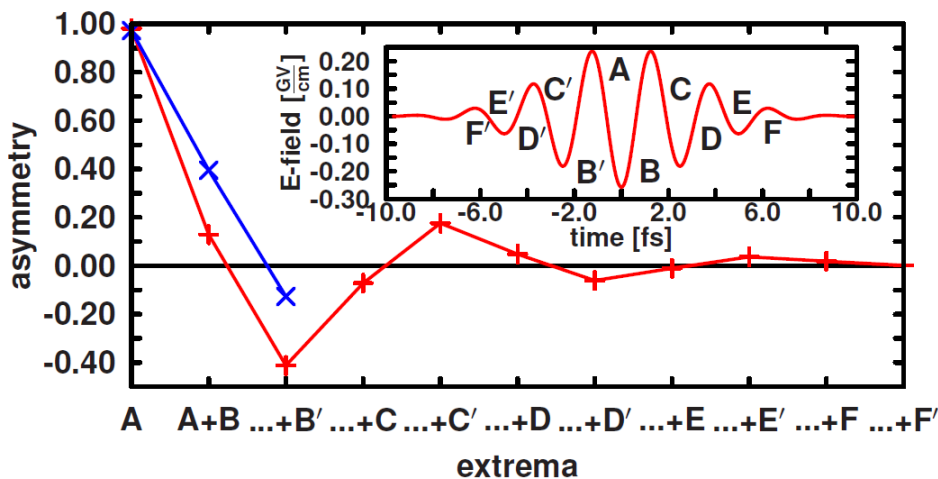


Figure 4.5: Calculated asymmetries (+ symbols connected by a red line) for various combinations of half-cycles of the laser field (shown in the inset, corresponding extrema are marked). The \times symbols show volume-averaged asymmetry contributions (connected by a blue line). From [24].

molecular ion preferentially points downwards. Considering local extrema C' , B' , A , B , and C would result into the preferential upward emission of C^+ fragments. Adding more contributing extrema rapidly decreases the asymmetry amplitude and at some point it reaches the zero value. A detailed description of the complete ionization treatment can be found in Ref. [97]. Ionization induced at five half-cycles agrees with the phase assignment used in the experiment (see in Fig. 4.1b) and indicates the laser pulse duration of ~ 5 fs. Similar situation has occurred in the case of Ref. [34] when five half-cycles were included in the treatment of coupled electron-nuclear dynamics for the dissociative ionization of D_2 in the presence of 5 fs few-cycle near-IR laser field.

The extremely short pulse duration used in the experiments (740 nm, 4–5 fs) is too short to cause a significant dynamic alignment before dissociation. Therefore, rotation of CO induced by the laser field was neglected. Field-free rotation is also neglected as it takes place on a much longer timescale (~ 8.7 ps for a full rotation of CO at its equilibrium distance). Field-free orientation of CO by an intense two-color (800 nm + 400 nm) femtosecond (about 45 fs) laser field is discussed in the next chapter.

If ionization would be only one step in the dissociative ionization of CO responsible for the CEP dependence, the experimentally observed asymmetry for all observed C^+ ions would be expected to be seen irrespective of their kinetic energy or angular distribution. However, in our experiments the angular range over which the asymmetry is observed depends on the fragment kinetic energy, suggesting that ionization might play a preferential

role but the experimental results can not solely be explained by the ionization mechanism.

4.1.5 Dissociation dynamics of CO in few-cycle laser fields

Another important component of asymmetry might arise from the dissociation process. The dissociation dynamics of CO^+ were theoretically treated in detail in Refs. [24, 35]. The focus of this section is to illuminate possible contributions from the dissociation step and furthermore draw a mechanistic picture for the steering of electrons in multielectron systems. The theoretical treatment of the dissociation of CO^+ described below is based on a recently introduced approach for coupled electron and nuclear dynamics [34]. The method differs from well-established quantum chemical approaches for propagating nuclear wave packets on coupled Born-Oppenheimer potentials, where the electronic motion is described accurately, however without a simultaneous treatment of nuclear motion [35]. In the method used here, the electronic wave function is propagated in the eigenstate basis and is coupled to the nuclear dynamics (propagated on a grid). The proper time step for both dynamics is evaluated recursively [35, 97]. The approach is i) the first scalable method treating more than one electron (5 active electrons are used) and ii) describes both the motion of an electronic and nuclear wave packet quantum dynamically. The Franck-Condon (FC) principle has been applied to determine the starting points of the wave packets on the excited states. Quantum dynamical simulations start after the recollision, assuming ionization of CO only at the maximum of the electric field and recollision of the electron after 1.7 fs [69]. Multiple recollisions of the ejected electron from subsequent half-cycles are less probable for such short pulses and can thus be neglected [69, 70]. The initially-formed nuclear wave packet is excited from the $X^2\Sigma^+$ and $A^2\Pi$ states to higher electronic states. A coherent superposition of several electronic states is created and simultaneously the electronic and nuclear wave packet motion is initiated. From the large set of CO^+ PES [24], the three potentials shown in Fig. 4.2 as typical representatives for the induced dynamics were chosen. The orientation of CO^+ ions relies on the angle-dependent ionization probability of CO and is found to peak around 45° to the laser polarization, so that all transitions between Σ and Π states are allowed. After comparison of experimental and calculated spectra from test calculations two states correlated with the $\text{C}^+ (^2P) + \text{O} (^1D)$ channel were included: $C^2\Sigma^+$ as the weakly bound state to obtain the structure in the low kinetic energy spectrum and the $E^2\Pi$ state to resemble the repulsive dynamics. The $H^2\Pi$ state was included because it is the first and only reachable state leading to the $\text{C} (^3P) + \text{O} (^4S)$ channel, hence delivering O^+ fragments as observed in the experiment.

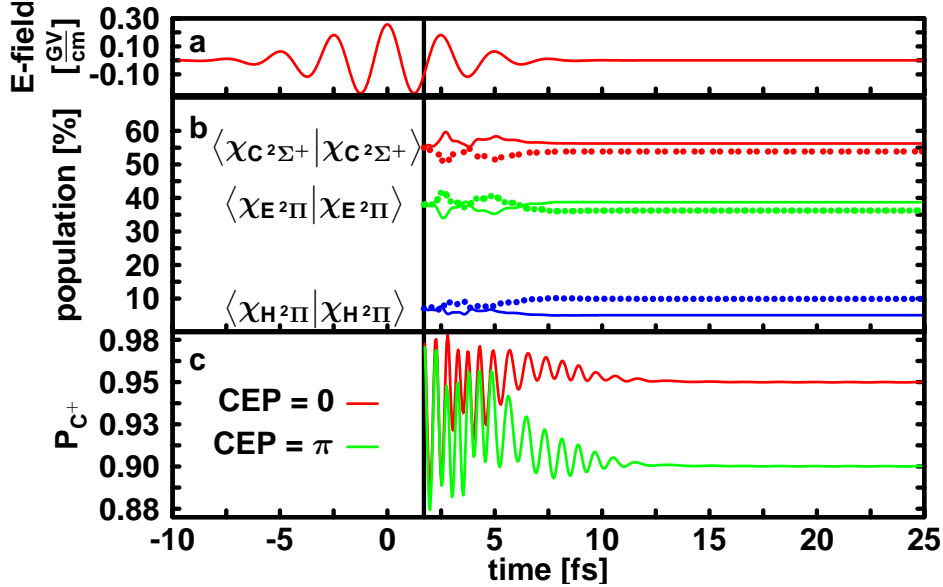


Figure 4.6: (a) Electric field of a cosine-pulse ($\varphi_{CEP} = 0$). (b) Time-dependent populations of the $C^2\Sigma^+$, $E^2\Pi$ and $H^2\Pi$ states of CO^+ after RCE (solid: $\varphi_{CEP} = 0$; dotted: $\varphi_{CEP} = \pi$). (c) Temporal evolution of the probability measuring a C^+ fragment P_{C^+} for $\varphi_{CEP} = 0$ (red line) and $\varphi_{CEP} = \pi$ (green line). From [24].

The molecular wave function Ψ_{mol} is set up as the sum over these three electronic states with index i , nuclear wave functions χ_i , and field-free electronic wave functions φ_i vs. nuclear R and electronic r coordinates and time t :

$$\Psi_{mol}(R, r, t) = \sum_i \varphi_i(r, t; R) \chi_i(r, t; R). \quad (4.3)$$

The initial wave packet is composed as a 55:38:7 distribution of the states involved, ordered in increasing energy. This population distribution was chosen as it delivers the experimentally observed ratio between C^+ and O^+ fragments. Further calculation details can be found in Ref. [35]. The temporal evolutions of (a) the laser field and (b) the population of selected electronic states are illustrated in Figs. 4.6a and b.

The origin of the observed energy distribution (Fig. 4.3a) can be explained based on the results of calculations (Fig. 4.3b). The low kinetic energy spectrum (0.15–1.5 eV) arises from the dynamics on the weakly bound $C^2\Sigma^+$ state and the spectrum in the range between 2.0 and 2.8 eV originates from the purely repulsive $E^2\Pi$ state. The high energy spectrum reflects the dynamics of the second repulsive $H^2\Pi$ state leading to O^+ fragments. The structure in the low kinetic energy spectrum (Figs. 4.3c, d) discloses an interference

effect. The recollision excitation produces a high energy wave packet consisting of both bound and continuum vibrational states on the $C^2\Sigma^+$ surface. During the break-up of CO^+ the bound vibrational states are trapped in the potential well and interfere with the outgoing part of the wave packet. The nuclear wave packet dynamics in CO^+ is fully explored in Ref. [97]. The spectra of fragments could be seen as an experimental evidence of the coupled dynamics theoretically described above. When the dynamics occurs on coupled electronic states, the electronic wave function is a superposition of all contributing electronic states and not separable. Therefore the recorded kinetic energy spectra should contain information about the C^+ and O^+ channels simultaneously. Both experimentally observed C^+ and O^+ spectra in fact look very similar and reveal three peaks.

In the experiment the yield of C^+ ions emitted in the upward or downward direction along the laser polarization axis (Fig. 4.1a) was measured. In the theoretical treatment the asymmetry from both the orientation-dependent ionization (Fig. 4.5) and from the time-dependent electron localization during the dissociation in the few-cycle laser field were calculated separately. Fig. 4.6c shows temporal evolution of the probability to find C^+ fragments in the upward or downward direction resulting from electron localization. In the experiment molecules are randomly oriented. Therefore the asymmetry cannot be derived from the electron density of a single molecule with only one specific orientation. In calculations the probability P_{C^+} of measuring a C^+ fragment for a given orientation is defined as

$$P_{\text{C}^+}(t) = \int_{x_{\min}}^{x_{\max}} dx \int_{y_{\min}}^{y_{\max}} dy \int_{z_{\min}}^0 dz \rho(r_1, t; R(t)) \quad (4.4)$$

where $\rho(r_1, t; R(t))$ is the electron density as a function of the electron coordinate r_1 , time t and nuclear coordinate $R(t)$; x , y and z refer to the molecular frame with z along the molecular axis and the O-atom oriented along negative z -values [35]. The experimentally observed CEP-dependent asymmetry can be approximated by the final P_{C^+} values from two different orientations. For a given orientation of the CO molecule where the C-atom points upward with respect to the laser polarization axis (Eq. 4.4), the electron density associated with C and O determines the probability of observing a C^+ ion or neutral C upon the break-up of the molecule in the upward direction. Changing the orientation of the molecule by 180° is equal to shifting the CEP by π as the transition dipole moment changes the sign. That means that for the opposite orientation of CO we obtain a high probability to find the C^+ ion or neutral C in the downward direction. Thus the CEP-

dependent asymmetry in the dissociation step can be calculated by $P_{C^+}(t)$ for two CEP values shifted by π . As is shown in Fig. 4.6c, the probability of measuring a C^+ fragment upon the break up of the molecule can be changed by $\sim 3\%$ through the CEP. A small value for the resulting asymmetry due to the electron localization notably confirms that the ionization makes a significant contribution to the total asymmetry.

4.1.6 Conclusion and perspectives

The results for CO have shown that the CEP-control of electron localization is not restricted to one-electron systems but can be found also in multielectron systems. First, the ionization of CO in a near-single-cycle phase-stable laser field is found to be orientation-dependent [24]. Second, excitation of CO^+ by the laser-driven recolliding electron, that was freed in the first ionization step, leads to dissociation and laser-induced coupling of potential energy curves of CO^+ , resulting in the formation of $C^+ + O$ and $C + O^+$ fragments and a CEP dependent asymmetry [35]. In this particular study, the individual contributions from the two mechanisms could not be clearly distinguished from the experimental data. Future studies, in particular on heteronuclear molecules are aimed into this direction. Note that a recent study on the controlled directional ion emission from CO driven by a few-cycle laser field at higher intensities ($3.5, 6$ and $12 \times 10^{14} \text{ W cm}^{-2}$) confirmed the dominant role of the ionization process [80].

4.2 Waveform control of orientation-dependent ionization of DCl in few-cycle laser fields

A diatomic molecule with a non-zero dipole moment represents a system where electrons are partially localized near one of the two nuclei. In this case one might expect distinct ionization probabilities for different orientations of the molecule with respect to the external electric field. The ionization rate depends strongly on the instantaneous intensity. In a few-cycle pulse the instantaneous intensity varies very strongly between half-cycles. Thus the asymmetry contributions from an ensemble of molecules interacting with different half-cycles with opposite sign are not equal and therefore the overall asymmetry (with respect to the electric field direction) will become larger than zero. However the amplitude of the resulting asymmetry generated by a few-cycle pulse might be decreased in comparison to an ideal case of a subcycle laser pulse with one field maximum. These considerations are

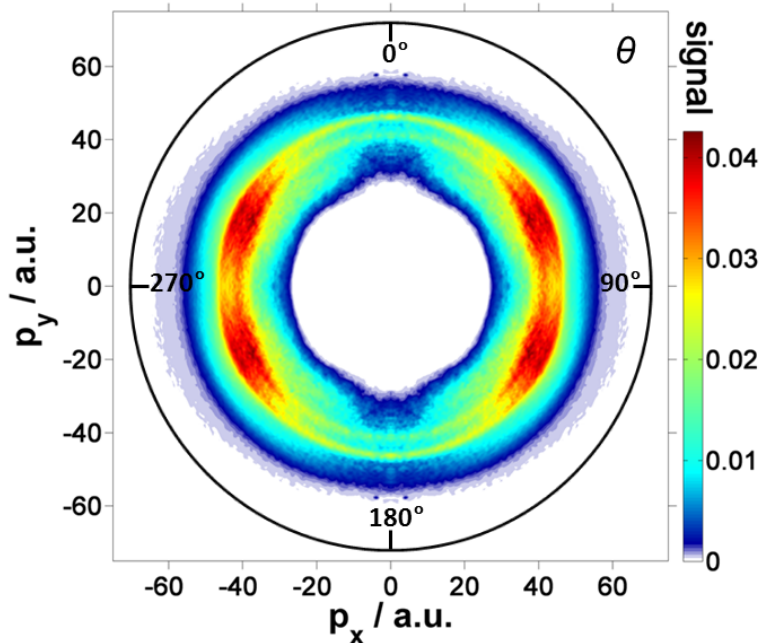


Figure 4.7: Momentum distribution of D^+ fragments from the dissociative ionization of DCl (the colorscale is linear). The image was left-right as well as up-down symmetrized and averaged over all CEP values to increase the signal-to-noise ratio. The laser is polarized along the p_y -direction. Adapted from [26].

important when a CEP-stabilized, few-cycle laser pulse interacts with a randomly oriented sample of neutral molecules and can lead to an asymmetric angular distribution of ionized molecules. In the case of a random CEP or for longer pulses, the asymmetry from the ionization will vanish. Deuterium chloride (DCl) has been investigated in the framework of this thesis towards its orientation-dependent ionization probability in a few-cycle phase-stabilized laser field [26]. The dipole moment of deuterium chloride (1.12 D [116]) is about 10 times larger than the dipole moment of carbon monoxide (0.122 D [117, 118]), making it an interesting candidate for studies on the role of the ionization step in generating an asymmetric momentum distribution of fragment ions.

4.2.1 Experiment

The fragmentation channels of the dissociative ionization of DCl resulting in $Cl^+ + D$ and $Cl + D^+$ are well known (see e.g. [119, 120]). While the CEP-dependent fragmentation of DCl^+ has been investigated theoretically [121], no experimental study on the CEP control of the dissociative ionization of DCl in few-cycle light fields was reported. In our

experiments DCl molecules were interacting with 5 fs CEP-stabilized, linearly polarized laser pulses at a central wavelength of 720 nm and an intensity of $1.3 \times 10^{14} \text{ W cm}^{-2}$. The momentum distributions of D^+ and Cl^+ fragments from the dissociative ionization of DCl were recorded with a VMI spectrometer.

Fig. 4.7 shows the momentum distribution for D^+ ions averaged over CEP. The image is left-right symmetrized with respect to the laser polarization (p_y -direction). The momentum distribution for Cl^+ ions has a similar structure. The minor difference is that at higher momenta of the D^+ ions narrow concentric rings are visible, which are not visible in the Cl^+ data. That might be due to the limited momentum resolution of the Cl^+ ions or less statistics caused by a much stronger signal from the DCl^+ parent ion, its nearest neighbor in the TOF spectrum, which could not be entirely suppressed.

Angle-integrated energy spectra for D^+ and Cl^+ ions obtained from their momentum distributions are shown in Figs. 4.8a and c, respectively. In order to illustrate the effect of the CEP on the fragment emission from the dissociative ionization of DCl the angle-integrated asymmetries $A(W, \varphi_{CEP})$ (Eq. 3.11) with $\alpha = 60^\circ$ for D^+ and Cl^+ ions are displayed in Figs. 4.8b and d. Both asymmetry maps exhibit energy independent oscillations. The data points of angle- and energy-integrated asymmetries $A(\varphi_{CEP})$ are shown in Fig. 4.8e. Solid lines correspond to fits by a cosine function. Blue (for D^+) and red (for Cl^+) curves are found to be offset in phase by approximately π . Measurements displayed here were taken for the same relative phases $\varphi_{CEP} = \varphi_0 + \varphi$, i.e. the unknown φ_0 remained constant.

4.2.2 The dissociation pathways

The mechanism of the dissociative ionization of DCl is quite similar to the previously discussed cases of D_2 and CO molecules. Tunnel ionization of DCl from its ground state $X^1\Sigma^+$ (the degenerate HOMOs are 3p Cl-orbitals) [109] and population of the $X^2\Pi$ electronic ground state of DCl^+ occurs at a peak of the laser field. After the ionization step the following dissociation scenarios can play a role: i) dissociation via BS [38] taking into account bound $X^2\Pi$ or $A^2\Sigma^+$ states; ii) subsequent RCE to higher-lying (predominantly repulsive) states of DCl^+ , including the $2^2\Pi$ state, which peaks at 7.9 eV and is also observed in the experiment (see the angle-integrated spectrum of D^+ ions in Fig. 4.8a). Dissociation via BS from either the $X^2\Pi$ or the $A^2\Sigma^+$ state, which might be reached by sequential laser excitation by three photons [109], would lead to low kinetic energies of the D^+ and Cl^+ fragments. Akagi *et al.* have recently observed fragments from such a dissociation

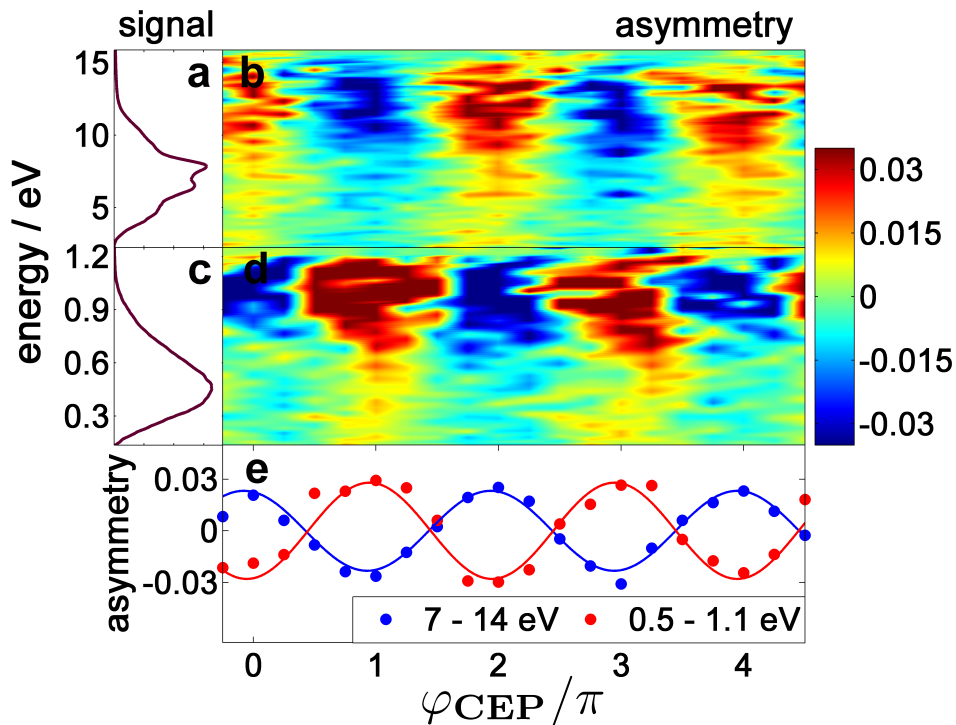


Figure 4.8: CEP-averaged fragment ion energy spectra and asymmetry maps $A(W, \varphi_{CEP})$ for D^+ ions, (a) and (b), and Cl^+ ions, (c) and (d). $A(W, \varphi_{CEP})$ was obtained by integrating the signal over an angular range from 0° to 60° along the polarization axis. The angle- and energy-integrated asymmetries $A(\varphi_{CEP})$ for D^+ and Cl^+ ions are shown in (e). Adapted from [26].

mechanism at kinetic energies below 2 eV (D^+) and below 0.05 eV (Cl^+) [109]. The energy spectra of D^+ and Cl^+ species observed in our experiments are much higher, therefore dissociation via BS is not considered in the following discussion. The coupling of various excited states of DCl^+ might explain the resembling momentum distributions for D^+ and Cl^+ fragments similar to the case of CO^+ [24].

4.2.3 Angle-dependent ionization rate of DCI

The theoretical treatment of the orientation-dependent ionization rates of DCI includes both HOMOs and goes beyond the one-center approximation. Therefore the ansatz of Ref. [58] is useful to calculate strong-field ionization probabilities in DCI [26]. The molecular orbitals of DCI were computed in the adiabatic approximation using a static electric field with the quantum chemistry package Molpro [92] on the CASSCF(6,9)/6-311G++ (2DF,2PD) level of theory and with electric field strength of 0.06 a.u. (corresponding to

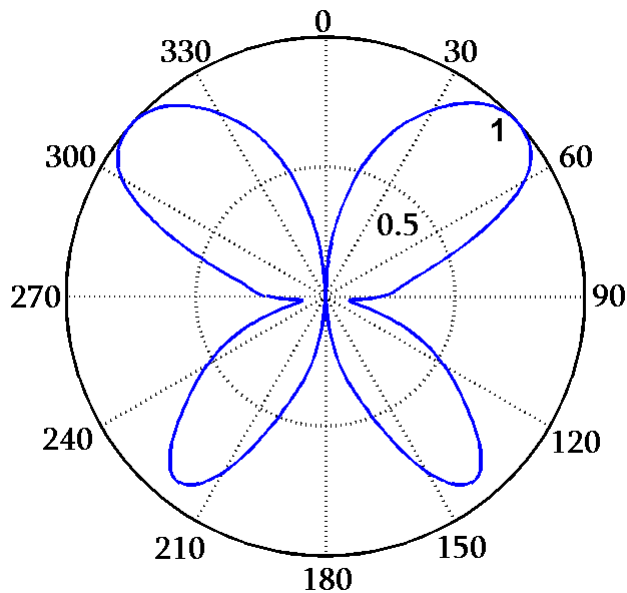


Figure 4.9: Calculated orientation-dependent ionization probability for the HOMOs of DCl at intensity of $1.3 \times 10^{14} \text{ W cm}^{-2}$, obtained for ionization at the field maximum of a cosine-type pulse ($\varphi = 0$). Adapted from [26].

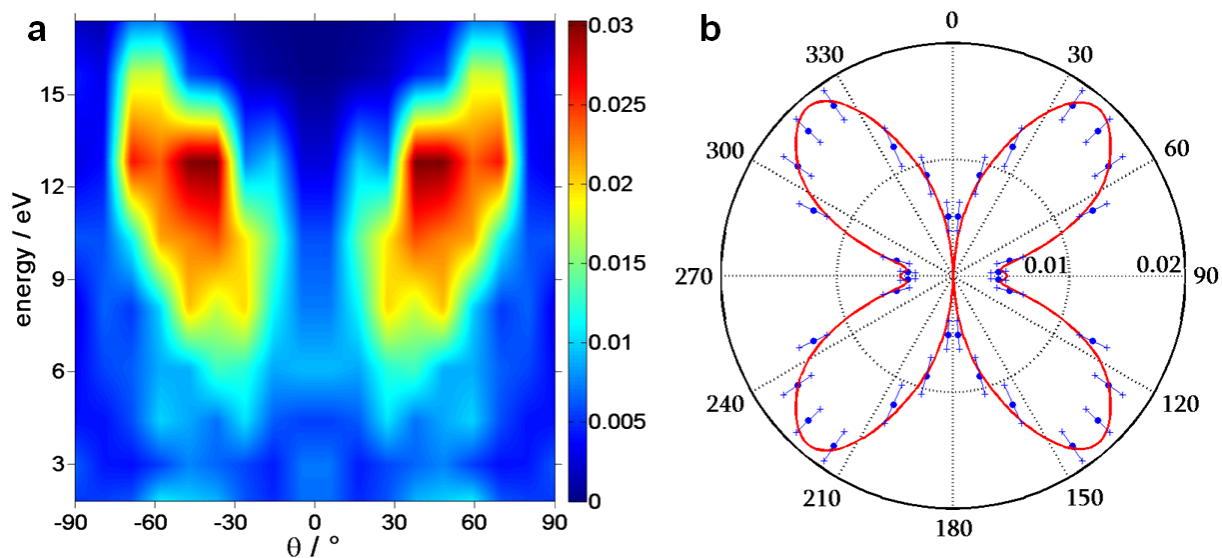


Figure 4.10: (a) Absolute value of the asymmetry amplitude $|A(W, \theta)|$ of D^+ fragments. The image is left-right symmetrized along the direction of the laser polarization (0°). (b) Energy-integrated (over 6–16 eV) asymmetry amplitude $|A(W, \theta)|$ derived from (a) (blue dots) as compared to the calculated symmetric ionization probability from the HOMOs of DCl (red line). From [26].

the peak intensity in the experiment). The calculated asymmetric angle-dependent ionization probabilities for an ideal cosine-type pulse ($\varphi = 0$, ionization only at one maximum) are plotted in Fig. 4.9. Note that when the electric field points upwards (the polarization of the laser is vertical), then the DCl molecules with the Cl-atom pointing upwards are preferentially ionized. Characteristic features of DCl molecule are distinct maxima of the ionization probability around $\pm 45^\circ$ and $\pm 135^\circ$ (see Fig. 4.9) and minima at 0° , $\pm 90^\circ$ and 180° . In order to shed light on the origin of the observed asymmetry in DCl the angular distributions of D^+ and Cl^+ fragments were analyzed. Under the axial recoil approximation and neglected dynamic alignment of the molecules in the few-cycle laser pulse, the measured D^+ ion angular distribution from an unaligned sample of DCl follows the ionization probability, i.e. the probability to remove an electron from DCl. The angle-dependent asymmetries obtained via Eq. 3.10 as functions of kinetic energy W , fragment emission angle θ and phase φ_{CEP} were fitted to a φ_{CEP} dependent cosine function (Eq. 3.13). The obtained result for D^+ ions is shown in Fig. 4.10a. The absolute value of the asymmetry amplitude $|A(W, \theta)|$ is maximal in the energy range between 9 and 14 eV and in the angular range between 30° and 60° . It becomes smaller towards emission angles of 0° and $\pm 90^\circ$, in other words along and perpendicular to the laser polarization direction. In order to show the angular dependence more clearly, the absolute value of the asymmetry amplitude $|A(W, \theta)|$ has been integrated from 6 to 16 eV. The resulting energy-integrated asymmetry amplitude $|A(\theta)|$ is shown in Fig. 4.10b (blue dots).

The energy-integrated asymmetry amplitude $|A(\theta)|$ is not dependent on the CEP. Therefore, the orientation-dependent ionization probability for a random CEP was obtained. For comparison to theory, averaging of the ionization probability over the two opposite field directions ($\varphi = 0^\circ$ and $\varphi = 90^\circ$) was done. For clarity, the direct comparison of experimental $|A(\theta)|$ and calculated ionization probability from the HOMOs of DCl is shown in Fig. 4.10b over the range of 360° . The butterfly shape of the asymmetry amplitude (blue dots) peaks at 45° and resembles the orientation-dependent symmetric ionization probability (red solid line). The momentum distributions of D^+ fragments are more pronounced at θ about $\pm 60^\circ$. These fragment angular distributions differ from the calculated ionization probability from the HOMOs of DCl (which peaks at $\pm 45^\circ$, Fig. 4.10b). This indicates that the angular distribution of preferentially ionized DCl^+ ions is further modified in processes following ionization, i.e. RCE and dissociation.

The good agreement between the angular dependence of the asymmetry amplitude and the ionization probability from the HOMOs of DCl suggests that the ionization is responsible for the observed asymmetry in the emission of charged fragments. The observed

π -phase shift in the CEP-dependence of the asymmetry of D^+ and Cl^+ fragments (shown in Fig. 4.7) further supports the proposed mechanism.

4.2.4 Conclusions and outlook

Few-cycle laser pulses preferentially ionize DCl oriented at certain angles relative to the direction of the electric field, so that the resulting DCl^+ ions are partially oriented. A π -phase shift of the electric field results in a π -phase shift of the DCl^+ orientation and fragment asymmetries. Thus, the orientation of DCl^+ is directly imprinted in the asymmetry of the fragment ion emission. The dissociation step has only been modeled for longer wavelengths [122]. Modeling the dissociation process for shorter wavelengths is still in progress.

Similar control can be achieved in other heteronuclear molecules with potentially higher degrees of orientation. Taking advantage of this control scheme (Fig. 4.11), near-single-cycle light fields may be used to produce samples of oriented molecular ions under field-free conditions for studies on their dynamics in the molecular frame.

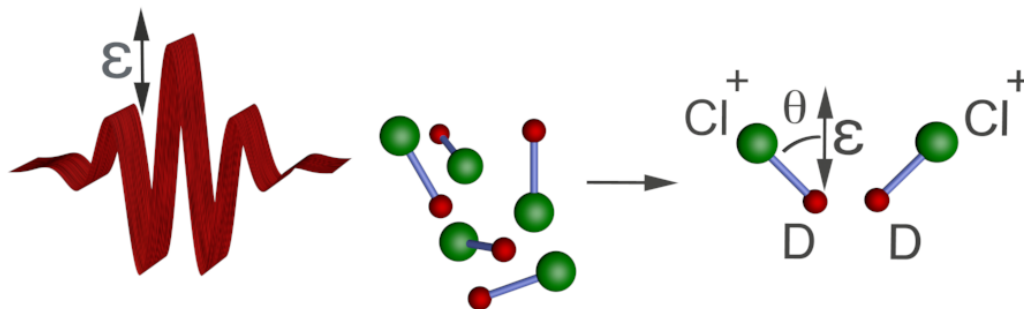


Figure 4.11: Schematic view of CEP-stabilized few-cycle laser pulse ($\varphi_{CEP} = 0$) permitting the control over the orientation of DCl^+ in the ionization of randomly oriented DCl molecules. Figure courtesy: Bernd Ullmann, MPQ.

Two-color laser-induced field-free molecular orientation 5

Aligned molecules have attracted widespread interest for applications such as ultrafast dynamic imaging [123], high harmonic orbital tomography [124, 125], laser-induced electron diffraction [126, 127], gas electron diffraction [128, 129], and photoelectron imaging using a HHG source [130]. Molecules have been successfully aligned in one and even three dimensions using strong, linearly-polarized laser fields [131]. For polar molecules, however, orientation is necessary to overcome the effect of averaging in two opposite directions.

Whereas the orientation of polar molecules is possible in strong DC fields [132] or by the combination of a laser field and a DC field [133, 134, 135] the presence of a strong DC field might influence the outcome of experiments on oriented molecular samples. The development of field-free orientation methods is crucial to avoid this limitation.

Laser-induced field-free orientation of polar molecules is much less studied than alignment. This chapter describes the first experimental observation of the nonadiabatic field-free orientation of the heteronuclear diatomic molecule carbon monoxide using a two-color femtosecond laser field. To aid the theoretical interpretation of the results, two alternative orientation mechanisms within the studied intensity range are proposed and discussed.

5.0.1 Orientation vs. alignment of molecules

A standard way to measure the molecular orientation is given by the expectation value of $\langle \cos \theta \rangle$ where θ is the angle between the molecular axis and a reference axis. An ensemble of molecules is considered to be oriented when its angular distribution is asymmetric with respect to the reflection plane perpendicular to the reference axis, i.e. $\langle \cos \theta \rangle \neq 0$. Orientation is always observed together with alignment, however, the opposite is not always the case. Alignment is measured as $\langle \cos^2 \theta \rangle$. Orientation differs from alignment where angular distribution is considered to be symmetric but not isotropic, i.e. $\langle \cos^2 \theta \rangle \neq \frac{1}{3}$ (see Fig. 5.1). Perfectly peaked along the reference axis alignment would be described by value of $\langle \cos^2 \theta \rangle = 1$ and angular distribution perpendicular to reference axis by $\langle \cos^2 \theta \rangle = 0$.

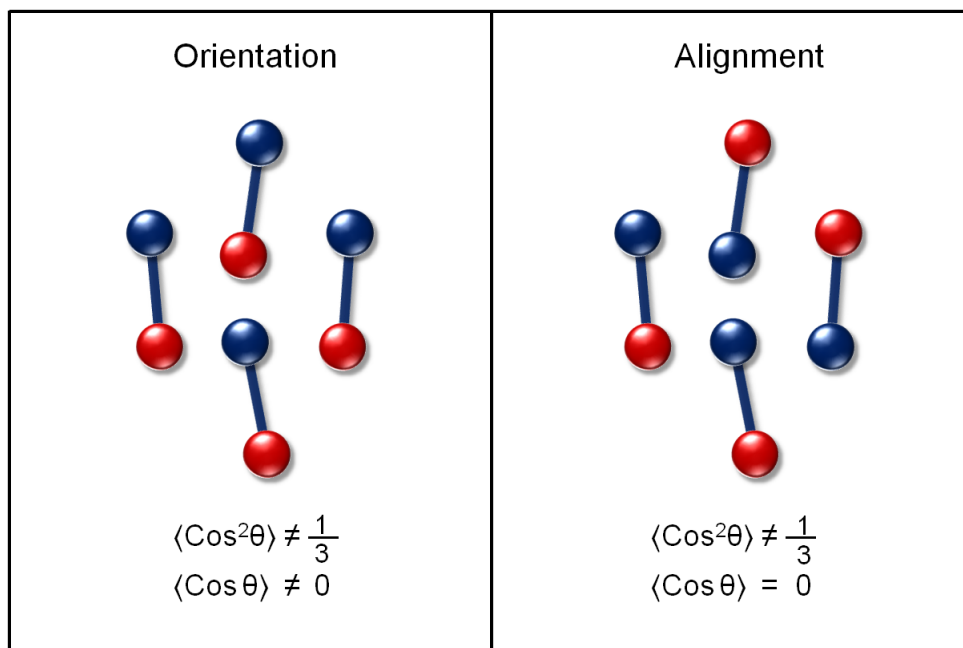


Figure 5.1: Schematic illustration of the difference between orientation and alignment for a sample of diatomic polar molecules. The reference axis is vertical.

5.0.2 Previous work on molecular orientation

Over the years since the initial work on orientation of molecules in the presence of a strong DC field [132], a few techniques for the field-free molecular orientation of molecules were proposed. For instance, the authors of Refs. [136, 137] have demonstrated laser-field-free transient molecular orientation. Sakai and co-workers have used a combination of a DC electric field and a laser pulse with adiabatic turn-on and nonadiabatic turn-off (switched laser field) to induce dynamic orientation in OCS molecules, which revives at full rotational periods [136]. Vrakking and co-workers used a hexapole state selector to produce NO molecules in a single quantum state and a combination of a DC field and an intense femtosecond laser field to induce orientation [137] of their samples. Although in both of these cases laser-field-free oriented molecules were obtained at full rotational revivals, the presence of a DC field was crucial to achieving orientation and might limit the application of these techniques.

Laser-induced field-free orientation using an IR and UV (ultraviolet) pulse pair was proposed in Ref. [138]. This approach considers sample diatomic molecules AB and was theoretically tested for CO. More recently, Fleischer and co-workers [139] demonstrated field-free orientation and alignment of OCS molecules using THz pulses.

Another method for laser-assisted field-free orientation without the necessity of a DC field was suggested by Kanai and Sakai [140] considering a FCN molecule as a sample and has been further explored theoretically for LiH, LiF, LiCl, OCS and CO molecules by Tehini and Sugny [141] and FCN molecules by Sakai and co-workers [142]. The approach is based on nonadiabatic excitation of both odd and even angular momentum states with a femtosecond two-color laser field, enabling net macroscopic orientation [143]. The following section describes first experimental studies using this technique, which have been implemented in the framework of this thesis.

5.1 Experimental results

This section focuses on the experimental observation of nonadiabatic, field-free orientation of the heteronuclear diatomic molecule CO induced by an intense two-color (800 and 400 nm) femtosecond laser field [56]. The field-free evolution of the rotational wave packet was created by a two-color orienting pump pulse and probed by the Coulomb explosion of the molecules using a delayed near-IR (800 nm) pulse. The orientation of the molecules was controlled by the relative phase of the two-color field (pump pulse).

In the experiment, the intensity of the two-color pump pulses was varied between $2.5 \times 10^{13} \text{ W cm}^{-2}$ and $1.2 \times 10^{14} \text{ W cm}^{-2}$. The intensity of probe pulse was $(2.6 \pm 0.6) \times 10^{14} \text{ W cm}^{-2}$. The data presented in Fig. 5.2 were taken for peak intensities of $1.2 \times 10^{14} \text{ W cm}^{-2}$ for both the 800 and 400 nm components of the pump pulses. The peak intensity of the orienting pulse was chosen so that the effect of orientation was maximal while ionization of the CO molecules by pump pulse was minimal. Strong-field ionization of CO by the probe pulse produces parent ions ranging from CO^+ to CO^{4+} . The fragmentation channels of parent ions were identified from comparison to results of COLTRIMS measurements [144]. The highest charged ionic fragments (C^{2+}) were chosen for accurate imaging of rotational wave packets of CO molecules. The evolution of the molecular alignment and orientation was analyzed by integration over the C^{2+} ionic fragments originating from the $\text{CO}^{3+} \rightarrow \text{C}^{2+} + \text{O}^+$ Coulomb explosion channel, which lies within the 10–16 eV kinetic energy range and is indicated by the letter B in Fig. 2.2 in the experimental methods section (chapter 2).

Fig. 5.2a displays a time-dependent evolution of the alignment parameter $\langle \cos^2 \theta_{exp} \rangle$ measured in the experiment vs. the two-color pump–single color probe delay for a two-color phase φ_1 . It should be noted that no significant dependence of the alignment parameter

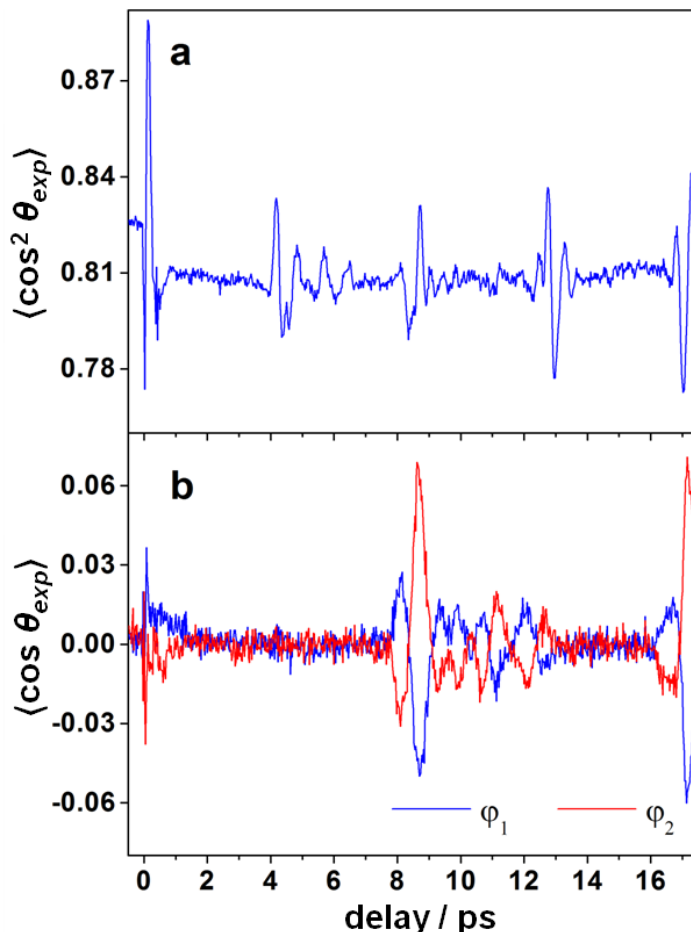


Figure 5.2: Experimentally observed evolution of the (a) alignment parameter $\langle \cos^2 \theta_{exp} \rangle$ and (b) orientation parameter $\langle \cos \theta_{exp} \rangle$ with pump-probe delay for two phases φ_1 and $\varphi_2 = \varphi_1 + \pi$ of the two-color pump pulse at intensities of $1.2 \times 10^{14} \text{ W cm}^{-2}$ for both the fundamental and second harmonic. Alignment and orientation parameters are obtained by integration of the C^{2+} fragments in kinetic energy range of 10 to 16 eV. Adapted from [56].

on the phase φ between the two-colors of the pump pulse was found. The alignment parameter $\langle \cos^2 \theta_{exp} \rangle$ peaks at $T_0 = 0.125 \text{ ps}$ (so called prompt net-alignment) and reveals the first two full revivals at $T_n = T_0 + nT_{rot}$ equal to 8.7 and 17.3 ps for $n = 1, 2$. Observed revival times are in good agreement with the expected rotation time $T_{rot} = 1/(2B_0c)$ of 8.64 ps where $B_0 = 1.93 \text{ cm}^{-1} = 8.79 \times 10^{-6} \text{ a.u.}$ [145] for CO and also in good agreement with earlier studies [146]. Net-alignment and anti-alignment also appear near fractional revival times $T_\eta = T_0 + \eta T_{rot}$. The alignment curve shows half-revivals near 4.3 and 12.9 ps. The contribution of additional alignment caused by the linearly polarized probe pulse [113] could be seen at negative delay times where the probe pulse comes first, before

the molecule interacts with the pump pulse. The experimental data show a quite high degree of alignment (0.83) as compared to an isotropic angular distribution corresponding to a value of 0.33. It should be noted that, since the alignment by the multicycle single color probe doesn't contribute to an existing up-down asymmetry in the ion image, this fact does not influence the results of the current studies on molecular orientation.

Fig. 5.2b presents the temporal evolution of the nonadiabatic orientation parameter $\langle \cos \theta_{exp} \rangle$. The control of the orientation direction was achieved with the phase φ of the two-color laser field. The presented data were obtained by integration over the Coulomb explosion channel mentioned above. The orientation signal $\langle \cos \theta_{exp} \rangle$ was optimized at a fixed delay between the pump and probe pulses corresponding to the first full revival of the alignment (at 8.7 ps). Different to the alignment parameter, the orientation parameter changes its sign when the phase φ between the two colors is shifted by π . For φ_1 (blue curve), $\langle \cos \theta_{exp} \rangle$ is negative, meaning the C^{2+} ions are emitted preferentially in the downward direction. Shifting the phase of the pump pulse by π ($\varphi_2 = \varphi_1 + \pi$, red curve), changes the C^{2+} ions emission to the opposite direction. Similar orientation data were recorded for O^{2+} fragments, where it was found that $\langle \cos \theta_{exp} \rangle$ is exactly out of phase with respect to the C^{2+} alignment parameter. This is consistent with the charged C and O fragments of the same molecule being emitted in opposite directions during the Coulomb explosion process. Different from the alignment (Fig. 5.2a), no noticeable effect of orientation is found at the fractional revival times of $\langle \cos \theta_{exp} \rangle$, field-free orientation was observed only at full rotational periods of CO.

5.2 The two-color field phase assignment

To obtain the absolute phase φ of the two-color pump pulses, the orientation experiments were accompanied by pump-only ω - 2ω measurements, where the preferential ionization of CO molecules by two-color laser fields was measured for different laser phases. It was shown recently that the phase dependence of the ionic fragment emission can be assigned to an absolute phase by comparison to the electron rescattering processes measured at the same laser parameters [115, 147, 148]. Ref. [148] measured both the photoelectrons and ionic fragments from CO simultaneously and Ref. [115] explored the rescattering electrons from Xe and ionic fragments of CO. Both methods gave similar results, concluding that the ionization probability of CO molecules is higher when the electric field points from C to O ions, as compared to the opposite direction. Similar to Ref. [115], asymmetry

maps for emission of C^{2+} , C^+ , O^+ ionic fragments of CO were recorded in our experiment. It was found that for the absolute phase $\varphi=0$ the C^{2+} ionic fragments are preferentially emitted in downward direction [115, 148], which corresponds to the orientation parameter for C^{2+} ions pointing upwards (red curve in Fig. 5.2b). Therefore, the phase assignment in Fig. 5.2b is the following: $\varphi_1 = \pi$ and $\varphi_2 = 0$. Note that this phase has been obtained from the recent work [115, 148] and the assignment of the absolute phase in CO experiments in Ref. [56] was incorrect as also stated in [115].

It was recently found that Stark-corrected MO-ADK theory predicts an opposite sign of the ionization direction, whereas Stark-corrected SFA calculations obtain a correct ionization direction [115]. Moreover, a combination of tunneling and multiphoton processes when both the 800 nm and 400 nm fields are applied to a molecular system might pose difficulties for strong-field tunneling approaches such as SFA and MO-ADK. A full theoretical treatment would need to employ a solution of the TDSE including the coupling of many electronic states of the neutral and ionic molecules [115].

5.3 Theoretical interpretation of the experimental data

5.3.1 The hyperpolarizability orientation mechanism

In this section, the theoretical model for the control of field-free molecular orientation by a two-color laser field is presented. Our theoretical treatment of the alignment and orientation of CO assumed a quantum mechanical rigid rotor model. A linearly polarized two-color laser field of the form $E(t) = E_\omega(t) \cos(\omega t) + E_{2\omega}(t) \cos(2\omega t + \varphi)$ was considered to interact with a polar linear molecule of carbon monoxide in its vibronic ground state. Any sample molecule placed in an electric field will experience a torque due to the angular-dependent interaction energy U between the induced dipole moment p and the field E . Considering a permanent dipole moment μ and both linear and nonlinear (only a second-order) responses of a medium with dipole polarizability $\alpha = \frac{\partial p}{\partial E} \Big|_{E=0}$ and hyperpolarizability $\beta = \frac{1}{2} \frac{\partial^2 p}{\partial E^2} \Big|_{E=0}$, the TDSE is given by

$$i \frac{\partial}{\partial t} \Psi(\theta, t) = [H_0 + U_d(\theta, t) + U_{pol}(\theta, t) + U_{hyp}(\theta, t)] \Psi(\theta, t) \quad (5.1)$$

where the corresponding dipole-interaction potentials can be written as described in Ref.[140]:

$$U_d(\theta, t) = -\mu E(t) \cos(\theta), \quad (5.2)$$

$$U_{pol}(\theta, t) = -\frac{1}{2}[\alpha_{\parallel}E^2(t)\cos^2\theta + \alpha_{\perp}E^2(t)\sin^2\theta] = -\frac{1}{2}(\Delta\alpha\cos^2\theta + \alpha_{\perp})E^2(t) \quad (5.3)$$

where $\Delta\alpha = \alpha_{\parallel} - \alpha_{\perp}$,

$$U_{hyp}(\theta, t) = -\frac{1}{6}[(\beta_{\parallel} - 3\beta_{\perp})\cos^3\theta + 3\beta_{\perp}\cos\theta]E^3(t). \quad (5.4)$$

For convenience, the above equations were written by using the angle θ being the polar angle between the molecular axis and the field polarization direction and substituting the linear and nonlinear terms of the induced dipole moment by components parallel (\parallel) and perpendicular (\perp) to the molecular axis. It was considered that a linear molecule has one dominant axes of polarizability $\alpha_{\parallel} > \alpha_{\perp}$. The dipole moment and polarizability anisotropy ($\Delta\alpha$) of carbon monoxide were taken from [118], the hyperpolarizability parameters (β_{\parallel} and β_{\perp}) were taken from [149]. Following the statement in Ref. [118] the hyperpolarizability and the dipole moment of CO exhibit the same sign. Thus, for convenience, the direction of the molecular axis is defined as the direction of the permanent dipole moment vector $\vec{\mu}$, i.e. pointing from the negative charge to the positive charge. In the case of the CO molecule the dipole moment C^-O^+ is pointing from C to O [118], therefore the angle θ and its time evolution would describe the orientation of CO with respect to the position of the O atom. This should be taken into account when comparing the theoretical and experimental results.

It should be noted that in the calculations ro-vibrational energies were used, therefore the field-free Hamiltonian H_0 in (Eq. 5.1) and wave function $\Psi(\theta, t)$ satisfy the relation

$$H_0\Psi(\theta, t) = [B_0J(J+1) - D_eJ^2(J+1)^2]\Psi(\theta, t) \quad (5.5)$$

with J being the orbital angular momentum quantum number and $D_e = 2.79 \times 10^{-11}$ a.u. [150, 151, 152] being the centrifugal distortion constant. The calculations have shown that in the case of the CO molecule the second component of the rotation energy including a centrifugal distortion is insignificant, i.e. the bond length of CO is almost unaffected by the rotation speed. $\Psi(\theta, t)$ was expanded in the basis of spherical harmonics and the resulting coupled differential equations were solved in time using a Crank-Nicolson propagation scheme [153]. To achieve convergence of the alignment and orientation parameters angular momenta up to $J = 100$ and a time step of 0.2 a.u. were used. In order to compare with the experiment, the results were thermally averaged over an initial Boltzmann distribution assuming a temperature of 60 K. Gaussian pulses of 45 fs FWHM were used

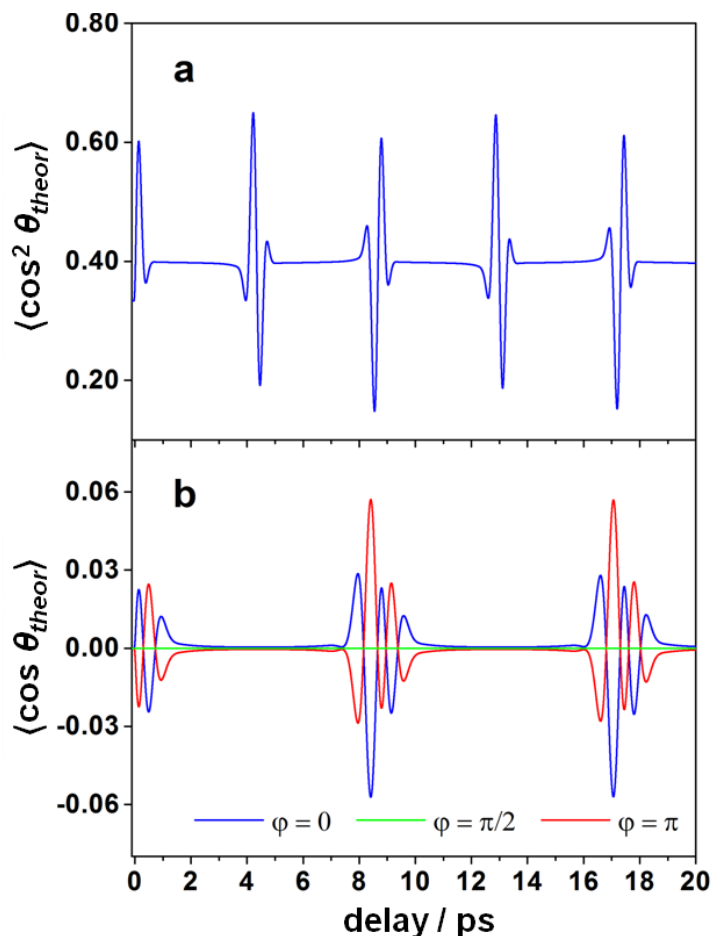


Figure 5.3: Theoretically obtained time evolution of the (a) alignment parameter $\langle \cos^2 \theta_{theor} \rangle$ and (b) orientation parameter $\langle \cos \theta_{theor} \rangle$ for the two-color excitation of CO at intensities of $7 \times 10^{13} \text{ W cm}^{-2}$ for both the fundamental and second harmonic. Note that in contrast to the experiment where C^{2+} fragments were measured, here the angle θ is defined with respect to the position of the O atom from CO. Adapted from [56].

in the calculations and a smaller peak intensity ($7 \times 10^{13} \text{ W cm}^{-2}$) than measured in the experiment was applied to account for volume effects.

Figs. 5.3a and b show the calculated time evolutions of the alignment and orientation parameters vs. the pump probe delay. The revival times for $\langle \cos^2 \theta \rangle$ agree well with the experimental data. The values of the alignment parameter are significantly lower than those measured in the experiment, which can be attributed to additional alignment by the strong probe in the experiment. The modulation of the $\langle \cos^2 \theta \rangle$ amplitude at the half and full revivals is significantly higher than in the experiment. However, we found that this amplitude strongly depends on the values of the dipole moment and the polarizability

anisotropy $\Delta\alpha$, the latter of which is not well known. Furthermore, the fact that both the polarizability and hyperpolarizability appear to be frequency-dependent [149, 154] adds additional complexity.

The theoretical prediction for the time evolution of the orientation parameter is in reasonable agreement with the experimental data. However, the appearance of the first revival of the orientation parameter $\langle \cos \theta \rangle$ might have a small time-shift. Our calculations predict a narrow peak at ~ 8.4 ps while a broader peak at ~ 8.7 ps was observed in the experiments. Similar to the experiment, the sign of the orientation is reversed by a change in the phase of the two-color laser field by π . Our calculations show that the permanent dipole of CO has very small contribution to the orientation of the molecule, as has been indicated in Ref. [141]. This can be explained by the small value of the dipole moment and also because the dipole interaction, averaged over the fast oscillations of the field, vanishes in a many-cycle pulse. Our calculations confirmed that within the model described above the hyperpolarizability is mainly responsible for the orientation of CO, in agreement with results of Ref. [141]. A phase assignment of $\varphi_2 = 0$ attributed to preferential orientation of CO molecules when the C atoms point up (red curve in Fig. 5.2b) is in agreement with a calculated trace at the same phase when the O atoms point down (blue curve in Fig. 5.3b).

The following theoretical papers, that have appeared recently, accentuate the role of hyperpolarizability in the field-free orientation mechanism. In particular Ref. [155] discusses in detail the mechanisms of orientation for the molecules with small (CO) and large (LiH) hyperpolarizability and Refs. [156, 157] analyze the control of field-free molecular orientation even at room temperature using a two-color two-pulse strategy considering a monochromatic prepulse at a specific delay prior to the two-color pulse. Furthermore, experiments on adiabatic orientation of carbonyl sulfide (OCS) molecules with nanosecond two-color laser field confirmed the importance of hyperpolarizability and polarizability interactions [158].

5.3.2 The ionization depletion mechanism

The hyperpolarizability orientation mechanism described in the previous section can be considered in simple terms as an asymmetrical force aligning the molecules along the laser polarization vector. Alternatively, a different orientation mechanism based on the preferential ionization of a sub-ensemble of the CO molecules by the two-color laser field might play an important role. In this case, the two-color laser field preferentially ionizes molecules at particular angles with respect to the polarization axis of the laser and thereby creates an

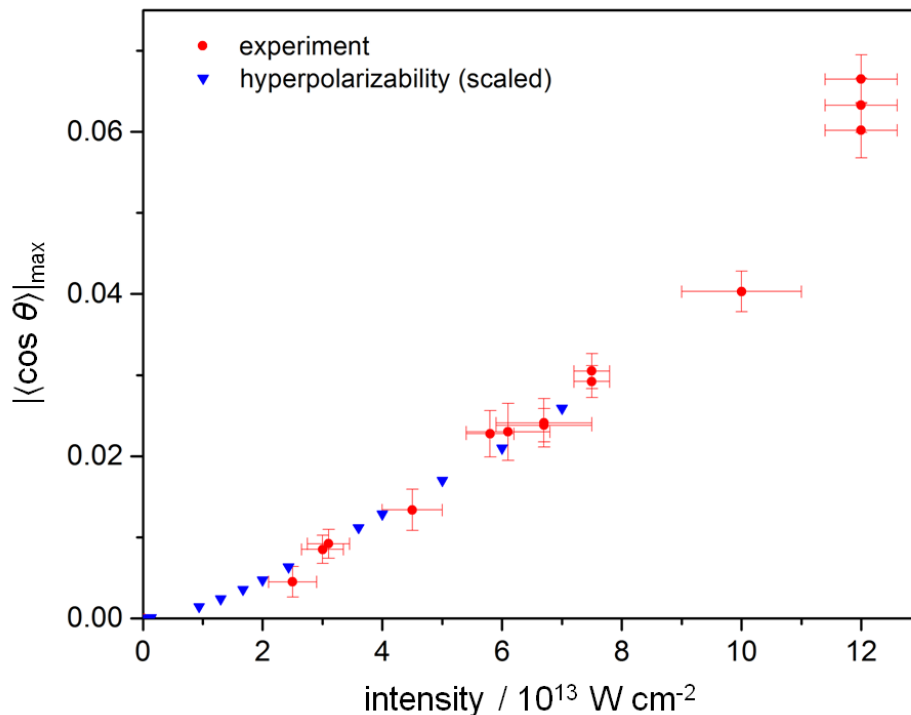


Figure 5.4: Maximum of the field-free orientation parameter observed in the experiment at the first full rotational revival for different intensities of the pump pulse (red dots) compared to the predictions from the hyperpolarizability mechanism (blue triangles). The horizontal error bars reflect uncertainties in the determination of the pump intensities and the vertical error bars the errors in the measured orientation values.

asymmetry in the original ensemble of neutral molecules and in the ensemble of molecular ions (orientation depletion mechanism). The time evolution of the simultaneously created rotational wave packet results in peaks of the orientation parameter $\langle \cos \theta \rangle$ at the revival times.

It appears logical that the orientation parameter $\langle \cos \theta \rangle$ resulting from different physical mechanisms, namely the hyperpolarizability orientation and orientation depletion mechanisms, should reveal their unique signatures in the intensity dependence. By recording the intensity dependence, the hyperpolarizability orientation and ionization depletion mechanisms may be distinguished.

The dependence of the field-free orientation amplitude on the intensity of the pump laser field was investigated both experimentally and theoretically. The maximal value of the orientation parameter for different pump intensities used in the experiments is shown in Fig. 5.4 as red dots. No ionization of CO molecules by the pump pulse is observed at the four lowest intensities (below $5 \times 10^{13} \text{ W cm}^{-2}$) and no production of C^+ ions is

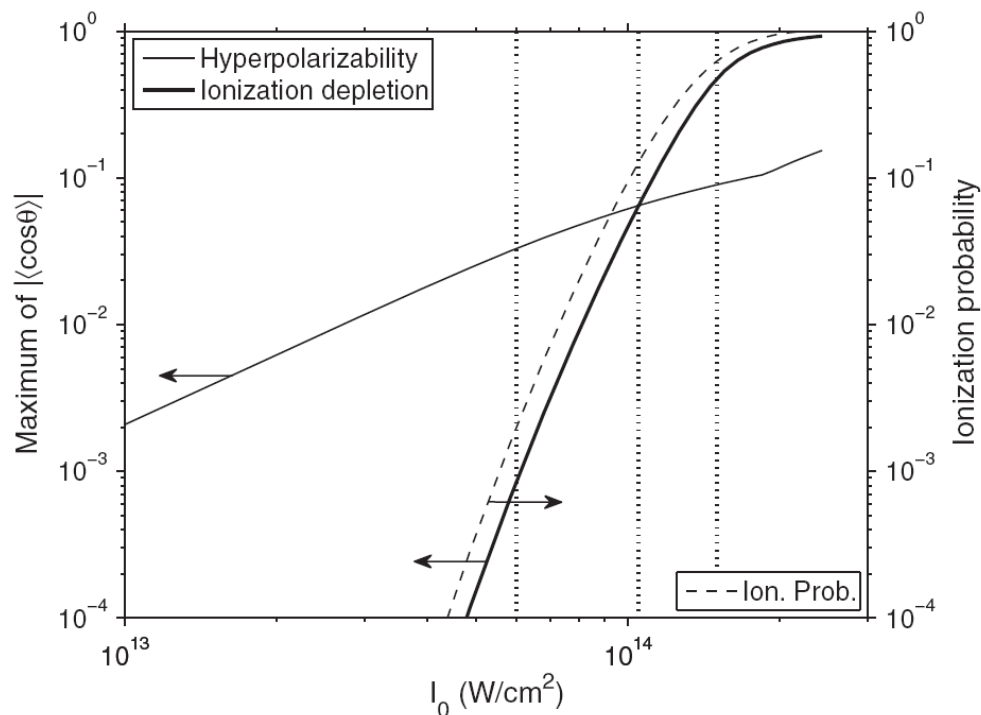


Figure 5.5: Maximum of the field-free orientation parameter vs. the intensity of the two-color pump pulse. Each of the two colors in the pump pulse has the intensity I_0 . The thin line corresponds to the hyperpolarizability mechanism, the thick line to the ionization depletion mechanism. The right axis designates the total ionization probability that is shown as dashed line. The vertical dotted lines correspond to the following intensities: 6×10^{13} , 1.05×10^{14} and 1.5×10^{14} W cm $^{-2}$. Courtesy of Ref. [159].

observed at the medium intensity, while fragmentation of CO^+ occurs at the highest intensity of the pump pulse. The field-free orientation is observed for all intensities above 2.5×10^{13} W cm $^{-2}$, below and above the ionization threshold of CO. The experimental values are compared to the predictions from the hyperpolarizability orientation mechanism (blue triangles). The theoretical $|\langle \cos \theta \rangle|_{max}$ values are scaled by a constant, intensity independent factor to give best quantitative agreement with the experimental data. The scaling also accounts for the volume averaging effect. To obtain intensities of the fundamental and second harmonic fields ATI spectra of xenon atoms were recorded at the same laser parameters and the intensities were calculated using classical $10 U_p$ cutoff law. From reference scans in xenon we found that the intensity ratio of the fundamental and second harmonic was of the order of one. Note that at the lowest intensities, where the rescattered electrons signal induced by the second harmonic field was too weak, the ratio $E_\omega = E_{2\omega}$ was estimated from first principles. At low intensities the aperture size is much

smaller than the incident beam diameter and the power of the fundamental and the second harmonic after the iris scales the same with the iris opening.

Recent theoretical studies [159] of both mechanisms have shown that the hyperpolarizability orientation mechanism dominates at low intensities, where the ionization probability is quite low, and shows a $I_0^{3/2}$ scaling (see Fig. 5.5). On the other hand, the ionization depletion mechanism prevails at high intensities—where substantial ionization occurs—and shows exponential scaling coming from the tunneling ionization rate. Fig. 5.5 shows the intensity dependence of the maximum orientation induced by these two mechanisms. The two curves cross at the intensity of 1.05×10^{14} W cm⁻² (assuming the following parameters in the model in Ref. [159]: $T_{rot}=50$ K, 30 fs pulse duration and $E_\omega=E_{2\omega}$). These results together with our experimental observations (Fig. 5.4) suggest that our experiments were done in the intermediate regime where both mechanisms contribute to the orientation process.

Ref. [159] also proposed a method to determine the active mechanism of orientation experimentally by comparing the relative timing between the peak of orientation and the expected rotation time T_{rot} for the first revival. The theoretical comparison of hyperpolarizability orientation and orientation depletion mechanisms has shown that the hyperpolarizability mechanism leads to peak orientation at early times relative to T_{rot} while the peak resulting from the ionization depletion is shifted to later times relative to T_{rot} . This effect is also seen in our experimental data at intensities below 8×10^{13} where the orientation parameter $\langle \cos \theta \rangle$ has a wide peak with a maximum at ~ 8.3 ps and a smaller amplitude. At the same time the orientation parameter at the highest pulse intensity of the pump used in our experiments (1.2×10^{14} W cm⁻²) has a peak at 8.7 ps. Therefore accordingly to theoretical predictions in [159] this data indicates the change from the hyperpolarizability orientation to the orientation depletion mechanism. The current experimental data does not, however, allow us to clearly distinguish the individual contributions of hyperpolarizability and ionization depletion mechanisms. Further studies of field-free molecular orientation are underway [160].

5.4 Conclusions and outlook

Nonadiabatic, field-free orientation of a heteronuclear molecule CO induced by a strong two-color femtosecond laser field was for the first time experimentally observed. Rotational revivals of the orientation are found after each full rotational period. At the revivals, an

oriented ensemble of heteronuclear molecules in the absence of any external electric field is produced. The approach demonstrated here is applicable to a variety of heteronuclear molecules. The demonstrated method can be applied to study molecular frame dynamics under field-free conditions in conjunction with a variety of spectroscopy methods, such as high-harmonic generation, electron diffraction, and molecular frame photoelectron emission. Although the degree of orientation found in the present work on CO is rather small, higher degree of orientation (up to 20% [161]) caused by the ionization depletion mechanism particularly at high pump pulse intensities ($> 1.05 \times 10^{14} \text{ W cm}^{-2}$ [159]) can be realized. Furthermore, decreasing the initial rotational temperature of the molecular samples would also increase the degree of molecular orientation.

Acknowledgments

Time glides insensibly away. Finally, it comes to the point to thank all my colleagues, friends, and other patient scientists with whom I have shared this encouraging and sometimes not easy journey.

I am truly and deeply indebted to a number of people for the completion of multiple projects presented in this thesis. First, I would like to thank the head of the joint LMU-MPQ Laboratory for Attosecond Physics Ferenc Krausz for giving me an exciting opportunity to get into the world of attosecond science. Foremost, I would like to express my sincere gratitude to my research supervisor Matthias F. Kling, without your professional guidance, friendly support, indomitable spirit and unfading enthusiasm this work would not have been possible. A giant thank you for bringing new exciting ideas (of which many have come true), giving me motivation and inspiring me on my scientific path. Thank you also for the exciting opportunity to be a part of the team of talented and fond of their work scientists in the Attosecond Imaging Group and the Laboratory for Attosecond Physics, and to work with research groups all over the world.

From those that I have interacted with, I would like to name a few: Sergey Zherebtsov, Boris Bergues, Xun Gu, Yunpei Deng, Gilad Marcus, Thorsten Uphues, Gernot Stania, Nick Karpowicz (Max Planck Institute of Quantum Optics, Garching); Waldemar Schneider, Sarah Stebbings, Simon Watson, Alexander Apolonskiy, Ernst Fill, Philipp von den Hoff, and Regina de Vivie-Riedle (Ludwig Maximilian University, Munich); Giuseppe Sansone and Mauro Nisoli (Politecnico di Milano, Milan); Thomas Remetter (Lund University, Lund); Sankar De, Dipanwita Ray, Nora G. Johnson, Irina A. Bocharova, Maia Magrakvelidze, Igor V. Litvinyuk, Lew Cocke, Itzik Ben-Itzhak, Fatima Anis, Brett D. Esry, Zhangjin Chen, Chii-Dong Lin (Kansas State University, Manhattan, KS); Gunter Urbasch, Karl-Michael Weitzel (Philipps-Universität Marburg, Marburg); Azra Gazibegović-Busuladžić, Mustafa Busuladžić, Dejan B. Milošević (University of Sarajevo, Sarajevo).

It was a great pleasure and a good interactive learning experience working with all of you! I am entirely honored by the opportunity to work with such a distinguished group of people.

Philipp von den Hoff and Regina de Vivie-Riedle, I am grateful for valuable discussions with you. You have an outstanding ability to find clear explanations for any experimentally measured phenomena forthcoming from general laws of physics. Thanks to you I realize the power of theory in the hands of a professional.

I would like to express my special appreciation and thanks to Sergey Zherebtsov. Your support has covered all areas of my life as a Ph.D. student, extending from the introduction to the AS-5 beamline to helping with writing this work. You are deliberate, patient, and kind; a person, in whose hands instruments find a new meaningful life. If the nanoparticles could speak they would avow their will to collaborate with you ;).

Nick Karpowicz, it was a great pleasure to share an office with you and being involved in scientific discussions that fascinated my mind. My hat is off to your programming genius! Also a big thank you for reading and correcting this thesis.

Irreplaceable moderator and excellent discussant Justin Gagnon, you are the person that brings a good mood to others. We were always looking forward to a new issue of your radio broadcast (whether it is about black holes or one of the Monty Python episodes) during a lunch break in the cafeteria at the MPQ.

I would like to express my great appreciation to the whole orientation team, especially Sankar De and Igor V. Litvinyuk. I will remember long days of preparations and sleepless nights of taking molecular orientation scans, when nobody wanted to sleep in expectation of exciting results. Since then, night scans remind me of Igor's suggestion for a night reading of the Landau and Lifshitz series as a source of answers to all known and unknown questions. I wish you many further successful experiments, do not lose this inspiring feeling. I also want to thank Tatiana Litvinyuk, Irina A. Bocharova, and Pat Strathman for a very warm welcome to Kansas, great accommodations and exceptional food, reliable help, infinite kindness, and essential companionship during my visits.

I wish to express my special sincere thanks to my former Laboratory of Photochemistry at the Institute of Chemical Kinetics and Combustion of SB RAS, Novosibirsk, especially Evgeni M. Glebov, Victor F. Plyusnin and Nikolai M. Bazhin for giving me a fundamental knowledge of Laser Physics and Photochemistry, and the research experience that brought me into the world of science. I am similarly grateful for the education and support that I received at the International Max Planck Research School of Advanced Photon Science (IMPRS-APS), I am especially thankful to the secretary Monika Wild and the coordinators Tobias Schätz, Matthias F. Kling, and Peter Hommelhoff.

Finally, I am much indebted to my mom and all my friends for being exceedingly supportive and patient throughout this difficult but explicitly productive 5-year-long journey. Dear mom, I wouldn't make it so far without your care and love that you entirely gave to me, your broad-based understanding and valuable admonitions. I'm grateful beyond words for your support.

References

- [1] Zewail, A. H. Femtochemistry: Atomic-scale dynamics of the chemical bond. *J. Phys. Chem. A* **104**(24), 5660 (2000).
- [2] Martin, M. M. & Hynes, J. T. (eds.) *Femtochemistry and Femtobiology* (Elsevier, Amsterdam, 2004).
- [3] Castleman, A. W., Jr. & Kimble, M. L. (eds.) *Femtochemistry VII* (Elsevier, Amsterdam, 2006).
- [4] Bonačić-Koutecký, V. *et al.* Analysis and control of ultrafast photon-induced processes. *Phys. Chem. Chem. Phys.* **13**, 8619 (2011).
- [5] Krausz, F. & Ivanov, M. Attosecond physics. *Rev. Mod. Phys.* **81**, 163 (2009).
- [6] Brumer, P. & Shapiro, M. Control of unimolecular reactions using coherent light. *Chem. Phys. Lett.* **126**, 541 (1986).
- [7] Shapiro, M., Hepburn, J. W. & Brumer, P. Simplified laser control of unimolecular reactions: Simultaneous (ω_1, ω_3) excitation. *Chem. Phys. Lett.* **149**, 451 (1988).
- [8] Lu, S.-P. *et al.* Coherent laser control of bound-to-bound transitions of HCl and CO. *J. Chem. Phys.* **96**, 6613 (1992).
- [9] Gordon, R. J. & Rice, S. A. Active control of the dynamics of atoms and molecules. *Annu. Rev. Phys. Chem.* **48**, 601 (1997).
- [10] Kling, M. F. *et al.* Control of electron localization in molecular dissociation. *Science* **312**, 246 (2006).
- [11] Kling, M. F. *et al.* Strong-field control of electron localization during molecular dissociation. *Mol. Phys.* **106**, 455 (2008).
- [12] Reichert, J. *et al.* Measuring the frequency of light with mode-locked lasers. *Opt. Commun.* **172**, 59 (1999).
- [13] Baltuška, A. *et al.* Attosecond control of electronic processes by intense light fields. *Nature* **421**, 611 (2003).

- [14] Milošević, D. B., Paulus, G. G. & Becker, W. High-order above-threshold ionization with few-cycle pulse: a meter of the absolute phase. *Opt. Express* **11**, 1418 (2003).
- [15] Gazibegović-Busuladžić, A. *et al.* Above-threshold ionization of diatomic molecules by few-cycle laser pulses. *Phys. Rev. A* **84**, 043426 (2011).
- [16] Abel, M. *et al.* Classical and quantum control of electrons using the carrier-envelope phase of strong laser fields. *Laser Phot. Rev.* **5**, 352 (2011).
- [17] Paulus, G. G. *et al.* Measurement of the phase of few-cycle laser pulses. *Phys. Rev. Lett.* **91**, 253004 (2003).
- [18] Johnson, N. G. *et al.* Single-shot carrier-envelope-phase-tagged ion-momentum imaging of nonsequential double ionization of argon in intense 4-fs laser fields. *Phys. Rev. A* **83**, 013412 (2011).
- [19] Süßmann, F. *et al.* Single-shot velocity-map imaging of attosecond light-field control at kilohertz rate. *Rev. Sci. Instrum.* **82**, 093109 (2011).
- [20] Brixner, T. & Gerber, G. Quantum control of gas-phase and liquid-phase femtochemistry. *Chem. Phys. Chem.* **4**, 418 (2003).
- [21] Dantus, M. & Lozovoy, V. V. Experimental coherent laser control of physicochemical processes. *Chemical Reviews* **104**, 1813 (2004).
- [22] Remacle, F., Levine, R. D. & Ratner, M. A. Charge directed reactivity: a simple electronic model, exhibiting site selectivity, for the dissociation of ions. *Chem. Phys. Lett.* **285**, 25 (1998).
- [23] Kremer, M. *et al.* Electron localization in molecular fragmentation of H₂ by carrier-envelope phase stabilized laser pulses. *Phys. Rev. Lett.* **103**, 213003 (2009).
- [24] Znakovskaya, I. *et al.* Attosecond control of electron dynamics in carbon monoxide. *Phys. Rev. Lett.* **103**, 103002 (2009).
- [25] Fischer, B. *et al.* Steering the electron in H₂⁺ by nuclear wave packet dynamics. *Phys. Rev. Lett.* **105**, 223001 (2010).
- [26] Znakovskaya, I. *et al.* Waveform control of orientation-dependent ionization of DCl in few-cycle laser fields. *Phys. Chem. Chem. Phys.* **13**, 8653 (2011).

- [27] Liu, Y. *et al.* Selective steering of molecular multiple dissociative channels with strong few-cycle laser pulses. *Phys. Rev. Lett.* **106**, 073004 (2011).
- [28] Znakovskaya, I. *et al.* Subcycle controlled charge-directed reactivity with few-cycle midinfrared pulses. *Phys. Rev. Lett.* **108**, 063002 (2012).
- [29] Posthumus, J. H. The dynamics of small molecules in intense laser fields. *Rep. Prog. Phys.* **67**, 623 (2004).
- [30] Alnaser, A. S. *et al.* Simultaneous real-time tracking of wave packets evolving on two different potential curves in H_2^+ and D_2^+ . *Phys. Rev. A* **72**, 030702 (2005).
- [31] Ergler, Th. *et al.* Spatiotemporal imaging of ultrafast molecular motion: Collapse and revival of the D_2^+ nuclear wave packet. *Phys. Rev. Lett.* **97**, 193001 (2006).
- [32] Gräfe, S. & Ivanov, M. Yu. Effective fields in laser-driven electron recollision and charge localization. *Phys. Rev. Lett.* **99**, 163603 (2007).
- [33] Bandrauk, A. D. *et al.* Attosecond localization of electrons in molecules. *Int. J. Quant. Chem* **100**, 834 (2004).
- [34] Geppert, D., von den Hoff, P. & de Vivie-Riedle, R. Electron dynamics in molecules: a new combination of nuclear quantum dynamics and electronic structure theory. *J. Phys. B: At. Mol. Opt. Phys.* **41**, 074006 (2008).
- [35] von den Hoff, P. *et al.* Attosecond control of the dissociative ionization via electron localization: A comparison between D_2 and CO . *Chem. Phys.* **366**, 139 (2009).
- [36] Keldysh, L. V. Ionization in the field of a strong electromagnetic wave. *Sov. Phys. JETP* **20**, 1307 (1965).
- [37] Hu, J. *et al.* Attosecond resolution quantum dynamics between electrons and H_2^+ molecules. *Phys. Rev. A* **74**, 063417 (2006).
- [38] Bucksbaum, P. H. *et al.* Softening of the H_2^+ molecular bond in intense laser fields. *Phys. Rev. Lett.* **64**, 1883 (1990).
- [39] Zavriyev, A. *et al.* Ionization and dissociation of H_2 in intense laser fields at 1.064 μm , 532 nm, and 355 nm. *Phys. Rev. A* **42**, 5500 (1990).

- [40] Niikura, H., Corkum, P. B. & Villeneuve, D. M. Controlling vibrational wave packet motion with intense modulated laser fields. *Phys. Rev. Lett.* **90**, 203601 (2003).
- [41] Roudnev, V., Esry, B. D. & Ben-Itzhak, I. Controlling HD^+ and H_2^+ dissociation with the carrier-envelope phase difference of an intense ultrashort laser pulse. *Phys. Rev. Lett.* **93**, 163601 (2004).
- [42] Schultze, M. *et al.* Powerful 170-attosecond XUV pulses generated with few-cycle laser pulses and broadband multilayer optics. *New J. Phys.* **9**, 243 (2007).
- [43] Ahmad, I. *et al.* Frontend light source for short-pulse pumped OPCPA system. *Appl. Phys. B* **97**, 529 (2009).
- [44] Ahmad, I. *et al.* Redshift of few-cycle infrared pulses in the filamentation regime. *New J. Phys.* **13**, 093005 (2011).
- [45] Zimmermann, M. *et al.* Optical clockwork with an offset-free difference-frequency comb: accuracy of sum- and difference-frequency generation. *Opt. Lett.* **29**, 310 (2004).
- [46] Jones, D. J. *et al.* Carrier-envelope phase control of femtosecond mode-locked lasers and direct optical frequency synthesis. *Science* **288**, 635 (2000).
- [47] Apolonski, A. *et al.* Controlling the phase evolution of few-cycle light pulses. *Phys. Rev. Lett.* **85**, 740 (2000).
- [48] Verhoef, A. J. *et al.* Few-cycle carrier envelope phase-dependent stereo detection of electrons. *Opt. Lett.* **31**, 3520 (2006).
- [49] Eppink, A. T. J. B. & Parker, D. H. Velocity map imaging of ions and electrons using electrostatic lenses: Application in photoelectron and photofragment ion imaging of molecular oxygen. *Rev. Sci. Instrum.* **68**, 3477 (1997).
- [50] Ghafur, O. *et al.* A velocity map imaging detector with an integrated gas injection system. *Rev. Sci. Instrum.* **80**, 033110 (2009).
- [51] Micheau, S. *et al.* Accurate retrieval of target structures and laser parameters of few-cycle pulses from photoelectron momentum spectra. *Phys. Rev. Lett.* **102**, 073001 (2009).

- [52] Kling, M. F. *et al.* Imaging of carrier-envelope phase effects in above-threshold ionization with intense few-cycle laser fields. *New J. Phys.* **10**, 025024 (2008).
- [53] Vrakking, M. J. J. An iterative procedure for the inversion of two-dimensional ion/photoelectron imaging experiments. *Rev. Sci. Instrum.* **72**, 4084 (2001).
- [54] Gu, X. *et al.* Generation of carrier-envelope-phase-stable 2-cycle 740- μ J pulses at 2.1- μ m carrier wavelength. *Opt. Exp.* **17**, 62 (2009).
- [55] Bergues, B. *et al.* Sub-cycle electron control in the photoionization of xenon using a few-cycle laser pulse in the mid-infrared. *New J. Phys.* **13**, 063010 (2011).
- [56] De, S. *et al.* Field-free orientation of CO molecules by femtosecond two-color laser fields. *Phys. Rev. Lett.* **103**, 153002 (2009).
- [57] Ray, D. *Photo-electron momentum distribution and electron localization studies from laser-induced atomic and molecular dissociations*. Ph.D. thesis, Kansas State University, Manhattan, Kansas, USA (2010).
- [58] von den Hoff, P. *et al.* Effects of multi orbital contributions in the angular-dependent ionization of molecules in intense few-cycle laser pulses. *Appl. Phys. B* **98**, 659 (2010).
- [59] Turner, D. W. & May, D. P. Franck-condon factors in ionization: Experimental measurement using molecular photoelectron spectroscopy. *J. Chem. Phys.* **45**, 471 (1966).
- [60] Nicholls, R. W. Franck-condon factors for ionizing transitions of O₂, CO, NO and H₂ and for the NO⁺ (*A*¹ Π - *X*¹ Σ) band system. *J. Phys. B: At. Mol. Phys.* **1**, 1192 (1968).
- [61] Peek, J. M. Eigenparameters for the $1s\sigma_g^+$ and $2p\sigma_u^+$ orbitals of H₂⁺. *J. Chem. Phys.* **43**, 3004 (1965).
- [62] Kelkensberg, F. *et al.* A semi-classical model of attosecond electron localization in dissociative ionization of hydrogen. *Phys. Chem. Chem. Phys.* **13**, 8647 (2011).
- [63] Kelkensberg, F. *Capturing atomic and electronic motion with high harmonic generation light pulses*. Ph.D. thesis, Radboud University Nijmegen, Nijmegen, the Netherlands (2011).

- [64] Kremer, M. *et al.* *Ein Wegweiser aus Licht für Elektronen* (Jahrbuch der Max-Planck-Gesellschaft, Forschungsbericht des MPI für Kernphysik, 2010). <http://www.mpg.de/346223/forschungsSchwerpunkt/>.
- [65] Siu, W. *Probing molecular dynamics using novel light sources*. Ph.D. thesis, Radboud University Nijmegen, Nijmegen, the Netherlands (2011).
- [66] Sansone, G. *et al.* Electron localization following attosecond molecular photoionization. *Nature* **465**, 763 (2010).
- [67] Tong, X. M., Zhao, Z. X. & Lin, C. D. Theory of molecular tunneling ionization. *Phys. Rev. A* **66**, 033402 (2002).
- [68] Tong, X. M. & Lin, C. D. Dynamics of light-field control of molecular dissociation at the few-cycle limit. *Phys. Rev. Lett.* **98**, 123002 (2007).
- [69] Niikura, H. *et al.* Sub-laser-cycle electron pulses for probing molecular dynamics. *Nature* **417**, 917 (2002).
- [70] Alnaser, A. S. *et al.* Routes to control of H₂ coulomb explosion in few-cycle laser pulses. *Phys. Rev. Lett.* **93**, 183202 (2004).
- [71] Weinkauff, R. *et al.* Elementary processes in peptides: Electron mobility and dissociation in peptide cations in the gas phase. *J. Phys. Chem.* **99**, 11255 (1995).
- [72] Sändig, K., Figger, H. & Hänsch, T. W. Dissociation dynamics of H₂⁺ in intense laser fields: Investigation of photofragments from single vibrational levels. *Phys. Rev. Lett.* **85**, 4876 (2000).
- [73] Ray, D. *et al.* Ion-energy dependence of asymmetric dissociation of D₂ by a two-color laser field. *Phys. Rev. Lett.* **103**, 223201 (2009).
- [74] Niikura, H. *et al.* Probing molecular dynamics with attosecond resolution using correlated wave packet pairs. *Nature* **421**, 826 (2003).
- [75] Moshhammer, R. *et al.* A 4 π recoil-ion electron momentum analyzer: a high-resolution "microscope" for the investigation of the dynamics of atomic, molecular and nuclear reactions. *Nucl. Instr. and Meth. in Phys. Res. B* **108**, 425 (1996).
- [76] Dörner, R. *et al.* Cold target recoil ion momentum spectroscopy: a 'momentum microscope' to view atomic collision dynamics. *Phys. Rep.* **330**, 95 (2000).

- [77] Ullrich, J. *et al.* Recoil-ion and electron momentum spectroscopy: reaction-microscopes. *Rep. Prog. Phys.* **66**, 1463 (2003).
- [78] Zherebtsov, S. *et al.* Controlled near-field enhanced electron acceleration from dielectric nanospheres with intense few-cycle laser fields. *Nature Phys.* **7**, 656 (2011).
- [79] Rathje, T. *et al.* Review of attosecond resolved measurement and control via carrier-envelope phase tagging with above-threshold ionization. *J. Phys. B: At. Mol. Opt. Phys.* **45**, 074003 (2012).
- [80] Betsch, K. J. *et al.* Controlled directional ion emission from several fragmentation channels of CO driven by a few-cycle laser field. *Phys. Rev. A* **86**, 063403 (2012).
- [81] Morishita, T. *et al.* Accurate retrieval of structural information from laser-induced photoelectron and high-order harmonic spectra by few-cycle laser pulses. *Phys. Rev. Lett.* **100**, 013903 (2008).
- [82] Le, A.-T., Morishita, T. & Lin, C. D. Extraction of the species-dependent dipole amplitude and phase from high-order harmonic spectra in rare-gas atoms. *Phys. Rev. A* **78**, 023814 (2008).
- [83] Chen, Z. *et al.* Origin of species dependence of high-energy plateau photoelectron spectra. *J. Phys. B: At. Mol. Opt. Phys.* **42**, 061001 (2009).
- [84] Abel, M. J. *et al.* Carrier-envelope phase-dependent quantum interferences in multiphoton ionization. *J. Phys. B: At. Mol. Opt. Phys.* **42**, 075601 (2009).
- [85] Roudnev, V. & Esry, B. D. General theory of carrier-envelope phase effects. *Phys. Rev. Lett.* **99**, 220406 (2007).
- [86] Wirth, A. *et al.* Synthesized light transients. *Science* **334**, 195 (2011).
- [87] Zuo, T. & Bandrauk, A. D. Charge-resonance-enhanced ionization of diatomic molecular ions by intense lasers. *Phys. Rev. A* **52**, R2511 (1995).
- [88] Bandrauk, A. D. Intense field ionization of molecules by ultrashort laser pulses. *Comments Atom. Molec. Phys.* **1(3)D**, 97 (1999).
- [89] Sansone, G. *et al.* Isolated single-cycle attosecond pulses. *Science* **314**, 443 (2006).

- [90] Sanz-Vicario, J. L., Bachau, H. & Martín, F. Time-dependent theoretical description of molecular autoionization produced by femtosecond xuv laser pulses. *Phys. Rev. A* **73**, 033410 (2006).
- [91] Uiberacker, M. *et al.* Attosecond real-time observation of electron tunnelling in atoms. *Nature* **446**, 627 (2007).
- [92] Werner, H.-J. *et al.* Molpro, version 2006.1, a package of ab initio programs (2006). <http://www.molpro.net>.
- [93] Whitten, J. L. Gaussian expansion of hydrogen-atom wavefunctions. *J. Chem. Phys.* **39**, 349 (1963).
- [94] Huzinaga, S. Gaussian-type functions for polyatomic systems. I. *J. Chem. Phys.* **42**, 1293 (1965).
- [95] Nubbemeyer, T. *et al.* Strong-field tunneling without ionization. *Phys. Rev. Lett.* **101**, 233001 (2008).
- [96] von den Hoff, P. *et al.* Electron dynamics and its control in molecules: From diatomics to larger molecular systems. *IEEE J. Select. Top. Quantum. Electron.* **18**, 119 (2012).
- [97] von den Hoff, P. T. *Gekoppelte Kern- und Elektronendynamik: Molekulare Systeme und deren Kontrolle durch die Bewegung der Elektronen*. Ph.D. thesis, Ludwig-Maximilians-Universität München, München, Deutschland (2012).
- [98] Alnaser, A. S. *et al.* Effects of orbital symmetries in dissociative ionisation of molecules by few-cycle laser pulses. *Phys. Rev. A* **71**, 031403 (2005).
- [99] Guo, C. Holding molecular dications together in strong laser fields. *Phys. Rev. A* **73**, 041401 (2006).
- [100] Perelomov, A. M., Popov, V. S. & Terent'ev, M. V. Ionization of atoms in an alternating electric field. *Sov. Phys. JETP* **23**, 924 (1966).
- [101] Smirnov, B. M. & Chibisov, M. I. The breaking up of atomic particles by an electric field and by electron collisions. *Sov. Phys. JETP* **22**, 585 (1966).
- [102] Ammosov, M. V., Delone, N. B. & Krainov, V. P. Tunnel ionization of complex atoms and atomic ions by an alternating electromagnetic field. *Sov. Phys. JETP* **64**, 1191 (1986).

- [103] Augst, S. *et al.* Tunneling ionization of noble gases in a high-intensity laser field. *Phys. Rev. Lett.* **63**, 2212 (1989).
- [104] Augst, S. *et al.* Nonsequential triple ionization of argon atoms in a high-intensity laser field. *Phys. Rev. A* **52**, R917 (1995).
- [105] Buerke, B. & Meyerhofer, D. D. Measurement of hydrogenic tunneling rates in a high-intensity laser focus. *Phys. Rev. A* **69**, 051402 (2004).
- [106] Faisal, F. H. M., Becker, A. & Muth-Böhm, J. Intense-field many-body S-matrix theory: applications to processes in femtosecond laser pulses. *Laser Phys.* **9**, 115 (1999).
- [107] Muth-Böhm, J., Becker, A. & Faisal, F. H. M. Suppressed molecular ionization for a class of diatomics in intense femtosecond laser fields. *Phys. Rev. Lett.* **85**, 2280 (2000).
- [108] Zhao, S.-F. *et al.* Effect of an improved molecular potential on strong-field tunneling ionization of molecules. *Phys. Rev. A* **82**, 035402 (2010).
- [109] Akagi, H. *et al.* Laser tunnel ionization from multiple orbitals in HCl. *Science* **325**, 1364 (2009).
- [110] McFarland, B. K. *et al.* High harmonic generation from multiple orbitals in N₂. *Science* **322**, 1232 (2008).
- [111] Smirnova, O. *et al.* High harmonic interferometry of multi-electron dynamics in molecules. *Nature* **460**, 972 (2009).
- [112] Tong, X. M. *et al.* Post ionization alignment of the fragmentation of molecules in an ultrashort intense laser field. *J. Phys. B: At. Mol. Opt. Phys.* **38**, 333 (2005).
- [113] Litvinyuk, I. V. *et al.* Alignment-dependent strong field ionization of molecules. *Phys. Rev. Lett.* **90**, 233003 (2003).
- [114] Pavičić, D. *et al.* Direct measurement of the angular dependence of ionization for N₂, O₂, and CO₂ in intense laser fields. *Phys. Rev. Lett.* **98**, 243001 (2007).
- [115] Li, H. *et al.* Orientation dependence of the ionization of CO and NO in an intense femtosecond two-color laser field. *Phys. Rev. A* **84**, 043429 (2011).

- [116] Werner, H.-J. & Rosmus, P. Theoretical dipole moment functions of the HF, HCl, and HBr molecules. *J. Chem. Phys.* **73**, 2319 (1980).
- [117] Muentzer, J. S. Electric dipole moment of carbon monoxide. *J. Mol. Spectrosc.* **55**, 490 (1975).
- [118] Peterson, K. A. & Dunning, T. H., Jr. The CO molecule: The role of basis set and correlation treatment in the calculation of molecular properties. *J. Mol. Struct. (Theochem)* **400**, 93 (1997).
- [119] Breunig, H. G., Lauer, A. & Weitzel, K.-M. Control of branching ratios in the dissociative ionization of deuterium chloride. *J. Phys. Chem. A* **110**, 6395 (2006).
- [120] Korolkov, M. V. & Weitzel, K.-M. On the competition between predissociation and direct dissociation in deuterium chloride ions DCl^+ . *J. Chem. Theory Comp.* **2**, 1492 (2006).
- [121] Korolkov, M. V. & Weitzel, K.-M. Laser pulse control of photofragmentation in DCl^+ : the effect of carrier envelope phase. *Chem. Phys.* **338**, 277 (2007).
- [122] Korolkov, M. V. & Weitzel, K.-M. Carrier envelope phase effects in photofragmentation: Orientation versus alignment. *Opt. Spectrosc.* **111**, 606 (2011).
- [123] Ivanov, M. Yu. & Marangos, J. P. Time-resolved imaging of atomic-scale electron and nuclear dynamics. *J. Mod. Opt.* **54**, 899 (2007).
- [124] Itatani, J. *et al.* Tomographic imaging of molecular orbitals. *Nature* **432**, 867 (2004).
- [125] Vozzi, C. *et al.* Generalized molecular orbital tomography. *Nature Phys.* **7**, 822 (2011).
- [126] Meckel, M. *et al.* Laser-induced electron tunneling and diffraction. *Science* **320**, 1478 (2008).
- [127] Lee, S. K., Lin, Y. F., Yan, L. & Li, W. Laser-induced low energy electron diffraction in aligned molecules. *J. Phys. Chem. A* **116**, 1950 (2012).
- [128] Reckenthaeler, P. *et al.* Time-resolved electron diffraction from selectively aligned molecules. *Phys. Rev. Lett.* **102**, 213001 (2009).

-
- [129] Hensley, C. J., Yang, J. & Centurion, M. Imaging of isolated molecules with ultrafast electron pulses. *Phys. Rev. Lett.* **109**, 133202 (2012).
- [130] Rouzée, A. *et al.* Photoelectron kinetic and angular distributions for the ionization of aligned molecules using a HHG source. *J. Phys. B: At. Mol. Opt. Phys.* **45**, 074016 (2012).
- [131] Viftrup, S. S. *et al.* Holding and spinning molecules in space. *Phys. Rev. Lett.* **99**, 143602 (2007).
- [132] Friedrich, B. & Herschbach, D. R. Spatial orientation of molecules in strong electric fields and evidence for pendular states. *Nature* **353**, 412 (1991).
- [133] Friedrich, B. & Herschbach, D. Enhanced orientation of polar molecules by combined electrostatic and nonresonant induced dipole forces. *J. Chem. Phys.* **111**, 6157 (1999).
- [134] Minemoto, S. *et al.* Observation of molecular orientation by the combination of electrostatic and nonresonant, pulsed laser fields. *J. Chem. Phys.* **118**, 4052 (2003).
- [135] Holmegaard, L. *et al.* Laser-induced alignment and orientation of quantum-state-selected large molecules. *Phys. Rev. Lett.* **102** (2009).
- [136] Goban, A., Minemoto, S. & Sakai, H. Laser-field-free molecular orientation. *Phys. Rev. Lett.* **101** (2008).
- [137] Ghafur, O. *et al.* Impulsive orientation and alignment of quantum-state-selected NO molecules. *Nature Phys.* **5**, 289 (2009).
- [138] Sokolov, A. V. *et al.* Orienting molecules via an ir and uv pulse pair: Implications for coherent raman spectroscopy. *Phys. Rev. A* **79**, 053805 (2009).
- [139] Fleischer, S. *et al.* Molecular orientation and alignment by intense single-cycle THz pulses. *Phys. Rev. Lett.* **107**, 163603 (2011).
- [140] Kanai, T. & Sakai, H. Numerical simulations of molecular orientation using strong, nonresonant, two-color laser fields. *J. Chem. Phys.* **115**, 5492 (2001).
- [141] Tehini, R. & Sugny, D. Field-free molecular orientation by nonresonant and quasiresonant two-color laser pulses. *Phys. Rev. A* **77**, 023407 (2008).

- [142] Muramatsu, M. *et al.* Field-free molecular orientation by an intense nonresonant two-color laser field with a slow turn on and rapid turn off. *Phys. Rev. A* **79**, 011403 (2009).
- [143] Vrakking, M. J. J. & Stolte, S. Coherent control of molecular orientation. *Chem. Phys. Lett.* **271**, 209 (1997).
- [144] Bocharova, I. A. *et al.* Time-resolved coulomb-explosion imaging of nuclear wavepacket dynamics induced in diatomic molecules by intense few-cycle laser pulses. *Phys. Rev. A* **83**, 013417 (2011).
- [145] Werner, H.-J. MCSCF calculation of the dipole moment function of CO. *Mol. Phys.* **44**, 111 (1981).
- [146] Pinkham, D. & Jones, R. R. Intense laser ionization of transiently aligned CO. *Phys. Rev. A* **72**, 023418 (2005).
- [147] Ray, D. *et al.* Momentum spectra of electrons rescattered from rare-gas targets following their extraction by one- and two-color femtosecond laser pulses. *Phys. Rev. A* **83**, 013410 (2011).
- [148] Ohmura, H., Saito, N. & Morishita, T. Quantum control of molecular tunneling ionization in the spatiotemporal domain. *Phys. Rev. A* **83**, 063407 (2011).
- [149] Pecul, M. Density functional and coupled cluster calculations of dynamic hyperpolarizabilities and their geometry derivatives. *Chem. Phys. Lett.* **404**, 217 (2005).
- [150] Albritton, D. L. *et al.* Calculation of centrifugal distortion constants for diatomic molecules from RKR potentials. *J. Mol. Spectrosc.* **46**, 25 (1973).
- [151] Hutson, J. M. Centrifugal distortion constants for diatomic molecules: An improved computational method. *J. Phys. B: At. Mol. Phys.* **14**, 851 (1981).
- [152] Falzon, C. T., Chong, D. P. & Wang, F. Prediction of spectroscopic constants for diatomic molecules in the ground and excited states using time-dependent density functional theory. *J. Comput. Chem.* **27**, 163 (2006).
- [153] Press, W. H. *et al.* *Numerical Recipes* (Cambridge University Press, Cambridge, 1992), 2nd edn.

-
- [154] Christiansen, O., Gauss, J. & Stanton, J. Frequency-dependent polarizabilities and first hyperpolarizabilities of CO and H₂O from coupled cluster calculations. *Chem. Phys. Lett.* **305**, 147 (1999).
- [155] Yun, H. *et al.* Parity-selective enhancement of field-free molecular orientation in an intense two-color laser field. *Phys. Rev. A* **84**, 065401 (2011).
- [156] Zhang, S. *et al.* Controlling field-free molecular orientation with combined single- and dual-color laser pulses. *Phys. Rev. A* **83**, 043410 (2011).
- [157] Tehini, R. *et al.* Field-free molecular orientation of ¹Σ and ²Π molecules at high temperature. *Phys. Rev. A* **85**, 043423 (2012).
- [158] Oda, K. *et al.* All-optical molecular orientation. *Phys. Rev. Lett.* **104**, 213901 (2010).
- [159] Spanner, M. *et al.* Mechanisms of two-color laser-induced field-free molecular orientation. *Phys. Rev. Lett.* **109**, 113001 (2012).
- [160] Znakovskaya, I. *et al.* Transition between mechanisms of laser-induced field-free molecular orientation (2013). ArXiv:1307.0303.
- [161] Frumker, E. *et al.* Oriented rotational wave-packet dynamics studies via high harmonic generation. *Phys. Rev. Lett.* **109**, 113901 (2012).

List of Publications

Publications in the framework of the Ph.D. thesis

”Light-waveform control of molecular processes”

I. Kling, M. F., Siedschlag, Ch., Znakovskaya, I., Verhoef, A. J., Zherebtsov, S., Krausz, F., Lezius, M. & Vrakking, M. J. J. Strong-field control of electron localization during molecular dissociation. *Mol. Phys.* **106**, 455 (2008).

◇ This project turned into a productive start into the attosecond control of molecular dynamics that essentially defined the key subject of my dissertation. At a later stage, this theme was extended further to the waveform control of molecular imaging and molecular orientation. I analyzed the experimental data successfully, learning the method for the mathematical reconstruction of 3D momentum distributions based on an Abel transformation (e.g. the iterative inversion algorithm developed by Marc Vrakking). I participated in the discussions of the dissociation mechanism including comparison of the prototype molecule D₂ and its isotope HD. Thereby, I could gain knowledge about the terminology and main physical mechanisms of complex dissociative ionization processes; I also prepared some figures for the manuscript and partially contributed to the writing of the paper.

II. Znakovskaya, I., von den Hoff, P., Zherebtsov, S., Wirth, A., Herrwerth, O., Vrakking, M. J. J., de Vivie-Riedle, R. & Kling, M. F. Attosecond control of electron dynamics in carbon monoxide. *Phys. Rev. Lett.* **103**, 103002 (2009).

◇ I was the key player in the experimental team. My involvement included running the experiments, analyzing the data, comparing the experimental and calculated results. Successful experiments were preceded by learning the operation of a complex few-cycle, 4 fs CEP-stabilized amplified Ti:sapphire laser system, which made the experiments a difficult task. I prepared the figures containing the experimental results and contributed to the long process of writing a *Phys. Rev. Lett.* paper. We had a stiff job trying to describe the electron dynamics in multielectron systems (here a carbon monoxide molecule). The steering of electrons in more complex systems, extending the approach from simple prototype molecules, was the state of the art at this stage of development of coherent control. To be

able to identify the absolute CEP in the experiments I have used reference measurements in xenon and a simulation code based on the QRS theory provided to us by Zhangjin Chen and Chii-Dong Lin from Kansas State University.

III. von den Hoff, P., Znakovskaya, I., Kling, M. F. & de Vivie-Riedle, R. Attosecond control of the dissociative ionization via electron localization: a comparison between D₂ and CO. *Chem. Phys.* **366**, 139 (2009).

◇ Following up our publication in *Phys. Rev. Lett.*, we wrote a longer paper that includes some additional experimental results and is primarily aimed at a detailed comparison of the attosecond control of the dissociative ionization of D₂ and CO molecules from a theoretical point of view. My contribution to this paper is similar to the previous paper [II]. From our experimental side I supported the theoreticians (Philipp von den Hoff and Regina de Vivie-Riedle) by the experimental part of the work.

IV. De, S., Znakovskaya, I., Ray, D., Anis, F., Johnson, N. G., Bocharova, I. A., Magrakvelidze, M., Esry, B. D., Cocks, C. L., Litvinyuk, I. V. & Kling, M. F. Field-free orientation of CO molecules by femtosecond two-color laser fields. *Phys. Rev. Lett.* **103**, 153002 (2009).

I was one of the key players in the experimental team. My involvement included running the experiments, analyzing the data, and doing model calculations. To compare the experimental results to the model, I ran the quantum mechanical rigid rotor calculations for different intensities and pulse durations using the code developed by Fatima Anis and Brett Esry from Kansas State University. In addition, I took a part in the discussions for the design of a novel high-energy VMI spectrometer, which was built by Sankar De in Kansas.

V. von den Hoff, P., Znakovskaya, I., Zherebtsov, S., Kling, M. F. & de Vivie-Riedle, R. Effects of multi orbital contributions in the angular-dependent ionization of molecules in intense few-cycle laser pulses. *Appl. Phys. B.* **98**, 659 (2010).

◇ The very distinct angular distributions of measured C⁺ fragments from the dissociative ionization of CO together with the already developed theoretical approach for papers [II,III] gave birth to an exciting idea of measuring molecular orbitals through the angle-

dependent ionization rate of molecules in intense few-cycle laser fields. Large molecules exhibit smaller energetic spacing such that the effect of multi-orbital contributions could play a role. We supported this theoretical project with experimental data, in particular by measuring the angular distributions for four molecules: D₂, N₂, O₂, and CO. I was the leading person responsible for the data acquisition and data analysis. In addition, I was involved in the discussions on the observed experimental angular distributions and I sketched the experimental setup and wrote the experimental part of the paper. On top of that, it was one of the first laser experiments performed at the freshly built AS-5 laser setup. I provided help to Sergey Zherebtsov to install the prism compressor for amplified laser pulses coming from the front end of the PFS laser system, mounting chirped mirrors sets and a hollow core fiber, and compressed the pulses to sub-5 fs. I also designed and built a Mach-Zehnder interferometer supporting this pulse duration in both arms, which was used later in pump-probe experiments with nanoparticles and clusters.

VI. Znakovskaya, I., von den Hoff, P., Schirmel, N., Urbasch, G., Zherebtsov, S., Bergues, B., de Vivie-Riedle, R., Weitzel, K.-M. & Kling, M. F. Waveform control of orientation-dependent ionization of DCl in few-cycle laser fields. *Phys. Chem. Chem. Phys.* **13**, 8653 (2011).

◇ The results reported here are from another experiment that was done at the AS-5 laser system. I was the key player in the experimental team. My contribution was on the same level as in [II]. The results came from our successful collaboration with the theory group of Regina de Vivie-Riedle and chemical experts from Karl-Michael Weitzel's group. We could deepen our understanding of the mechanism of multi-orbital contributions and even observed the orientation-dependent molecular ionization. Among other things, I spent some time developing the tools for the angular-dependent analysis of asymmetry scans, which were used to obtain the key result of the publication.

VII. Znakovskaya, I., von den Hoff, P., Marcus, G., Zherebtsov, S., Bergues, B., Gu, X., Deng, Y., Vrakking, M. J. J., Kienberger, R., Krausz, F., de Vivie-Riedle, R. & Kling, M. F. Subcycle controlled charge-directed reactivity with few-cycle midinfrared pulses. *Phys. Rev. Lett.* **108**, 063002 (2012).

◇ I was the leading person performing the measurements, analyzing the data, and writing the paper. We had an exclusive chance to apply mid-infrared laser pulses to control molec-

ular dissociation, observing a high degree of charge-directed reactivity.

Other publications:

VIII. Ray, D., He, F., De, S., Cao, W., Mashiko, H., Ranitovic, P., Singh, K. P., Znakovskaya, I., Thumm, U., Paulus, G. G., Kling, M. F., Litvinyuk, I. V. & Cocke, C. L. Ion-energy dependence of asymmetric dissociation of D_2 by a two-color laser field. *Phys. Rev. Lett.* **103**, 223201 (2009).

IX. Sansone, G., Kelkensberg, F., Pérez-Torres, J. F., Morales, F., Kling, M. F., Siu, W., Ghafur, O., Johnsson, P., Swoboda, M., Benedetti, E., Ferrari, F., Lépine, F., Sanz-Vicario, J. L., Zherebtsov, S., Znakovskaya, I., L'Huillier, A., Ivanov, M. Yu., Nisoli, M., Martín, F. & Vrakking, M. J. J. Electron localization following attosecond molecular photoionization. *Nature* **465**, 763 (2010).

X. Mauritsson, J., Remetter, T., Swoboda, M., Klünder, K., L'Huillier, A., Schafer, K. J., Ghafur, O., Kelkensberg, F., Siu, W., Johnsson, P., Vrakking, M. J. J., Znakovskaya, I., Uphues, T., Zherebtsov, S., Kling, M. F., Lépine, F., Benedetti, E., Ferrari, F., Sansone, G. & Nisoli, M. Attosecond electron spectroscopy using a novel interferometric pump-probe technique. *Phys. Rev. Lett.* **105**, 053001 (2010).

XI. Zherebtsov, S., Fennel, T., Plenge, J., Antonsson, E., Znakovskaya, I., Wirth, A., Herrwerth, O., Süßmann, F., Peltz, C., Ahmad, I., Trushin, S. A., Pervak, V., Karsch, S., Vrakking, M. J. J., Langer, B., Graf, C., Stockman, M. I., Krausz, F., Rühl, E. & Kling, M. F. Controlled near-field enhanced electron acceleration from dielectric nanospheres with intense few-cycle laser fields. *Nature Phys.* **7**, 656 (2011).

XII. Zherebtsov, S., Wirth, A., Uphues, T., Znakovskaya, I., Herrwerth, O., Gagnon, J., Korbman, M., Yakovlev, V. S., Vrakking, M. J. J., Drescher, M. & Kling, M. F. Attosecond imaging of XUV-induced atomic photoemission and Auger decay in strong laser fields. *J. Phys. B: At. Mol. Opt. Phys.* **44**, 105601 (2011).

XIII. Bergues, B., Zherebtsov, S., Deng, Y., Gu, X., Znakovskaya, I., Kienberger, R., Krausz, F., Marcus, G., Kling, M. F. Sub-cycle electron control in the photoionization of xenon using a few-cycle laser pulse in the mid-infrared. *New J. Phys.* **13**, 063010 (2011).

XIV. De, S., Magrakvelidze, M., Bocharova, I. A., Ray, D., Cao, W., Znakovskaya, I., Li, H., Wang, Z., Laurent, G., Thumm, U., Kling, M. F., Litvinyuk, I. V., Ben-Itzhak, I. & Cocke, C. L. Following dynamic nuclear wave packets in N₂, O₂, and CO with few-cycle infrared pulses. *Phys. Rev. A* **84**, 043410 (2011).

XV. Gazibegović-Busuladžić, A., Hasović, E., Busuladžić, M., Milošević, D. B., Kelkensberg, F., Siu, W. K., Vrakking, M. J. J., Lépine, F., Sansone, G., Nisoli, M., Znakovskaya, I. & Kling, M. F. Above-threshold ionization of diatomic molecules by few-cycle laser pulses. *Phys. Rev. A* **84**, 043426 (2011).

XVI. Li, H., Ray, D., De, S., Znakovskaya, I., Cao, W., Laurent, G., Wang, Z., Kling, M. F., Le, A. T. & Cocke, C. L. Orientation dependence of the ionization of CO and NO in an intense femtosecond two-color laser field. *Phys. Rev. A* **84**, 043429 (2011).

XVII. Zhrebtsov, S., Süßmann, F., Peltz, C., Plenge, J., Betsch, K. J., Znakovskaya, I., Alnaser, A. S., Johnson, N. G., Kübel, M., Horn, A., Mondes, V., Graf, C., Trushin, S. A., Azzeer, A., Vrakking, M. J. J., Paulus, G. G., Krausz, F., Rühl, E., Fennel, T. & Kling, M. F. Carrier-envelope phase-tagged imaging of the controlled electron acceleration from SiO₂ nanospheres in intense few-cycle laser fields. *New J. Phys.* **14**, 075010 (2012).

Selected Papers (I - VII)

Paper I

Strong-field control of electron localization during molecular dissociation.

Kling, M. F., Siedschlag, Ch., Znakovskaya, I., Verhoef, A. J., Zherebtsov, S., Krausz, F., Lezius, M. & Vrakking, M. J. J.
Mol. Phys. **106**, 455 (2008).

RESEARCH ARTICLE

Strong-field control of electron localisation during molecular dissociation

M.F. Kling^{ab*}, Ch. Siedschlag^a, I. Znakovskaya^b, A.J. Verhoef^b, S. Zherebtsov^b,
F. Krausz^{bc}, M. Lezius^b and M.J.J. Vrakking^a^a*FOM Instituut voor Atoom en Molecuul Fysica (AMOLF), 1098 SJ Amsterdam, The Netherlands;*^b*Max-Planck-Institut für Quantenoptik, D-85748 Garching, Germany;*^c*Department für Physik, Ludwig-Maximilians-Universität München,
D-85748 Garching, Germany**(Received 24 October 2007; final version received 10 December 2007)*

We demonstrate how the waveform of light can be used to control a molecular dissociation by the steering and localisation of electrons. Experimental results have been obtained for the dissociative ionisation of the homonuclear and heteronuclear hydrogen derivatives D₂ and HD. Asymmetric ejection of the ionic fragments reveals that light-driven electronic motion prior to dissociation localises the electron on one of the two ions in diatomic molecular ions in a controlled way. Extension of these results to electron transfer in complex molecules suggests a new paradigm for controlling photochemistry.

Keywords: strong-field control; few-cycle laser pulses; charge localisation

1. Introduction

Coherent control of molecular dynamics has entered a new and exciting regime with the advent of intense few-cycle phase-stabilised laser pulses [1]. Laser technology now allows for the generation and control of electromagnetic fields, where the electric field can be switched between 0 and several a.u. with a temporal accuracy of a few 100 as [2]. Obviously, only electrons can respond on this timescale, and atomic centers will remain frozen. If the laser intensity is chosen carefully, the extreme nonlinearity of the strong field tunneling probability due to the Gamov factor $\exp(-2(2U_1)^{3/2}/3|E(t)|)$, with U_1 the ionisation potential and $E(t)$ the electric field, leads to situations where electrons are liberated from a molecule within a fraction (100–300 as) of the cycle of the carrier wave. A full cycle of this carrier wave typically lasts about 2660 as at 800 nm when using Ti:sapphire lasers. Subsequently, these electrons are driven by the laser field [3], which leads to daughter processes that can, in principle, be precisely synchronised with respect to the original ionisation event. Typical cases are recombination and high-order harmonic generation [4], scattering and high-energy above-threshold ionisation (ATI) [5,6], as well as attosecond electron diffraction [7]. All of these processes take place about one-third of the laser cycle after strong field ionisation (SFI) has happened

close to the peak electric field [3], when the electron revisits its parent near a zero-crossing of the electric field. The electron rescattering process can also lead to population transfer into excited states above the ionic ground state, which is usually prepared during the strong field tunneling process. This is especially attractive to molecular physics, because the preparation of higher excited molecular states can thus be very precisely timed. Furthermore, because electron rescattering is approximately equal to classical electron impact excitation of ions, no strong selection rules apply, in contrast to the optical case. Only if during rescattering recombination takes place, will the molecule preferentially end up in its initial state, and excess energy will be given away as harmonic radiation. This has been used with advantage for the prominent tomographic imaging of molecular orbitals by Itatani *et al.* [8]

Molecular electron rescattering physics can, and has been, investigated intensively by various groups in recent years with multi-cycle laser pulses. However, for the case where the laser pulse duration approaches the optical period, one enters the few-cycle regime and the electromagnetic driver fields become increasingly asymmetric. Such fields have recently opened up new avenues for coherent control. Spatial control of electron emission has been observed and has become a major tool for

*Corresponding author. Email: matthias.kling@mpq.mpg.de

long-term stabilisation of the laser phase [9]. It has also been possible to control total fragment particle momenta [10]. The prerequisite for such experiments, control of the carrier-envelope phase (CEP) itself, has become available as a laser control parameter since the ground-breaking work of Hänsch and coworkers [11], and its extension to amplified laser systems by Baltuska *et al.* [2]. The latter has paved the way into the strong field community. Stabilisation and control of the laser phase with comparably high precision has made many experiments possible that are directly related to attosecond physics [12–18]. The relation between the CEP and attosecond physics itself can be easily understood, since control over the CEP is virtually equal to control of a light field with attosecond precision. CEP control applied to the few-cycle regime, however, enables access to mono-cycle strong field ionisation. In such cases, subsequent steering of isolated attosecond electron wavepackets is feasible and gives access to controlled time-dependent and intense polarisation of the target system. In combination with molecular alignment or orientation selection via SFI the technique can be used to control the final localisation of charge during molecular dissociation, as has been previously demonstrated for the D–D homonuclear dimer [15]. In this paper, we extend the discussion of such experiments to the heteronuclear dimer H–D, and to additional aspects in the CEP control of charge redistribution, which may be attributed to phase control of bond-softening processes.

Hydrogen ionisation and dissociation has been attractive to the femtosecond community for several years (see, e.g., reference 19 and references therein). Some reasons for this are, firstly, H₂ intra-nuclear vibrational wavepacket dynamics is very fast and requires a temporal resolution in the few-fs regime [20]. Second, because only two electrons and two protons are involved, the system can be numerically accessed with high accuracy [21]. As such, it has model character for the treatment of more complex molecules and with regard to chemistry perhaps more interesting cases. Third, the lower ionic levels in hydrogen are energetically well separated [22,23]. Because of this, IR multiphoton ionisation ends up mostly in one single electronic state ($1s\sigma_g^+$). Subsequent electron rescattering events then populate a superposition of higher states, e.g. create a synchronised electronic wavepacket. The corresponding coupled electron–nuclear dynamics evolving within the rapidly decaying strong laser field can be made responsible for final charge localisation [15,24–26].

2. Experimental

The experimental scheme used here has been described earlier [15]. In brief, transform-limited laser pulses of 25 fs duration with 1 mJ pulse energy were generated with a 3 kHz phase-stabilised amplified Ti:sapphire laser system (Femtolasers, Femtopower Compact Pro). The pulse was spectrally broadened using a 1 m long hollow-core fiber of 250 μm diameter filled with 3.8 bar neon gas. The laser pointing into the fiber was controlled with high precision with a home-built stabiliser system consisting of a CCD camera and a motorised mirror mount. The output pulses from the fiber exhibited a significantly broadened spectrum [27] and were compressed down to a near-transform limited duration of ~ 5 fs using eight reflections in a chirped mirror compressor. By tuning of the gas pressure in the hollow-core fiber the pulse length was adjusted precisely between 25 and 5 fs. The pulse duration was monitored online with a commercial dispersion balanced autocorrelator. The laser phase was stabilised with a feedback loop [28,29]. The polarisation is rectified using three 5 μm thick pellicles at the Brewster angle. Fine tuning of the pulse duration and varying the CEP was done by changing the amount of material dispersion with a pair of fused-silica wedges after the hollow fibre. The phase jitter was smaller than 150 mrad. Phase-stabilised, linearly polarised pulses at a central wavelength of 760 nm were focused with a spherical mirror ($R=80$ cm) into the center of the ion optics of a velocity-map imaging spectrometer (Figure 1(a)) [20]. In the focus intensities of up to $5 \times 10^{14} \text{ W cm}^{-2}$ were realised, and an adjustable iris was used to vary the intensity in the focus. Ions and electrons were generated at the crossing point between the laser and the molecular beam (with a particle density of approximately 10^{13} cm^{-3}) and were accelerated and focused with the ion optics onto a MCP phosphor screen assembly (Hamamatsu, F2226-24PX). The molecular beam was produced by a pulsed nozzle of 1 mm diameter and operated at 50 Hz. The molecular beam was differentially pumped and passed a skimmer of 1 mm diameter 10 cm downstream before entering the interaction region. The sensitivity of the MCP detector was switched so that only ions or electrons from every 60th laser pulse were detected. This allowed for a low background pressure in the chamber (typically 2×10^{-7} mbar). The velocity map images were recorded with a CCD camera (Pulnix, TM-9701) and were typically averaged over 60 s of data acquisition for each setting of the laser phase.

Figure 1(B) shows a typical experimental momentum map of D⁺ ions recorded with 5 fs excitation at $10^{14} \text{ W cm}^{-2}$ without CEP stabilisation. The laser

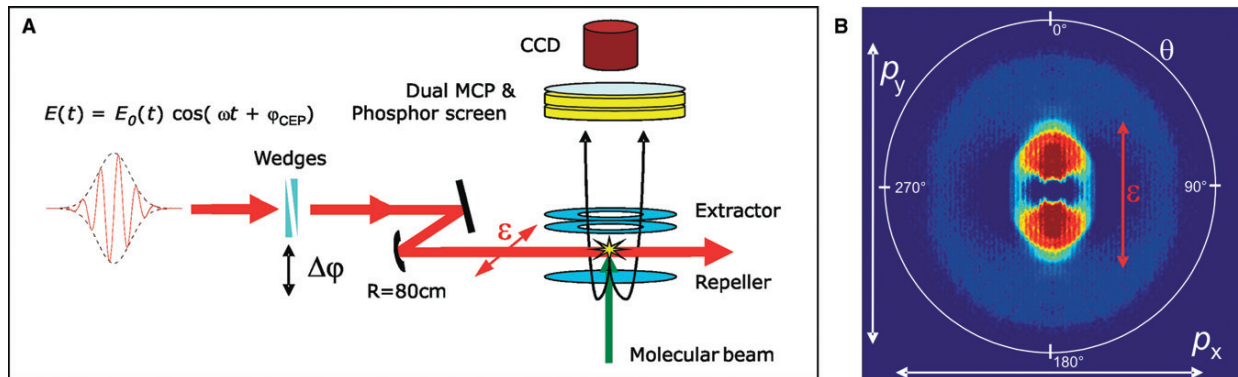


Figure 1. (a) Schematic view of the velocity map imaging experiment. Laser pulses are CEP controlled using a pair of wedges. The beam is focused with a spherical mirror ($f=40$ cm) into the center of the ion optics, where it crosses a molecular beam. The resulting ions are extracted and analysed using a dual microchannel and phosphor screen detector. (b) A typical velocity map image from the detection of D^+ ions in the dissociation of D_2 with 5 fs pulses at 10^{14} $W\text{ cm}^{-2}$ without phase stabilisation.

was polarised along the p_y axis. Two main contributions are visible in both upwards and downwards emission direction: a strong peak at lower energies with a relatively narrow angular distribution and a contribution at larger momenta with a wide angular distribution. After inversion of the image using an iterative inversion procedure [31], the original 3D momentum distribution can be reconstructed. By integration of the inverted image over the full solid angle the energy spectrum displayed in Figure 2(A) is derived. The spectral features can be attributed to the following reaction pathways (as sketched in Figure 2(C)).

- (A) Following strong-field tunnel ionisation of D_2 with the production of an electron and a D_2^+ ion in the $1s\sigma_g^+$ state, recollisional excitation (RCE) [32,33] to the $2p\sigma_u^+$ state by the returning electron leads to dissociation and formation of D^+ and D fragments with energies above 3 eV. This channel shows a broad angular distribution as seen in Figure 2(B), in agreement with earlier observations [34]. Note that no ions at these energies are observed with circular polarised light (Figure 2(A)), strongly supporting recollision to be responsible for their production.
- (B) Close to the outer turning point of the nuclear wavepacket, bond softening (BS) [19,35,36] becomes a prominent process, leading to very low fragment energies below 3 eV with its main contribution between 0 and 2 eV.
- (C) At the intensities used in these studies, Coulomb explosion of D_2 with the production of two D^+ ions is possible via enhanced

ionisation (EI). This channel is, however, unwanted for the present investigations and therefore we tried to keep such signals at a minimum. In fact, only a minor contribution of EI is seen between 2 and 3 eV, which exhibits a smaller angular distribution than the BS pathway (see Figure 2(B)).

3. Results I: electron localisation in D_2

In order to elucidate the role of the CEP in the experimental ion momentum distributions, the laser phase was scanned carefully over a range of multiple cycles. The angle-integrated asymmetry in the ion momentum distribution at a certain energy $W=p^2/(2m)$ and phase φ was obtained from

$$A(W,\varphi) = \frac{P_{\text{up}}(W,\varphi) - P_{\text{down}}(W,\varphi)}{P_{\text{up}}(W,\varphi) + P_{\text{down}}(W,\varphi)}, \quad (1)$$

with

$$P_{\text{up}}(W,\varphi) = \int_{330}^{360} \int_0^{360} P(W,\theta,\phi,\varphi) d\phi \sin\theta d\theta + \int_0^{30} \int_0^{180} P(W,\theta,\phi,\varphi) d\phi \sin\theta d\theta, \quad (2)$$

and

$$P_{\text{down}}(W,\varphi) = \int_{150}^{210} \int_0^{360} P(W,\theta,\phi,\varphi) d\phi \sin\theta d\theta, \quad (3)$$

with θ and φ being the polar and azimuthal angles, respectively. We chose to analyse ion emission within a

458

M.F. Kling et al.

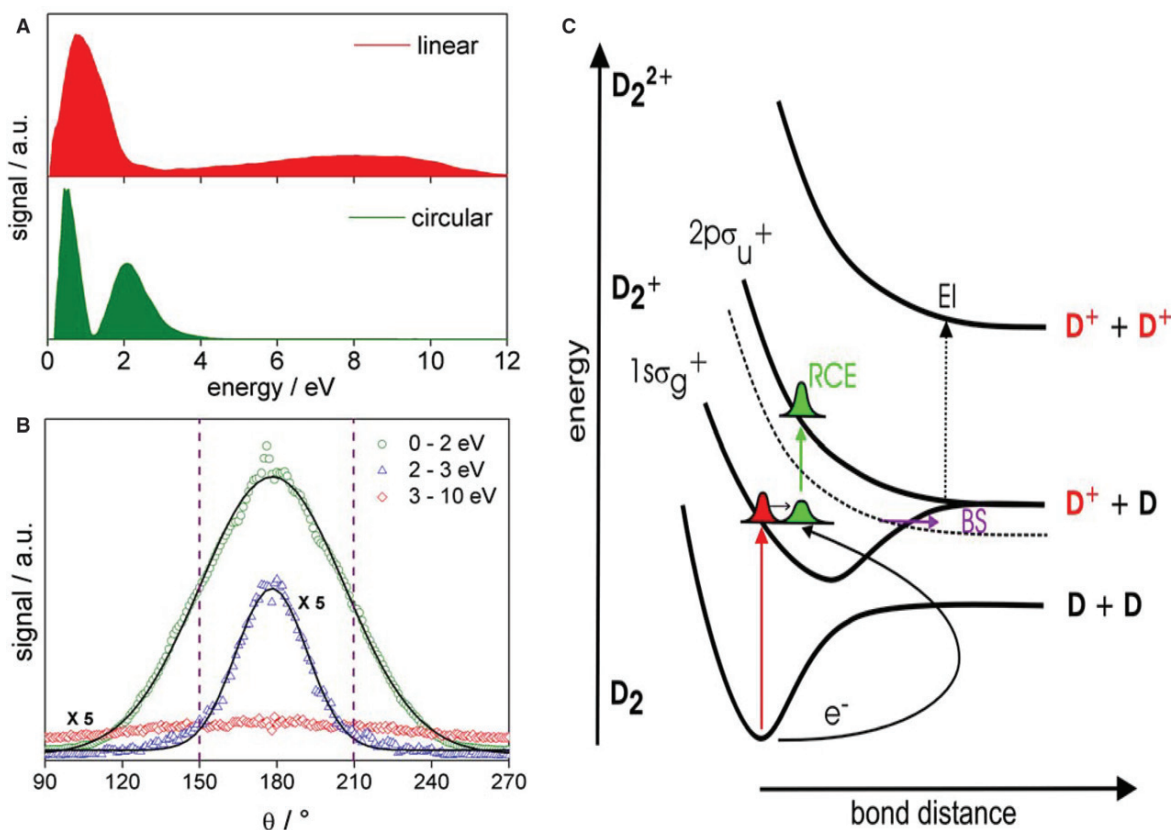


Figure 2. (A) D^+ kinetic energy spectrum from the interaction of D_2 with 5 fs linear and circular polarised laser pulses at $10^{14} \text{ W cm}^{-2}$ without phase stabilization. (B) Angular distributions for D^+ from D_2 within three energy windows corresponding to the BS (0–2 eV), EI (2–3 eV) and RCE (3–8 eV) channels as measured for the conditions in (A) for linear polarization. (C) Schematic diagram showing the different dissociation pathways that yield D^+ ions from D_2 via dissociation of the molecular ion via recollisional excitation (RCE) or Coulomb explosion of D_2^{2+} in enhanced ionisation (EI); in strong laser fields, bond softening (BS) may lead to dissociation of the molecular ion, where the avoided crossing between the diabatic potentials that are dressed by the laser field (as an example, the $2p\sigma_u^+$ potential dressed with (-1) photon is drawn as a dashed line) results in an energy gap that gives rise to dissociation from vibrational levels that were originally bound [35]. BS has been studied in great detail for different light intensities and pulse durations [47]. Note that further channels playing a role at higher intensities than in the present studies are omitted from the scheme.

restricted angular range because our ability to control electron motion in hydrogen requires that the laser couples the two lowest-lying electronic states. For molecules aligned orthogonally to the laser polarisation axis, this coupling would be absent.

The contour plot in Figure 3(A) shows the measured angle-integrated asymmetry $A(W, \varphi_{\text{CEP}})$ for dissociative ionisation of D_2 into $D^+ + D$ as a function of the carrier-envelope phase φ_{CEP} (x axis) and the kinetic energy W of the D^+ ion fragment (y axis, see also Figure 2). Note that here the laser phase is only given as a relative number as the absolute phase has not been determined. Figure 3(A) shows that, in the energy range between 3 and 8 eV, locking of the laser phase in the few-cycle limit causes a remarkable asymmetry in the upward and downward emission. Regions in Figure 3(A) where the asymmetry oscillates

as a function of the phase represent the final energies of the D^+ ions where the direction of their emission is effectively controlled by the sub-cycle evolution of the laser field driving the photodissociation. The extent of this ability to control is further illustrated in Figure 3(B), which displays asymmetries that are integrated over selected energy intervals. The highest degree of asymmetry, with a modulation depth of up to 45%, is observed between 3 and 8 eV. Above 8 eV, the asymmetry appears to cease completely. A very small phase dependence is seen between 1 and 2 eV (see also Figure 3(B)), which represents the typical energy range for bond softening. Most interestingly, this low-energy channel for charge localisation appears to be out of phase by ca. $\pi/2$ with respect to the high-energy channel. In principle, when using 5 fs laser pulses, bond softening would not be expected, since this process

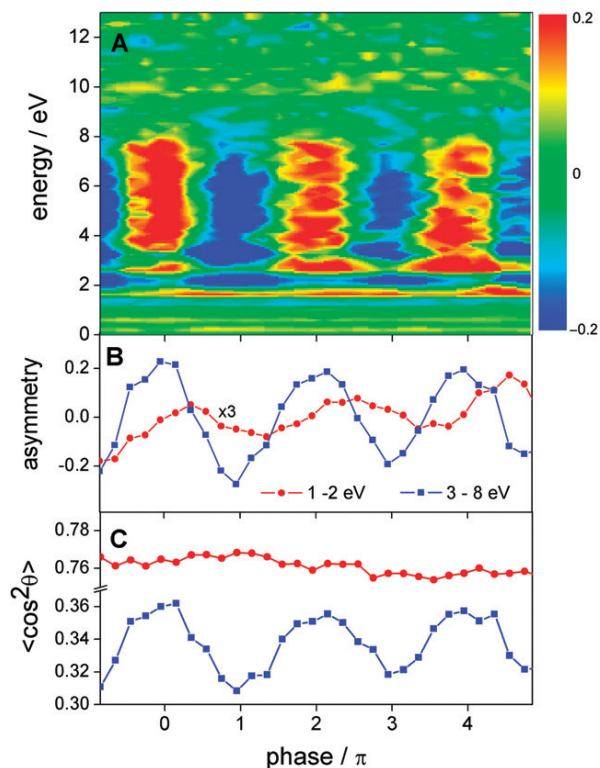


Figure 3. (A) Map of asymmetry parameter $A(W, \theta)$ as a function of the D^+ kinetic energy W and the carrier envelope phase φ_{CEP} (measured over a range of 6π with a step size of 0.1π). (B) Asymmetry integrated over several energy ranges versus the CEP. (C) Degree of alignment of D^+ ions (represented by the expectation value of $\cos^2(\theta)$) versus the CEP for the same energy intervals as in (B).

requires motion of the vibrational wave packet that is formed by tunnel ionisation to the outer turning point of the $1s\sigma_g^+$ potential well. This is expected to take about half a vibrational period, i.e. 12 fs in the case of D_2 [37]. However, in our experiments the pulse contrast was not ideal. The background present in the few-cycle pulses amounted to ca. 10% in intensity at times when the internuclear distance moves into the BS region and might contribute to the asymmetry [26].

Plots of the expectation value of the alignment parameter $\cos^2(\theta)$ versus the phase φ_{CEP} are given in Figure 3(C) and show the degree of alignment of D^+ ions within the energy ranges used in Figure 3(B). A strong phase dependence is again seen for the energy range between 3 and 8 eV. This phase dependence is not present in the low-energy contribution. A comparison of Figures 3(B) and (C) indicates that the observation of a large asymmetry between 3 and 8 eV correlates with a greater degree of alignment.

The relation between the charge localisation process and the angular distribution of the fragment ions is further explored in Figure 4(A), where the amplitude $A_0(W, \theta)$ of the asymmetry oscillation $A(W, \theta, \varphi_{\text{CEP}}) = A_0(W, \theta) \sin((\varphi_{\text{CEP}} + \varphi_0 W, \theta))$ is shown as a function of kinetic energy W and fragment angle θ . Clearly, for fragment angles $\theta > 50^\circ$ the asymmetry vanishes. Moreover, a butterfly shape of the asymmetry amplitude is apparent and indicates different mechanisms for the generation of the asymmetry at low and high energies. This will be discussed in more detail below. Additionally, Figure 4(B) shows the asymmetry dependence on the pulse duration, which declines quasi-exponentially from ca. 45% close to 5 fs towards 1% above 9 fs. This behaviour reveals that the asymmetry of the field is driving the charge localisation process and that few-cycle pulses are an important prerequisite for the electron localisation control that has been achieved.

4. Theoretical interpretation of the charge localisation effect in D_2

The electron localisation control in the fragmentation of D_2 arises due to a phase control mechanism that consists of two parts. The first part has already been partially discussed in relation to the results shown in Figure 2(A). The absence of fragments in the kinetic energy range between 3 and 8 eV (where the observed asymmetry is most pronounced) in experiments using circularly polarised light strongly suggests the involvement of a re-collision of the electron that is ejected in the tunnel ionisation that produces the D_2^+ ion. Our interpretation is that re-collision of this electron with the D_2^+ ion leads to excitation of the D_2^+ ion from the $1s\sigma_g^+$ state to the dissociative $2p\sigma_u^+$ state. Further, indirect support for this is provided by the observation of D^+ fragments with a kinetic energy of up to 12 eV, consistent with acceleration along a repulsive curve starting from an internuclear distance close or equal to the internuclear distance in the neutral ground state. However, this re-collision excitation by itself is not enough to cause an asymmetry. If the observation of a high kinetic energy D^+ fragment could be used as an indication of the fact that a fragment had been detected that was dissociating along the $2p\sigma_u^+$ potential curve, then the molecule would retain its parity up to the point of detection, and – parity being a symmetry property of the electronic wave function – the distribution of the electron over the two D^+ ions involved in the dissociation would necessarily have to be symmetric. A second ingredient is required, which breaks the parity of the electronic wave function.

460

M.F. Kling et al.

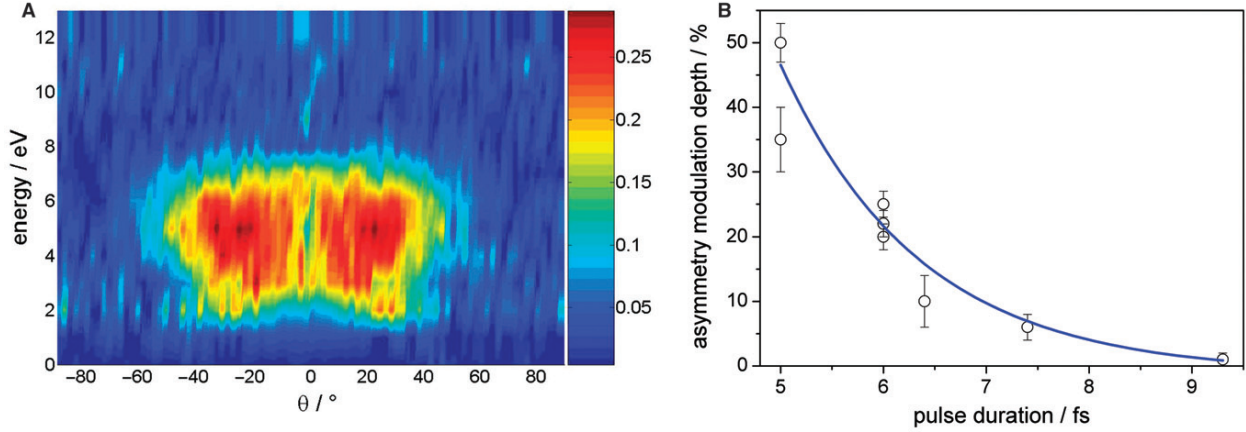


Figure 4. (A) Maximum degree of asymmetry $A_0(W, \theta)$ in the emission of D^+ ions from the dissociative ionization of D_2 as a function of the emission angle and energy. The phase-dependent asymmetry oscillations have been fit to sine functions $A(W, \theta, \varphi_{\text{CEP}}) = A_0(W, \theta) \sin(\varphi_{\text{CEP}} + \varphi_0(W, \theta))$ to obtain the parameter $A_0(W, \theta)$. The effect is limited to $\theta = \pm 50^\circ$. The butterfly shape of the effect indicates two different mechanisms, based on RCE for high energies and BS for small ion energies (see text). (B) Experimental dependence of the asymmetry modulation depth in the emission of D^+ ions between 3 and 8 eV from dissociation of D_2 on the laser pulse duration.

As has been proposed [15], and subsequently confirmed in more detailed theoretical treatments [21,25], laser-induced coupling between the $2p\sigma_u^+$ and the $1s\sigma_g^+$ states can convert the dissociative wave packet that starts out on the $2p\sigma_u^+$ state into a coherent superposition state containing contributions from both the $2p\sigma_u^+$ state and the $1s\sigma_g^+$ state and – importantly – with a broken parity.

According to the presented semiclassical model [15] the time evolution of the wave function for the hydrogen molecule after recollision can be calculated by expanding the full wave function for the electronic coordinate and the internuclear distance in terms of the lowest-lying electronic states,

$$\Psi(\mathbf{r}, R; t) \approx |g\rangle\psi_g(R; t) + |u\rangle\psi_u(R; t), \quad (4)$$

where $|g\rangle$ and $|u\rangle$ correspond to the $1s\sigma_g^+$ and $2p\sigma_u^+$ states, respectively, and where $\psi_{g/u}$ represent the corresponding nuclear wave packets. In accordance with our observation that the asymmetry is primarily detected for fragments that are ejected along the laser polarisation axis, the molecule is assumed to be aligned along the axis of the laser field. Further support for this assumption comes from the fact that aligned molecules are preferentially ionised via SFI. By inserting this Ansatz into the time-dependent Schrödinger equation, one obtains the coupled equations:

$$i\frac{\partial}{\partial t} \begin{pmatrix} \psi_g(R; t) \\ \psi_u(R; t) \end{pmatrix} = \begin{pmatrix} -\frac{1}{M} \frac{\partial^2}{\partial R^2} + V_g(R) & V_{gu}(R) \\ V_{gu}^*(R) & -\frac{1}{M} \frac{\partial^2}{\partial R^2} + V_u(R) \end{pmatrix} \begin{pmatrix} \psi_g(R; t) \\ \psi_u(R; t) \end{pmatrix}, \quad (5)$$

with the binding potential curve $V_g(R)$, the dissociative curve $V_u(R)$ and the coupling between them $V_{gu}(R)$. Tabulated values for the potential curves were used [22]. Integration of Equation (5) yields the time-dependent nuclear wave functions. The initial condition directly after the recollision consists of placing the vibrational ground state, obtained by relaxation on the respective potential curve [23], onto the dissociative potential curve of the molecular ion ($2p\sigma_u^+$). The recollision time for the first recollision is 1.7 fs after ionisation [32]. Due to the fact that the experiment employed few-cycle pulses, later recollision events are considered to be efficiently suppressed [21,34]. We note that the ionisation is considered as a single event that occurs at the maximum of the laser electric field. This is a simplification, since the application of ADK theory [38] would predict that the ionisation may occur during more than a single half-cycle of the laser, and, furthermore, during a finite time interval within each half-cycle. A very rigorous theoretical treatment of the dynamics that goes well beyond the approach here and includes the ionisation and recollision steps was recently presented by Gräfe and Ivanov [25]. However, a computational treatment of hydrogen dissociation starting with an ADK treatment of the ionisation is beyond the scope of the present paper, where our main aim is to qualitatively explain the physics responsible for the observed phase control.

In the approach used here, for the calculation of the asymmetry, the electronic basis is changed to two states that are localised on the left and on the right

nucleus, respectively. Without loss of generality, we define

$$|l\rangle = \frac{1}{\sqrt{2}}(|g\rangle + |u\rangle), \quad (6)$$

and

$$|r\rangle = \frac{1}{\sqrt{2}}(|g\rangle - |u\rangle). \quad (7)$$

By projecting onto these states, the corresponding nuclear wave functions are obtained:

$$\psi_l(R; t) = \frac{1}{\sqrt{2}}(\psi_g(R; t) + \psi_u(R; t)), \quad (8)$$

$$\psi_r(R; t) = \frac{1}{\sqrt{2}}(\psi_g(R; t) - \psi_u(R; t)). \quad (9)$$

From these expressions the (t - as well as R -dependent) probabilities for the electron remaining on the left or on the right atom are calculated:

$$P_l(R, t) = \frac{1}{2}|\psi_g(R; t) + \psi_u(R; t)|^2, \quad (10)$$

$$P_r(R, t) = \frac{1}{2}|\psi_g(R; t) - \psi_u(R; t)|^2. \quad (11)$$

The time-dependent electron localisation parameter is then defined as

$$\frac{\int (P_l(R, t) - P_r(R, t)) dR}{\int (P_l(R, t) + P_r(R, t)) dR}. \quad (12)$$

From these expressions we can immediately see that it is the coherent superposition of the two electronic states $1s\sigma_g^+$ and $2p\sigma_u^+$ that is responsible for the asymmetry in the charge localisation.

Figure 5 displays the temporal evolution of the laser field and the time-dependent electron localisation parameter quantifying the localisation on the upper/lower nucleus. The initial asymmetry that develops in the electron density is synchronised to the laser frequency, the intuitive picture being that the laser drives the electron back-and-forth (on attosecond timescales) between the two nuclei. However, as the molecule dissociates, the oscillatory motion of the electron between the two nuclei is impeded by the emergence of a potential barrier between the two nuclei. For an internuclear distance that is close to the internuclear distance where enhanced ionisation would occur, the electron oscillation stops and the electron density is found to localise predominantly on one of the atoms. In agreement with the experimental observation, shifting the CEP by π turns the laser field and thus the asymmetry around.

The observation of asymmetric D^+ emission as a result of electron localisation requires that, in our

velocity-resolved D^+ measurements, we are unable to identify the quantum path (i.e. the $1s\sigma_g^+$ or the $2p\sigma_u^+$ curve) along which the measured ions were created. This restricts the kinetic energy range where an asymmetric emission may be expected. In good agreement with experiment, the asymmetry is calculated to peak at around 6 eV. Importantly, no electron localisation is observed at the very highest kinetic energies that occur in the experiment, since the wave packet that dissociates on the $1s\sigma_g^+$ curve is necessarily slower than the wave packet that dissociates on the repulsive $2p\sigma_u^+$ curve. In the intermediate energy range between 2 and 8 eV the charge localisation phase dependence exhibits, if at all, only weak substructures. This behaviour may originate from the electron rescattering process, which allows for access to a broad energetic range in molecular excitation during the sub-cycle rescattering event. The interpretation of the low KER regime is, however, more complicated. Simulations [21] show a larger phase offset of $\sim\pi$ between BS and RCE. As suggested by Roudnev and Esry [39], asymmetries could be the result of pure interference between the $1s\sigma_g^+$ and $2p\sigma_u^+$ molecular channels populated directly via sequential optical excitation. If the nuclei are dissociating in two different molecular channels, they can still contribute at the same kinetic energy. In the few-cycle case, laser bandwidth and Stark-shifting of the initial state may be strong enough to create this overlap of nuclear wavepackets, so that the relative phase between the final components still depends on the CEP.

Another, quite interesting aspect comes into play from the θ dependence of the asymmetry as illustrated in Figures 3(C) and 4(A). Within our simplified model, interference at low dissociation energies means that the low-energy tail of the dissociative excited state wavepacket is interfering with a wavepacket that must have been stimulated from $2p\sigma_u^+$ to $1s\sigma_g^+$ by the laser field relatively early after the rescattering excitation process. We suggest that early de-excitation should be more dependent on the molecular alignment, which would explain why, in Figure 4, the low-energy region populates a smaller angular range. On the other hand, interference at high energy means that the downward transition takes place relatively late. When the gap between the two potential curves becomes less than a photon, it should suddenly become very difficult to induce a transition and only the very well aligned molecules may still succeed. Again, the angular selection becomes stricter, as observed in our experiment.

To conclude, within our modeling, we understand final charge localisation during molecular dissociation in the following way. The molecular ions are formed in a (single) ionisation event that occurs at the

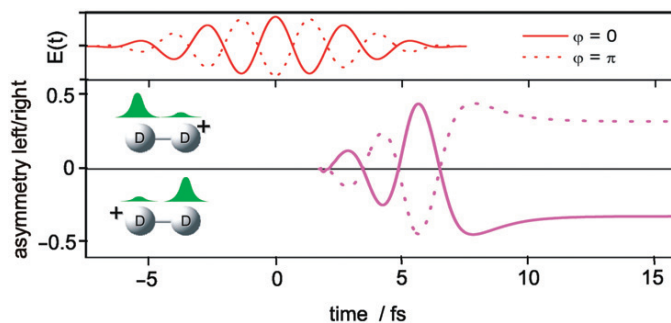


Figure 5. Results of the simulations: about two-thirds of an optical cycle after an electron has been liberated from the neutral molecule (accompanied by the production of a wave packet evolving along the ground ionic state $1s\sigma_g^+$), this electron recollides with the parent and excites the part of the population that is relevant for the explanation of the experimental results for the $2p\sigma_u^+$ state. Superposition of both the $1s\sigma_g^+$ and $2p\sigma_u^+$ states is formed in the laser field by population transfer. This breaks the parity of the electronic wavefunction, and allows control of the final localisation of the charge on the ‘left’ and the ‘right’ part of the molecule.

maximum of the laser electric field. The ionisation event starts a vibrational wave packet in the $1s\sigma_g^+$ ground electronic state of D_2^+ that mimics the vibrational ground-state wave function of D_2 before excitation. Rescattering then leads to population transfer from the $1s\sigma_g^+$ ground electronic state to the $2p\sigma_u^+$ excited electronic state at a delay of ~ 1.7 fs after ionisation [32]. Because of the strongly repulsive nature of the $2p\sigma_u^+$ state, the excited D_2^+ molecule rapidly dissociates and the resulting fragments acquire significant kinetic energies up to 10 eV. During molecular dissociation the laser field can, however, transfer part of the $2p\sigma_u^+$ population back into the $1s\sigma_g^+$ state, thereby producing a dissociative wave packet with large excess kinetic energy. The emerging coherent superposition of the two electronic states results in a time-dependent localisation of the electron density on the upper or lower nucleus due to the gerade and ungerade nature of the two states.

5. Results II: electron localisation in HD

Following the experimental demonstration of CEP control of electron localisation in D_2 , further experiments were performed exploring the possibility of controlling electron localisation in HD. Figure 6(A) shows the D^+ ion kinetic energy spectrum that is obtained after excitation of HD with 5 fs laser pulses at $10^{14} \text{ W cm}^{-2}$. Unlike the case of D_2 , the HD measurements were successfully accompanied by a measurement of above-threshold ionisation in Xe, allowing us to assign a CEP of $\pi/5$. The insert depicts a typical velocity map image, from which the energy spectrum was obtained after angular integration. By varying the CEP an asymmetry map $A(W, \varphi_{\text{CEP}})$ was obtained (see Figure 6(B)). In comparison with the homonuclear

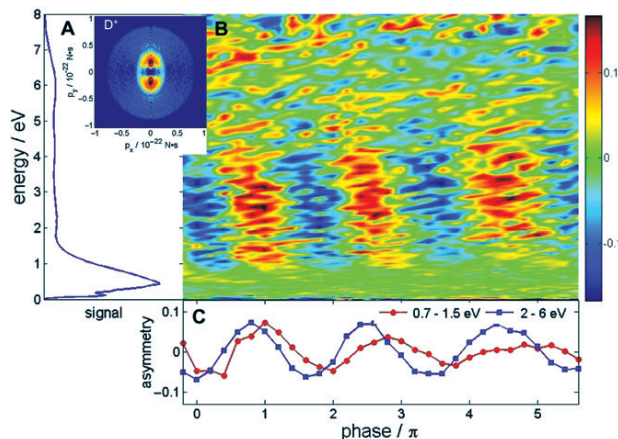


Figure 6. Asymmetry data obtained for the case of HD, D^+ ions. (A) Sample image and kinetic energy spectrum for D^+ ions from the dissociation of HD with 5 fs, $10^{14} \text{ W cm}^{-2}$ pulses. (B) Map of the asymmetry parameter $A(W, \theta)$ as a function of the D^+ kinetic energy W and phase φ_{CEP} . (C) Asymmetry parameter integrated over selected energy ranges (as indicated) versus the CEP.

D_2 case, quite similar asymmetries are obtained for the heteronuclear molecule. Figure 7(A) shows related data for H^+ from HD for the same excitation conditions (5 fs, $10^{14} \text{ W cm}^{-2}$). Note that the energy spectra differ by approximately a factor of 2 due to momentum conservation during the dissociation process. In general, proton spectra tend to show more noise, because of an increased background from ionisation of H_2O . Apart from this additional noise, the D^+ and H^+ ion spectra shown in Figures 6 and 7 show very comparable asymmetry features. The asymmetries are also very similar to the homonuclear case displayed in Figure 3. As seen in Figure 6(B), for D^+ the asymmetry becomes prominent

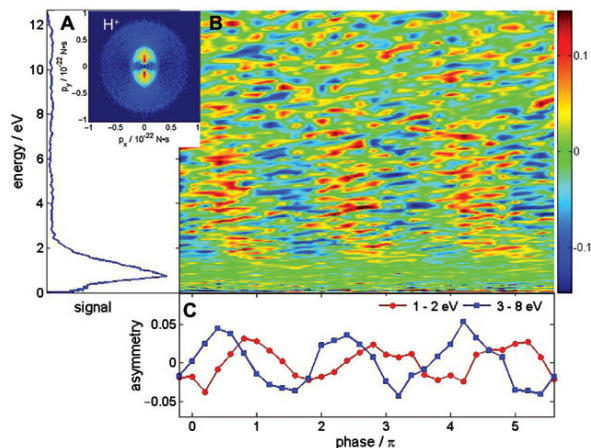


Figure 7. Asymmetry data obtained for the case of HD, H^+ ions. (A) Sample image and kinetic energy spectrum for H^+ ions from the dissociation of HD with 5 fs, $10^{14} \text{ W cm}^{-2}$ pulses. (B) Map of the asymmetry parameter $A(W, \theta)$ as a function of the H^+ kinetic energy W and phase φ_{CEP} . (C) Asymmetry parameter integrated over selected energy ranges versus the CEP.

from 2 to 6 eV and for H^+ , shown in Figure 7(B), between 3 and 8 eV. Note that the phase features of H^+ and D^+ in Figures 6 and 7 do not coincide fully, which is possibly due to the low signal-to-noise ratio in the H^+ measurements. As for D_2 , an asymmetry oscillation is also observed for HD at lower ion kinetic energies within the range of the bond softening contribution (0.7–1.5 and 1–2 eV for D^+ and H^+ , respectively). Again, a shift of the phase of the asymmetry oscillation between the low- and high-energy channels of approximately $\pi/2$ is seen (see Figures 6(C) and 7(C)).

Figure 8 shows the energy and angular dependence of the amplitude $A_0(W, \theta)$ of the asymmetry oscillation $A(W, \theta, \varphi_{\text{CEP}}) = A_0(W, \theta) \sin(\varphi_{\text{CEP}} + \varphi_0(W, \theta))$ that was obtained for D^+ ions from the dissociative ionisation of HD. Similar to Figure 4(A), where this analysis was performed for D_2 , the asymmetry is restricted to angles $\theta < 50^\circ$ and shows a significant difference in the angular distribution of the asymmetry between the low- (0.7–1.5 eV) and high-energy (above 2 eV) channels. The kinetic energy range where the asymmetries are observed for H^+ and D^+ from HD is lower than the kinetic range where these effects were observed for D_2 . A possible reason for this may be the fact that the vibrational period of HD is shorter than that of D_2 , meaning that the vibrational wave packet that is initially produced in the $1\sigma_g$ ground electronic state moves farther out during the 1.7 fs separating the ionisation and the recollision event. If so, recollision excitation promotes the nuclear wave packet to a somewhat lower position on the repulsive $2p\sigma_u$ curve.

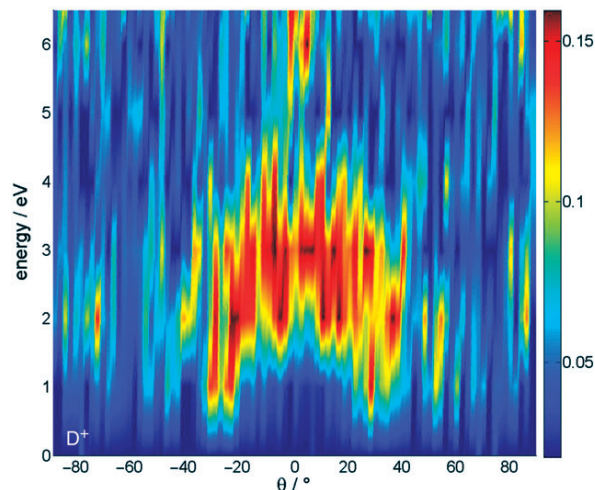


Figure 8. Maximum degree of asymmetry $A_0(W, \theta)$ in the emission of D^+ ions from the dissociative ionisation of HD as a function of the emission angle and energy. The phase-dependent asymmetry oscillations have been fit to sine functions $A(W, \theta, \varphi_{\text{CEP}}) = A_0(W, \theta) \sin(\varphi_{\text{CEP}} + \varphi_0(W, \theta))$ to obtain the parameter $A_0(W, \theta)$.

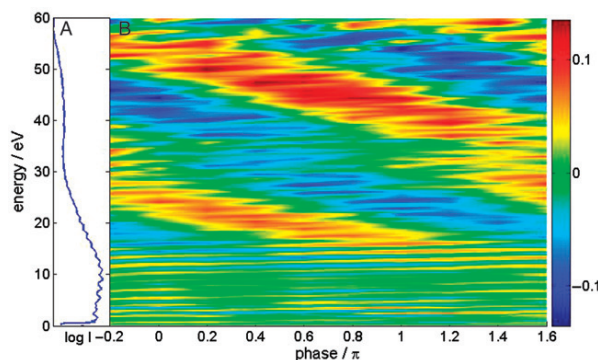


Figure 9. (A) Spectrum and (B) asymmetry map $A(W, \varphi_{\text{CEP}})$ for the emission of electrons in the above-threshold ionisation of Xe with 5 fs pulses at $10^{14} \text{ W cm}^{-2}$. The phase was set to zero at the maximum asymmetry for cut-off electrons and used to calibrate the phase axis in Figures 6 and 7.

The CEP in Figures 6 and 7 was determined *in situ* as an absolute phase via a reference measurement of the asymmetry $A(W, \varphi_{\text{CEP}})$ in the electron emission in the above-threshold ionization (ATI) of Xe (see Figure 9(A) for the ATI spectrum and 9(B) for the asymmetry map). The CEP was set to zero at positions where the cut-off electron emission reaches its maximum in the upward direction [40]. This should facilitate direct comparison with theoretical studies of the system. Interestingly, in HD, in agreement with recent theoretical findings [21], the emission of ions to one of the two sides of the laser polarisation does not

necessarily coincide with phase values of $\varphi_{\text{CEP}} = n\pi$ (with integer number n).

The phase difference between the high-energy (recollision) and low-energy (bond softening) channels in both D_2 and HD of $\sim\pi/2$ is reminiscent of shifts that have been reported between direct and rescattered ATI photoelectron spectra for rare gas atoms, which, for direct (low-energy) electrons, have been explained as a manifestation of double slits in time [14]. In the present experiment, however, the mechanism is slightly different. Based on inspection of the kinetic energy distributions in Figures 6 and 7 we have attributed the asymmetries at low energies to the onset of contributions from a (direct) bond softening (BS) channel, while higher energies have been attributed to (indirect) recollisional excitation (RCE). The difference in the ionisation mechanism is therefore, in principle, similar to that presented in reference 14. However, in the molecular case the closely coupled electron–nuclear dynamics has to be additionally taken into account. Thus, the asymmetry of the BS channel should rather be understood in terms of an n -photon pathway interference between the two respective trajectories for the dissociation of the hydrogen molecular ion. During evolution of the molecule the laser field can couple the gerade and the ungerade states directly when the wavepacket approaches the outer potential well [26]. This coupling may be responsible for the observed phase dependence as calculated by Roudnev and Esry for HD^+ [39]. Moreover, weak phase shifted asymmetries for total ion kinetic energies below 5 eV have been observed [21] in D_2 model calculations, and have been attributed to asymmetric dissociation [24].

6. Conclusion

Electron-transfer processes play a pivotal role in chemistry. Presently, following the generation and measurement of a single sub-femtosecond pulse made possible by unprecedented control of bound and free atomic electrons, respectively, with the sub-cycle evolution of a strong light field [41], it may be possible to observe electron-transfer processes on the fastest timescales that these processes take place. When attosecond pulses are used to initiate electron dynamics in molecules, the high photon energy of the attosecond pulse generally results in ionisation. As discussed by Remacle and Levine [42], removal of an electron on attosecond timescales will often result in the formation of electronic wave packets, because the electron–hole density that results from removing an electron from the highest-occupied molecular orbital (HOMO) does not match the electron–hole density in the singly occupied

HOMO of the cation formed on ionisation. Ultrafast removal of an electron therefore not only forms the ground electronic state of the cation, but, rather, a coherent superposition of electronic states. Remacle and Levine [42] have argued that the formation of this wave packet may lead to electron transport across the ionic structure that is formed. For example, the photo-ionisation of the neutral tetrapeptide molecule TrpLeu₃ is expected to lead to population of the HOMO-1 and the HOMO of the TrpLeu₃⁺ cation. The shape of these orbitals and the 3 eV energy splitting between the two orbitals suggest that electron transfer from one end of the molecule to the other occurs in less than 1 fs. Comparing a wide range of electronic systems, Breidbach and Cederbaum [43] observed that the sudden removal of an electron is accompanied by a characteristic time response completed in approximately 50 as. This time response is interpreted in terms of a filling – upon ionisation – of the exchange-correlation hole associated with the electron ionised by its neighbouring electrons.

The time that sub-femtosecond pulses are used to initiate the formation and subsequently probe of an electron wavepacket that transfers electron density across a large molecule has not yet come. However, in the present paper we have extended sub-femtosecond electron control to molecules and obtained the first evidence of its usefulness in controlling reaction dynamics. We have controlled the dissociation of D_2^+ and HD^+ by steering electron wave packet motion with the sub-cycle, i.e. sub-femtosecond evolution of the electric field of a few-cycle light wave. A coherent superposition of two electronic states in the molecular ion is responsible for an oscillating electron density and the final localisation of the electron. While the computed electron and nuclear dynamics are consistent with our measurement, deeper insight into the role of field-controlled electron dynamics in driving chemical reactions will require time-resolved investigations [25,44,45]. The door to such studies is now open thanks to the availability of sub-femtosecond extreme-ultraviolet (XUV) pulses synchronised with the few-cycle control pulse [41]. Synthesised ultrawide-band (multi-colour) waveforms (comprising near-infrared, visible and possibly ultraviolet light), which can now both be produced and measured, may dramatically enhance the efficiency of steering reactions by creating electronic wave packets and subsequently driving them towards selected sites in complex molecular systems. Indeed, recent theoretical work suggests that circular electronic motion in ring-shaped molecules can be induced by controlled light-fields [46].

Electron-transfer processes are extremely important in chemistry and biology. For example, rapid electron transfer can promote both damage and repair of DNA base-pairs. Our results for the intense-field dissociative ionisation of D₂ and HD constitute a first example of the control of intra-molecular electronic dynamics under the influence of a laser phase and thus provide a first clue that intra-molecular electron transfer processes may be controllable by light fields of controlled evolution.

Acknowledgements

We acknowledge contributions by Y. Ni, J.I. Khan, M. Schultze, T. Uphues, J. Rauschenberger, M. Uiberacker and M. Drescher to these studies. We thank the European Union for support by the Marie Curie Research Training Network XTRA, MRTN-CT-2003-505138, a Marie Curie Intra-European Fellowship, MEIF-CT-2003-500947, and a European Reintegration Grant. The research of M.F.K., C.S. and M.J.J.V. is part of the research program of the 'Stichting voor Fundamenteel Onderzoek der Materie (FOM)', which was financially supported by the 'Nederlandse Organisatie voor Wetenschappelijk Onderzoek (NWO)'. M.F.K., I.Z. and S.Z. acknowledge support by the Max-Planck Society and by the German Science Foundation via the Emmy-Noether program. This work was partly supported by the Cluster of Excellence 'Munich Center for Advanced Photonics' (MAP).

References

- [1] M. Lenzner, *et al.*, IEICE Trans. **E81-C** (2), 112 (1998).
- [2] A. Baltuska, *et al.*, Nature. **421** (6923), 611 (2003).
- [3] M. Lewenstein, *et al.*, Phys. Rev. A **49** (3), 2117 (1994).
- [4] X.F. Li, *et al.*, Phys. Rev. A. **39** (11), 5751 (1989).
- [5] R.R. Freeman, *et al.*, Phys. Rev. Lett. **59** (10), 1092 (1987).
- [6] G.G. Paulus, *et al.*, Phys. Rev. Lett. **72** (18), 2851 (1994).
- [7] M. Spanner, *et al.*, J. Phys. B. **37** (12), L243 (2004).
- [8] J. Itatani, *et al.*, Nature. **432** (7019), 867 (2004).
- [9] G.G. Paulus, *et al.*, Phys. Rev. Lett. **91** (25), 253004 (2003).
- [10] X. Liu, *et al.*, Phys. Rev. Lett. **93** (26), 263001 (2004).
- [11] J. Reichert, *et al.*, Opt. Comm. **172** (1–6), 59 (1999).
- [12] E. Goulielmakis, *et al.*, Science. **305**, 1267 (2004).
- [13] R. Kienberger, *et al.*, Nature. **427** (6977), 817 (2004).
- [14] F. Lindner, *et al.*, Phys. Rev. Lett. **95** (4), 040401 (2005).
- [15] M.F. Kling, *et al.*, Science. **312** (5771), 246 (2006).
- [16] G. Sansone, *et al.*, Science. **314** (5798), 443 (2006).
- [17] M. Uiberacker, *et al.*, Nature. **446** (7136), 627 (2007).
- [18] A.L. Cavalieri, *et al.*, Nature. **449**, 1029 (2007).
- [19] J.H. Posthumus, Rep. Prog. Phys. **67** (5), 623 (2004).
- [20] A.S. Alnaser, *et al.*, Phys. Rev. A. **72** (3), 030702 (2005).
- [21] X.M. Tong and C.D. Lin, Phys. Rev. Lett. **98**, 123002 (2007).
- [22] J.M. Peek, J. Chem. Phys. **43** (9), 3004 (1965).
- [23] W. Kolos, K. Szalewicz, and H.J. Monkhorst, J. Chem. Phys. **84** (6), 3278 (1986).
- [24] A.D. Bandrauk, S. Chelkowski, and H.S. Nguyen, Int. J. Quant. Chem. **100** (6), 834 (2004).
- [25] S. Gräfe and M. Ivanov, Phys. Rev. Lett. **99**, 163603 (2007).
- [26] P. Haljan, M.Y. Ivanov, and P.B. Corkum, Laser Phys. **7** (3), 839 (1997).
- [27] A.L. Cavalieri, *et al.*, New J. Phys. **9** (7), 242 (2007).
- [28] J. Rauschenberger, *et al.*, Laser Phys. Lett. **3** (1), 37 (2006).
- [29] A.J. Verhoef, *et al.*, Opt. Lett. **31** (23), 3520 (2006).
- [30] F. Lepine, *et al.*, Phys. Rev. A **70**, 033417 (2004).
- [31] M.J.J. Vrakking, Rev. Sci. Instr. **72** (11), 4084 (2001).
- [32] H. Niikura, *et al.*, Nature. **417** (6892), 917 (2002).
- [33] H. Niikura, *et al.*, Nature. **421** (6925), 826 (2003).
- [34] A.S. Alnaser, *et al.*, Phys. Rev. Lett. **93** (18), 183202 (2004).
- [35] P.H. Bucksbaum, *et al.*, Phys. Rev. Lett. **64** (16), 1883 (1990).
- [36] H. Niikura, P.B. Corkum, and D.M. Villeneuve, Phys. Rev. Lett. **90** (20), 203601 (2003).
- [37] T. Ergler, *et al.*, Phys. Rev. Lett. **97** (19), 193001 (2006).
- [38] M.V. Ammosov, N.B. Delone, and V.P. Krainov, Sov. Phys. JETP. **64**, 1191 (1986).
- [39] V. Roudnev and B.D. Esry, Phys. Rev. A. **76**, 023403 (2007).
- [40] M.F. Kling, *et al.*, New J. Phys., submitted (2007).
- [41] E. Goulielmakis, *et al.*, Science. **317** (5839), 769 (2007).
- [42] F. Remacle and R.D. Levine, Proc. Natn Acad. Sci. U.S.A. **103** (18), 6793 (2006).
- [43] J. Breidbach and L.S. Cederbaum, Phys. Rev. Lett. **94**, 033901 (2005).
- [44] H. Niikura, *et al.*, J. Mod. Opt. **52** (2/3), 453 (2005).
- [45] G.L. Yudin, *et al.*, Phys. Rev. A. **72** (5), 051401 (2005).
- [46] I. Barth and J. Manz, Angew. Chem. Int. Ed. **45**, 2962 (2006).
- [47] K. Sändig, H. Figger, and T.W. Hänsch, Phys. Rev. Lett. **85** (23), 4876 (2000).

Paper II

Attosecond control of electron dynamics in carbon monoxide.

Znakovskaya, I., von den Hoff, P., Zherebtsov, S., Wirth, A., Herrwerth, O., Vrakking, M. J. J., de Vivie-Riedle, R. & Kling, M. F. *Phys. Rev. Lett.* **103**, 103002 (2009).

Attosecond Control of Electron Dynamics in Carbon Monoxide

I. Znakovskaya,¹ P. von den Hoff,² S. Zherebtsov,¹ A. Wirth,¹ O. Herrwerth,¹ M. J. J. Vrakking,³
R. de Vivie-Riedle,^{2,*} and M. F. Kling^{1,†}¹Max-Planck Institute of Quantum Optics, Hans-Kopfermann-Str. 1, 85748 Garching, Germany²Department für Chemie und Biochemie, Ludwig-Maximilians-Universität München, D-81377 München, Germany³FOM-Institute AMOLF, Science Park 113, 1098 XG Amsterdam, The Netherlands

(Received 5 February 2009; published 1 September 2009)

Laser pulses with stable electric field waveforms establish the opportunity to achieve coherent control on attosecond time scales. We present experimental and theoretical results on the steering of electronic motion in a multielectron system. A very high degree of light-waveform control over the directional emission of C⁺ and O⁺ fragments from the dissociative ionization of CO was observed. *Ab initio* based model calculations reveal contributions to the control related to the ionization and laser-induced population transfer between excited electronic states of CO⁺ during dissociation.

DOI: 10.1103/PhysRevLett.103.103002

PACS numbers: 33.80.Wz, 31.15.A-, 31.70.Hq

Coherent control of chemical reactions and photobiological processes has been achieved by manipulating the laser frequency, phase and polarization in closed loop experiments [1]. Control of the electric field waveform $E(t) = E_0(t) \cos(\omega t + \phi)$, with envelope $E_0(t)$, and frequency ω , by the carrier envelope phase (CEP) ϕ constitutes a new paradigm of coherent control. This control became accessible with CEP stabilization and opened the door to steer electrons in atomic and molecular systems on attosecond time scales [2]. Waveform controlled few-cycle pulses have only recently been used to control electron localization in the dissociative ionization of the prototype molecules D₂ [3,4] and HD [4]. The same processes were also theoretically studied (see e.g., [5–9] and references cited therein). After initial ionization, these systems only contain a single electron. The important question arises, whether the steering of electrons in more complex systems is feasible and—if yes—can we understand the role of the initial ionization or excitation process and the following strong-field coupling of the various potential energy surfaces at the observed control?

We describe experiments, where control of electron dynamics in carbon monoxide (CO) was achieved by the light waveform. Phase-stabilized 4 fs, linearly polarized laser pulses at 740 nm and at an intensity of $8 \times 10^{13} \text{ W cm}^{-2}$ were applied to dissociatively ionize CO. The directional emission of ionic fragments was monitored via velocity-map imaging (VMI). We compare the experimental results to full quantum calculations allowing a mechanistic interpretation and understanding of the observed control.

The dynamics of molecules in strong laser fields typically includes ionization and dissociation. While there is a wealth of work on the dissociation of small molecules in strong laser fields (see e.g., [10] and references cited therein), only a limited number of studies have been performed on CO. Guo studied the multiphoton induced dissociative ionization of CO at 800 nm and an intensity of

$3.8 \times 10^{13} \text{ W cm}^{-2}$ [11]. The yield of C⁺ ions from the dissociation was found to be more than an order of magnitude higher than that of O⁺ fragments. Experiments reported by Alnaser *et al.* [12] using 8 fs pulses at 800 nm and an intensity of $6 \times 10^{13} \text{ W cm}^{-2}$ showed an angular distribution of the ionic fragments from the Coulomb explosion of CO with a maximum along the laser polarization axis, for which the shape of the highest occupied molecular orbital (HOMO) of the CO molecule was held to be responsible. Here, we report on the CEP-dependent directional emission of ionic fragments from the dissociative ionization of CO. To demonstrate the complexity of the molecular system, we show in Fig. 1 the calculated potential energy surfaces (PES) of the lowest $^2\Sigma^+$ and $^2\Pi$ states relevant for the photodissociation of CO⁺ at our laser intensities. In the initial ionization, the low-lying bound electronic states X and A of CO⁺ can be populated. Higher electronic states of CO⁺ can be reached by recollision or multiphoton excitation starting the dissociation process. At our intensity the recollision energy of the electron from the initial ionization is up to 13 eV.

The setup used in these experiments was described earlier [13]. Briefly, phase-stabilized few-cycle pulses

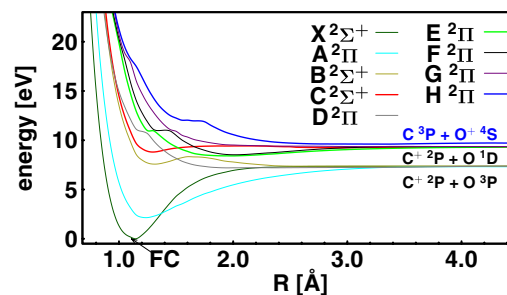


FIG. 1 (color online). PES of CO⁺ and Frank Condon point (FC) for the ionization from neutral CO obtained by calculations described in the text.

were focused into the center of the ion optics of a VMI spectrometer using a spherical mirror ($f = 125$ mm). Ions and electrons that were generated at the crossing point of the laser (linearly polarized along the y axis and propagating along the x axis) and an effusive atomic or molecular beam were projected (along the z axis) onto a multichannel plate (MCP) phosphor screen assembly and recorded with a cooled CCD camera. Inversion of the recorded projections using an iterative procedure allowed reconstruction of the original 3D ion momentum distributions. Figure 2(a) shows a cut through the 3D momentum distribution in the xy plane at $p_z = 0$ for C^+ ions and for a CEP $\approx \pi$ pulse. An up-down (positive p_y versus negative p_y values) asymmetry in the C^+ fragment emission is visible and the contributions may be best identified as three rings, where the first ring is the broadest (from $p = 0$ to 1×10^{-22} Ns) and most intense and exhibits additional sharp lines. The other rings appear between momenta of 1.1 to 1.3 and 1.4 to 1.6×10^{-22} Ns. The dominant features show angular

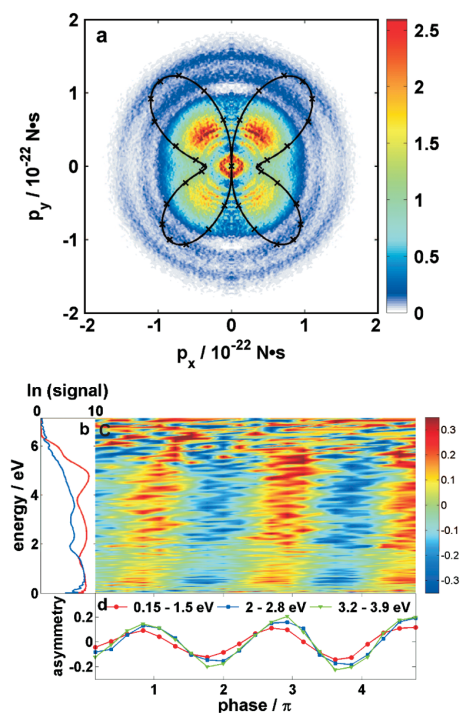


FIG. 2 (color). (a) Inverted two-dimensional C^+ momentum image (the laser polarization is vertical) and calculated ionization rate of CO in arb. un. (black line) for CEP $\approx \pi$; (b) measured (blue) and theoretical (red) C^+ kinetic energy spectrum for CO dissociative ionization. (c) Asymmetry of C^+ ion emission along the laser polarization (integrated over 120°) vs kinetic energy and phase. (d) Asymmetry integrated over indicated energy ranges vs CEP. The CEP was calibrated by reference measurements in Xe and comparison to calculations based on the quantitative rescattering theory according to a recently published method [17]. From the evaluation of this data we obtain an error in the absolute CEP of $\pm 0.04\pi$.

distributions with minima around 0, 90, 180 and 270 with varying modulation depths. This angular distribution of the C^+ fragments differs from the findings in Ref. [12] and indicates contributions from the HOMO (5σ) and the HOMO-1 ($1\pi_{x/y}$). The solid black line in Fig. 2(a) displays the calculated volume-averaged angle-dependent ionization rate as described below in the theory section. Figure 2(b) shows the kinetic energy spectrum derived from Fig. 2(a) by angular integration (blue line) together with the calculated spectrum obtained within the theoretical approach described below (red line). Comparison with experiments using circularly polarized light at twice the intensity as for linear polarization, which suppresses the recollision excitation, reveals a distinct decrease in intensity of all three rings. Thus, we conclude that recollision excitation is responsible for the production of the observed ionic fragments at our experimental conditions. In the fragmentation of CO^+ , the $C^+ + O$ channel is energetically favored over the $C + O^+$ channel (see Fig. 1). We find the C^+ yield to be approximately 20 times larger than the O^+ yield. Throughout the measured CEP range a pronounced phase dependence in the directional ion emission is found for C^+ as well as for O^+ ions. The directional emission is represented by the asymmetry $A(W, \phi) = \frac{P_{up}(W, \phi) - P_{down}(W, \phi)}{P_{up}(W, \phi) + P_{down}(W, \phi)}$ as a function of the fragment kinetic energy W and the laser phase ϕ . $P_{up}(W, \phi)$ and $P_{down}(W, \phi)$ are the angle integrated ion yields in the up and down directions. Figure 2(c) displays the observed asymmetry $A(W, \phi)$ for the dissociative ionization of CO into C^+ and O as a function of the CEP and the kinetic energy W of the C^+ ion fragments. Figure 2(d) shows the asymmetry parameter integrated over selected energy ranges. The observed asymmetry in the directional emission of C^+ ions is very pronounced and almost equally strong throughout the kinetic energy spectrum. A similar asymmetry map (not shown here) was recorded for O^+ ions, showing the same features. Because of the significantly weaker O^+ signal, however, the asymmetry map exhibits a lower signal-to-noise ratio, making it also difficult to determine the phase-shift between the points, where a maximum asymmetry is found for C^+ and O^+ ions.

In the experiment, the asymmetry can arise from contributions of all three steps: ionization, recollisional excitation, and laser-induced population transfer between excited electronic states of CO^+ . The initial population of excited states by recollision is likely dependent on the CEP, but its calculation is currently out of scope for larger molecules [6]. We can, however, focus on the remaining two steps. The ionization probability of a molecule in a laser field is determined by the electron flux induced by this external electric field [14]. To calculate the angular dependent ionization probability for a given static electric field, we performed quantum chemical calculations under various orientation angles with respect to the polarization of the applied external field. In the spirit of [14] we record the electron flux through a surface placed at the outer

turning points of a given orbital. When ionization from the HOMO only is considered as in Ref. [12], our calculated angular distribution matches the reported results therein. For our experimental conditions we allow ionization from the HOMO (leading to the $X^2\Sigma^+$ state of CO^+) and the HOMO-1 (leading to the $A^2\Pi$ state) reproducing the observed angular distribution [Fig. 2(a)]. This is achieved by a basis transformation forming the orbitals HOMO + HOMO-1 and HOMO-HOMO-1. By integration of the calculated ionization probabilities over the appropriate orientation angles, the asymmetry in the ionization step caused by a phase-stabilized electric laser field can be extracted. Assuming ionization only at the extrema of the field, we calculated the asymmetries for various contributions of half-cycles as shown in Fig. 3 (solid line). The volume-averaged angular dependent ionization probability is obtained for a spatial Gaussian intensity profile and is shown in Fig. 2(a) (black line) for the combination of the three most prominent half-cycles and a CEP = π pulse. The related volume-averaged asymmetries are presented in Fig. 3 (dashed line). The remaining less intense half-cycles can be neglected as they do not cause recollision excitation. The good agreement between theory and experiment shows that the angular distribution arises from the ionization out of two orbitals. Its asymmetry originates from phase stable electric fields. The corresponding calculated asymmetry amplitude of 0.14 is below the experimentally observed total asymmetry amplitude of 0.2. If only ionization would be responsible for the observed CEP dependence, the asymmetry would be expected to be seen for all observed C^+ ions irrespective of their kinetic energy or angular distribution. Experimentally, we do however find that the angular range over which the asymmetry is observed depends on the fragment kinetic energy, suggesting that the experimental result is not solely explained by the ionization mechanism.

To calculate to what extent the asymmetry may arise in the dissociation process we used our recently introduced approach to describe coupled electron and nuclear dynamics [8]. We follow the dominant recollision excitation path-

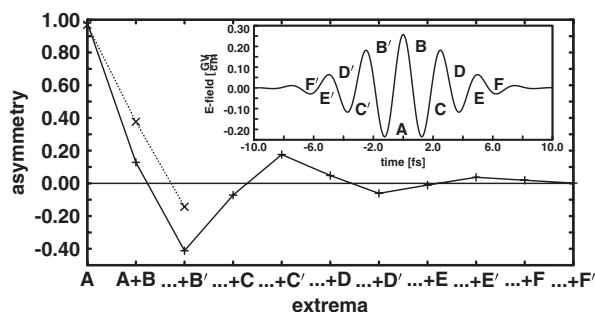


FIG. 3. Calculated asymmetries (+ symbols and solid line) for various combinations of half-cycles of the laser field (shown in the inset). The x symbols show volume-averaged asymmetry contributions (dashed line).

way, assuming ionization of CO only at the electric field maximum of the laser pulse used in the experiment and recollision of the electron after 1.7 fs [15]. Our quantum dynamical simulations start after the recollision. The initially formed nuclear wave packet is excited from the X and A state to higher electronic states. Thereby a coherent superposition of several electronic states is created and simultaneously the electronic and nuclear wave packet motion is initiated. The PES for the CO electronic ground state and for the ionic states are calculated with MOLPRO [16]. From the set of CO^+ PES we chose three potentials as typical representatives for the induced dynamics which moreover allow all transitions among each other. We include the $C^2\Sigma^+$ state as the weakly bound state and the $E^2\Pi$ state to resemble the repulsive dynamics. Both states correlate with the $\text{C}^+(^2P) + \text{O}(^1D)$ channel. As third PES we include the $H^2\Pi$ state which is the first state leading to the $\text{C}(^3P) + \text{O}(^4S)$ channel, delivering O^+ fragments as observed in the experiment. The initial wave packet is composed as a 55:38:7 distribution of the states involved, ordered in increasing energy, assuming a Gaussian energy distribution for the recolliding electron with a cutoff energy of 13 eV. Choosing these particular values for the initial populations also reflects the experimentally observed ratio between C^+ and O^+ fragments. In the calculations the CO^+ ions are taken to be aligned at 45° to the laser polarization as the ionization peaks along this direction and all transitions between Σ and Π states are allowed. The molecular wave function $\Psi_{\text{mol}} = \sum_i \chi_i(R, t) \varphi_i(r, t; R)$ is set up as the sum over these three electronic states i with χ_i the nuclear wave functions, φ_i the field-free electronic wave functions, the nuclear and electronic coordinates R and r and the time t . Figure 4 shows the temporal evolution of the laser field (a) and of the population in the three selected electronic states (b). The calculated kinetic energy spectrum [Fig. 2(b)] derived from the nuclear dynamics is in reasonable qualitative

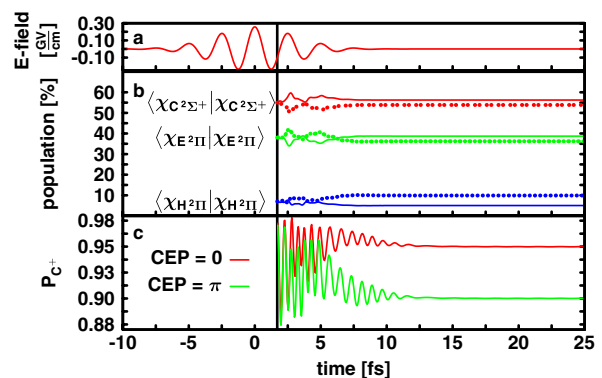


FIG. 4 (color online). (a) Electric field (CEP = $\varphi = 0$). (b) Time-dependent populations of the $C^2\Sigma^+$, $E^2\Pi$, and $H^2\Pi$ states after recollision excitation (solid: CEP = 0; dotted: CEP = π). (c) Temporal evolution of the probability measuring a C^+ fragment P_{C^+} .

agreement with the experimental data supporting the selection made for the representative states. On the basis of these results, we can explain the origin of the observed energy distribution. The low kinetic energy spectrum arises from the dynamics on the weakly bound state while the spectrum between 2.0–2.8 eV originates from the purely repulsive state. The high energy spectrum reflects the dynamics of the second repulsive state correlating with the O^+ channel. The sharp peaks in the low kinetic energy spectrum, also present in the experimental data [Figs. 2(a) and 2(b)], arise from interference of bound and dissociative vibrational states in the nuclear wave packet on the $C^2\Sigma^+$ state. The electronic density $\rho(r_1, t; R)$ is expressed as a function of the electronic coordinate r_1 and time. The total molecular wave function is integrated over the nuclear and over the $N - 1$ electronic coordinates (with N the total number of electrons):

$$\begin{aligned} \rho(r_1, t; R) &= \int \Psi_{\text{mol}}^* \Psi_{\text{mol}} dR dr_2 \dots dr_N \\ &= \sum_{i=1}^3 a_i(t)^2 |\varphi_i(r_1, t_0; R)|^2 \\ &\quad + \sum_{i=1}^3 \sum_{j>i} 2\text{Re}\{\langle \chi_i(R, t) | \chi_j(R, t) \rangle_R \varphi_i(r_1, t_0; R) \\ &\quad \times \varphi_j(r_1, t_0; R)\} e^{-i\Delta E_{ji}(R(t))\Delta t + \phi(t-\Delta t)}, \end{aligned} \quad (1)$$

with $a_i(t) = \sqrt{\langle \chi_i(t) | \chi_i(t) \rangle_R}$ and $a_i^2(t)$ the population of the electronic states, the interference term $\langle \chi_i(t) | \chi_j(t) \rangle_R$ and the energy difference $\Delta E_{ij}(t) = E_j(t) - E_i(t)$ between the electronic states i and j . The electronic wave functions $\varphi_i(r, t_0; R)$ are represented as Slater determinants. The time evolution of the electronic wave packet is calculated by propagation in the eigenstate basis. The coupling of the fast electron to the slower nuclear dynamics enters through the time-dependent population and through the interference term, which specifies the degree of electronic coherence induced in the molecular system. The probability $P_{C^+}(t)$ of measuring a C^+ fragment is given by $P_{C^+}(t) = \int_{x_{\min}}^{x_{\max}} dx \int_{y_{\min}}^{y_{\max}} dy \int_{z_{\min}}^0 dz \rho(r_1, t; R(t))$ where x , y , and z refer to the molecular frame with z along the molecular axis and the O-atom oriented along negative z values [8]. In the first 6 fs the electron dynamics, reflected in $P_{C^+}(t)$ [e.g., red curve in Fig. 4(c)], results from a competition between the influence of the light pulse, the dynamics of the linear combination and the interference term of the nuclear wave functions. As soon as the population transfer between the electronic states stops [approximately after 8 fs, see Fig. 4(b)] $P_{C^+}(t)$ oscillates with decreasing amplitude converging after 12 fs to its final value. This decay arises from the reduced overlap of the superimposed molecular orbitals, which become soon located on the two different nuclei during the dissociation process. Consequently, the last term of Eq. (1) vanishes and hence the dynamics of the electronic linear combination. The probability $P_{C^+}(t)$ is finally given by the prepared population distribution of the

coupled reaction channels leading either to C^+ or O^+ . This ratio is steered very precisely by the CEP modulating the relative intensities between half-cycles and is only significant in ultrashort laser pulses. When multiple half-cycles are taken into account the mechanism of the observed control stays the same. A shift of the CEP by π while keeping the molecular orientation leads to a different result [green curve in Fig. 4(c)]. Changing the orientation of the molecule by 180° is equal to shifting the CEP by π as the transition dipole moment changes the sign. Thus the CEP-dependent asymmetry in the dissociation step can be calculated by $P_{C^+}(t)$ for two CEP values shifted by π . As shown in Fig. 4(c), the probability of measuring a C^+ fragment upon the break up of the molecule can be changed by 5% through the CEP.

We presented experimental and theoretical results on the steering of electrons in a multielectron system. As possible mechanisms for the observed CEP control of the directional fragment emission in the dissociative ionization of CO, we have discussed contributions from the ionization step as well as from the laser-induced dynamics during the dissociation. The current experimental data does not allow us to clearly distinguish the individual contributions. Further studies are underway that aim into this direction.

We acknowledge F. Krausz for his support and we thank Z. Chen and C. D. Lin for their help with the CEP calibration. The work of M. J. J. V. is part of the research program of FOM (financially supported by NWO). We are grateful for support by the DFG via the Emmy-Noether program and the Cluster of Excellence: Munich Center for Advanced Photonics.

*regina.de_vivie@cup.uni-muenchen.de

†matthias.kling@mpq.mpg.de

- [1] T. Brixner and G. Gerber, Chem. Phys. Chem. **4**, 418 (2003).
- [2] R. Kienberger *et al.*, J. Mod. Opt. **54**, 1985 (2007).
- [3] M. F. Kling *et al.*, Science **312**, 246 (2006).
- [4] M. F. Kling *et al.*, Mol. Phys. **106**, 455 (2008).
- [5] V. Roudnev, B. D. Esry, and I. Ben-Itzhak, Phys. Rev. Lett. **93**, 163601 (2004).
- [6] S. Gräfe and M. Y. Ivanov, Phys. Rev. Lett. **99**, 163603 (2007).
- [7] X. M. Tong and C. D. Lin, Phys. Rev. Lett. **98**, 123002 (2007).
- [8] D. Geppert *et al.*, J. Phys. B **41**, 074006 (2008).
- [9] A. D. Bandrauk *et al.*, Int. J. Quantum Chem. **100**, 834 (2004).
- [10] J. H. Posthumus, Rep. Prog. Phys. **67**, 623 (2004).
- [11] C. Guo, Phys. Rev. A **73**, 041401(R) (2006).
- [12] A. S. Alnaser *et al.*, Phys. Rev. A **71**, 031403(R) (2005).
- [13] M. Schultze *et al.*, New J. Phys. **9**, 243 (2007).
- [14] B. M. Smirnov and M. I. Chibisov, Sov. Phys. JETP **22**, 585 (1966).
- [15] H. Niikura *et al.*, Nature (London) **417**, 917 (2002).
- [16] H.-J. Werner and P. J. Knowles *et al.*, MOLPRO, version 2006.1 (2006).
- [17] S. Micheau *et al.*, Phys. Rev. Lett. **102**, 073001 (2009).

Paper III

Attosecond control of the dissociative ionization via electron localization: a comparison between D₂ and CO.

von den Hoff, P., Znakovskaya, I., Kling, M. F. & de Vivie-Riedle, R.
Chem. Phys. **366**, 139 (2009).



Attosecond control of the dissociative ionization via electron localization: A comparison between D₂ and CO

P. von den Hoff^a, I. Znakovskaya^b, M.F. Kling^b, R. de Vivie-Riedle^{a,*}

^aDepartment für Chemie und Biochemie, Ludwig-Maximilians-Universität München, Butenandt-Strasse 11, 81377 München, Germany

^bMax-Planck-Institut für Quantenoptik, Hans-Kopfermann-Strasse 1, 85748 Garching, Germany

ARTICLE INFO

Article history:

Received 12 June 2009

Accepted 25 September 2009

Available online 2 October 2009

Keywords:

Attosecond control
Dissociative ionization
Electron localization
Electron dynamics
Carbon monoxide
D₂

ABSTRACT

Laser pulses with stable electric field waveforms establish the opportunity to achieve coherent control on attosecond timescales. A first successful example of electron localization and its control could be demonstrated for the molecules D₂⁺ and HD⁺. These molecules constitute simple model systems with only one electron and left the question open, whether electron localization in multi-electron systems can be achieved and controlled. In this context, we recently reported results where a high degree of light-waveform control over the directional emission of C⁺ and O⁺ fragments from the dissociative ionization of CO was observed [1]. Here, we compare and analyze the mechanisms leading to electron localization in the two different molecular systems D₂⁺ and CO⁺. We use our recently introduced method for multi-electron systems that allows us to describe the formation of an electronic wavepacket and to follow its evolution during the dissociation process.

© 2009 Elsevier B.V. All rights reserved.

1. Introduction

Coherent control of chemical reactions and photobiological processes has been achieved within the last decade [2,3] using pulse shapers to manipulate the light field parameters frequency, phase and polarization. Typical timescales of these processes lie in the femtosecond range. The recent accessibility of pulses with a duration of a few femtoseconds or even attoseconds [4] sparked the interest to control the dynamics of the much faster electrons. One exciting idea is to steer a chemical reaction by guiding an electronic wavepacket to the wanted position inside the molecule to form or break bonds. At least two requirements must be fulfilled, first the formation of a localizable electronic wavepacket and second its stabilization at the wanted position. An electronic wavepacket can be formed by superimposing two or more electronic states by an electric field. The sign of the applied field determines whether the positive or negative linear combination is created at the beginning of the reaction. This new paradigm of coherent control is accessible by controlling the electric field waveform $E(t) = E_0(t) \cos(\omega t + \phi)$, with envelope $E_0(t)$ and frequency ω , through the carrier envelope phase (CEP) ϕ [5].

CEP-stabilized few-cycle pulses have only recently been used to steer the electron motion in the dissociative ionization of the molecule D₂ and its isotopologues [6,7]. The asymmetric D⁺(H⁺) ion

ejection in the dissociative ionization of D₂ and HD was also theoretically studied (see e.g. [8–13] and references cited therein). After the initial ionization, these prototype systems contain a single electron. The steering of this electron originates from a CEP controlled coherent superposition of the two electronic states X²Σ_g⁺ and A²Σ_u⁺ (see Fig. 1a) that localize the electron density and finally controls the directional emission of charged and uncharged fragments upon the dissociation of the molecule.

These initial results stimulated an important question: is it possible to control the localization of electrons during reactions in more complex systems using a similar scheme? And moreover, can we identify and understand the underlying processes in the observed control? The knowledge about the processes involved is an important step towards the control of electron dynamics in molecules of chemical or biological interest. Along this line experiments on CO were performed showing encouraging results in terms of the CEP controlled electron localization during the dissociation. Control of dissociative reactions has been achieved previously by different approaches relying, e.g either on the control of the nuclear dynamics [14,15] or on the control of multipath multi-photon processes [16]. Here we focus on the reaction control through electron localization via the CEP.

The dynamics of molecules in strong laser fields typically includes ionization, recollision excitation or recombination and dissociation. In principle all these processes are steerable by the electric field waveform, and have to be considered in order to understand or even predict the outcome of a strong field experiment. While there is a wealth of work on the strong field dissocia-

* Corresponding author.

E-mail addresses: matthias.kling@mpq.mpg.de (M.F. Kling), regina.de_vivie@cup.uni-muenchen.de (R. de Vivie-Riedle).

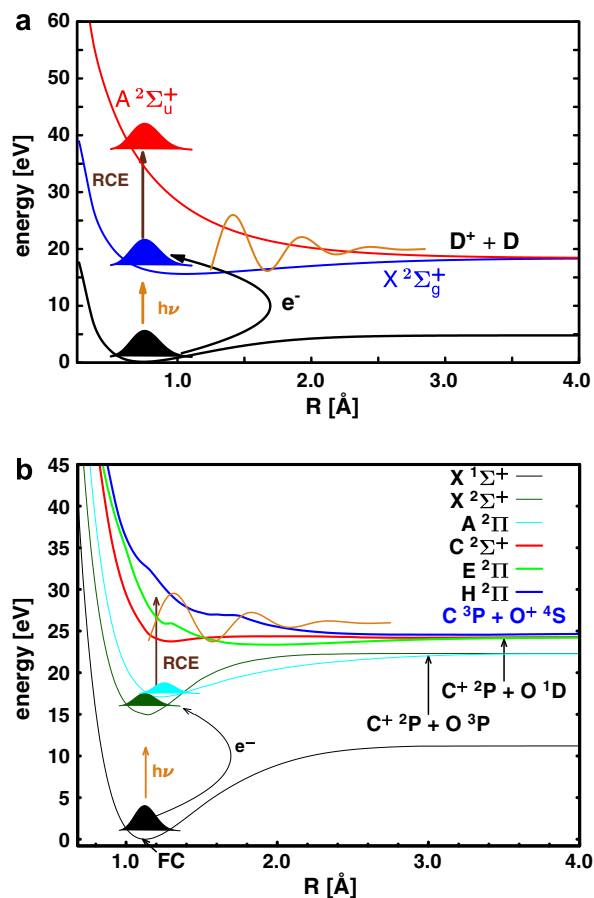


Fig. 1. (a) Potential energy surfaces (PES) of D_2, D_2^+ obtained by calculations described in the text. Pathway for the formation of D^+ ions from D_2 by dissociation of the molecular ion through ionization ($h\nu$) and recollision excitation (RCE). (b) PES of CO, CO^+ and Franck-Condon point (FC) for the ionization from neutral CO obtained by calculations described in the text. Pathway for the formation of $C^+ (O^+)$ ions from CO by dissociation of the molecular ion through ionization ($h\nu$) and recollision excitation (RCE). For both figures it is indicated which electronic states are coupled by the remaining laser field (solid orange line). (For interpretation of the references to colour in this figure legend, the reader is referred to the web version of this article.)

tion of small molecules (see, e.g. [17] and references cited therein), only a few studies have been performed on carbon monoxide (CO) [18,19]. Very recently we reported first experimental and theoretical results on the influence of the CEP on the strong field dissociative ionization of the CO molecule [1].

In this paper we present a detailed and comparative theoretical analysis of the electron localization in the dissociative ionization of the two molecules D_2 and CO. These two molecules can be regarded as prototypes for homo- and heteronuclear systems as well as for single and multi-electron systems. We shortly refer to the experimental setup and results, as they define the initial conditions for the theoretical treatment. For the theoretical analysis, we applied our recently developed method to describe the coupled nuclear and electron dynamics simultaneously for multi-electron systems [11].

2. Experimental setup

The laser and vacuum setup used for the experiments was described in detail in [20]. The parameters for the experiments on

D_2 and CO were as follows: we generated 5 fs (D_2) and 4 fs (CO) linearly polarized, phase-stabilized pulses at 760 nm (D_2) and 740 nm (CO) with 3 kHz repetition rate. The few-cycle pulses were focused into the center of the ion optics of a velocity-map imaging (VMI) spectrometer using a spherical mirror ($f = 500$ mm (D_2)/ $f = 125$ mm (CO)). The D_2 and CO experiments with linear polarization of the laser were carried out at intensities of 1.2 and 0.8×10^{14} W/cm², respectively. Ions and electrons that were generated at the crossing point of the laser (x-axis) and an effusive atomic/molecular jet were accelerated and focused (along the z-axis) with the ion optics (see Fig. 2 consisting of a repeller, extractor and grounded time-of-flight region (from left to right in the figure) onto an MCP-phosphor screen assembly (Hamamatsu, F2226-24PX). The polarization of the laser was chosen along the y-axis, i.e. parallel to the xy-plane of the MCP detector. Images were recorded with a CCD camera. Inversion of the recorded images using an iterative inversion procedure [21] allowed reconstructing the original 3D ion momentum distributions. The pulse duration and CEP of the pulses were adjusted by insertion of fused silica into the laser beam via a pair of wedges. In the case of CO the CEP was calibrated by reference measurements in Xe and comparison to calculations based on quantitative rescattering theory according to a recently published method [22]. From the evaluation of this data the CEP is determined with an error of $\pm 0.04\pi$. For D_2 the data was recorded as a function of a relative CEP-change.

3. Experimental results

The formation of fragment ions occurs in both cases (D_2 and CO) via a two-step mechanism (schematically shown in Fig. 1a for D_2 and (b) for CO) in which initially the molecule is ionized by the laser field (Fig. 1a and b, orange arrows) and a vibrational wavepacket is created in the low-lying bound potential energy surfaces (PES) $X^2\Sigma_g^+$ for D_2 (X and A in CO^+). The dissociation is triggered by excitation to repulsive electronic states either by laser induced coupling (LC) or by recollision excitation (RCE).

The emission of fragment ions from the dissociation of D_2 and CO in intense few-cycle laser fields was monitored with VMI allowing to retrieve their full 3D-momentum distribution. Previous studies have revealed several pathways in the dissociation of D_2 and its isotopes in intense laser fields [17]. In the double ionization of these systems, two momentum-matched ions are produced that

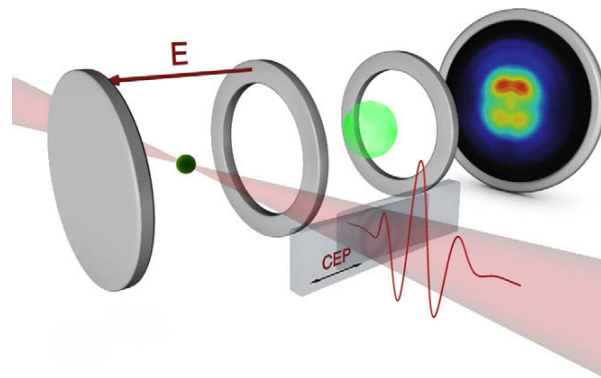


Fig. 2. Schematic of velocity-map imaging (VMI) of the directional emission of ionic fragments from the dissociative ionization of D_2 and CO with phase-stable few-cycle pulses. The CEP is shifted by the insertion of fused silica into the laser beam using a pair of wedges. Ions that are created at the crossing point of an effusive molecular jet and the focused laser beam are projected by the ion optics of the VMI, consisting of a repeller, extractor and ground plate with a grounded time-of-flight region (from left to right), onto an MCP/phosphor screen assembly. The projections (C^+ ions from CO in the schematic) are recorded by a CCD camera.

are symmetrically emitted along the molecular axis, irrespective of the evolution of the driving fields. Light-waveform control of the dissociation of D₂ thus requires to avoid double ionization pathways. The important remaining channels in the dissociative ionization of D₂ at our laser conditions are bond softening and recollision excitation [6]. Bond softening is visible by contributions to the kinetic energy spectrum of D⁺ ions between 0 and 2 eV. Recollision excitation (by the electron that is emitted upon ionization of D₂) gives higher D⁺ kinetic energies between 3 and 8 eV. The spectral contribution from recollision excitation vanishes with circular polarization. Fig. 3a shows the kinetic energy spectrum for the C⁺ fragments from the dissociation of CO in an intense few-cycle laser field. Three main spectral peaks are visible in energy ranges of 0.15–1.5 eV, 2–2.8 eV and 3.2–3.9 eV. In the low kinetic energy range between 0.15 and 1.5 eV a distinct structure can be seen (see inset of Fig. 3a). Comparison with experiments using circular polarized (CP) light at twice the intensity as for linear polarization to achieve the same field strength, which suppresses the recollision excitation, reveal a distinct decrease of the observed C⁺ ions. The resulting kinetic energy spectrum (CP) is shown in Fig. 3a. We conclude that recollision excitation is the dominant process leading to the observed fragmentation pattern while laser induced excitation from bound electronic states to dissociative states of CO⁺ plays only a minor role.

No difference in the emission along the laser polarization axis (up versus down in the recorded images) is observed with a randomly varying phase. With CEP stabilization a pronounced phase dependence in the directional ion emission is found throughout the measured CEP range for D⁺ ions from D₂ and C⁺/O⁺ ions from CO. The directional emission is represented by the angle-integrated asymmetry

$$A(W, \phi) = \frac{P_{\text{up}}(W, \phi) - P_{\text{down}}(W, \phi)}{P_{\text{up}}(W, \phi) + P_{\text{down}}(W, \phi)} \quad (1)$$

as a function of the fragment kinetic energy W and the laser phase ϕ . $P_{\text{up}}(W, \phi)$ and $P_{\text{down}}(W, \phi)$ are the measured ion yields in the up and down directions along the laser polarization axis. The ion yields were integrated over an angular range of 120° around the polarization axis over which we observed a pronounced asymmetry for both molecules (see, e.g. Fig. 4a in Ref. [7]) with almost the same amplitude. Fig. 4 shows the evolution of the asymmetry parameter $A(\phi)$ that has been obtained by integration of $A(W, \phi)$ over chosen energy intervals for D⁺ ions from D₂ (panel a) and C⁺ (panel b)/O⁺ (panel c)

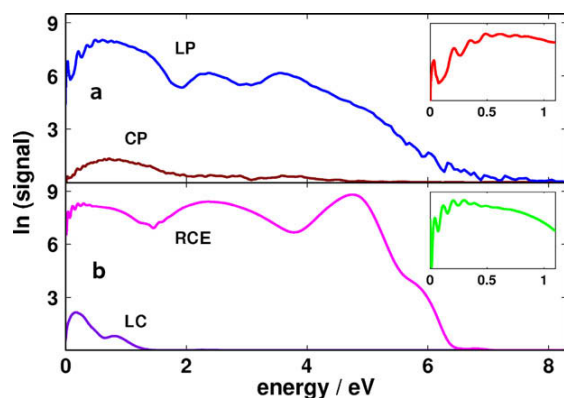


Fig. 3. (a) Experimentally observed C⁺ kinetic energy spectra for CO dissociative ionization by linear (LP) and circular (CP) polarized light pulses without phase stabilization (integrated over 120°), (b) calculated C⁺ kinetic energy spectrum including recollision excitation (RCE) and laser induced coupling (LC) of the bound and repulsive electronic states at the same conditions; the insets in (a) and (b) show the enlarged lower energy range for experimental and calculated spectra.

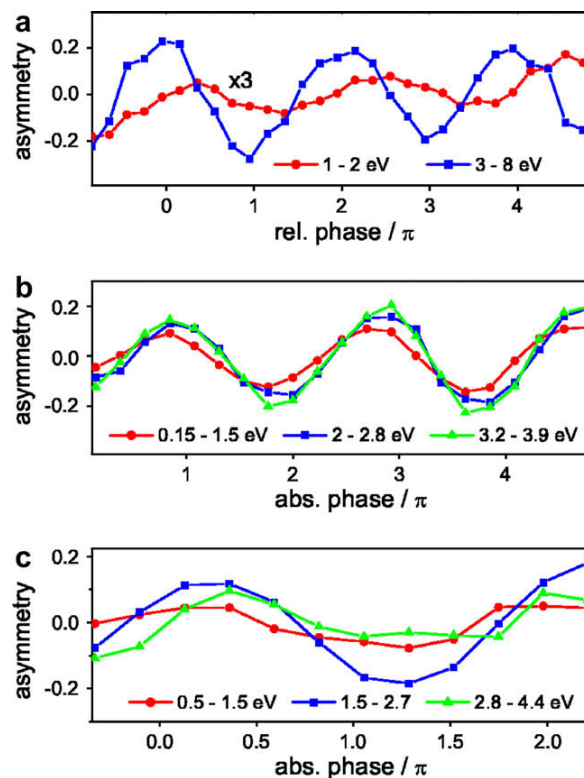


Fig. 4. Experimental asymmetry $A(\phi)$ integrated over several energy ranges (as indicated) versus the CEP for D⁺ ions from D₂ (a) and C⁺ ions (b)/ O⁺ ions (c) from CO. For D₂ the data were recorded as a function of a relative CEP-change (rel. phase). In the case of CO the CEP was calibrated by reference measurements in Xe and comparison to calculations based on quantitative rescattering theory [22] (abs. phase).

ions from CO. In all cases the asymmetry oscillates as a function of the phase representing conditions where the direction of the ionic emission is effectively controlled. We will elaborate here further, how the mechanisms for the observed control differ for these homo- and heteronuclear systems.

For D₂ the highest degree of control is observed for D⁺ fragments, whose creation has involved recollision excitation (i.e. in the energy range between 3 and 8 eV). It has been argued in [6] that the bond softening contribution might have been affected by a temporally longer (10–20 fs) pedestal to the few-cycle pulses (of ca. 10% in intensity). Still a weak oscillation of the asymmetry in the range between 0 and 2 eV is visible and is observed to be phase-shifted with respect to the asymmetry oscillation at higher energies. Fig. 4b shows the asymmetry for C⁺ ions integrated over energy ranges corresponding to the three main contributions in Fig. 3a. The observed asymmetry in the directional emission of the C⁺ ions is almost equally strong throughout the whole kinetic energy spectrum with a maximum value around 0.2. Analogous to the dependence of the asymmetric emission of O⁺ ions was recorded for CO, showing the same features (see Fig. 4c). Due to a 20 times weaker O⁺ signal, however, the data exhibit a lower signal-to-noise ratio. Thus it is difficult to determine the phase-shift between the points, where a maximum asymmetry is found for C⁺ and O⁺ ions.

4. Theoretical method

A theoretical description of electron dynamics in multi-electron molecules is still a challenge. Most approaches use time-dependent

analogs of well-established quantum chemical methods. Based upon the time-dependent Hartree–Fock theory [23] and the (explicitly) time-dependent density-functional theory [24] there are many expansions to incorporate the correlation of the electrons and make use of post-Hartree–Fock methods like TD-CI [25,26], TD-MCSCF [27] and MC-TDHF [28]. In other approaches the electronic wavefunction is directly propagated using Green's function formalism [29] or in the basis of electric eigenstates [30]. While these methods describe the electronic motion very accurately, a simultaneous quantum mechanical treatment of the nuclear motion is computationally demanding. Calculations along this line has very recently been presented for bound 4-electron system LiH [31]. The group of Takatsuka [32] therefore introduced an ansatz to couple electron dynamics in the eigenstate system to classical nuclear motion.

Recently we presented a new method to treat electron and nuclear quantum dynamics simultaneously for multi-electron systems [11]. This method was tested for the control of electron localization in D_2^+ and then applied to describe the experimental results on the dissociative ionization of CO [1]. Here, we focus on a comparison of the mechanisms leading to the electron localization observed in the dissociative ionizations of D_2 and CO and the consequences for the CEP controlled asymmetry. For both prototype molecules the ionization step determines the angular distribution of the ionic fragments recorded by the VMI spectrometer (see Fig. 2). The D^+ ion distribution from D_2 is aligned along the laser polarization, while C^+ and O^+ fragments from CO show distinct maxima around 45° , 135° , 225° and 315° [1]. The angular distribution also defines the optical transitions addressable for a given laser polarization. For the heteronuclear molecule, one can expect orientational dependent ionization probabilities for phase-stabilized lasers and thus a contribution from the ionization to the total observed asymmetry [1]. Homonuclear diatomic molecules always show a symmetric angular distribution in the ionization step. The contributions from the recollision are still unknown and their calculation is currently out of scope for many electron molecules [9].

For the calculations of the asymmetry produced in the dissociation process, we follow the dominant recollision excitation pathway, assuming ionization at the electric field maximum of the strong ultrashort laser pulse and recollision of the electron 1.7 fs later (corresponding to the first recollision time [33]). Thereby the initially formed nuclear wavepacket is excited from the X (and A state in case of CO^+) to higher electronic states. Simultaneously, the electronic and nuclear wavepacket motion is launched. Important for the starting conditions of our theoretical analysis are the differences in the recollision excitation between the two molecular ions D_2^+ and CO^+ . In the case of D_2^+ the recollision excitation only populates the repulsive $A^2\Sigma_u^+$ state (see Fig. 1a). In contrast, the recollision can excite various close lying electronic states in the CO^+ molecule (see Fig. 1b). Our quantum dynamical simulations start after the recollision event. We summarize briefly our method [11] and highlight the expressions especially important for the aspired comparison. The molecular wavefunction Ψ_{mol} is set up in a product ansatz as the sum over the electronic states i involved in the subsequent laser pulse interaction:

$$\begin{aligned}\Psi_{\text{mol}}(R, r, t) &= \sum_i \varphi_i(r, t; R) \chi_i(R, t) \\ &= \sum_i \varphi_i(r, t_0; R) e^{-iE_i(R)t} \sum_j c_{ij} \xi_{ij}(R) e^{-iv_{ij}t} \\ &= \sum_i \varphi_i(r, t_0; R) \sum_j c_{ij} \xi_{ij}(R) e^{-i(E_i(R) + v_{ij})t}\end{aligned}\quad (2)$$

with χ_i the nuclear wavepackets in the i th electronic state composed of the ξ_{ij} vibrational eigenfunctions, $\varphi_i(r, t_0; R)$ the stationary

electronic wavefunction defined at time zero ($t_0 \hat{=} t = 0$), $E_i(R)$ the electronic eigenenergy, v_{ij} the relative energy of the vibrational levels, the nuclear and electronic coordinates R and r and the time t . To follow first the nuclear wavepacket motion we, multiply the time-dependent Schrödinger equation from left with $\varphi_i^*(r, t_0; R)$ and integrate over the electronic coordinate r . This leads to the usual time-dependent Schrödinger equation for the selected coupled electronic states:

$$i \frac{\partial}{\partial t} \begin{pmatrix} \chi_1 \\ \chi_2 \\ \chi_3 \\ \vdots \end{pmatrix} = \begin{pmatrix} T_{\text{nuc}} + V_1 & -\mu_{12}\epsilon(t) & -\mu_{13}\epsilon(t) & \dots \\ -\mu_{12}\epsilon(t) & T_{\text{nuc}} + V_2 & -\mu_{23}\epsilon(t) & \dots \\ -\mu_{13}\epsilon(t) & -\mu_{23}\epsilon(t) & T_{\text{nuc}} + V_3 & \dots \\ \vdots & \vdots & \vdots & \ddots \end{pmatrix} \begin{pmatrix} \chi_1 \\ \chi_2 \\ \chi_3 \\ \vdots \end{pmatrix}\quad (3)$$

with the kinetic Hamiltonian T_{nuc} , the Born–Oppenheimer potentials V_i and the dipole coupling which is treated semiclassically with the transition dipole moment μ_{ij} times the electric field $\epsilon(t)$. μ_{ij} depends on the internuclear separation and on the angle between the molecular and the laboratory frames. The transition dipole moment is a vector defined in the molecular frame. We project the total vector for a given alignment angle onto the polarization axis defined in the laboratory frame. For the nuclear quantum dynamics we used this projection. The time-dependent Schrödinger equation for the nuclei (Eq. (3)) is solved numerically on a one-dimensional grid with the split operator scheme [34]. For the D_2 calculations we used a spatial grid with 1200 points ranging from 0.25 to 13.23 Å. The nuclear wavefunctions were propagated for 23 fs with a time step of 0.0096 fs. The CO^+ calculations were performed on a spatial grid with 1200 points ranging from 0.5 to 10.0 Å. For the coupled electron and nuclear dynamics, the nuclear wavefunctions were propagated for 24 fs with a time step of 0.0096 fs.

The derived total nuclear wavefunction $\chi_{\text{tot}} = (\chi_1, \chi_2, \chi_3, \dots)$ is a multi-dimensional vector, spanned by the coupled wavefunctions. Their square gives the probability density of the nuclei as a function of the nuclear coordinates R .

With the help of χ_{tot} the electronic density $\rho(r_1, t; R(t))$ is expressed as a function of the electronic coordinate r_1 and time t . The total molecular wavefunction is integrated over the nuclear and over the $N - 1$ electronic coordinates (with N the total number of electrons), thereby extracting explicitly the time dependence of the electronic wavefunctions:

$$\begin{aligned}\rho(r_1, t; R(t)) &= \int \Psi_{\text{mol}}^* \Psi_{\text{mol}} dR dr_2, \dots, dr_N \\ &= \sum_{i=1}^k a_i(t)^2 |\varphi_i(r_1, t_0; R(t))|^2 \\ &+ \sum_{i=1}^k \sum_{j>i}^k 2\text{Re}\{ \langle \chi_i(R, t) | \chi_j(R, t) \rangle_R \varphi_i(r_1, t_0; R(t)) \\ &\quad \times \varphi_j(r_1, t_0; R(t)) e^{-i\Delta E_{ij}(R(t))\Delta t + \phi(t-\Delta t)} \}\end{aligned}\quad (4)$$

where $\rho(r_1, t; R(t))$ indicates the parametric dependence of the electron density on the nuclear coordinate R , with $R(t) = \langle \chi_{\text{tot}}(R, t) | R | \chi_{\text{tot}}(R, t) \rangle$ which is the total expectation value of the internuclear distance of the nuclear wavepacket [11]. The coefficients $a_i(t) = \sqrt{\langle \chi_i(t) | \chi_i(t) \rangle_R}$ and $a_i^2(t)$ trace the population evolution of the electronic states, $\langle \chi_i(t) | \chi_j(t) \rangle_R$ is the interference term and $\Delta E_{ij}(t) = E_j(t) - E_i(t)$ the energy difference between the electronic states i and j . k is the total number of included electronic states. The electronic wavefunctions $\varphi_i(r, t_0; R(t))$ are represented as Slater determinants. At $t = 0$ they are completely real wavefunctions as calculated from quantum chemistry. They will oscillate through phase space with a velocity given by their eigenenergies.

The electron density of the electronic state i is given by $|\varphi_i(r_1, t_0; R(t))|^2 = \sum_{n=1}^m c_n^i |\zeta_n(r_1, t_0; R(t))|^2$, with c_n^i the occupation number of the molecular orbital ζ_n in the electronic state i and the sum is over all occupied orbitals. The time evolution of the electronic wavepacket is defined by the last term of Eq. (4) and is calculated by propagation in the eigenstate basis. The coupling of the fast electron to the slower nuclear dynamics enters through the time-dependent population $a_i(t)^2$, through the interference term $\langle \chi_i(t) | \chi_j(t) \rangle_R$, which weights the degree of electronic coherence $\langle \varphi_i(r_1, t_0; R(t)) | \varphi_j(r_1, t_0; R(t)) \rangle e^{-i\Delta E_{ji}(R(t))\Delta t + \phi(t-\Delta t)}$ induced in the molecular system. The phase factor $e^{-i\Delta E_{ji}(R(t))\Delta t + \phi(t-\Delta t)}$ in Eq. (4) has to be calculated recursively to retain the memory of the progressing electronic phase evolution during the propagation of the nuclear wavepackets. This is necessary as we need the absolute phase factor in Eq. (4), which is multiplied by the calculated (completely real) electronic wavefunctions at each time step of the nuclear wavepacket propagation. Here, $\phi(t - \Delta t)$ is the absolute phase of the previous time step needed for the recursive calculation. Moreover this procedure allows us to adjust the time step (Δt in Eq. (4)) to the much faster electron dynamics. We used a one-hundredth of the time step applied in the nuclear dynamics. For $E_j(t)$ we take the eigenenergy at time t at $R(t)$. This approximation is justified as the nuclear wavepackets, produced by ultrashort laser pulses, are highly localized and the energy values corresponding to the faster and slower components of the nuclear wavepackets compensate each other. Note, the time-dependence of $E_j(t)$ can lead to a change of the group velocity of the electronic wavepacket. In case non-adiabatic coupling terms are needed to describe the system dynamics, they can be included according to the method published in [35].

From Eq. (4) it is evident that two terms, the overlap of the nuclear wavepackets propagating on different potential energy surfaces and the product of the different electronic wavefunctions are important for the electronic coherence and thus for the survival of the electronic wavepacket. If one of the terms in the double sum vanish the electron dynamics collapses. These terms also play an important role in the comparison of the electron localization in both molecules. In case one of the nuclear wavepacket separates during the propagation only the part, relevant for the described dissociative process, has to be included.

Fourier-transformation of the total nuclear wavefunction after the dissociation gives the momentum spectrum of the molecular system. It can be used to calculate the momentum distribution for the individual fragments, as both nuclei are accelerated during the dissociation with the identical force but have different masses. The kinetic energy spectra for given fragments can be obtained from their momentum distribution. Thus the kinetic energy spectrum will reflect contributions from all involved electronic states with their specific dissociation dynamics.

5. Theoretical results

5.1. Nuclear dynamics and kinetic energy spectra

For our analysis, we first have to decide, which electronic states should be included in the calculation. In the case of D₂⁺ this is trivial under the current laser conditions, here only two electronic states can interact through the light field. The PES for the D₂⁺ electronic ground state (X²Σ_g⁺) and the repulsive A²Σ_u⁺ state have been calculated with the quantum chemistry package Molpro [36] on the CASSCF(1,2)/6-311++G** level of theory (see Fig. 1a). The D₂⁺ ions are taken to be aligned along the laser polarization axis in accordance with the maxima found in the experimental ionic fragment distribution. The kinetic energy spectrum derived from the nuclear dynamics shows only one broad contribution produced by recollision excitation between 3 and 8.0 eV in good agreement with the

experimental result. The experimentally observed spectrum between 0 and 2.0 eV originates from bond softening [8,37] and is not considered in the theoretical treatment.

In case of CO⁺ the choice of the electronic states is more demanding and guidance from the experiment is needed. Selection criteria are the energy distribution of the recolliding electron and the kinetic energy of the ionic fragments (e.g. C⁺ ions from the dissociation of CO⁺ into C⁺ + O). The first criterium defines the upper energetic limit for the excited states participating in the dissociative ionization. The cut-off energy for this excitation for the present laser parameters is about 13 eV (3.17 U_p where U_p is the ponderomotive potential). Therefore the PES for the CO electronic ground state, the first three ²Σ states and the first six ²Π states for the CO⁺ molecular ion (Fig. 1b) are calculated with the quantum chemistry package Molpro [36] on the CASSCF(6,12)/aug-cc-pVQZ and CASSCF(5,12)/aug-cc-pVQZ level of theory. This selection includes the highest lying σ and π electrons in the active space for the electron correlation. From the reachable excited state manifold we chose three potential curves to represent the induced dissociative dynamics resulting in the observed asymmetry and kinetic energy spectrum of the ejected ionic fragments. A further selection criterium was that all transitions among the selected states were allowed. We performed test calculations by exchanging the electronic states. From comparison with the experimental kinetic energy spectrum we could deduce that the C²Σ⁺ and H²Π states are needed, the C state as a weakly bound state to obtain the structure in the low kinetic energy spectrum and the H state, as the first and only reachable state leading to the C(³P) + O(⁴S) channel, to allow localization of the electron density also on the C-atom (delivering O⁺ fragments). The E²Π state is included to mimic the manifold of similar repulsive states. Exchange of this state with any other state in the reachable energetic region does not change neither the underlying mechanism nor the features of the kinetic energy spectrum. For the recollision excitation we assume a gaussian energy distribution for the returning electron performing the excitation likewise an ultrashort electric light field and start with a 55:38:7 distribution of the states involved (ordered in increasing energy). This population distribution was chosen as it delivers the experimentally observed ratio between C⁺ and O⁺ fragments. Whether the initial population of the excited states caused by the recollision is slightly dependent on the CEP or not is an open question, but its calculation is currently out of scope for larger molecules [9]. Multiple recollisions of the ejected electron from subsequent half-cycles are less probable under the current laser conditions and are thus neglected in the calculations [33,38].

The CO⁺ ions are taken to be aligned at an angle of 45° to the laser polarization, allowing on one hand all transitions between the Σ and Π states. On the other hand the 45° orientation coincides with the angle for the maximum number of experimentally detected ionic fragments. Field-free rotation is neglected in the calculations as it takes place on a much longer timescale (approx. 8.5 ps for a full rotation of CO at its equilibrium distance). Also dynamic alignment before dissociation induced by the laser field is neglected because of the extremely short pulse duration used in the experiments on CO (4 fs).

The kinetic energy spectrum for the C⁺ ions derived from the nuclear dynamics is shown in Fig. 3b and is in reasonable qualitative agreement with the experimental data supporting again the selection made for the representative states. On the basis of these results, we can explain the origin of the observed energy distribution. The low kinetic energy spectrum (0.15–1.5 eV) arises from the dynamics on the weakly bound C²Σ⁺ state and the spectrum in the range between 2.0 and 2.8 eV from the purely repulsive E²Π state. Both states correlate with the second dissociation channel (C(²P) + O(¹D)). The high energy spectrum reflects the dynamics of the second repulsive H²Π state correlating with the third

reaction channel ($C(^3P) + O(^4S)$). The reason why this channel, leading to O^+ fragments, is observable in the recorded C^+ signal lies in the quantum nature of the nuclear wavefunction involved and was explained in Section 4. The structure in the low kinetic energy spectrum follows from interference effects in the nuclear wavepacket on the $C^2\Sigma^+$ state and can also be seen in the experimental spectrum. This interference appears because the recollision excitation produces a high energy wavepacket consisting of both bound and continuum vibrational states on the $C^2\Sigma^+$ surface. During the break-up of CO^+ the bound vibrational states are trapped in the potential well and interfere with the outgoing part of the wavepacket (see Fig. 5). The temporal evolution of the interference pattern can be directly connected to the vibrational levels of the $C^2\Sigma^+$ state (likewise demonstrated in Ref. [39] for D_2^+). The kinetic energy spectrum of the O^+ fragments (not shown here) reveals similar features.

The minor route of laser induced excitation from low lying bound electronic states $X^2\Sigma^+$ and $A^2\Pi$ to the dissociative states of CO^+ that was observed in the experiments using circular polarization (CP) was also included in the calculations. Fig. 3b (LC) shows the resulting kinetic energy spectrum. Only small contributions are recognizable in the kinetic energy ranges 0.15–1.5 eV and 2.0–2.5 eV (not visible within the graphical resolution of the figure).

5.2. Electron localization and asymmetry

The temporal evolution of the electronic state population during the laser pulse interaction is shown in Fig. 6a and c for both molecules. In the case of D_2^+ the nuclear dynamics starts in the $A^2\Sigma_u^+$ state prepared after the recollision excitation event. Here the nuclear dynamics is fast enough to reach the region where the energy difference between the $X^2\Sigma_g^+$ and $A^2\Sigma_u^+$ state comes into resonance with the light field. As a result, we observe a strong molecule light interaction with a large population exchange, nearly leading to a population inversion. Almost the same population transfer is found when the CEP is flipped by π (see Fig. 6a). Contrarily, in CO^+ the population of the individual states is mirrored when the CEP is flipped by π . Moreover only a weak coupling between the electronic states is achieved because the conditions for resonance are never fulfilled (see Fig. 6c).

In Fig. 6b and d we show the magnitudes derived from the electron density, which visualize the electron wavepacket motion and are connected to the experimentally observed asymmetry (see Eq. (1)). In D_2^+ we plotted the asymmetry in the electron density A

$$A = \frac{P_{\text{up}} - P_{\text{down}}}{P_{\text{up}} + P_{\text{down}}} \quad (5)$$

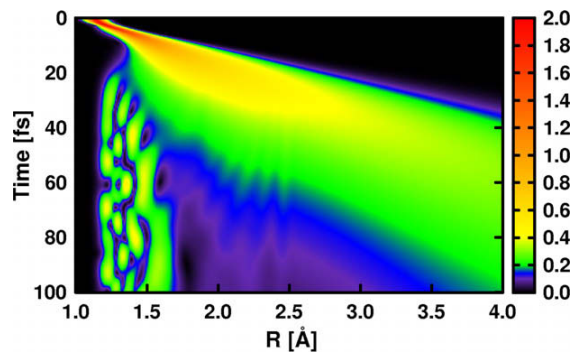


Fig. 5. Time evolution of the probability amplitude of the nuclear wavepacket in the $C^2\Sigma^+$ state of CO^+ as a function of the internuclear distance.

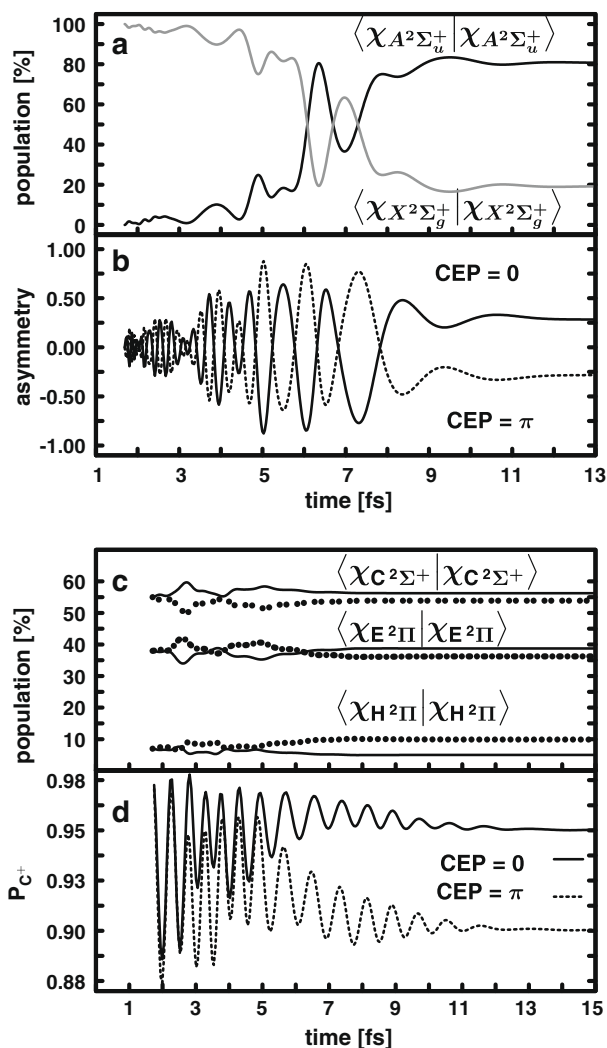


Fig. 6. (a) Time-dependent population of the $X^2\Sigma_g^+$ and $A^2\Sigma_u^+$ state of D_2^+ during the dissociation. (b) Temporal evolution of the asymmetry of D_2^+ starting from the time of recollision (solid: CEP = 0; dotted: CEP = π). (c) Time-dependent populations of the $C^2\Sigma^+$, $E^2\Pi$ and $H^2\Pi$ states of CO^+ after recollision excitation (solid: CEP = 0; dotted: CEP = π). (d) Temporal evolution of the probability measuring a C^+ fragment P_C^+ for the dissociative ionization of CO^+ after recollision (solid: CEP = 0; dotted: CEP = π).

directly connected to the experimentally measured asymmetry, with P_{up} and P_{down} the probability density to find the electron on the upper or lower D atom, respectively, given by

$$P_{\text{up}} = \int_{x_{\text{min}}}^{x_{\text{max}}} dx \int_{y_{\text{min}}}^{y_{\text{max}}} dy \int_{z_{\text{min}}}^0 dz |\varphi_{\text{tot}}(r, t_f; R(t_f))|^2 \quad (6)$$

$$P_{\text{down}} = \int_{x_{\text{min}}}^{x_{\text{max}}} dx \int_{y_{\text{min}}}^{y_{\text{max}}} dy \int_0^{z_{\text{max}}} dz |\varphi_{\text{tot}}(r, t_f; R(t_f))|^2 \quad (7)$$

The overall dynamics of the asymmetry in D_2^+ (Fig. 6b) results from a competition between the influence of the light pulse, the time evolution of the linear combination which oscillates with $\Delta E_{ij}(t)$ and the interference term of the nuclear wavefunctions, which weighs the degree of electronic coherence. During the dissociation the amplitude of the oscillation increases as the two states involved couple most efficiently. The electron dynamics stops when the two states become degenerate. By flipping the CEP by π the evolution of

the asymmetry is exactly mirrored. The maximum value for the resulting asymmetry is around 0.2 and thus close to the experiment.

In case of CO⁺ the definition of the asymmetry is slightly more complex. Here the experimentally measured asymmetry arises from the ensemble of randomly oriented CO molecules. Thus P_{up} and P_{down} , respectively, are assigned to the different orientations. From both orientations C⁺ and O⁺ fragments can be detected and the asymmetry cannot be derived directly from the electron density of a single molecule with only one specific orientation. In our calculations we have direct access to the probability $P_C^+(t)$ of measuring a C⁺ fragment for a given orientation. This probability is given by

$$P_C^+(t) = \int_{x_{\min}}^{x_{\max}} dx \int_{y_{\min}}^{y_{\max}} dy \int_{z_{\min}}^0 dz \rho(r_1, t; R(t)) \quad (8)$$

where x, y and z refer to the molecular frame with z along the molecular axis and the O-Atom oriented along negative z -values. Now the CEP dependent asymmetry as observed in the experiment can be approximated by the final $P_C^+(t)$ values from two different orientations.

The electron dynamics reflected in $P_C^+(t)$ (e.g. solid curve in Fig. 6d) results like in D₂⁺, but only in the first 6 fs, from a competition between the influence of the light pulse, the time evolution of the linear combination and the interference term of the nuclear wavefunctions. As soon as the light induced population transfer between the electronic states stops (approximately after 8 fs, see Fig. 6c), the oscillation in $P_C^+(t)$ decreases rapidly converging after 12 fs to its final value. Responsible for the decay is the reduced overlap of the superimposed electric wavefunctions. This effect can be visualized by the molecular orbitals which discriminate the different Slater determinants and become soon located on the two different nuclei during the dissociation (see Fig. 7b). Therefore the term containing the overlap of the Slater determinants ($\varphi_i(r_1, t; R)\varphi_j(r_1, t; R)$ see Eq. (4)) becomes zero. Consequently, the last term of Eq. (4) vanishes and with it the dynamics of the electronic linear combination. The damping of the oscillations in $P_C^+(t)$ reflects the decay of the initially prepared electronic wavepacket. The probability $P_C^+(t)$ upon the break up of the molecule is given by the final population distribution of the coupled reaction channels leading either to C⁺ or O⁺ fragments. This ratio is steered very precisely by the CEP of ultrashort laser pulses. A shift of the CEP by π while keeping the molecular orientation leads to a different result (dotted curve in Fig. 6d). Changing the orientation of the molecule by 180° is equal to shifting the CEP by π as the transition dipole moment changes the sign. Thus in practise, the CEP dependent asymmetry in the dissociation step can be calculated by $P_C^+(t)$ for two CEP values shifted by π . The maximum value for the resulting asymmetry due to the electron localization is around 0.03, but is not directly comparable to the experimental values as the ionization has significant contributions to the total asymmetry [1].

5.3. Mechanisms for electron localization

Comparison of the attosecond control mechanisms for electron localization in both molecules shows three major differences. The first one occurs already in the preparation step. In D₂⁺ the superposition of the electronic states is created by the interaction with the light pulse. Thus the sign of the initial superposition is directly controlled by the CEP. Consequently, the electronic wavepackets prepared with opposite CEP values show already from the beginning exactly mirrored asymmetry values. In the case of CO⁺, the electron localization dynamics is triggered by the recollision excitation. Thus the oscillation in $P_C^+(t)$ for the different CEP values is prepared and proceeds almost in phase in the beginning of the dissociation and is controlled later by the laser pulse interaction. As a

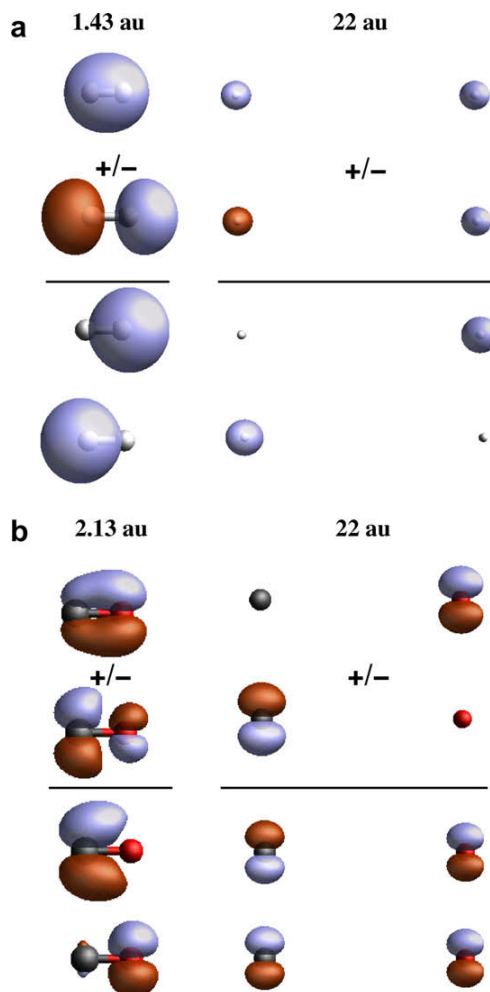


Fig. 7. (a) σ^- , σ^+ -orbitals of the D₂⁺ molecule at internuclear distances 1.43 (left) and 22 au (right). The solid line separates the initial orbitals (upper half) from the calculated linear combinations of these orbitals (lower half). The positive linear combination is plotted first. For both internuclear distances the linear combinations are localized on one atomic center. (b) π_x^- , π_x^+ -orbitals of the CO⁺ molecule at internuclear distances 2.13 (left) and 22 au (right). The solid line separates the initial orbitals (upper half) from the calculated linear combinations of these orbitals (lower half). The positive linear combination is plotted first. For internuclear distances around the minimum geometry (left) the linear combination can localize the electron density on one atomic center. For larger distances (right) the linear combinations are delocalized.

second difference the electron localization in D₂⁺ shows much larger amplitudes compared to CO⁺, because only for the lighter molecule the nuclear dynamics is fast enough to hit the resonance with the laser frequency.

The third major difference lies in the ending of the electron dynamics. In the case of the D₂⁺ molecule the dynamics only stops when the two electronic states involved become degenerate and consequently the exponent in Eq. (4) becomes zero. Simultaneously, the dissociation process is completed and the degree of electron localization is determined, beside the mixing ratio of the electronic states, by the final phase of the exponential factor. For the CO⁺ molecule the dynamics stops because the overlap of the electronic wavefunctions becomes zero as soon as the outer orbitals localize on one atomic center. This mechanism is shown in Fig. 7. For internuclear distances around the minimum geometry the valence molecular orbitals of both molecules are delocalized

over both centers (Fig. 7a and b left side above solid line). By forming the positive or the negative linear combination of the corresponding Slater determinants, the electron density in both cases is localized on one atom (Fig. 7a and b, left side below solid line). For larger internuclear distances the situation changes completely (Fig. 7a and b, right). In the case of the homonuclear D_2^+ the two orbitals are still delocalized over the molecule (Fig. 7a right side above solid line) and the linear combination still localizes the electron density (Fig. 7a right side below solid line). The same effect will appear for its isotopologues HD^+ and HD_2^+ as the electronic structure does not change compared to D_2^+ . For the heteronuclear CO^+ the molecular orbitals localize during the dissociation (Fig. 7b right side above solid line). Thus the electron density of the superposition state delocalizes (Fig. 7b right side below solid line). Consequently, the degree of electron localization is not determined by the phase evolution (second term of Eq. (4)) but by the populations of the electronic states which localize the electron on one or the other nucleus in their asymptotic limits (e.g. C^+ or O^+ channels). These populations are controllable by the CEP on the attosecond timescale.

6. Conclusion

For two different types of molecules, we compared the attosecond control mechanism of electron localization observed in the dissociative ionization with intense ultrashort phase-stabilized light fields. We chose the molecules D_2 and CO , which can be regarded as representatives for homo- and heteronuclear diatomics. In addition these molecules differ in the complexity of the electronic structure and most notably for both molecules experimental data were available to us [1,6]. To follow the process of electron localization during the dissociation, we applied our method for the simultaneous treatment of the coupled nuclear and electron wavepacket dynamics. Our analysis revealed significant differences in the attosecond control mechanisms. They occur already in the formation of the electronic wavepacket. In D_2^+ the electronic wavepacket is created exclusively through the light field induced coupling of only two electronic states. Thus the sign of the initial superposition is defined and controllable by the CEP. In CO^+ it is essential that the electronic wavepacket is already formed in the recollision step. Here the CEP control arises from the subsequent interaction of the laser pulse with the previously prepared electronic wavepacket and is due to the interplay of the signs of the light field and the transition dipole moments. The explanation for the differences in the preparation step can be found in the electronic structure of both molecules. In the multi-electron system many close lying electronic states exist, which are simultaneously populated by recollision excitation. We also observed differences in the electron dynamics during the dissociation. Crucial for driving the electron motion in D_2^+ is that the oscillation frequency of the electronic wavepacket comes into resonance with the laser frequency. As this never happens in the case of CO^+ the decay of the electronic wavepacket is much faster and the dominant feature. Decisive for the final degree of localization is again the electronic structure of the molecules. In D_2^+ the structure of the molecular orbitals hold the localization of the electron density in the superposition upon the break up of the molecule. This is not possible for CO^+ . Here, the electronic structure results in a delocalized electron density. For the final asymmetry we can state that for D_2^+ the phase of the superposition (exponent in Eq. (4)) imprinted by the CEP defines its final value. In the case of CO^+ the asymmetry arises from the CEP controlled population ratio between the coupled reaction channels leading either to C^+ or O^+ . It should be noted that the experimentally observed asymmetry in the case of CO is also affected by the ionization in a few-cycle phase-stable laser field

as described in [1]. With the current experimental data it is not possible to distinguish clearly between contributions from the ionization and laser-induced electron localization mechanisms in CO . Future studies are aimed into this direction. We have shown that electron localization is not restricted to one-electron systems but can be found also in multi-electron systems and understood by our theoretical calculations. Moreover, we can deduce that multiple molecular dependent pathways exist to realize electron localization. However, it will still be a great challenge to guide and stabilize an electronic wavepacket inside a given molecule to control the outcome of a reaction.

Acknowledgments

We acknowledge F. Krausz and M.J.J. Vrakking for support and fruitful discussion. We are grateful for support by the DFG via the Emmy-Noether program and the Cluster of Excellence: Munich Center for Advanced Photonics (<http://www.munich-photonics.de>).

References

- [1] I. Znakovskaya, P. von den Hoff, S. Zherebtsov, A. Wirth, O. Herrwerth, M. Vrakking, R. de Vivie-Riedle, M. Kling, Attosecond control of electron dynamics in carbon monoxide, *Phys. Rev. Lett.* 103 (2009) 103002.
- [2] P. Nuernberger, G. Vogt, T. Brixner, G. Gerber, Femtosecond quantum control of molecular dynamics in the condensed phase, *Phys. Chem. Chem. Phys.* 9 (2007) 2470.
- [3] T. Brixner, G. Gerber, Quantum control of gas-phase and liquid-phase femtochemistry, *Chem. Phys. Chem.* 4 (2003) 418.
- [4] F. Krausz, M. Ivanov, Attosecond physics, *Rev. Mod. Phys.* 81 (2009) 163.
- [5] R. Kienberger, M. Uiberacker, M.F. Kling, F. Krausz, Attosecond physics comes of age: from tracing to steering of electrons at sub-atomic scales, *J. Mod. Opt.* 54 (2007) 1985.
- [6] M.F. Kling, C. Siedschlag, A.J. Verhoef, J.I. Khan, M. Schultze, T. Uphues, Y. Ni, M. Uiberacker, M. Drescher, F. Krausz, M.J.J. Vrakking, Control of electron localization in molecular dissociation, *Science* 312 (2006) 246–248.
- [7] M.F. Kling, C. Siedschlag, I. Znakovskaya, A.J. Verhoef, S. Zherebtsov, F. Krausz, M. Lezius, M.J.J. Vrakking, Strong-field control of electron localization during molecular dissociation, *Mol. Phys.* 106 (2008) 455.
- [8] V. Roudnev, B. Esry, I. Ben-Itzhak, Controlling HD^+ and H_2^+ dissociation with the carrier-envelope phase difference of an intense ultrashort laser pulse, *Phys. Rev. Lett.* 93 (16) (2004) 163601.
- [9] S. Gräfe, M.Y. Ivanov, Effective fields in laser-driven electron recollision and charge localization, *Phys. Rev. Lett.* 99 (2007) 163603.
- [10] X.M. Tong, C.D. Lin, Dynamics of light-field control of molecular dissociation at the few-cycle limit, *Phys. Rev. Lett.* 98 (2007) 123002.
- [11] D. Geppert, P. von den Hoff, R. de Vivie-Riedle, Electron dynamics in molecules: a new combination of nuclear quantum dynamics and electronic structure theory, *J. Phys. B: At. Mol. Opt. Phys.* 41 (2008) 074006.
- [12] A.D. Bandrauk, S. Chelkowski, H.S. Nguyen, Attosecond localization of electrons in molecules, *Int. J. Quant. Chem.* 100 (6) (2004) 834–844.
- [13] A.D. Bandrauk, S. Chelkowski, P.B. Corkum, J. Manz, G.L. Yudin, Attosecond photoionization of a coherent superposition of bound and dissociative molecular states: effect of nuclear motion, *J. Phys. B: At. Mol. Opt. Phys.* 42 (2009) 134001.
- [14] H. Lippert, J. Manz, M. Oppel, G.K. Paramonov, W. Radloff, H.-H. Ritze, V. Stert, Control of breaking strong versus weak bonds of $BaFCH_3$ by femtosecond IR + VIS laser pulses: theory and experiment, *Phys. Chem. Chem. Phys.* 6 (2004) 4283–4295.
- [15] B. Amstrup, N.E. Henriksen, Control of HOD photodissociation dynamics via bond-selective infrared multiphoton excitation and a femtosecond ultraviolet laser pulses, *J. Chem. Phys.* 97 (1992) 8285.
- [16] I. Thanopoulos, M. Shapiro, Enhanced selectivity and yield in multichannel photodissociation reactions: application to CH_3I , *J. Chem. Phys.* 125 (2006) 133314.
- [17] J.H. Posthumus, The dynamics of small molecules in intense laser fields, *Rep. Prog. Phys.* 67 (2004) 623.
- [18] C. Guo, Holding molecular dications together in strong laser fields, *Phys. Rev. A* 73 (2006) 041401.
- [19] A.S. Alnaser, C.M. Maharjan, X.M. Tong, B. Ulrich, P. Ranitovic, B. Shan, Z. Chang, C.D. Lin, C.L. Cocke, I.V. Litvinyuk, Effects of orbital symmetries in dissociative ionisation of molecules by few-cycle laser pulses, *Phys. Rev. A* 71 (2005) 031403.
- [20] M. Schultze, E. Goulielmakis, M. Uiberacker, M. Hofstetter, J. Kim, D. Kim, F. Krausz, U. Kleineberg, Powerful 170-attosecond XUV pulses generated with few-cycle laser pulses and broadband multilayer optics, *New J. Phys.* 9 (2007) 243.
- [21] M.J.J. Vrakking, An iterative procedure for the inversion of two-dimensional ion/photoelectron imaging experiments, *Rev. Sci. Instr.* 72 (2001) 4084.

- [22] S. Micheau, Z. Chen, A.T. Le, J. Rauschenberger, M.F. Kling, C.D. Lin, Accurate retrieval of target structures and laser parameters of few-cycle pulses from photoelectron momentum spectra, *Phys. Rev. Lett.* 102 (2009) 073001.
- [23] K.C. Kulander, Time-dependent Hartree–Fock theory of multiphoton ionization: helium, *Phys. Rev. A* 36 (6) (1987) 2726–2738.
- [24] E. Runge, E.K.U. Gross, Density-functional theory for time-dependent systems, *Phys. Rev. Lett.* 52 (12) (1984) 997.
- [25] T. Klamroth, Laser-driven electron transfer through metal–insulator–metal contacts: time-dependent configuration interaction singles calculations for a Helium model, *Phys. Rev. B* 68 (2003) 245421.
- [26] N. Rohringer, A. Gordon, R. Santra, Configuration-interaction-based time-dependent orbital approach for ab initio treatment of electronic dynamics in a strong optical laser field, *Phys. Rev. A* 74 (2006) 043420.
- [27] T. Kato, H. Kono, Time-dependent multiconfiguration theory for electronic dynamics of molecules in an intense laser field, *Chem. Phys. Lett.* 392 (2004) 533.
- [28] J. Zanghellini, M. Kitzler, T. Brabec, A. Scrinzi, Testing the multi-configuration time-dependent Hartree Fock method, *J. Phys. B: At. Mol. Opt. Phys.* 37 (2004) 763.
- [29] A.I. Kuleff, J. Breidbach, L.S. Cederbaum, Multielectron wave-packet propagation: general theory and application, *J. Chem. Phys.* 123 (2005) 044111.
- [30] I. Barth, J. Manz, Y. Shigeta, K. Yagi, Unidirectional electronic ring current driven by a few cycle circularly polarized laser pulse: quantum model simulations for Mg–Porphyrin, *J. Am. Chem. Soc.* 128 (2006) 7043–7049.
- [31] M. Nest, The multi-configuration electron-nuclear dynamics method, *Chem. Phys. Lett.* 472 (2009) 171.
- [32] K. Yagi, K. Takatsuka, Nonadiabatic chemical dynamics in an intense laser field: electronic wave packet coupled with classical nuclear motions, *J. Chem. Phys.* 123 (2005) 224103.
- [33] H. Niikura, F. Légaré, R. Hasbani, A.D. Bandrauk, M.Y. Ivanov, D.M. Villeneuve, P.B. Corkum, Sub-laser-cycle electron pulses for probing molecular dynamics, *Nature* 417 (2002) 917.
- [34] C. Leforestier, R.H. Bisseling, C. Cerjan, M.D. Feit, R. Friesner, A. Gulberg, A. Hammerich, G. Jolicard, W. Karrlein, H.-D. Meyer, N. Lipkin, O. Roncero, R. Kosloff, A comparison of different propagation schemes for the time dependent Schrödinger equation, *J. Comp. Phys.* 94 (1991) 59–80.
- [35] L.S. Cederbaum, Born-oppenheimer approximation and beyond for time-dependent electron processes, *J. Chem. Phys.* 128 (2008) 124101.
- [36] H.-J. Werner, P.J. Knowles, R. Lindh, F.R. Manby, M. Schütz, et al., Molpro, Version 2006.1, A Package of Ab Initio Programs, 2006.
- [37] V. Roudnev, B.D. Esry, HD⁺ in a short strong laser pulse: practical consideration of the observability of carrier-envelope phase effects, *Phys. Rev. A* 76 (2007) 023403.
- [38] A.S. Alnaser, X.M. Tong, T. Osipov, S. Voss, C.M. Maharjan, P. Ranitovic, B. Ulrich, B. Shan, Z. Chang, C.D. Lin, C.L. Cocke, Routes to control of H₂ coulomb explosion in few-cycle laser pulses, *Phys. Rev. Lett.* 93 (2004) 183202.
- [39] U. Thumm, T. Niederhausen, B. Feuerstein, Time-series analysis of vibrational nuclear wave-packet dynamics in D₂⁺, *Phys. Rev. A* 77 (2008) 063401.

Paper IV

Field-free orientation of CO molecules by femtosecond two-color laser fields.

De, S., Znakovskaya, I., Ray, D., Anis, F., Johnson, N. G., Bocharova, I. A., Magrakvelidze, M., Esry, B. D., Cocke, C. L., Litvinyuk, I. V. & Kling, M. F.

Phys. Rev. Lett. **103**, 153002 (2009).



Field-Free Orientation of CO Molecules by Femtosecond Two-Color Laser Fields

S. De,¹ I. Znakovskaya,² D. Ray,¹ F. Anis,¹ Nora G. Johnson,¹ I. A. Bocharova,¹ M. Magrakvelidze,¹ B. D. Esry,¹
C. L. Cocke,¹ I. V. Litvinyuk,^{1,†} and M. F. Kling^{1,2,*}

¹*J.R. Macdonald Laboratory, Physics Department, Kansas State University, Manhattan, Kansas 66506, USA*

²*Max-Planck Institute of Quantum Optics, Hans-Kopfermann-Strasse 1, 85748 Garching, Germany*

(Received 18 July 2009; published 5 October 2009)

We report the first experimental observation of nonadiabatic field-free orientation of a heteronuclear diatomic molecule (CO) induced by an intense two-color (800 and 400 nm) femtosecond laser field. We monitor orientation by measuring fragment ion angular distributions after Coulomb explosion with an 800 nm pulse. The orientation of the molecules is controlled by the relative phase of the two-color field. The results are compared to quantum mechanical rigid rotor calculations. The demonstrated method can be applied to study molecular frame dynamics under field-free conditions in conjunction with a variety of spectroscopy methods, such as high-harmonic generation, electron diffraction, and molecular frame photoelectron emission.

DOI: 10.1103/PhysRevLett.103.153002

PACS numbers: 33.80.-b, 33.80.Wz

Aligned molecules have attracted widespread interest for applications such as ultrafast dynamic imaging [1], molecular tomography [2], and electron diffraction [3]. Molecules have been successfully aligned in one and even three dimensions using strong linearly polarized laser fields [4]. Aligned, but unoriented, gas samples of heteronuclear diatomic molecules, however, suffer from an averaging effect over the two opposite molecular orientations. To overcome this limitation, it is necessary to develop methods for their orientation. While the orientation of polar molecules is possible in strong dc fields (see, e.g., [5]) or by the combination of a laser field and a dc field [6–8], the presence of a strong field may influence the outcome of experiments on oriented molecular targets. It is thus of particular interest to study and implement methods for field-free orientation and its control. In this letter, we report on the nonadiabatic field-free orientation of a heteronuclear diatomic molecule (CO) using a two-color laser field.

The control of molecular alignment can be achieved both adiabatically [9] and nonadiabatically [10]. Nonadiabatic alignment can be used to produce aligned samples of molecules under field-free conditions and, hence, is desirable for some applications. In laser-induced orientation, in addition, a head versus tail order of the molecules is established. Only recently, two groups have demonstrated laser-field-free transient molecular orientation [11,12]. Sakai and co-workers have used a combination of a dc electric field and a laser pulse with adiabatic turn-on and nonadiabatic turn-off (switched laser field) to induce dynamic orientation in OCS molecules, which revives at full rotational periods [11]. Vrakking and co-workers used a hexapole state selector to produce NO molecules in a single quantum state and a combination of a dc field and an intense femtosecond laser field to induce orientation [12] of their samples. Although in both of these cases laser-field-free oriented molecules were obtained at

full rotational revivals, the presence of a dc field was crucial to achieving orientation and might limit the application of these techniques in, e.g., the imaging of low-energy photoelectrons from oriented molecules. Another “all-optical” route to field-free orientation without the necessity of a dc field was suggested by Kanai and Sakai [13] and has been further explored theoretically, most recently by Tehini and Sugny [14] and by Sakai and co-workers [15]. The approach is based on the nonadiabatic excitation of both odd and even angular momentum states with a femtosecond two-color laser field, enabling net macroscopic orientation [16]. So far, the technique has not been experimentally studied.

In this Letter, we describe experiments where an intense two-color laser field

$$E(t) = E_{\omega}(t) \cos(\omega t) + E_{2\omega}(t) \cos(2\omega t + \varphi) \quad (1)$$

with wavelengths 800 and 400 nm corresponding to ω and 2ω and the phase φ was used to control the field-free orientation of carbon monoxide. The degree of orientation was probed by Coulomb explosion imaging. The setup is displayed in Fig. 1. Pulses with 45 fs duration at 800 nm produced from a Ti:sapphire laser were split into a pump and a probe arm of a Mach-Zehnder interferometer. In the pump arm, the second harmonic of 800 nm was created using a 250 μm thick beta barium borate (BBO) crystal. To ensure temporal overlap of the two-colors, two calcite plates of thickness 600 μm were used. Together both the calcite crystals compensate the group delay between the two-colors caused by the BBO crystal while the second calcite plate also serves to adjust the relative phase φ between the two colors of the excitation field. The phase was calibrated by comparison of above-threshold ionization data from Xe to quantitative rescattering theory calculations [17]. A dual $\lambda/2$ plate (which rotates the fundamental and the second-harmonic fields by 90° and

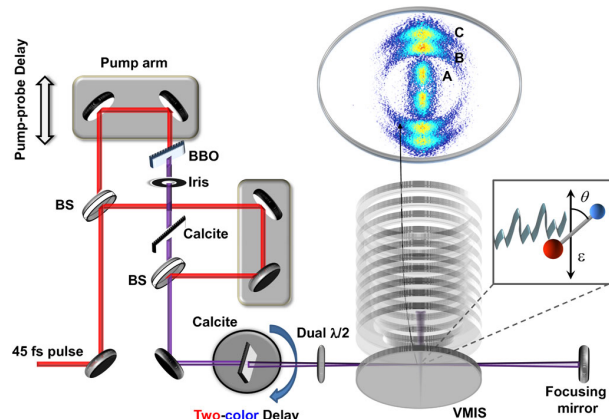


FIG. 1 (color online). Schematic of the experimental setup used to induce and monitor field-free molecular orientation. A, B, and C indicate channels for the formation of C^{2+} ions as described in the text.

180° , respectively) was used to rotate the polarization of all fields to be vertical in the experiment. An iris placed in the pump arm gives control over the intensity of the excitation field. The resulting field-asymmetric two-color excitation pulses (schematically shown for $\varphi = 0$ in the inset of Fig. 1) were focused onto a supersonic jet of CO molecules ($T_{\text{rot}} \approx 60$ K) inside a velocity-map imaging spectrometer (VMIS) by a spherical mirror ($f = 75$ mm) placed at the rear side of the VMIS. The CO molecules were Coulomb exploded at a varying time delay by a single-color (800 nm) laser pulse from the probe arm and the resulting fragment ions were projected by ion optics of the VMIS onto a MCP-phosphor screen assembly. Images were recorded with a CCD camera. Note that a dc field on the ion optics orthogonal to the laser polarization direction was used to image the fragment ions; however, this dc field does not take any role in the orientation of the molecules and could even be made zero for, e.g., the imaging of electrons from oriented molecules by zero-field time-of-flight spectroscopy.

A typical image of C^{2+} ions from the Coulomb explosion of CO recorded in our experiment is shown in Fig. 1. The image shows three main contributions peaked along the vertical laser polarization axis, which we attribute to different channels for the production of C^{2+} , where in addition to C^{2+} a neutral (A), singly charged (B) and doubly charged (C) oxygen is formed. The energy and angular distributions of the fragments can be directly derived from the image after inversion using an iterative inversion procedure [18]. The angle θ is defined as the angle between the momentum of C^{2+} ions and the laser polarization direction. For Coulomb explosion channels (B and C in Fig. 1), we assume the fragmentation occurs along the molecular axis (axial recoil approximation). Within this approximation θ reflects the angle between the molecular axis and the laser polarization as depicted in the inset of Fig. 1.

Figure 2(a) shows a trace of the experimental parameter $\langle \cos^2 \theta_{\text{exp}} \rangle$ versus the two-color pump—Coulomb explosion probe delay time for $\varphi = 0$. The parameter $\langle \cos^2 \theta_{\text{exp}} \rangle$ was obtained by integration over the Coulomb explosion channel B in Fig. 1 corresponding to a kinetic energy range of 10 to 16 eV and reflects the alignment of the molecules. The data were taken for peak intensities of 1.3×10^{14} W/cm 2 for both the 800 and 400 nm pump pulses and 2.4×10^{14} W/cm 2 for the 800 nm probe pulse. No significant dependence of the alignment parameter on the phase φ between the two colors of the pump pulse was found. The alignment parameter $\langle \cos^2 \theta_{\text{exp}} \rangle$ peaks at $T_0 = 0.125$ ps and shows the first two full revivals at $T = T_0 + nT_{\text{rot}} = 8.7$ and 17.3 ps for $n = 1, 2$ in good agreement with the expected rotation time $T_{\text{rot}} = 1/(2B_0c)$ of 8.64 ps (with $B_0 = 1.93$ cm $^{-1}$) [19] for CO and also in good agreement with earlier studies [20]. The alignment curve also shows half-revivals at 4.3 and 12.9 ps. Before interaction with the pump, i.e., at negative delay times, we already find a high value of $\langle \cos^2 \theta_{\text{exp}} \rangle$ of 0.83 (an isotropic angular distribution corresponds to a value of 0.33), which we attribute to additional alignment caused by the linearly polarized probe pulse [21]. The alignment by the probe, however, cannot affect an existing up-down asymmetry in the ion image and therefore does not influence the results of the current studies on molecular orientation.

In addition to the nonadiabatic alignment of CO seen in Fig. 2(a), we investigated the nonadiabatic orientation with the two-color laser field and the possible control of the orientation direction by the phase φ . Along these lines, we

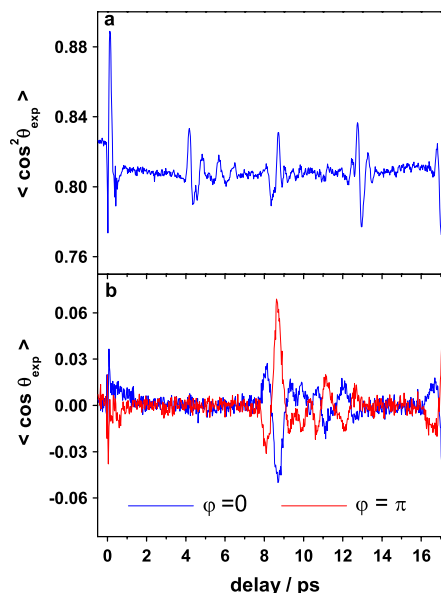


FIG. 2 (color online). Evolution of the (a) alignment parameter $\langle \cos^2 \theta_{\text{exp}} \rangle$ and (b) orientation parameter $\langle \cos \theta_{\text{exp}} \rangle$ with pump probe delay time for two opposite phases φ of the two-color pump.

performed a pump—probe experiment at a fixed delay between the two pulses corresponding to the first full revival of the alignment (at 8.7 ps) and recorded $\langle \cos\theta_{\text{exp}} \rangle$ parameter as a function of the kinetic energy of the resulting C^{2+} fragments and the phase φ .

Figure 3(a) shows the relevant part of the kinetic energy spectrum of recorded C^{2+} ions (obtained by full angular integration) for the Coulomb explosion channels *B* and *C*. Within the axial recoil approximation the directional emission of these fragments may be used to obtain information on the orientation. Figure 3(b) displays the orientation parameter $\langle \cos\theta_{\text{exp}} \rangle$ versus the kinetic energy of the C^{2+} fragments and the phase φ , where nonzero values of $\langle \cos\theta_{\text{exp}} \rangle$ indicate a net macroscopic orientation of the molecular ensemble. An oscillatory behavior of $\langle \cos\theta_{\text{exp}} \rangle$ with φ is seen throughout the displayed kinetic energy spectrum and $\langle \cos\theta_{\text{exp}} \rangle$ changes its sign at every π phase shift between the two colors.

The orientation is effectively controlled by the phase of the two-color laser field. At $\varphi = 0$, $\langle \cos\theta_{\text{exp}} \rangle$ is negative, meaning the C^{2+} ions are emitted preferentially downwards, while at $\varphi = \pi$, $\langle \cos\theta_{\text{exp}} \rangle$ is positive and more C^{2+} ions are emitted upwards. Note that we recorded similar data for O^{2+} fragments, which show $\langle \cos\theta_{\text{exp}} \rangle$ shifted in φ by π relative to the C^{2+} data. This is consistent with the charged C and O fragments of the same molecule being emitted in opposite directions within the axial recoil approximation. At phases of $\varphi = 0$ and $\varphi = \pi$, where $\langle \cos\theta_{\text{exp}} \rangle$ peaks in Fig. 3(b), we have recorded the full time dependence of the orientation parameter. The resulting two curves are shown in Fig. 2(b). No sign of orientation is found at the half revivals of $\langle \cos^2\theta_{\text{exp}} \rangle$ [seen in Fig. 2(a)]. Nonadiabatic field-free orientation manifests itself in Fig. 2(b) in the revivals of $\langle \cos\theta_{\text{exp}} \rangle$ at full rotational periods of CO. In our experiments, we studied the dependence of the degree of orientation on the pump pulse peak intensity and found that orientation decreases rapidly for lower pump intensities.

Our theoretical treatment of the alignment and orientation of CO assumed a quantum mechanical rigid rotor

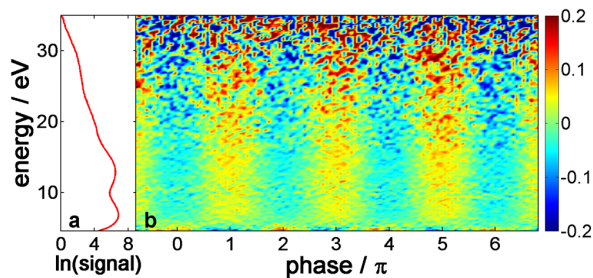


FIG. 3 (color online). (a) Kinetic energy spectrum of C^{2+} ions obtained by full angular integration for $\varphi = 0$ at the first full revival (8.7 ps) of the alignment and (b) map of $\langle \cos\theta_{\text{exp}} \rangle$ at this delay as a function of the C^{2+} kinetic energy and the phase φ of the two-color laser field.

model. In the time-dependent Schrödinger equation for the system,

$$i \frac{\partial}{\partial t} \Psi(\theta, t) = [\mathbf{H}_0 + E(t)V_d(\theta) + E^2(t)V_{\text{pol}}(\theta) + E^3(t)V_{\text{hyp}}(\theta)]\Psi(\theta, t), \quad (2)$$

the interaction with the two-color laser field ($E(t)$) took into account the permanent dipole moment (V_d), dipole polarizability (V_{pol}), and hyperpolarizability (V_{hyp}) contributions as described in Ref. [13] with the parameters taken from [22,23]. The field-free Hamiltonian \mathbf{H}_0 and wave function $\Psi(\theta, t)$ satisfy the relation $\mathbf{H}_0\Psi = [B_0J(J+1) - D_eJ^2(J+1)^2]\Psi$, with J being the orbital angular momentum quantum number and $D_e = 2.79 \times 10^{-10}$ a.u. being the centrifugal distortion constant. We expanded $\Psi(\theta, t)$ on spherical harmonics and solved the resulting coupled differential equations in time using a Crank-Nicolson propagation scheme. To achieve convergence of the alignment and orientation parameters, we used angular momenta up to $J = 100$ and a time step of 0.2 a.u. In order to compare with the experiment, the results were thermally averaged over an initial Boltzmann distribution assuming a temperature of 60 K. We used Gaussian pulses of 45 fs FWHM and a smaller intensity (7×10^{13} W/cm²) than in the experiment to approximately account for volume effects.

Figures 4(a) and 4(b) show the calculated time evolutions of the alignment and orientation parameters with respect to the pump probe delay, respectively. The revival times for $\langle \cos^2\theta \rangle$ and $\langle \cos\theta \rangle$ agree well with the experimental data. The values of the alignment parameter are significantly lower than in the experimental data, which we attributed earlier to alignment by the multiphoton probe in the experiment. The modulation of the $\langle \cos^2\theta \rangle$ amplitude at the half and full revivals is significantly higher than in the experiment. However, we found that this amplitude depends critically on the values of the dipole moment and the polarizability, the latter of which is not well known. The theoretical prediction for the orientation trace is in reasonable agreement with the experimental data. The sign of the orientation is reversed by a change in the phase φ of the two-color laser field as also observed in the experiment. Our calculations show that the permanent dipole of CO contributes very little to the orientation of the molecule as has been indicated in Ref. [14], partly because the dipole moment is very small and partly because the dipole interaction averaged over the fast oscillations of the field vanishes in a many-cycle pulse. It is thus the hyperpolarizability that is responsible for the orientation of CO [14]. Within this model, a phase shift observed in the experiment between the preferential emission of carbon ions in ionization and orientation is in agreement with a positive sign of the hyperpolarizability. Following the statement in Ref. [22] that the hyperpolarizability and the dipole moment of CO exhibit the same sign, our results are in agreement with the dipole of CO being $\text{C}^- - \text{O}^+$ [22].

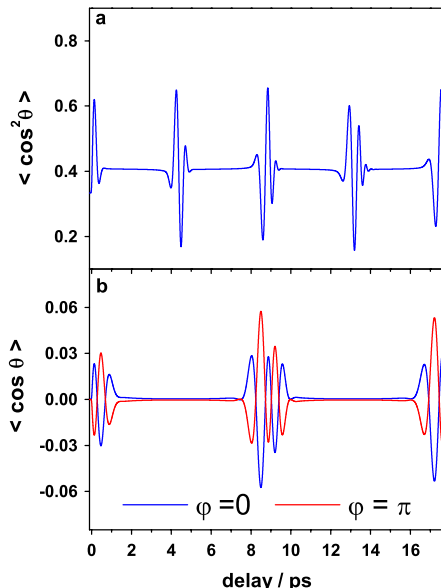


FIG. 4 (color online). Theoretically obtained time evolution of the alignment parameter $\langle \cos^2\theta \rangle$ and the orientation parameter $\langle \cos\theta \rangle$ for the two-color (800 and 400 nm) excitation of CO.

We have also studied the directional emission of C^{2+} ions in the ionization of CO by the two-color laser field. The recorded C^{2+} ions are found to be preferentially emitted in the direction of the electric field vector at a phase of $\varphi = 0$. This finding is consistent with calculations of the ionization of CO [24,25]. The intensity used for the experimental data shown here is, in fact, above the ionization threshold of CO. Note that we do, however, also observe field-free orientation for lower intensities below the ionization threshold of CO.

Significant ionization might lead to depletion of CO molecules in the direction of the electric field vector of the excitation field, corresponding to negative $\langle \cos\theta_{\text{exp}} \rangle$ values at $\varphi = 0$. We do expect orientation created by depletion to peak at the time of temporal overlap (defined as time zero in the experimental traces) between the two-color excitation field and the probe. A close look near $t = 0$ in Fig. 2(b) reveals a temporal shift of 0.125 ps between the temporal overlap of the pump and probe pulses (time zero) and the first peak of the orientation. On this basis we conclude that orientation by ionization depletion is at most minor.

In summary, we have reported on nonadiabatic field-free orientation of a heteronuclear molecule (CO) induced by a strong two-color femtosecond laser field. Rotational revivals of the orientation are found after each full rotational period. At the revivals, an oriented ensemble of heteronuclear molecules in the absence of any external electric field is produced. The approach demonstrated here is applicable for a variety of heteronuclear molecules. These field-free oriented molecules can be used to study angle-differential

properties of heteronuclear molecules, such as various ionization and scattering cross-sections and may also enable applications such as high-harmonic generation and electron diffraction studies from oriented molecules. Theoretical calculations indicate that the hyperpolarizability is responsible for the orientation of CO. Although the degree of orientation found in the present work on CO is rather small, higher degrees of orientation are expected for other systems at similar laser parameters [14]. A subject for further investigations is to apply shaped laser fields or tailored excitation pulse sequences in order to increase the degree of orientation by two-color laser fields.

We acknowledge support by the Chemical Sciences, Geosciences and Biosciences Division of the U.S. Department of Energy. I. Z. and M. F. K. are grateful for support by the DFG via the Emmy-Noether program and the Cluster of Excellence: Munich Center for Advanced Photonics.

*matthias.kling@mpq.mpg.de

†ivl@phys.ksu.edu

- [1] M. Yu Ivanov and Jon P. Marangos, *J. Mod. Opt.* **54**, 899 (2007).
- [2] J. Itatani *et al.*, *Nature (London)* **432**, 867 (2004).
- [3] M. Meckel *et al.*, *Science* **320**, 1478 (2008).
- [4] S. Viftrup *et al.*, *Phys. Rev. Lett.* **99**, 143602 (2007).
- [5] B. Friedrich and D. Herschbach, *Nature (London)* **353**, 412 (1991).
- [6] B. Friedrich and D. Herschbach, *J. Chem. Phys.* **111**, 6157 (1999).
- [7] S. Minemoto *et al.*, *J. Chem. Phys.* **118**, 4052 (2003).
- [8] L. Holmegaard *et al.*, *Phys. Rev. Lett.* **102**, 023001 (2009).
- [9] H. Tanji, S. Minemoto, and H. Sakai, *Phys. Rev. A* **72**, 063401 (2005).
- [10] H. Stapelfeldt and T. Seideman, *Rev. Mod. Phys.* **75**, 543 (2003).
- [11] A. Goban, S. Minemoto, and H. Sakai, *Phys. Rev. Lett.* **101**, 013001 (2008).
- [12] O. Ghafur *et al.*, *Nature Phys.* **5**, 289 (2009).
- [13] T. Kanai and H. Sakai, *J. Chem. Phys.* **115**, 5492 (2001).
- [14] R. Tehini and D. Sugny, *Phys. Rev. A* **77**, 023407 (2008).
- [15] M. Muramatsu, M. Hita, S. Minemoto, and H. Sakai, *Phys. Rev. A* **79**, 011403 (2009).
- [16] M. J. J. Vrakking and S. Stolte, *Chem. Phys. Lett.* **271**, 209 (1997).
- [17] S. Mischeau *et al.*, *Phys. Rev. Lett.* **102**, 073001 (2009).
- [18] M. J. J. Vrakking, *Rev. Sci. Instrum.* **72**, 4084 (2001).
- [19] NIST (<http://webbook.nist.gov>).
- [20] D. Pinkham and R. R. Jones, *Phys. Rev. A* **72**, 023418 (2005).
- [21] I. V. Litvinyuk *et al.*, *Phys. Rev. Lett.* **90**, 233003 (2003).
- [22] K. A. Peterson and T. H. Dunning, Jr., *J. Mol. Struct. (Theochem)* **400**, 93 (1997).
- [23] M. Pecul, *Chem. Phys. Lett.* **404**, 217 (2005).
- [24] A. S. Alnaser *et al.*, *Phys. Rev. A* **71**, 031403 (2005).
- [25] I. Znakovskaya *et al.*, *Phys. Rev. Lett.* **103**, 103002 (2009).

Paper V

Effects of multi orbital contributions in the angular-dependent ionization of molecules in intense few-cycle laser pulses.

von den Hoff, P., Znakovskaya, I., Zherebtsov, S., Kling, M. F. & de Vivie-Riedle, R.

Appl. Phys. B. **98**, 659 (2010).

Effects of multi orbital contributions in the angular-dependent ionization of molecules in intense few-cycle laser pulses

P. von den Hoff · I. Znakovskaya · S. Zherebtsov ·
M.F. Kling · R. de Vivie-Riedle

Received: 26 August 2009 / Revised version: 11 November 2009 / Published online: 18 December 2009
© The Author(s) 2009. This article is published with open access at Springerlink.com

Abstract We outline the details of our new method to calculate angular-dependent ionization probabilities based on electronic structure theory for diatomic and larger systems. To demonstrate its abilities, we compare our calculations to measured ionization probabilities of the four molecules D_2 , N_2 , O_2 and CO in the strong-field regime. The calculated angular distributions yield better agreement with the experimental data than those obtained from the widely used MO-ADK theory. For CO the measured angular distributions of ionic fragments indicate contributions to the ionization from both the HOMO and the HOMO-1 orbital, an effect that is addressed by the theory.

Keywords Angular resolved ionization · Strong laser fields · Electron flux · Molecules · Electronic structure theory · Velocity-map imaging · Few-cycle pulses

1 Introduction

Intense laser pulses of a few femtoseconds or even attoseconds are discussed as forthcoming tool for the coherent control of quantum dynamics in chemical systems. One perspective is to control molecular processes via the much faster electrons by preparing and directing an electronic

wavepacket to form or break bonds with a high selectivity. State of the art experiments on molecules in strong laser fields typically include ionization and subsequent processes like recollision excitation, high-harmonic generation, double ionization and dissociation. Here, we focus on the first step, the ionization caused by an electric field, which is a fundamental step for a multitude of phenomena observed in high-field physics.

Together with new advanced imaging techniques, which provide full momentum resolution of ionic fragments and electrons produced in a strong-field experiment, such as velocity-map imaging (VMI) or cold target recoil ion momentum spectroscopy (COLTRIMS), the knowledge of the angular-dependent ionization rates is particularly important to understand or even predict the outcome of strong-field experiments. Therefore it is desirable to have a reliable method to calculate these angular dependencies.

The ionization of atoms in intense laser fields has been investigated extensively in the last decades, both theoretically and experimentally [1–7]. Common methods to calculate the ionization rates for atoms are the ADK (Ammosov–Delone–Krainov) [3] and the strong-field approximation (SFA) [8]. Extensions for both models to the molecular case introducing molecular orbitals (MO) lead to the so called MO-SFA [9] and MO-ADK [10] models. Both approaches are proven to deliver good angular-dependent ionization rates for small systems in particular for linear molecules. Ionization from a single MO, essentially the highest occupied molecular orbital (HOMO) is assumed in both models. Recent strong-field experiments, however, give evidence that molecules with energetically close lying occupied valence orbitals allow ionization not only from the HOMO but also from the next lower lying orbitals, e.g. the HOMO-1 [11–13].

P. von den Hoff · R. de Vivie-Riedle (✉)
Department für Chemie und Biochemie,
Ludwig-Maximilians-Universität München, 81377 München,
Germany
e-mail: regina.de_vivie@cup.uni-muenchen.de

I. Znakovskaya · S. Zherebtsov · M.F. Kling
Max-Planck Institute of Quantum Optics,
Hans-Kopfermann-Str. 1, 85748 Garching, Germany

As research interest aims to investigate and control larger systems of especially biological interest, it is important to have a method that is capable to calculate accurate angular-dependent ionization rates for larger molecules. Such molecules are not necessarily symmetric, so that the one-center approximation is not longer valid. Moreover the outer molecular orbitals exhibit smaller energetic spacings such that more orbitals may contribute to the angular-dependent ionization probabilities.

In this paper we outline the details of our new approach to calculate angular-dependent ionization probabilities based on electronic structure calculations that is capable to handle also complex molecular systems. In addition this ansatz is able to treat the ionization from more than one single MO. To demonstrate the ability of this new method, we compare our theoretical results with MO-ADK calculations and with experimental angular-dependent ionization probabilities. As test candidates we used the theoretically as well as experimentally well studied diatomic molecules D_2 , N_2 , O_2 and CO . We selected the same pulse parameters as in the experiment, where we ionize the molecules with an intense few-cycle linearly polarized laser and detect the emitted ionic fragments (D^+ , N^+ , O^+ and C^+) with full momentum resolution via VMI.

2 Experimental setup

The laser and vacuum setup used for the experiments was described in detail elsewhere [14]. For the measurements of the angular-dependent ionization of the molecules D_2 and CO we generated 5 fs and 4 fs, linearly polarized (LP) pulses at 760 nm (D_2) and 740 nm (CO) and at intensities of 1.2 and 0.8×10^{14} W/cm², respectively, with 3 kHz repetition rate. For the N_2 and O_2 experiments, we used a slightly different laser setup generating 5 fs, linearly polarized pulses at 730 nm and an intensity of 1.6×10^{14} W/cm² with 1 kHz repetition rate. These few-cycle pulses were focused into the center of the ion optics of a VMI spectrometer using a spherical mirror. Ions and electrons that were generated at the crossing point of the laser (x -axis) and an effusive molecular beam were accelerated and focused (along the z -axis) with the ion optics onto an MCP-phosphor screen assembly. The polarization of the laser was chosen along the y -axis, i.e. parallel to the xy -plane of the MCP detector. Images were recorded with a cooled CCD camera. Inversion of the recorded images using an iterative inversion procedure [15] allowed reconstruction of the original 3D ion momentum distributions.

3 Experimental results

In Fig. 1 cuts through the 3D momentum distributions of the ionic fragments (D^+ from D_2 (a), N^+ from N_2 (b),

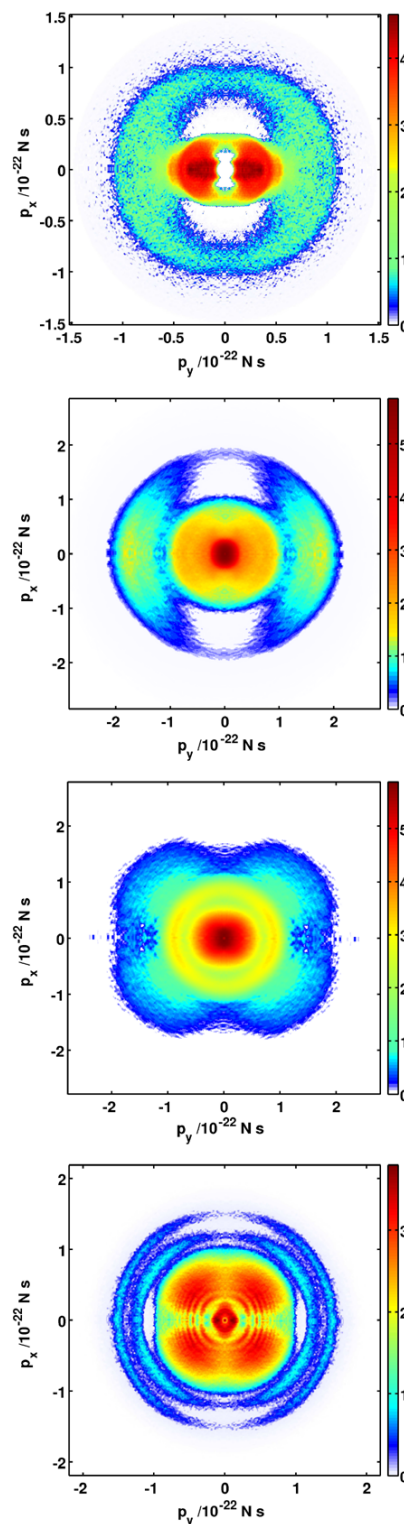


Fig. 1 Inverted two-dimensional momentum image (the laser polarization is horizontal) for the ionic fragments D^+ from D_2 [16] (a) N^+ from N_2 (b) O^+ from O_2 (c) C^+ from CO [12] (d) under the experimental conditions described in the text

O^+ from O_2 (c), C^+ from CO (d)) that are created under the described experimental conditions in the xy -plane for $p_z = 0$ are shown. The two-dimensional D^+ momentum distribution from the dissociative ionization of D_2 (Fig. 1(a)) shows two main contributions [16]. The first ranges from $0-0.6 \times 10^{-22}$ Ns and originates from bond softening and enhanced ionization [16]. The angular distributions in this momentum range show a clear maximum along and a distinct minimum perpendicular to the polarization axis. The second contribution ranges from $0.6-1.0 \times 10^{-22}$ Ns arising from recollisional excitation [16] and exhibits also a maximum along the polarization axis and a weaker minimum perpendicular to this axis.

The two-dimensional N^+ momentum distribution from the dissociative ionization of N_2 (Fig. 1(b)) shows also two main contributions. The first contribution ranges from $0-1.2 \times 10^{-22}$ Ns and exhibits background from the doubly ionized parent ion N_2^{2+} , having the same mass to charge ratio and thus time-of-flight as N^+ and cannot be separated in the experimental detection. Thus the measured angular distribution at low momenta is a convolution of the distributions arising from the N^+ and N_2^{2+} ions and does not display the angular-dependent ionization rate. The second contribution ranges from $1.2-2.2 \times 10^{-22}$ Ns and shows in agreement with the literature [17, 18] a maximum of the ionization rate along the polarization axis of the laser field and a minimum perpendicular to this axis. These ions partly arise from recollisional excitation of higher lying excited states in N_2^+ . Note that the recollisional excitation is not expected to significantly change the angular distributions.

In the two-dimensional O^+ momentum distribution from the dissociative ionization of O_2 (Fig. 1(c)) the contribution below 1.2×10^{-22} Ns comprise, like the low momentum distribution of N^+ (Fig. 1(b)), background from the doubly ionized parent ion O_2^{2+} . The contribution between $1.2-2.2 \times 10^{-22}$ Ns exhibits maxima around 45° , 135° , 225° , 315° and minima around 0° , 90° , 180° and 270° and is as well as the angular-dependent ionization rate of O^+ in good agreement with the literature [17]. As in N_2 , these ions partly arise from recollisional excitation of higher lying excited states in O_2^+ .

In Fig. 1(d) the momentum distribution for the C^+ fragments from the dissociative ionization of CO is shown. Three circular contributions are visible in the ranges $0.3-0.9 \times 10^{-22}$ Ns, $1.1-1.3 \times 10^{-22}$ Ns and $1.4-1.6 \times 10^{-22}$ Ns. The first ring is the broadest and most intense. All three rings show similar angular distributions with minima around 0° , 90° , 180° and 270° , however, with varying modulation depths. This angular distribution of the C^+ fragments differs from the findings reported by Alnaser et al. [19] and indicates contributions not only from the HOMO (5σ) but also from the HOMO-1 ($1\pi_{x/y}$) as will be discussed in this paper.

4 Theoretical description

The ionization probability of a molecule in a laser field is determined by the induced electron flux through the barrier of the combined molecular field and external electric field [4] (atomic units $m = \hbar = e = 1$ are used throughout the paper):

$$W(t) = \int_S j(r, t) dS,$$

$$j(r, t) = -\frac{i}{2}(\Psi(r, t)\nabla\Psi(r, t)^* - \Psi(r, t)^*\nabla\Psi(r, t)). \quad (1)$$

Here $j(r, t)$ is the electron flux density and $\Psi(r, t)$ the electronic wavefunction in the presence of the electric field inducing the electron flux $W(t)$. For the surface S it is convenient to choose a plane perpendicular to the direction of the electric field. As the ionization takes place only at the edges of the electronic wavefunction, we choose, in the spirit of MO-ADK [10], the surface at the outer turning points of the electronic wavefunction to calculate the induced electron flux. Beyond these points the exponentially decaying term in the electron wavefunction becomes dominant. Here the wavefunction enters the classical forbidden region from where tunneling solely can occur.

In order to evaluate (1) the electronic wavefunction $\Psi(r)$ in the presence of the electric field is needed. In principle the electronic wavefunction can be calculated with the quantum chemistry package MOLPRO [20], but as this wavefunction is completely real the flux density $j(r, t)$ (1) is zero.

To overcome this problem, we calculate the electron flux by means of the electron density $\rho(r, t)$. Using the divergence theorem

$$\int_S j(r, t) dS = \int_{V'} \nabla j(r, t) dV' \quad (2)$$

and the continuity equation

$$\frac{d}{dt}\rho(r, t) = -\nabla j(r, t) \quad (3)$$

we rewrite (1) in the spirit of [21] in to

$$W(t) = -\int_{V'} \nabla j(r, t) dV' = \frac{d}{dt} \int_{V'} \rho(r, t) dV'. \quad (4)$$

In this case V' is the part of the total volume V in which $\Psi(r)$ is defined that is spanned by the surface S and the vector of the electric field (perpendicular to S) in the direction away from the nuclei. In order to calculate the tunneling probability $T(t; S)$ for the electron passing through the potential barrier (e.g. the fractional amount of electrons passing through the surface S into the volume V') we need the electronic wavefunction with and without the external field. In this sense we now integrate (4) from the initial time t_i (corresponding to the electron wavefunction without the

electric field) to the final time t_f (corresponding to the electron wavefunction in the presence the electric field),

$$T(t; S) = \int_{V'} \rho(r, t_f) dV' - \int_{V'} \rho(r, t_i) dV'. \quad (5)$$

In this way we perform quantum chemical calculation for a given molecule with and without a static electric field. The obtained electronic wavefunction is represented on a three-dimensional grid. The grid parameters were chosen to ensure that the electron density of both wavefunctions is below a threshold of $1.0e^{-6}$. Based on these two wavefunctions, we extract numerically the tunneling probability $T(t; S)$ through the chosen surface S according to (5). We then analyze $T(t; S)$ induced by the electric field in the individual molecular orbitals to evaluate the ionization probability from the frontier orbitals, e.g. the HOMO. To calculate the angular-dependent ionization probability for a given electric field, we performed these calculations under various orientation angles with respect to the polarization of the applied external field. Within this procedure we follow the principal concept of [4] and MO-ADK [10], which are well established, but without restrictions to the one-center approximation and an effective core potential fixed at the center of mass. Moreover the calculated electronic wave functions contain the full electron correlation provided by the used quantum chemical method.

To treat ionization from more than one single orbital we solve the working equations derived above for a linear combination of the selected molecular orbitals. This implies a basis transformation rewriting the two orbitals (e.g. HOMO and HOMO-1) in the Slater determinant into the orbitals HOMO+HOMO-1 and HOMO-HOMO-1, allowing a coherent ionization of the electron from both initially chosen orbitals.

For the quantum chemical calculations it is particular important to check whether the energetic ordering of the molecular orbitals is correct and in agreement with experimental data. A wrong ordering will lead to a false prediction for the ionization probability. This problem arises in the calculations concerning the N_2 molecule [22] and will be discussed later. For the MCSCF orbitals we used the canonical representation of the individual molecular orbitals as only for these orbitals the energy values are available. In the natural representation this is not the case, because the orbital energies provided by the quantum chemistry package MOLPRO are taken as the diagonal elements of the Fock-matrix in the basis of the natural orbitals. If the off diagonal elements in such a Fock-matrix are large the energetic order of the molecular orbitals can change. In the canonical representation the Fock-matrix is by definition diagonal and the energetic ordering of the molecular orbitals can be directly read out from the matrix.

Table 1 The ionization energy, equilibrium distance, and the expansion coefficients for the spherical harmonics C_l for D_2 , N_2 , O_2 and CO

	I_p	R Å	$C_{l=0}$	$C_{l=2}$	$C_{l=4}$	
$D_2 (\sigma_g)$	15.47	0.742	2.51	0.06	0.00	
$N_2 (\sigma_g)$	15.58	1.098	2.02	0.78	0.04	
$O_2 (\pi_g)$	12.03	1.208	0.00	0.62	0.03	
			$C_{l=0}$	$C_{l=1}$	$C_{l=2}$	$C_{l=3}$
CO (σ)	14.01	1.128	1.43	0.76	0.28	0.02

For the MO-ADK calculations used as reference for the above introduced method (see Sect. 5), we follow the procedure described in [10]. The required expansion coefficients for the spherical harmonics C_l (see [10]) as well as the ionization energies and equilibrium distances are also taken from [10] and listed in Table 1.

For both approaches we assume a static electric field during the ionization corresponding to the maximum intensity of the experimental ultra-short (4 and 5 fs) light pulse. This is justified as the other half cycles are less intense and thus have a significantly lower ionization probability.

5 Results and discussion

We used the above introduced method to calculate the angular-dependent ionization probabilities for the molecules D_2 , N_2 , O_2 and CO and compare the results with the angular-dependent ionization probabilities calculated with MO-ADK theory as well as with experimentally measured angular-dependent ionization rates. Note that in the experiments an ensemble of molecules is ionized that is not aligned or oriented. The angular distribution of detected ionic fragments reflects the angular-dependent ionization rates for laser pulses with sufficiently short duration and low intensity [23]. Moreover no significant change of the angular distributions is expected neither through recollisional excitation nor through dynamic or post ionization alignment [23]. For all presented examples the electronic wavefunction with and without the presence of the external electric field is calculated with the quantum chemistry package MOLPRO [20] applying the default criteria for convergence. We used sufficiently large basis sets including polarization and diffuse functions in all cases except for N_2 (see Sect. 5.2). Both types of functions improve the description of the electron at large distances from the nuclei. In case of CASSCF calculations all electrons except the core electrons are included in the active space. In order to be able to compare the individual ionization probabilities from the experiment and from the theoretical calculations we have normalized all data, setting the largest value to one.

5.1 Angular-dependent ionization probabilities for D₂

The D₂ calculations were performed on the CASSCF(2,8)/6-311++G** level of theory and for an electric field strength of 0.058 a.u. (corresponding to the intensity of 1.2×10^{14} W/cm² used in the experiment). To scan the angular dependence, we performed the quantum chemistry calculation for 37 orientation of the molecule with respect to the applied electric field ranging from 0° (molecular axis parallel to the laser polarization) to 360° with a step size of 10°. The resulting angular-dependent ionization probability is plotted in Fig. 2 as black solid line. The black crosses indicate the actually calculated angles. Our calculations show a clear maximum in the ionization probability for molecular orientations along the laser polarization axis and a weak minimum for orientations perpendicular to this axis. We find that the ionization is 2.1 times higher for parallel alignment (0°) than for perpendicular alignment (90°).

The experimental angular-dependent ionization rate is derived from the VMI momentum image (Fig. 1(a)) by integration over the contribution arising from recollision excitation ($0.6\text{--}1.0 \times 10^{-22}$ ns) and is plotted in Fig. 2 as gray solid line. The angular dependence exhibits a maximum along the polarization axis and a minimum perpendicular to this axis. The parallel vs. perpendicular ratio is around 3.0.

The results of the angle-dependent MO-ADK calculations for the same field strength of 0.058 a.u. are plotted as black dashed line in Fig. 2 and show roughly the same ionization probability for all angles. The parallel vs. perpendicular ratio calculated according to MO-ADK is 1.2.

From Fig. 2 it can be seen that our new approach is in good agreement with the experimental data. Not only the parallel vs. perpendicular ratio is reproduced well but also

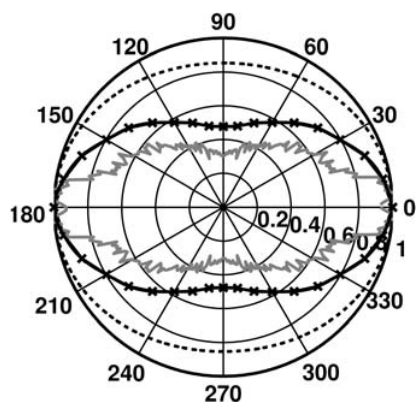


Fig. 2 Black solid line: calculated angular-dependent ionization probability for the HOMO of D₂ (the crosses indicate the actually calculated points). Black dashed line: angular-dependent ionization probability for the HOMO of D₂ calculated with the MO-ADK model. Gray solid line: experimentally measured angular-dependent ionization rate for D₂

the overall shape of the angular distribution. The MO-ADK calculations predict a lower parallel vs. perpendicular ratio as well as a false shape of the total angular distribution. Presumably this is due to the one-center approximation. To describe the σ_g orbital of the D₂ molecule a huge contribution of the spherical harmonic with $l = 0$ is used in the linear combination and only a weak contribution of $l = 2$ (0.06 see Table 1) to break the spherical symmetry. Thus the shape of the σ_g orbital is not reproduced correctly. Moreover the potential formed by the nuclei and one of the two electrons is treated with an effective potential ($-\frac{Z_{\text{eff}}}{r}$) which presumably also contributes to the error made for perpendicular orientations. Here the tunneling electron is affected by both nuclei. In our method all these effects are already included in the quantum chemistry calculations.

5.2 Angular-dependent ionization probabilities for N₂

The electric field strength was set to 0.067 a.u., equivalent to the experimentally used intensity of 1.6×10^{14} W/cm². In the case of N₂ Hartree Fock and MCSCF calculations carried out with basis sets larger than STO-3G predict the wrong energetic ordering of the valence orbitals. The HOMO in the N₂ molecule is the $3\sigma_g$ orbital, not the $1\pi_u$. This is a well known problem in quantum chemistry [22]. The correct order leads to the experimentally found N₂⁺ ground state of $^2\Sigma_g^+$ symmetry. The interchanged ordering would not only result in the wrong ionic ground state of N₂⁺ ($^2\Pi_g$) but also in the wrong angular-dependent ionization rates. Even molecular orbitals derived from MCSCF calculations including electron correlation also for spin paired electrons cannot overcome this problem. For N₂ we therefore used the HF/STO-3G level of theory. In the isoelectronic molecule CO, treated below, the orbital ordering is correct. Here the outer molecular orbitals 4σ and the 5σ have the same symmetry and can interact with each other. In N₂ the corresponding orbitals ($2\sigma_u$ and $3\sigma_g$) belong to different irreducible representations and cannot repel each other. In the HF/STO-3G calculations the $3\sigma_g$ orbital is “accidentally right” and the highest occupied orbital. Therefore we refrain from the higher accuracy normally provided by larger basis sets in favor to maintain the right molecular orbital order. For the angular dependence we scan, as in the previous section, over 37 orientation of the molecule with respect to the applied electric field ranging from 0° (molecular axis parallel to the laser polarization) to 360° with a constant step size of 10°. The angular-dependent ionization probability is plotted in Fig. 3 as black solid line and shows a maximum in the ionization probability for molecules oriented along the laser polarization axis and a minimum for orientations perpendicular to this axis (parallel vs. perpendicular ratio is 3.5). This calculated angular distribution is in reasonable agreement with the experimental one, derived

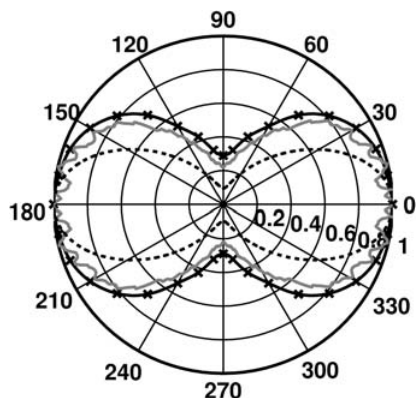


Fig. 3 *Black solid line*: calculated angular-dependent ionization probability for the HOMO of N_2 (the *crosses* indicate the actually calculated points). *Black dashed line*: angular-dependent ionization probability for the HOMO of N_2 calculated with the MO-ADK model. *Gray solid line*: experimentally measured angular-dependent ionization rate for N_2

from the VMI spectrum (Fig. 1(b)) by integration over the momentum range from 1.1 eV to 2.2×10^{-22} Ns and shown in Fig. 3 as gray solid line. The measured parallel vs. perpendicular ratio is around 4.5 which is in excellent agreement with the literature [18] (4.5).

The angular-dependent ionization probabilities calculated according to the MO-ADK theory (field strength of 0.067 a.u.) are plotted in Fig. 3 as black dashed line. Its shape shows also a reasonable agreement with the experimental data. The predicted parallel vs. perpendicular ratio, however, with 10.5 is far off from the experimental value.

5.3 Angular-dependent ionization probabilities for O_2

The electronic wavefunctions for the O_2 molecule are calculated on the CASSCF(12,10)/6-311+G* level of theory and an electric field strength of 0.067 a.u. equivalent to the experimentally used intensity. O_2 in its electronic ground is a diradical where both of the degenerated $1\pi^*$ orbitals (π_g symmetry) are occupied with one electron. The degeneration of the two orbitals is not lifted in the presence of the electronic fields and the ionization can occur from both orbitals. To accommodate this fact, we allow the electron a priori to tunnel from both orbitals with the same probability, by calculating the ionization probability from the linear combination of the $1\pi_x^*$ and $1\pi_y^*$ orbital. The resulting angular-dependent ionization pattern is shown in Fig. 4 as black solid line and fits very good with the experimental data (Fig. 4 gray solid line). The experimental data have been derived by integration of the VMI momentum image over the contribution between 1.1 and 2.2×10^{-22} Ns and is in good agreement with the literature [17].

For the MO-ADK calculations we used according to the literature [10, 17] only the π_g orbital lying in the plane

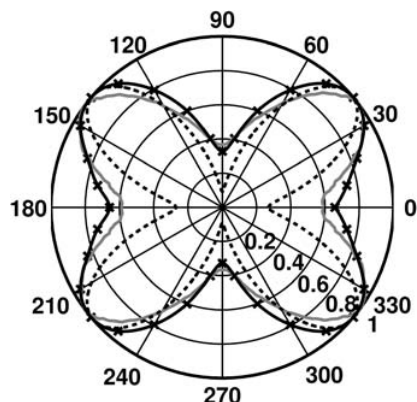


Fig. 4 *Black solid line*: calculated angular-dependent ionization probability for the HOMO (Linear combination of $1\pi_x^*$ and $1\pi_y^*$) of O_2 (the *crosses* indicate the actually calculated points). *Black dashed line*: angular-dependent ionization probability for the HOMO of O_2 calculated with the MO-ADK model. *Gray solid line*: experimentally measured angular-dependent ionization rate for O_2

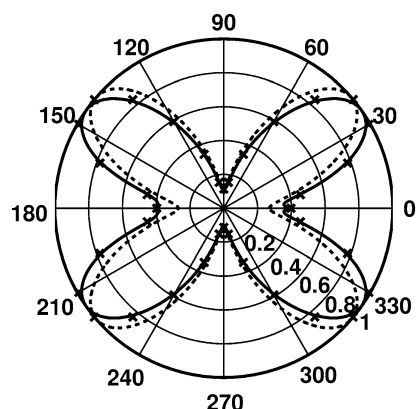


Fig. 5 *Black solid line*: calculated angular-dependent ionization probability for the HOMO of O_2 (the *crosses* indicate the actually calculated points). *Black dashed line*: angular-dependent ionization probability for the HOMO of O_2 calculated with the MO-ADK model

perpendicular to the rotation axis used for the angular-dependent calculations. Again the field strength corresponds to the intensity used in the experiment. In general the results are also in good agreement with the experimental (Figs. 4 and 5 black dashed line) data apart from the fact, that the minimum in ionization rate for parallel and perpendicular alignment to the laser field is overestimated. According to our calculations this can be assigned to the assumption that the ionization takes place from one orbital only. This is verified in Fig. 5, when we likewise include only one π_g in our new approach (Fig. 5 black solid line) we reproduce a similar result as the MO-ADK theory. Only when we include both π_g (π_x and π_y) orbitals the minima around 0° , 90° , 180° and 270° and the overall shape fit much better with the experiment (see Fig. 4).

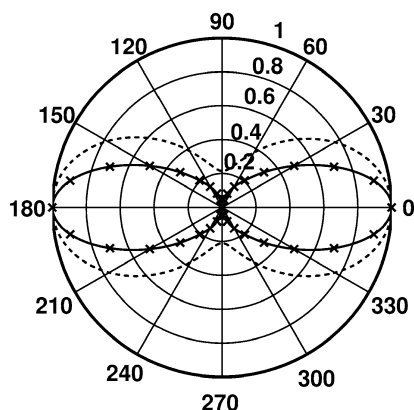


Fig. 6 *Black solid line*: calculated angular-dependent ionization probability for the HOMO (5σ) of CO (the crosses indicate the actually calculated points). *Black dashed line*: angular-dependent ionization probability for the HOMO of CO calculated with the MO-ADK model

5.4 Angular-dependent ionization probabilities for CO

The CO molecule serves here as an example for heteronuclear diatomic molecules. For this class of molecules the molecular orbitals are not symmetrically distributed over the molecule, but partially localized on one of the nuclei. Thus one can expect different ionization probabilities for different orientation (CO vs. OC) of the molecule with respect to the laser polarization. This effect is averaged out without phase stabilization and for long laser pulses, while it creates an asymmetric angular distribution in an ensemble of the ionized molecules with phase stabilized pulses. In this case one can expect an asymmetry caused by the field induced ionization for the CO molecule. Indeed this effect (amongst others) has been studied experimentally and theoretically with the presented method in [12]. Here we will focus on the symmetric angular distributions produced with non phase stabilized laser pulses.

The electronic wavefunctions for the CO molecule are calculated on the CASSCF(10,11)/6-311+G* level of theory and an electric field strength of 0.047 a.u. equivalent to the experimental intensity. When we assume the ionization only from the HOMO (5σ) our calculated angular-dependent ionization probabilities (Fig. 6 black solid line) matches reasonably well with the angular distribution calculated with MO-ADK (Fig. 6 black dashed line) and the experimental findings from Alnaser and coworkers [19] who studied the angular-dependent fragmentation pattern from CO^{2+} .

However, this angular-dependent ionization probability does not reflect the angular distribution measured under the above described experimental conditions showing maxima around 45° , 135° , 225° , 315° and minima around 0° , 90° , 180° and 270° (see Fig. 7 gray solid line). These angular-dependent ionization rates are obtained by integration of the

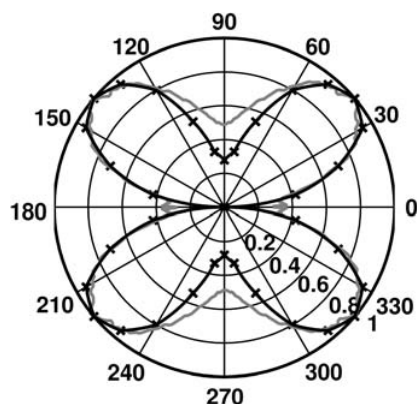


Fig. 7 *Black solid line*: calculated angular-dependent ionization probability for the HOMO and HOMO-1 (5σ and $1\pi_{x/y}$) of CO. *Gray solid line*: experimentally measured angular-dependent ionization rate for CO

VMI momentum map over the most pronounced contribution between 0.3 and 0.9×10^{-22} Ns. If we now include in our calculations the HOMO-1 ($1\pi_{x/y}$), we obtain the angular distribution plotted in Fig. 7 (black solid line) which is in good agreement with the experimental data. Even the more distinct minima for parallel than for perpendicular alignment can be reproduced within our calculations.

6 Conclusion

We presented experimental and theoretical results on orbital symmetry effects on the recorded angular distributions of ions from the dissociative ionization of the molecules D_2 , N_2 , O_2 and CO in intense few-cycle laser fields. Our theoretical approach goes beyond the one orbital and one-center approximation in MO-ADK. We compare the theoretical results based on the new approach with MO-ADK calculations and with experimental angular-dependent ionization probabilities. Very good agreement is found between the new theoretical and the experimental data. The angular-dependent ionization rate at intensities close to 10^{14} W/cm² for D_2 , N_2 and O_2 is found to reflect the orbital symmetries of the HOMO orbitals in agreement with earlier observations [19], for CO, however, both the HOMO and the HOMO-1 orbitals contribute.

Acknowledgement We acknowledge F. Krausz and M.J.J. Vrakking for their support, fruitful discussions and the use of specialized equipment. We are grateful for support by the DFG via the Emmy-Noether program and the Cluster of Excellence: Munich Center for Advanced Photonics (www.munich-photonics.de).

Open Access This article is distributed under the terms of the Creative Commons Attribution Noncommercial License which permits any noncommercial use, distribution, and reproduction in any medium, provided the original author(s) and source are credited.

References

1. A.M. Perelomov, V.S. Popov, M.V. Terent'ev, *Sov. Phys. JETP* **23**, 924 (1966)
2. A.M. Perelomov, V.S. Popov, M.V. Terent'ev, *Sov. Phys. JETP* **23**, 924 (1966)
3. M. Ammosov, N. Delone, V. Krainov, *Sov. Phys. JETP* **64**, 1191 (1986)
4. B.M. Smirnov, M.I. Chibisov, *Sov. Phys. JETP* **22**, 585 (1966)
5. B. Buerke, D.D. Meyerhofer, *Phys. Rev. A* **69**, 051402 (2004)
6. S. Augst, D. Strickland, D.D. Meyerhofer, S.L. Chin, J.H. Eberly, *Phys. Rev. Lett.* **63**, 2212 (1989)
7. S. Augst, A. Talebpour, S.L. Chin, Y. Beaudoin, M. Chaker, *Phys. Rev. A* **52**, 914 (1995)
8. F.H.M. Faisal, A. Becker, J. Muth-Böhm, *Laser Phys.* **9**, 115 (1999)
9. J. Muth-Böhm, A. Becker, F.H.M. Faisal, *Phys. Rev. Lett.* **85**, 2280 (2000)
10. X.M. Tong, Z. Zhao, C.D. Lin, *Phys. Rev. A* **66**, 033402 (2002)
11. B.K. McFarland, J.P. Farrell, P.H. Bucksbaum, M. Gühr, *Science* **322**, 1232 (2008)
12. I. Znakovskaya, P. von den Hoff, S. Zherebtsov, A. Wirth, O. Herwerth, M. Vrakking, R. de Vivie-Riedle, M. Kling, *Phys. Rev. Lett.* **103**, 103002 (2009)
13. O. Smirnova, Y. Mairesse, S. Patchkovskii, N. Dudovich, D. Villeneuve, P. Corkum, M.Y. Ivanov, *Nature* **460**, 972 (2009)
14. M. Schultze, E. Goulielmakis, M. Uiberacker, M. Hofstetter, J. Kim, D. Kim, F. Krausz, U. Kleineberg, *New J. Phys.* **9**, 243 (2007)
15. M.J.J. Vrakking, *Rev. Sci. Instrum.* **72**, 4084 (2001)
16. M.F. Kling, C. Siedschlag, A.J. Verhoef, J.I. Khan, M. Schultze, T. Uphues, Y. Ni, M. Uiberacker, M. Drescher, F. Krausz, M.J.J. Vrakking, *Science* **312**, 246 (2006)
17. D. Pavičić, K.F. Lee, D.M. Rayner, P.B. Corkum, D.M. Villeneuve, *Phys. Rev. Lett.* **98**, 243001 (2007)
18. I. Litvinyuk, K.F. Lee, P. Dooley, D. Rayner, D. Villeneuve, P.B. Corkum, *Phys. Rev. Lett.* **90**, 233003 (2003)
19. A.S. Alnaser, C.M. Maharjan, X.M. Tong, B. Ulrich, P. Ranitovic, B. Shan, Z. Chang, C.D. Lin, C.L. Cocke, I.V. Litvinyuk, *Phys. Rev. A* **71**, 031403 (2005)
20. H.-J. Werner, P.J. Knowles, R. Lindh, F.R. Manby, M. Schütz, P. Celani, T. Korona, A. Mitrushenkov, G. Rauhut, T.B. Adler, R.D. Amos, A. Bernhardsson, A. Berning, D.L. Cooper, M.J.O. Deegan, A.J. Dobbyn, F. Eckert, E. Goll, C. Hampel, G. Hetzer, T. Hrenar, G. Knizia, C. Köppl, Y. Liu, A.W. Lloyd, R.A. Mata, A.J. May, S.J. McNicholas, W. Meyer, M.E. Mura, A. Nicklass, P. Palmieri, K. Pflüger, R. Pitzer, M. Reiher, U. Schumann, H. Stoll, A.J. Stone, R. Tarroni, T. Thorsteinsson, M. Wang, A. Wolf, *Molpro*, version 2006.1 (2006)
21. I. Barth, H.-C. Hege, H. Ikeda, A. Kenfack, M. Koppitz, J. Manz, F. Marquardt, G.K. Paramonov, *Chem. Phys. Lett.* **481**, 118 (2009)
22. A. Szabo, N.S. Ostlund, *Modern Quantum Chemistry* (Dover, New York, 1996)
23. X.M. Tong, Z.X. Zhao, A.S. Alnaser, S. Voss, C.L. Cocke, C.D. Lin, *J. Phys. B: At. Mol. Opt. Phys.* **38**, 333 (2005)

Paper VI

Waveform control of orientation-dependent ionization of DCl in few-cycle laser fields.

Znakovskaya, I., von den Hoff, P., Schirmel, N., Urbasch, G., Zherebtsov, S., Bergues, B., de Vivie-Riedle, R., Weitzel, K.-M. & Kling, M. F.

Phys. Chem. Chem. Phys. **13**, 8653 (2011).

Cite this: *Phys. Chem. Chem. Phys.*, 2011, **13**, 8653–8658

www.rsc.org/pccp

PAPER

Waveform control of orientation-dependent ionization of DCI in few-cycle laser fields

I. Znakovskaya,^a P. von den Hoff,^b N. Schirmel,^c G. Urbasch,^c S. Zherebtsov,^a B. Bergues,^a R. de Vivie-Riedle,^{*b} K.-M. Weitzel^{*c} and M. F. Kling^{*ad}

Received 1st December 2010, Accepted 17th March 2011

DOI: 10.1039/c0cp02743j

Strong few-cycle light fields with stable electric field waveforms allow controlling electrons on time scales down to the attosecond domain. We have studied the dissociative ionization of randomly oriented DCI in 5 fs light fields at 720 nm in the tunneling regime. Momentum distributions of D⁺ and Cl⁺ fragments were recorded *via* velocity-map imaging. A waveform-dependent anti-correlated directional emission of D⁺ and Cl⁺ fragments is observed. Comparison of our results with calculations indicates that tailoring of the light field *via* the carrier envelope phase permits the control over the orientation of DCI⁺ and in turn the directional emission of charged fragments upon the breakup of the molecular ion.

1. Introduction

Laser pulses with stable electric field waveforms of a few cycles duration allow us to control electronic motion on timescales reaching down to the attosecond regime.¹ Ultimately this is expected to provide means for controlling chemical processes.² The generation of laser pulses with a well-defined electric field waveform $E(t) = E_0(t)\cos(\omega t + \varphi)$, with envelope $E_0(t)$ and frequency ω , became possible by the stabilization of the carrier envelope phase (CEP) φ . CEP-stable few-cycle pulses have been applied to the control of electron localization in the dissociative ionization of the prototype molecules D₂,^{3,4} HD⁴ and H₂.⁵ After initial ionization, these systems only contain a single electron. The steering of this electron is achieved *via* light-induced coherent superposition of two electronic states with CEP dependent amplitudes and phases. This process has been the subject of a large number of theoretical investigations (see *e.g.* ref. 6–10 and references cited therein). The light-field induced electron localization leads to a directional emission of charged and uncharged fragments upon the break-up of the molecule. The single-color CEP control is related to multi-color relative phase-control first introduced by Brumer and Shapiro.^{11,12} Among many other studies, the $\omega_2 = 3\omega_1$ phase control of the ionization and dissociation of a variety of diatomic molecules has

been investigated (see *e.g.* ref. 13 and 14). As a recent example in the femtosecond domain, studies using a two-color laser field $E(t) = E_1(t)\cos(\omega t) + E_2(t)\cos(2\omega t + \varphi_{\text{two-color}})$ with ω and 2ω corresponding to 800 nm and 400 nm, respectively, have shown that the directional emission of D⁺ and D fragments from the dissociative ionization of D₂ can be tailored with the relative phase $\varphi_{\text{two-color}}$.¹⁵

Light-waveform control of electron dynamics in a more complex molecule was recently demonstrated for carbon monoxide.^{16,17} In this study, 4 fs, linearly polarized laser pulses at 740 nm and an intensity of 8×10^{13} W cm⁻² have been applied to dissociatively ionize CO. Quantum calculations indicated that two mechanisms are responsible for the observed asymmetry in the C⁺ and O⁺ ion emission. First, the ionization of CO in a near-single cycle phase-stable laser field is found to be orientation-dependent.¹⁸ Second, excitation of CO⁺ by the laser-driven recolliding electron, that was freed in the first ionization step, leads to dissociation and laser-induced coupling of potential energy curves of CO⁺, resulting in the formation of C⁺ + O and C + O⁺ and a CEP dependent asymmetry.¹⁷ In this particular study, the individual contributions from the two mechanisms could not be clearly distinguished from the experimental data.

Here, we report on studies on the dissociative ionization of DCI in few-cycle CEP-stable laser fields. DCI is an interesting target, for which the fragmentation channels Cl⁺ + D and Cl + D⁺ are well known (see *e.g.* ref. 19 and 20). While the CEP dependent fragmentation of DCI⁺ has been investigated theoretically,²¹ no experimental study on the CEP control of the dissociative ionization of DCI in few-cycle light fields was reported. In our experiments, velocity-map imaging was utilized to record the momentum distributions of D⁺ and Cl⁺ fragments from the dissociative ionization of DCI. We find an

^a Max-Planck-Institut für Quantenoptik, Hans-Kopfermann-Str. 1, 85748 Garching, Germany. E-mail: matthias.kling@mpq.mpg.de

^b Department für Chemie und Biochemie, Ludwig-Maximilians-Universität München, 81377 München, Germany. E-mail: regina.de_vivie@cup.uni-muenchen.de

^c Fachbereich Chemie, Philipps-Universität Marburg, Hans Meerweinstr., 35032 Marburg, Germany. E-mail: weitzel@chemie.uni-marburg.de

^d J. R. Macdonald Laboratory, Department of Physics, Kansas State University, Manhattan, KS 66506, USA

anti-correlated, CEP dependent directional emission of D^+ and Cl^+ fragments (the asymmetries of the D^+ and Cl^+ fragments are phase shifted by π). Our calculations indicate that the observed control at the chosen laser parameters can be explained by a single mechanism: the orientation-dependent ionization of DCl molecules that is controlled *via* the CEP of the few-cycle laser pulse.

2. Experimental results

The experimental scheme is similar to the one described in ref. 3. In brief, transform-limited, phase-stable laser pulses at 790 nm central wavelength of *ca.* 25 fs duration with 1 mJ energy per pulse at 1 kHz repetition rate have been generated by an amplified Ti:sapphire laser system (Femtopower Compact Pro, Femtolasers) at the AS-5 infrastructure at the Max Planck Institute of Quantum Optics. The pulses were spectrally broadened using a 1 m long hollow-core fiber of 250 μm diameter filled with 2.5 bar Neon gas. The laser pointing into the fiber was controlled with high precision using a commercial beam stabilization system (Beamlock, TEM Messtechnik). The output pulses from the fiber were compressed to a near-transform limited duration of ~ 5 fs at a central wavelength of 720 nm in a chirped-mirror compressor. The pulse duration was monitored online with a commercial dispersion balanced autocorrelator (Femtometer, Femtolasers). The laser phase has been actively stabilized using two feedback loops as described in ref. 22. The phase jitter was smaller than 150 mrad. The CEP φ was varied in the experiment by insertion of dispersive material *via* a pair of wedged fused silica plates. The measured phase φ_{CEP} discussed in this paper contains a phase-offset φ_0 relative to the absolute phase φ : $\varphi_{\text{CEP}} = \varphi_0 + \varphi$. The phase offset φ_0 can be determined by comparing experimental data to theoretical predictions (see *e.g.* ref. 23).

The phase-stabilized, linearly polarized pulses were focused with a spherical mirror ($f = 50$ cm) into a velocity-map imaging (VMI) spectrometer.^{24,25} A peak intensity in the focus of $1.3(\pm 0.3) \times 10^{14}$ W cm^{-2} was determined from the cutoff in electron spectra recorded for Xe ^{23,26} under the same

experimental conditions as for the molecular experiments. Ions or electrons that were generated at the laser focus in the VMI spectrometer were projected onto an MCP/phosphor screen assembly using a static electric field. The velocity map images have been recorded with a low-noise CCD camera (Sensicam, PCO). Different ionic species were distinguished by their time-of-flight (TOF) towards the detector and appropriate gating of the MCP with a laser-triggered, fast high-voltage switch (Behlke). 3D momentum distributions of recorded ions and electrons are obtained from the 2D projections by an iterative inversion procedure.²⁷ In the convention used here, the images lie in the x - y plane. The y -axis is the laser polarization axis and the axis of symmetry for the cylindrically symmetric VMI images. The polar angle θ is defined as the angle between a momentum vector \vec{p} and the positive part of the y -axis, and the z -axis is the projection coordinate, lying along the detector (TOF) axis. Fig. 1 shows cuts through the 3D momentum distributions at $p_z = 0$ for D^+ and Cl^+ ions recorded without CEP stabilization. The laser is linearly polarized along the p_y -axis and propagates along p_x . Note that the signal from DCl^+ ions could not be completely suppressed in the recording of Cl^+ ions due to their close TOF proximity and the much stronger DCl^+ signal. The DCl^+ background in the center was therefore subtracted from the Cl^+ images, potentially obscuring Cl^+ signals at momenta below 20 a.u.

Within the axial recoil approximation and neglecting field-induced orientation, which is reasonable for the short pulses used here, the angle θ for the detected fragments reflects the orientation of the molecule. Both ionic species exhibit maxima in their angular distributions at angles around 60° relative to the laser polarization axis. For the D^+ ions concentric rings are visible at higher momenta, which are not visible in the Cl^+ data (note that the momentum resolutions were limited to 0.2 a.u. (D^+) and 0.4 a.u. (Cl^+)). Angular integrated energy spectra obtained from the images shown in Fig. 1 are shown in Fig. 2a and c for D^+ and Cl^+ ions, respectively.

In order to elucidate the effect of the CEP on the experimental ion momentum distributions, the phase φ_{CEP} was scanned over a range of 5π . In our analysis of the experimental

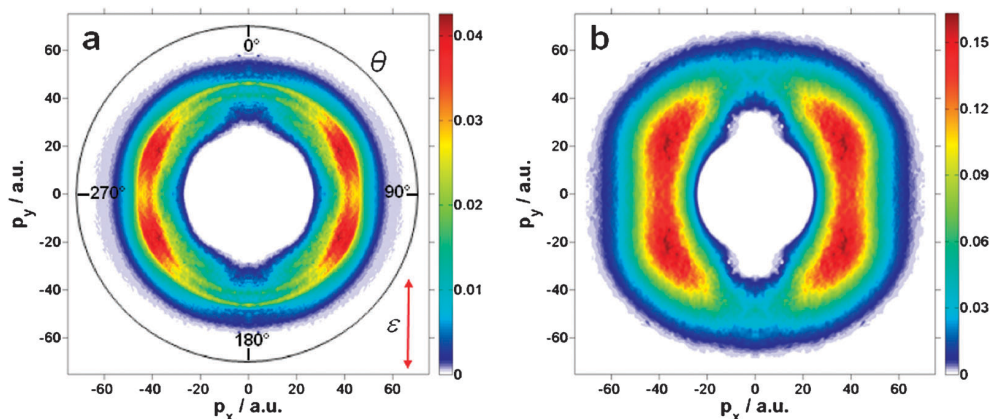


Fig. 1 Momentum distributions (p_y versus p_x for $p_z = 0$) of fragment D^+ (a) and Cl^+ (b) ions from the dissociative ionization of DCl at 1.3×10^{14} W cm^{-2} . The laser is polarized along the y -direction (red arrow). The momentum distributions are averaged over the CEP and left–right as well as up–down symmetrized to increase the signal-to-noise ratio.

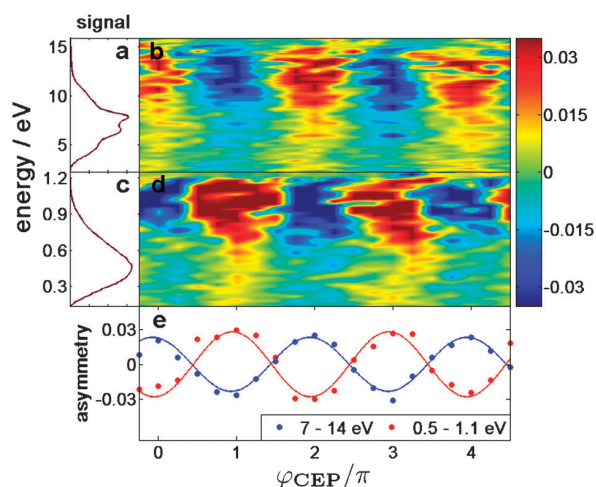


Fig. 2 Fragment ion energy spectra (CEP averaged) and asymmetry maps $A(W, \varphi_{\text{CEP}})$ for D^+ ions, (a) and (b), and Cl^+ ions, (c) and (d). $A(W, \varphi_{\text{CEP}})$ was obtained by integrating the signal over an angular range from -60° to 60° along the polarization axis. The angular and energy integrated asymmetries $A(\varphi_{\text{CEP}})$ for D^+ and Cl^+ ions are shown in (e). Note that $\varphi_{\text{CEP}} = \varphi_0 + \varphi$, where the offset phase φ_0 is the same for the data displayed in (b), (d) and (e).

data, the images were left–right symmetrized (with respect to the symmetry axis (p_y)). For each ionic species with mass m and energy $W = p^2/(2m)$ the asymmetry $A(W, \theta, \varphi_{\text{CEP}})$ in the ion momentum distribution $P(W, \theta, \varphi_{\text{CEP}})$ was obtained for the right half of the image ($p_x > 0$) from

$$A(W, \theta, \varphi_{\text{CEP}}) = \frac{P(W, \theta, \varphi_{\text{CEP}}) - P(W, \pi - \theta, \varphi_{\text{CEP}})}{P(W, \theta, \varphi_{\text{CEP}}) + P(W, \pi - \theta, \varphi_{\text{CEP}})} \quad (1)$$

for $\theta \in [0, \frac{\pi}{2}]$.

The angle integrated asymmetry $A(W, \varphi_{\text{CEP}})$ within the angular range $[0, \alpha]$ can then be derived as follows:

$$A(W, \varphi_{\text{CEP}}) = \frac{\int_0^\alpha P(W, \theta, \varphi_{\text{CEP}}) \sin \theta d\theta - \int_0^\alpha P(W, \pi - \theta, \varphi_{\text{CEP}}) \sin \theta d\theta}{\int_0^\alpha P(W, \theta, \varphi_{\text{CEP}}) \sin \theta d\theta + \int_0^\alpha P(W, \pi - \theta, \varphi_{\text{CEP}}) \sin \theta d\theta} \quad (2)$$

We chose to analyze the ion emission within a restricted angular range $[0, \alpha]$ with $\alpha = 60^\circ$ to improve the signal-to-noise ratio. These angle integrated asymmetries $A(W, \varphi_{\text{CEP}})$ for D^+ and Cl^+ ions from the dissociative ionization of DCI are displayed in Fig. 2b and d. Both asymmetry maps (for D^+ and Cl^+ ions) exhibit an energy independent oscillation with the CEP over the entire range of recorded fragment energies. The two asymmetry maps have been energy integrated to obtain the data points shown in Fig. 2e (the solid lines correspond to fits of the data points to a sine function). The two curves are offset in phase by approximately π .

3. Theoretical results

The ionization of small molecules in strong laser fields has been treated previously with the MO-SFA²⁸ and MO-ADK^{29,30} models. Both approaches provide orientation-dependent ionization rates for ionization from a given molecular orbital (MO), *e.g.* the highest occupied molecular orbital (HOMO), within the one-center approximation. Recent strong-field experiments, however, provided evidence that in molecules with energetically close lying valence orbitals, ionization occurs not only from the HOMO but also from lower lying orbitals, *e.g.* the HOMO – 1.^{16,31–33} Moreover, it was shown that for heteronuclear molecules it is important to go beyond the one-center approximation in order to achieve a good agreement with experimental data.¹⁸

In the heteronuclear molecule DCI the HOMO is a lone-pair 3p Cl-orbital, which is twofold degenerate ($3p_x, 3p_y$) and thus, ionization from both MOs has to be considered in the theoretical treatment. Here, we use the ansatz of ref. 18 to calculate strong-field ionization probabilities in DCI going beyond the one-center approximation, while taking into account the ionization from the two degenerate HOMOs. A detailed description of the method can be found in ref. 18. In the following we present the most important aspects, necessary to understand the results presented below.

The orientation dependent ionization rate $w(\theta, t)$ of a molecule in an intense laser field can be calculated as the induced electron flux through the barrier of the combined molecular and external electric fields:³⁴

$$w(\theta, t) = -\frac{d}{dt} \int_V \rho(\vec{r}, \theta, t) dV, \quad (3)$$

here $\rho(\vec{r}, \theta, t) = \sum_{n \leq n_{\text{HOMO}}} |\psi_n(\vec{r}, \theta, t)|^2$ is the electron density and $\psi_n(\vec{r}, \theta, t)$ are the MOs of the molecule in the presence of the external field. The angle θ is the angle between the intramolecular axis and the external field. Within the axial recoil approximation this angle corresponds to the angle θ in the experimental images, under which the fragments formed by the dissociation of the molecule are observed. The MOs are calculated in the adiabatic approximation using a static electric field with the quantum chemistry package Molpro³⁵ and are represented on a three dimensional grid.

The integral in eqn (4) is taken over the volume V which is confined within a surface S . Following the basic idea of MO-ADK the surface S is spanned by all the outer turning points of $\psi_n(\vec{r}, \theta, t_i)$.³⁴ Beyond these points the exponentially decaying term in the electron wavefunction becomes dominant and the wavefunction enters the classical forbidden region relevant for the tunneling process. The surface S can be determined on the three dimensional grid by numerical evaluation of the first and second derivative of $\psi_n(\vec{r}, \theta, t_i)$ starting from maximal \vec{r} values.

In our simulations the ionization probability

$$T(t, \theta; S) = \int_V \rho(\vec{r}, \theta, t_i) dV - \int_V \rho(\vec{r}, \theta, t) dV \quad (4)$$

was evaluated numerically at the time t , where the field and hence the ionization rate is maximal. The maximal strength

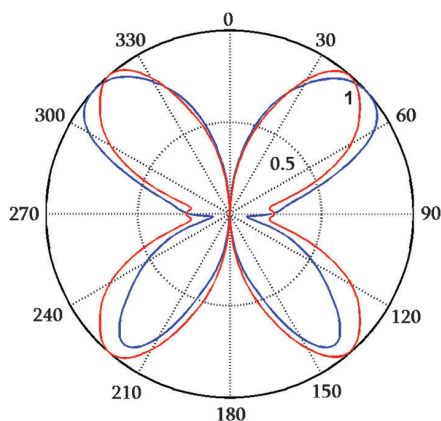


Fig. 3 Calculated angular-dependent relative ionization probability for the HOMOs of DCl at $1.3 \times 10^{14} \text{ W cm}^{-2}$. The symmetric probability (red line) corresponds to a CEP average, while the asymmetric probability (blue line) is obtained for ionization at the field maximum of a cosine-type pulse ($\varphi = 0$).

and the direction of the field directly depend on the CEP. The initial time t_i corresponds to a time where the electric field is zero. To obtain the orientation dependent ionization probability for a random CEP, we average the ionization probability over the two opposite field directions. Ionization from multiple MOs can also be treated within this ansatz (see ref. 18).

The DCl MO-calculations were performed at the CASSCF(6,9)/6-311G++(2DF,2PD) level of theory and for an electric field strength of 0.06 a.u. (corresponding to the intensity of $1.3 \times 10^{14} \text{ W cm}^{-2}$ used in the experiment). In order to account for the random molecular orientations in the experiment, we performed the calculation for 36 orientations θ of the molecule with respect to the laser polarization axis ranging from 0° to 360° in equidistant steps of 10° .

In the hetero-nuclear diatomic DCl the electrons are not symmetrically distributed over the two nuclei, but partially localized on one of the nuclei. Thus one can expect different ionization probabilities for different orientations of the molecule with respect to the external electric field. This effect is averaged out for pulses without phase stabilization, while with phase stabilization it creates an asymmetric angular distribution of the ionized molecules starting from an ensemble of randomly oriented neutral molecules. The calculated asymmetric (blue line; CEP = 0) and symmetric (red line; random CEP) angular dependent ionization probabilities are plotted in Fig. 3. For the asymmetric distribution shown in Fig. 3, the electric field points upwards and DCl is oriented such that the Cl-atom points upwards. Both angular dependent ionization probabilities show distinct maxima around 45° , 135° , 225° , 315° and minima around 0° , 90° , 180° and 270° .

4. Discussion

In order to discuss the angular distribution of fragments in more detail, we show in Fig. 4 the relevant potential energy curves of DCl and DCl^+ (adapted from ref. 36 and 37). Tunnel ionization of DCl at a laser intensity of

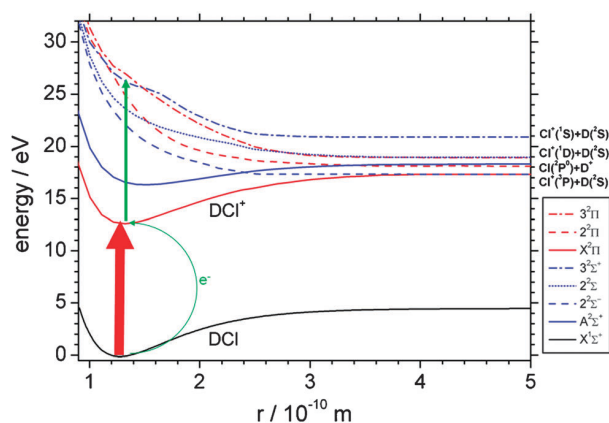


Fig. 4 Relevant potential energy curves for DCl and DCl^+ (adapted from ref. 36 and 37). The red arrow indicates tunnel ionization of DCl. The green arrows indicate further excitation by electron recollision with an energy of up to 19.9 eV to excited states of DCl^+ including the $2^2\Pi$ state leading to the formation of high energy D^+ ions.

$1.3 \times 10^{14} \text{ W cm}^{-2}$ predominantly occurs from the degenerate HOMOs ($3p$ Cl-orbitals)³¹ and leads to population of the $X^2\Pi$ electronic ground state of DCl^+ (solid red line in Fig. 4). The ejected electron originates from a chlorine lone-pair orbital, which leads to the stable electronic ground state of DCl^+ , such that neither D^+ nor Cl^+ ions can be detected after the ionization without additional excitation. The electron that was released upon the ionization of DCl and is accelerated by the oscillatory field of the laser pulse can recollide with the DCl^+ ion and lead to further excitation (solid green lines in Fig. 4). At the laser parameters in our experiment, the maximum recollision energy of the electron can be estimated as $3.17 U_p = 19.9 \text{ eV}$. U_p is the ponderomotive potential, defined as $U_p = I/4\omega^2$ (a.u.), where I is the laser intensity. The detection of D^+ fragments in the experiment with kinetic energies between 3 and 16 eV (peaking at *ca.* 7.9 eV) indicates that excitation of higher lying states including the $2^2\Pi$ state is important. Dissociation *via* bond softening³⁸ from either the $X^2\Pi$ or the $A^2\Sigma$ state, which might be reached by a sequential laser excitation by three photons,³¹ would lead to low kinetic energies of the D^+ and Cl^+ fragments. Akagi *et al.* have recently observed fragments from such a dissociation mechanism at kinetic energies below 0.05 eV (Cl^+) and below 2 eV (D^+).³¹ Since the strongest D^+ and Cl^+ signals are observed at much higher kinetic energies in our experiment, dissociation *via* bond-softening is not considered in the following discussion. After initial population of individual excited states of the DCl^+ ion by electron recollision, laser induced coupling of these states might occur. The coupling of various of the repulsive excited states might explain the similar momentum distributions for D^+ and Cl^+ fragments (since the initial population of a potential leading to D^+ fragments could ultimately result in the final formation of Cl^+ fragments, similar to what was observed in the case of coupling of excited states of CO^+ in a previous experiment).¹⁶ The ring-type pattern observed in the momentum distribution of the D^+ fragments shown in Fig. 1 might have a similar origin. Further insight into the fragmentation mechanisms requires advanced

theoretical modeling of the (recollision and) dissociation step, which remains a challenge for future work.

The angular distributions of the D^+ and Cl^+ fragment yields shown in Fig. 1 are similar and peak at around $\pm 60^\circ$ with respect to the laser polarization axis (0°). These angular distributions differ from the orientation dependent ionization probability of the HOMOs (which peaks at $\pm 45^\circ$) and indicate that the angular distribution that is imprinted on the DCI^+ ions in the ionization step is further modified in processes following ionization, *i.e.* recollisional excitation and dissociation.

The angular distribution of the asymmetric D^+ fragment ion emission from the dissociative ionization of DCI at the current laser parameters is further explored in Fig. 5a. The angle dependent asymmetries (see eqn (1)) have been fitted to $A(W, \theta, \varphi_{CEP}) = A_0(W, \theta) \cos(\varphi_{CEP})$ in order to determine the amplitude of the asymmetry $A_0(W, \theta)$ as a function of the kinetic energy W and the fragment emission angle θ . Although CEP-dependent observables do not have to follow a cosine (or sine) function, the fits shown in Fig. 2e give an indication that the asymmetries follow to a good approximation a cosine (or sine)-like behavior. This finding is in agreement with previous studies, where CEP-dependent asymmetries were explored (see *e.g.* ref. 5, 16, 39, and 40). Although the overall asymmetry amplitude is small, it can be seen in Fig. 5a that the absolute value of the asymmetry amplitude $|A_0(W, \theta)|$ peaks at energies in the range between 9 and 14 eV and angles around $\pm 45^\circ$. The amplitude becomes smaller towards emission angles of 0° and $\pm 90^\circ$. In order to show the angular dependence more clearly, the asymmetry map shown in Fig. 5a has been integrated from 6 to 16 eV for the polar presentation shown in Fig. 5b. The butterfly shape of the asymmetry amplitude resembles the orientation dependent ionization probability of the HOMOs (shown as solid line in Fig. 5b). The good agreement between the angular dependence of the asymmetry amplitude and the ionization probability from the HOMOs of DCI suggests that the ionization is responsible for the observed asymmetry in the emission of charged fragments.

The observed π -phase shift in the CEP-dependence of the asymmetry of D^+ and Cl^+ fragments (shown in Fig. 2) further supports the proposed mechanism. Since the DCI^+ ions are partially oriented and their orientation depends on the direction of the electric field, a π phase shift of the electric field also results in a π phase shift of the DCI^+ orientation. The orientation is directly reflected in the asymmetry of the ionic fragment emission.

Although we have not theoretically analyzed any additional contributions to the asymmetry from the dissociation step, preliminary calculations show that these contributions are small at the wavelength used in the current study.⁴¹ This is in contrast to previous theoretical studies at a wavelength around $6.4 \mu\text{m}$, where a pronounced CEP dependent asymmetry from the dissociation step was found.²¹ A full theoretical treatment of the dissociative ionization of DCI in few-cycle laser fields, including the ionization, recollisional excitation and dissociation steps, is a challenging task for future work.

5. Conclusions

We have studied the dissociative ionization of DCI in phase-stabilized, 5 fs laser fields at $1.3 \times 10^{14} \text{ W cm}^{-2}$. The measured angular distributions of the resulting D^+ and Cl^+ ions are similar and exhibit an anti-correlated CEP dependence. Importantly, the angular distribution of the asymmetry of D^+ ions resembles the orientation-dependent ionization probability of the HOMOs of DCI. These findings indicate that mainly the ionization step is responsible for the asymmetry in the fragment emission. Preferential ionization of DCI molecules with suitable orientation towards the laser electric field permits the control over the orientation of DCI^+ ions, which is reflected in the ionic fragment emission.

We believe that a similar control can be achieved in other heteronuclear molecules with potentially higher degree of orientation. Taking advantage of this control scheme, near single-cycle light fields may be used to produce samples of oriented molecular ions under field-free conditions

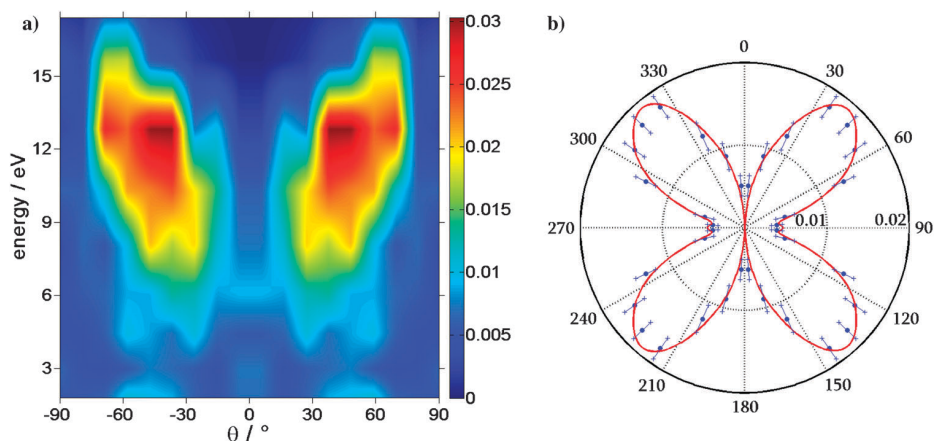


Fig. 5 (a) Absolute value of the asymmetry amplitude $|A_0(W, \theta)|$ of D^+ fragment ions (left–right symmetrized versus $\theta = 0$). (b) Polar plot of the energy-integrated (over 6–16 eV) asymmetry derived from (a) (blue dots) as compared to the calculated symmetric ionization probability from the HOMOs of DCI (red line). For visibility, the data and calculated results (which are up–down and left–right symmetric) are shown over a range of 2π .

(which are present after the ionization pulse has passed the sample) suitable for studies on their dynamics in the molecular frame.

Acknowledgements

We acknowledge Marc Vrakking and Ferenc Krausz for their support and the use of specialized equipment. We are grateful for support from the Chemical Sciences, Geosciences, and Biosciences Division, Office of Basic Energy Sciences, Office of Science, U.S. Department of Energy, the National Science Foundation under CHE-0822646 and the DFG via the grant We 1330/13, the Emmy-Noether program, the International Collaboration in Chemistry program and the Cluster of Excellence: Munich Center for Advanced Photonics (MAP).

References

- R. Kienberger, M. Uiberacker, M. F. Kling and F. Krausz, *J. Mod. Opt.*, 2007, **54**, 1985.
- K. M. Weitzel, *ChemPhysChem*, 2007, **8**, 213.
- M. F. Kling, C. Siedschlag, A. J. Verhoef, J. I. Khan, M. Schultze, T. Uphues, Y. Ni, M. Uiberacker, M. Drescher, F. Krausz and M. J. J. Vrakking, *Science*, 2006, **312**, 246.
- M. F. Kling, C. Siedschlag, I. Znakovskaya, A. J. Verhoef, S. Zherebtsov, F. Krausz, M. Lezius and M. J. J. Vrakking, *Mol. Phys.*, 2008, **106**, 455.
- M. Kremer, B. Fischer, B. Feuerstein, V. L. B. de Jesus, V. Sharma, C. Hofrichter, A. Rudenko, U. Thumm, C. D. Schröter, R. Moshhammer and J. Ullrich, *Phys. Rev. Lett.*, 2009, **103**, 213003.
- A. D. Bandrauk, S. Chelkowski and H. S. Nguyen, *Int. J. Quantum Chem.*, 2004, **100**, 834.
- D. Geppert, P. von den Hoff and R. de Vivie-Riedle, *J. Phys. B: At., Mol. Opt. Phys.*, 2008, **41**, 074006.
- S. Gräfe and M. Y. Ivanov, *Phys. Rev. Lett.*, 2007, **99**, 163603.
- V. Roudnev, B. D. Esry and I. Ben-Itzhak, *Phys. Rev. Lett.*, 2004, **93**, 163601.
- X. M. Tong and C. D. Lin, *Phys. Rev. Lett.*, 2007, **98**, 123002.
- P. Brumer and M. Shapiro, *Chem. Phys. Lett.*, 1986, **126**, 541.
- M. Shapiro, J. W. Hepburn and P. Brumer, *Chem. Phys. Lett.*, 1988, **149**, 451.
- R. J. Gordon and S. A. Rice, *Annu. Rev. Phys. Chem.*, 1997, **48**, 601.
- S.-P. Lu, S. M. Park, Y. Xie and R. J. Gordon, *J. Chem. Phys.*, 1992, **96**, 6613.
- D. Ray, F. He, S. De, W. Cao, H. Mashiko, P. Ranitovic, K. P. Singh, I. Znakovskaya, U. Thumm, G. G. Paulus, M. F. Kling, I. V. Litvinyuk and C. L. Cocke, *Phys. Rev. Lett.*, 2009, **103**, 223201.
- I. Znakovskaya, P. von den Hoff, S. Zherebtsov, A. Wirth, O. Herrwerth, M. J. J. Vrakking, R. de Vivie-Riedle and M. F. Kling, *Phys. Rev. Lett.*, 2009, **103**, 103002.
- P. von den Hoff, I. Znakovskaya, M. F. Kling and R. de Vivie-Riedle, *Chem. Phys.*, 2009, **366**, 139.
- P. von den Hoff, I. Znakovskaya, S. Zherebtsov, M. F. Kling and R. de Vivie-Riedle, *Appl. Phys. B: Lasers Opt.*, 2010, **98**, 659.
- H. G. Breunig, A. Lauer and K. M. Weitzel, *J. Phys. Chem. A*, 2006, **110**, 6395.
- M. V. Korolkov and K. M. Weitzel, *J. Chem. Theory Comput.*, 2006, **2**, 1492.
- M. V. Korolkov and K. M. Weitzel, *Chem. Phys.*, 2007, **338**, 277.
- A. J. Verhoef, A. Fernandez, M. Lezius, K. O'Keeffe, M. Uiberacker and F. Krausz, *Opt. Lett.*, 2006, **31**, 3520.
- S. Micheau, Z. Chen, A. T. Le, J. Rauschenberger, M. F. Kling and C. D. Lin, *Phys. Rev. Lett.*, 2009, **102**, 073001.
- A. T. J. B. Eppink and D. H. Parker, *Rev. Sci. Instrum.*, 1997, **68**, 3477.
- O. Ghafur, W. Siu, P. Johnsson, M. F. Kling, M. Drescher and M. J. J. Vrakking, *Rev. Sci. Instrum.*, 2009, **80**, 033110.
- M. F. Kling, J. Rauschenberger, A. J. Verhoef, E. Hasovic, T. Uphues, D. B. Milosevic, H. G. Muller and M. J. J. Vrakking, *New J. Phys.*, 2008, **10**, 025024.
- M. J. J. Vrakking, *Rev. Sci. Instrum.*, 2001, **72**, 4084.
- J. Muth-Böhm, A. Becker and F. H. M. Faisal, *Phys. Rev. Lett.*, 2000, **85**, 2280.
- X. M. Tong, Z. Zhao and C. D. Lin, *Phys. Rev. A: At., Mol., Opt. Phys.*, 2002, **66**, 033402.
- S. F. Zhao, C. Jin, A. T. Le and C. D. Lin, *Phys. Rev. A: At., Mol., Opt. Phys.*, 2010, **82**, 035402.
- H. Akagi, T. Otobe, A. Staudte, A. Shiner, F. Turner, R. Dörner, D. M. Villeneuve and P. B. Corkum, *Science*, 2009, **325**, 1364.
- B. K. McFarland, J. P. Farrell, P. H. Bucksbaum and M. Gühr, *Science*, 2008, **322**, 1232.
- O. Smirnova, Y. Mairesse, S. Patchkovskii, N. Dudovich, D. Villeneuve, P. Corkum and M. Y. Ivanov, *Nature*, 2009, **460**, 972.
- B. M. Smirnov and M. I. Chibisov, *JETP Lett. Engl. Transl.*, 1966, **22**, 585.
- H. J. Werner and P. J. Knowles *et al.*, *Molpro, version 2006.1*, 2006.
- V. S. Gurin, M. V. Korolkov, V. E. Matulis and S. K. Rkhmanov, *J. Chem. Phys.*, 2007, **126**, 124321.
- A. D. Pradhan, K. P. Kirby and A. Dalgarno, *J. Chem. Phys.*, 1991, **95**, 9009.
- P. H. Bucksbaum, A. Zavriyev, H. G. Muller and D. W. Schumacher, *Phys. Rev. Lett.*, 1990, **64**, 1883.
- N. G. Johnson, O. Herrwerth, A. Wirth, S. De, I. Ben-Itzhak, M. Lezius, B. Bergues, M. F. Kling, A. Senftleben, C. D. Schröter, R. Moshhammer, J. Ullrich, K. J. Betsch, R. R. Jones, A. M. Saylor, T. Rathje, K. Rühle, W. Müller and G. G. Paulus, *Phys. Rev. A: At., Mol., Opt. Phys.*, 2011, **83**, 013412.
- M. F. Kling and M. J. J. Vrakking, *Annu. Rev. Phys. Chem.*, 2008, **59**, 463.
- M. V. Korolkov and K. M. Weitzel, unpublished.

Paper VII**Subcycle controlled charge-directed reactivity with few-cycle midinfrared pulses.**

Znakovskaya, I., von den Hoff, P., Marcus, G., Zherebtsov, S., Bergues, B., Gu, X., Deng, Y., Vrakking, M. J. J., Kienberger, R., Krausz, F., de Vivie-Riedle, R. & Kling, M. F.

Phys. Rev. Lett. **108**, 063002 (2012).

Subcycle Controlled Charge-Directed Reactivity with Few-Cycle Midinfrared Pulses

I. Znakovskaya,¹ P. von den Hoff,² G. Marcus,^{1,3} S. Zhrebtsov,¹ B. Bergues,¹ X. Gu,¹ Y. Deng,¹ M. J. J. Vrakking,⁴
R. Kienberger,¹ F. Krausz,¹ R. de Vivie-Riedle,² and M. F. Kling^{1,5}¹Max-Planck Institute of Quantum Optics, Hans-Kopfermann-Strasse 1, D-85748 Garching, Germany²Department für Chemie und Biochemie, Ludwig-Maximilians-Universität München, Butenandt-Strasse 11,
D-81377 München, Germany³Department of Applied Physics, The Benin School of Engineering and Computer Science,
The Hebrew University of Jerusalem, Jerusalem, 91904, Israel⁴Max-Born-Institut, Max-Born Strasse 2A, D-12489 Berlin, Germany⁵J. R. Macdonald Laboratory, Kansas State University, Cardwell Hall 116, Manhattan, Kansas 66506, USA

(Received 19 August 2011; published 8 February 2012)

The steering of electron motion in molecules is accessible with waveform-controlled few-cycle laser light and may control the outcome of light-induced chemical reactions. An optical cycle of light, however, is much shorter than the duration of the fastest dissociation reactions, severely limiting the degree of control that can be achieved. To overcome this limitation, we extended the control metrology to the midinfrared studying the prototypical dissociative ionization of D_2 at $2.1 \mu\text{m}$. Pronounced subcycle control of the directional D^+ ion emission from the fragmentation of D_2^+ is observed, demonstrating unprecedented charge-directed reactivity. Two reaction pathways, showing directional ion emission, could be observed and controlled simultaneously for the first time. Quantum-dynamical calculations elucidate the dissociation channels, their observed phase relation, and the control mechanisms.

DOI: 10.1103/PhysRevLett.108.063002

PACS numbers: 33.80.Wz, 31.15.A-, 31.70.Hq

Coherent control of photochemical reactions has been achieved in the past decades by manipulating the laser frequency, phase, and polarization [1]. An exciting novel perspective is to directly control a molecular rearrangement by the waveform of a carrier-envelope phase (CEP) stabilized few-cycle laser pulse $E(t) = E_0(t) \cos(\omega t + \varphi)$ for an envelope function $E_0(t)$, angular carrier frequency ω , and CEP φ . The CEP adds a new dimension to the existing control parameters and offers the potential to very significantly enhance the possibilities for achieving control over chemical reactions by steering the electrons [2]. Note that the CEP control is related to but not identical to an $\omega - 2\omega$ phase control (see, e.g., [3,4]). The steering of electron motion in molecules can be achieved by superimposing two or more electronic states of different parity with a well-defined phase relationship that depends on the CEP. The CEP guided electron motion inside the molecule may break or even form chemical bonds in the sense of charge-directed reactivity [5].

CEP-stabilized few-cycle pulses in the near infrared have been used to control the dissociative ionization of diatomic molecules [6–11]. To facilitate an efficient CEP control, it is necessary to adjust the time scale of the few-cycle pulse to the time scale of the nuclear motion. As an example, the dissociation time for the molecular hydrogen ion via bond softening (BS) [12] may be estimated as approximately half of a vibrational period, corresponding to 12 fs [13].

The dependence of the CEP-controlled electron localization in molecular hydrogen has been explored as a function of

the laser intensity [14] and pulse duration [15]. Previous experiments and theory have indicated that the CEP control decreases exponentially with the number of laser cycles [6,15–17], making it necessary to keep the number of laser cycles for CEP control small. Therefore, the application of this control scheme to larger molecules with longer dissociation times necessarily requires larger wavelengths λ with optical periods $T = \lambda/c$ (where c is the speed of light) that are significantly longer in time than their counterparts in the near infrared. Here, we open the path to CEP control at larger wavelengths via experimentally and theoretically exploring the subcycle control of the dissociative ionization of D_2 in intense few-cycle CEP-stable midinfrared laser fields. The demonstration of efficient control of charge-directed reactivity in this proof-of-principle study is relevant to the control of larger molecules and complex molecular processes. As an example, the branching ratio at conical intersections is expected to be strongly dependent on charge localization induced by a midinfrared few-cycle pulse [18].

Midinfrared pulses at $2.1 \mu\text{m}$ were generated at a repetition rate of 1 kHz by an optical parametric chirped-pulse amplification system [19]. The experimental setup essentially resembles the one described in [20]. The experiments reported here were carried out with 25 fs linearly polarized laser pulses. The relative CEP φ_{CEP} in the experiment was varied by changing the amount of dispersive material in the beam path. The laser pulses were focused to an intensity of $(6.2 \pm 1.5) \times 10^{13} \text{ W cm}^{-2}$ in the center of a velocity-map imaging spectrometer [21] with a CaF_2 lens ($f = 30 \text{ cm}$), where they intersected an effusive D_2 gas jet.

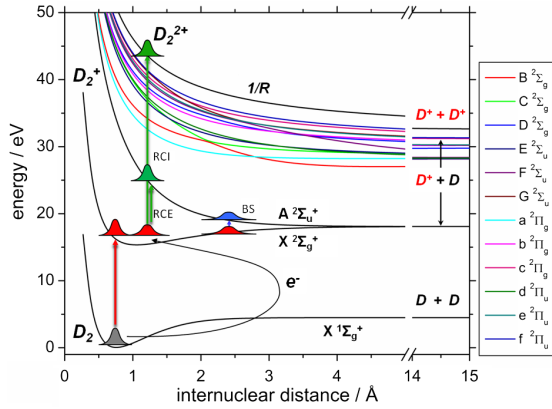


FIG. 1 (color online). Relevant potential energy surfaces of D₂, D₂⁺, and D₂²⁺ obtained by *ab initio* calculations described in the text. The higher lying excited electronic states of D₂⁺ above the A state are labeled alphabetically according to their symmetry. The red arrow indicates tunnel ionization of D₂, the blue arrow bond softening (BS), and the green arrows recollision induced excitation (RCE) and ionization (RCI).

The principle pathways for the dissociative ionization of D₂ are displayed in Fig. 1. D₂⁺ is produced from D₂ by tunnel ionization in the intense laser field (red arrow). Thereby a nuclear wave packet is launched on the X²Σ_g⁺ potential. This initial step can be followed by several processes leading to the dissociation of the molecular ion: (i) bond softening via the laser-induced coupling of the X²Σ_g⁺ and A²Σ_u⁺ states [12] (BS, blue arrow), (ii) recollisional excitation (RCE), (iii) recollisional ionization (RCI) (green arrows), and (iv) laser-induced excitation to higher lying D₂⁺ states (not shown). In our study, two pathways [(i) and (ii)] leading to the directional D⁺ ion emission can be differentiated and controlled within the same experiment. The results, including the complex phase relation between the different channels, can be understood from our time-dependent Schrödinger equation calculations.

Figure 2(a) shows a cut for $p_z = 0$ through the 3D momentum distribution of the D⁺ ions. The electric field was polarized along the p_y axis. The corresponding measured D⁺ kinetic energy spectrum, integrated over the full solid angle, is displayed in Fig. 2(b) (black solid line). The spectrum reveals 4 regions, which are separated in Fig. 2(a) by dashed circles. The most intense contribution in the spectrum between 0 to 1 eV is assigned to BS. Three additional contributions can be identified at higher energies in the ranges 1–4 eV, 4–9 eV, and 9–13 eV. The identification of these channels together with our theoretical treatment is discussed below.

The directional D⁺ ion emission as a function of the measured phase φ_{CEP} (which exhibits a phase offset with respect to the absolute CEP φ) and momentum p is analyzed by the angle-integrated asymmetry parameter

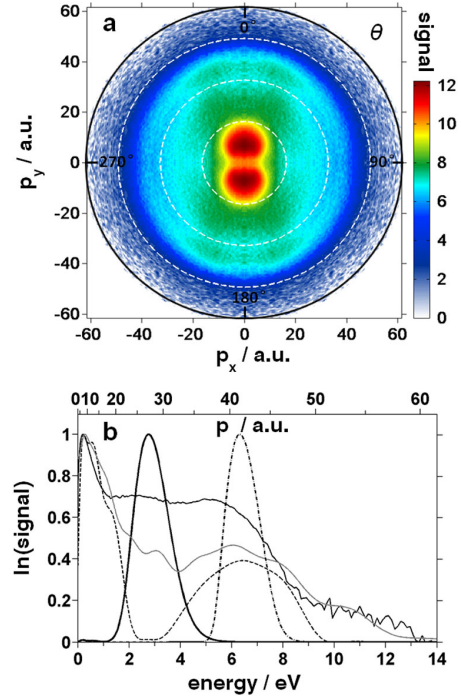


FIG. 2 (color online). (a) Inverted, CEP-averaged two-dimensional D⁺ momentum distribution (p_y versus p_x at $p_z = 0$). The laser is polarized along the p_y axis. The momentum distribution was left-right as well as up-down symmetrized to increase the signal-to-noise ratio. The dashed circles separate the four contributions discussed in the text. A logarithmic color scale was used. (b) Angular integrated kinetic energy spectrum of D⁺ ions obtained from the experimental data (black solid line) and calculated spectra for the bond-softening dissociation involving only the X and A states of D₂⁺ (dashed line) and also the 11 higher states of D₂⁺ shown in Fig. 1 (gray solid line). The theoretical results for the dissociation via recollision induced excitation and ionization are shown as bold and dash-dotted black lines, respectively.

$$A(p, \varphi_{\text{CEP}}) = \frac{N_{\text{up}}(p, \varphi_{\text{CEP}}) - N_{\text{down}}(p, \varphi_{\text{CEP}})}{N_{\text{up}}(p, \varphi_{\text{CEP}}) + N_{\text{down}}(p, \varphi_{\text{CEP}})}, \quad (1)$$

with the ion yields $N_{\text{up}}(p, \varphi_{\text{CEP}})$ and $N_{\text{down}}(p, \varphi_{\text{CEP}})$ in the up and down directions, respectively. The ion yields were integrated over an opening angle of 20° along the laser polarization axis. The asymmetry $A(p, \varphi)$ is shown in Fig. 3(a), where the experimental phase offset was calibrated to achieve best agreement between theory and experiment in the CEP-dependent asymmetry oscillation for the BS channel. A high degree of asymmetry (with an amplitude exceeding 0.2) is found at energies below 1 eV, the energy range corresponding to the BS channel. The asymmetry in this channel shows a tilt in kinetic energy of its oscillation with CEP and an additional phase jump at 0.17 eV, which has not been observed in an earlier study in the near infrared [7]. A second asymmetry

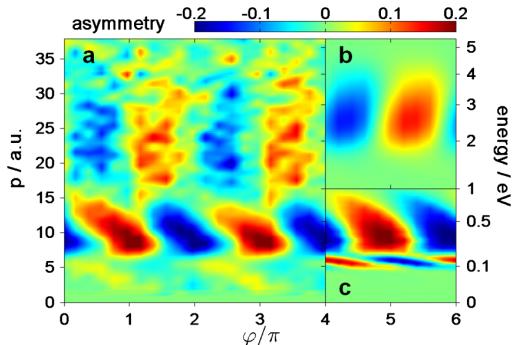


FIG. 3 (color online). (a) D^+ ion emission asymmetry as a function of the fragment momentum (corresponding kinetic energy scale on the right) and relative phase φ_{CEP} of the D^+ ion emission obtained by integrating over a full opening angle of 20° along the laser polarization axis. (b) Asymmetry obtained by the calculations for the RCE channel. (c) Same as (b) for the BS channel.

contribution in the energy range 1–4 eV has a weaker (maximum 0.1) amplitude and its oscillation with CEP is independent of kinetic energy. A π phase jump between the two channels is observed at approximately 1 eV. The observation of CEP control for various dissociation channels and their phase relation is very remarkable when compared to earlier results obtained in the near infrared [6,7], where this was not feasible so far. Above 4 eV only vanishingly small or no asymmetry was measured under the present experimental conditions (compared to asymmetry contributions up to approximately 8 eV in the near infrared [6]).

We model the dissociative ionization of D_2 using our previously published approach to treat the coupled electron and nuclear wave packet dynamics [17]. For details, see the Supplemental Material [22]. The required potential energy surfaces were calculated using the quantum chemistry package MOLPRO [23] on the CASSCF(1, 15) level of theory using the $(11s, 7p) \rightarrow [6s, 5p]$ contracted Gaussian basis set introduced by Whitten and Huzinaga [24,25]. The calculations were performed for molecules, aligned along the laser polarization axis, under the experimental laser conditions.

To simulate the BS mechanism we projected the vibrational ground state wave function of the D_2 molecule on the $X^2\Sigma_g^+$ potential and assumed that ionization only takes place at the peaks of the electric field (corresponding to the highest ionization probability). In the case of the RCE mechanism the wave packet is initially propagated on the $X^2\Sigma_g^+$ surface and projected to the $A^2\Sigma_u^+$ surface (for RCE) and the D_2^+ surface (for RCI) at the time of recollision (which is $\frac{2}{3}$ of an optical cycle, i.e., 4.7 fs at 2.1 μm [26]).

Figure 2(b) shows the theoretical results for different dissociation channels and conditions. The dashed curve shows the calculated D^+ kinetic energy spectrum for the

laser-induced dissociation mechanism including only the $X^2\Sigma_g^+$ and $A^2\Sigma_u^+$ surfaces of D_2^+ . The gray curve shows the result, where also the 11 higher excited states shown in Fig. 1 have been included. The experimental spectrum below 2 eV is reproduced well by both theoretical results and assigned to the BS channel. The contribution in the energy range 4–9 eV results from the instantaneous population of the A state within the ionizing half-cycle. The high-energy tail of the measured D^+ spectrum above 9 eV is only captured by the calculations that include the higher excited states [gray curve in Fig. 2(b)]. Such a high-energy tail has also been observed in earlier experimental work at 760 nm [6], but has not been explained yet. The spectrum resulting from a calculation for the RCE dissociation is shown as a bold black curve. The resulting contribution can explain the strong experimental signal between 2 and 4 eV. We also computed the spectrum resulting from RCI (dash-dotted curve), which may occur due to the high ponderomotive potential in the midinfrared and thus high recollision energy (reaching up to 84.5 eV at $6.2 \times 10^{13} \text{ W cm}^{-2}$). Double ionization results in the Coulomb explosion of the molecule and production of two D^+ fragments that are emitted into opposite directions along the laser polarization axis. D^+ fragments from this dissociation channel cannot produce any asymmetry in the ion emission, and spectral overlap with other channels would reduce or even mask observable asymmetries.

The calculated asymmetries corresponding to the dissociation of D_2^+ by RCE and BS are shown in Figs. 3(b) and 3(c), respectively (each channel is calculated separately). In order to facilitate a comparison of the theoretical results with the experimental data, the asymmetries were calculated assuming ionization by the 5 most intense peaks of the laser electric field. Inclusion of further peaks did not lead to significant changes. Although volume averaging effects have not been considered in our theoretical treatment, the asymmetry amplitude and its energy-dependent oscillatory behavior with the CEP are well reproduced by the calculations. Note that the two calculations were performed for the same CEP φ and were not shifted against each other afterwards. The phase jump at 0.17 eV in the BS channel is also reproduced.

In the calculations shown in Fig. 3(b) we included only the first recollision after the initial ionization. Calculations, considering later recollisions, are contained in the Supplemental Material [22] and indicate that the experimentally observed lower kinetic energies in the RCE channel (below 2 eV) may arise from subsequent recollisions. We find that at 2.1 μm the first three recollision events result in the same sign for the asymmetry. Autoionization and/or photoionization of highly excited neutral D_2 molecules, which is more likely in the tunneling regime [27], may also produce an asymmetry in the breakup of hydrogen [28]. These mechanisms may explain some remaining differences between the experimental and theoretical data.

Their theoretical treatment at long wavelengths and high laser intensities is, however, beyond current computing capabilities and was therefore not considered here.

Within the framework of our model, the subcycle control is understood as follows: the laser-induced coupling of multiple electronic states produces a coherent superposition of these states, which results in the localization of the electron in D_2^+ and the asymmetric breakup of the molecule. The phase of the coherent superposition, defining the localization of the electron, is controlled by the phase of the applied electric field (here via the CEP). In the case of the BS mechanism an initially prepared wave packet on the X state of D_2^+ moves toward the outer turning point of the potential and is efficiently coupled to the $A^2\Sigma_u^+$ state at large internuclear distances (see Fig. 1). Our quantum mechanical calculations reproduce the observed tilt of the asymmetry with kinetic energy and the phase jump at 0.17 eV (see Fig. 3). The phase jump likely originates from the laser coupling with the slowest components of the dissociating wave packet. Future studies involving semiclassical approaches [29] and full two-electron calculations including correlation effects [30] might be helpful to elucidate this aspect in more detail.

The higher energy contribution in the BS channel between 4 and 10 eV (see Fig. 2) originates from the direct, laser-induced population of the A state right after ionization with subsequent dissociation. As this fast component of the wave packet is not coupled back to the X state, the symmetry is not broken and thus no asymmetry is observable in this energy range. In the RCE mechanism the A state is populated by recollision at later times. Because of the potential shape, this results in lower kinetic energies in the range between 2 and 4 eV. During the dissociation the remaining laser couples population from the A state back to the X state, leading to a coherent superposition of both states and an observable asymmetry. The electronic states are superimposed in the BS and RCE mechanisms with different phases, resulting in the π phase jump in the asymmetry at 1 eV.

The wavelength dependence of the asymmetry is further analyzed by calculations shown in Fig. 4. The energy integrated asymmetry amplitudes for the BS channel considering ionization at the peak electric field (for $\varphi = 0$) using a 3.5-cycle pulse for different wavelengths are shown in Fig. 4(a). The asymmetry oscillates close to zero around 800 nm, explaining the difficulty to observe the CEP control in this channel with near-infrared few-cycle pulses. With increasing wavelength, the asymmetry amplitude reaches higher values. This behavior supports our initial statement that the duration of the few-cycle laser pulse has to match the time scale of the chemical reaction. A further example for 2-cycle pulses is shown in the Supplemental Material [22]. The wavelength dependence of the RCE dissociation is shown in Fig. 4(b) as a function of the D^+ fragment kinetic energy and the recollision time. With

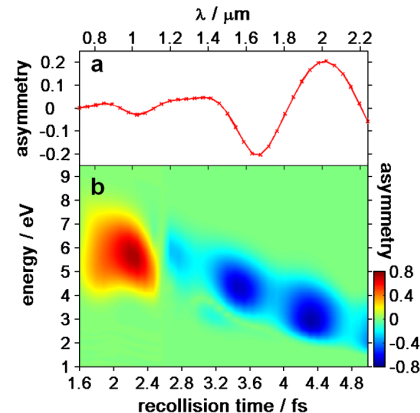


FIG. 4 (color online). (a) Calculated energy integrated asymmetry amplitude in the BS channel for various laser wavelength assuming a 3.5-cycle pulse. (b) Calculated asymmetry map for the RCE channel as a function of kinetic energy and recollision time (corresponding to the wavelength given on the top axis).

increasing wavelength, the recollision time increases, leading to an excitation to the A state at larger internuclear distances. As a result the kinetic energy of the D^+ fragments is decreasing from initially around 6 eV at 760 nm to less than 3 eV at 2.1 μm .

The sign of the asymmetry in the BS and RCE dissociation channels is strongly dependent on the wavelength. Therefore, the relative phase between the CEP-dependent asymmetry oscillation of the two channels depends on the wavelength as well. Coincidentally, at 2.1 μm the asymmetries of the two channels exhibit an opposite sign, reproducing the experimental observation [see Fig. 3(a)].

Comparing the current results to earlier work using near-infrared few-cycle laser pulses [6,7], it is evident that the CEP control of electron localization in the dissociation of D_2 is much more efficient for the BS channel when mid-infrared pulses are applied. The larger wavelength implies a better match between the duration of the laser pulse and the dissociation time of the molecule, while the number of optical cycles is kept small. Thus for the few-cycle pulses used here, the wave packet in the X state can be efficiently coupled to the A state at large internuclear distances. Both aspects lead to the observed high degree of control of charge-directed reactivity in the dissociation reaction.

The simultaneous observation and control of the asymmetry resulting from the BS and the RCE dissociation channels is novel to the present study. Our time-dependent Schrödinger equation calculations identified the underlying mechanism leading to the observed asymmetries and reproduced well the general features of both channels that are controllable by the CEP. The details in the energy and CEP-dependent asymmetry provide strong constraints to theoretical models.

We acknowledge discussions of these results with B. Esry, I. Ben-Itzhak, and F. Martin. We are grateful for

support by the Chemical Sciences, Geosciences, and Biosciences Division, Office of Basic Energy Sciences, Office of Science, U.S. Department of Energy, the National Science Foundation under CHE-0822646, the European network ATTOFEL, Laserlab Europe, the German Science Foundation via the Emmy-Noether program, and the Cluster of Excellence: Munich Center for Advanced Photonics.

-
- [1] T. Brixner and G. Gerber, *Chem. Phys. Chem.* **4**, 418 (2003).
- [2] M. F. Kling and M. J. J. Vrakking, *Annu. Rev. Phys. Chem.* **59**, 463 (2008).
- [3] D. Ray *et al.*, *Phys. Rev. Lett.* **103**, 223201 (2009).
- [4] M. Abel *et al.*, *Laser Photon. Rev.* **5**, 352 (2011).
- [5] R. Weinkauff *et al.*, *J. Phys. Chem.* **99**, 11 255 (1995).
- [6] M. F. Kling *et al.*, *Science* **312**, 246 (2006).
- [7] M. Kremer *et al.*, *Phys. Rev. Lett.* **103**, 213003 (2009).
- [8] I. Znakovskaya *et al.*, *Phys. Rev. Lett.* **103**, 103002 (2009).
- [9] B. Fischer *et al.*, *Phys. Rev. Lett.* **105**, 223001 (2010).
- [10] I. Znakovskaya *et al.*, *Phys. Chem. Chem. Phys.* **13**, 8653 (2011).
- [11] Y. Liu *et al.*, *Phys. Rev. Lett.* **106**, 073004 (2011).
- [12] P. H. Bucksbaum *et al.*, *Phys. Rev. Lett.* **64**, 1883 (1990).
- [13] T. Ergler *et al.*, *Phys. Rev. Lett.* **97**, 193001 (2006).
- [14] F. He, A. Becker, and U. Thumm, *Phys. Rev. Lett.* **101**, 213002 (2008).
- [15] M. F. Kling *et al.*, *Mol. Phys.* **106**, 455 (2008).
- [16] V. Roudnev and B. D. Esry, *Phys. Rev. Lett.* **99**, 220406 (2007).
- [17] D. Geppert, P. von den Hoff, and R. de Vivie-Riedle, *J. Phys. B* **41**, 074006 (2008).
- [18] P. von den Hoff *et al.*, *IEEE J. Sel. Top. Quantum Electron.* (in press).
- [19] X. Gu *et al.*, *Opt. Express* **17**, 62 (2009).
- [20] B. Bergues *et al.*, *New J. Phys.* **13**, 063010 (2011).
- [21] O. Ghafur *et al.*, *Rev. Sci. Instrum.* **80**, 033110 (2009).
- [22] See Supplemental Material at <http://link.aps.org/supplemental/10.1103/PhysRevLett.108.063002> for a description of the theoretical methods and further calculations.
- [23] H.-J. Werner and P. J. Knowles *et al.*, MOLPRO, version 2006.1, 2006.
- [24] J. L. Whitten, *J. Chem. Phys.* **39**, 349 (1963).
- [25] S. Huzinaga, *J. Chem. Phys.* **42**, 1293 (1965).
- [26] J. Hu *et al.*, *Phys. Rev. A* **74**, 063417 (2006).
- [27] T. Nubbemeyer *et al.*, *Phys. Rev. Lett.* **101**, 233001 (2008).
- [28] G. Sansone *et al.*, *Nature (London)* **465**, 763 (2010).
- [29] F. Kelkensberg *et al.*, *Phys. Chem. Chem. Phys.* **13**, 8647 (2011).
- [30] S. Gräfe and M. Y. Ivanov, *Phys. Rev. Lett.* **99**, 163603 (2007).

